SUPER-RESOLUTION OF PHOTODYNAMIC EMITTERS BY FLUORESCENCE FLUCTUATION ANALYSIS

By

Rémi Louis Jean Boulineau

THIS DISSERTATION IS SUBMITTED
FOR THE DEGREE OF
DOCTOR OF PHILOSOPHY
AT
The University of Sussex
Falmer
Sussex, UK
January 2014

I hereby declare that this thesis has not been and will not be, submitted in whole or in part to another University for the award of any other degree.

Signature:.....

Date:.....

« En vérité, le chemin importe peu, la volonté d'arriver suffit à tout. »

Albert Camus

Le mythe de Sisyphe

A mes parents

Abstract

A range of fluorescence fluctuation analysis methods were developed and applied to labels commonly used in biological samples. Various super-resolution techniques were demonstrated *in vitro* and *in vivo* using objective-type Total Internal Reflection Fluorescence Microscopy (TIRFM).

An experimental Fluorescence Correlation Spectroscopy (FCS) setup was developed along with associated post-acquisition data algorithms. The technique was applied to investigate the stoichiometry of a protein subunit of ribonucleotide reductase (RNR). FCS method was adapted with an Electron Multiplying Charge Coupled Device (EMMCD) detection scheme and applied to inorganic Quantum Dots (QDs) diffusing in solutions of different viscosities.

Super-resolution Optical Fluctuation Imaging (SOFI) algorithm was implemented in ImageJ software and conclusive results obtained on reference samples of QDs and combed DNA. Potential applications of temporal correlation analysis to the study of diffusive processes and single particle tracking were also discussed.

A new super-resolution technique applicable to multiple adjacent fluorescent molecules called Direct Object Resolution by Image Subtraction (DORIS) was developed and tested with QD complexes. The method enables one to accurately map the position of two emitters displaying intermittency in their fluorescence emission and separated by a distance below the diffraction limit, without the need of complex instrumentation or analysis. The technique relies on the subtraction of the Point Spread Function (PSF) of each single fluorescent probe, and is in theory applicable to any blinking or flickering dye. The principle was first demonstrated on simulated data and experimentally on QDs coupled by 100-basepair double-stranded DNA constructs. Super-resolution by image subtraction was further applied *in vivo* in *S. pombe* cells, where distances between clustered fluorescent fusion proteins were accurately determined. The selective activation of photoswitchable probes mEos3 was exploited to optimise the DORIS subtraction process and provided a simple method to determine the relative positions of closely spaced emitters within an aggregate, as encountered in association sites or multimeric complexes.

Acknowledgments

As the end of my thesis approaches, I can say that I truly enjoyed my time as a postgraduate at the University of Sussex. This is because I was lucky enough to be part of an exciting multidisciplinary project during which I met a lot of friendly people and great scientists.

My first thanks obviously goes to Dr Mark Osborne for his inspirational take on science, friendly advices and contagious enthusiasm. For all this support, and much more, I am immensely grateful. Thank you also to my co-supervisor Prof. Antony Carr for the cross-disciplinary PhD opportunity and his guidance on the project.

I would wish to gratefully acknowledge the European Commission for providing the funding for my PhD through a Marie Curie Action Fellowship.

I would also like to thank all the people I have encountered at the Genome Damage and Stability Centre (GDSC), especially Ann-Sofie from whom I have learnt a great deal at the beginning of my PhD and Tom for his enthusiasm to apply the DORIS technique *in vivo* and the fun discussions in the lab about football, music or any particularly random subject that helped me to cope with the malediction of the C-focus! Thanks to Sophie for her assistance in the process of building and characterisation of the PALM microscope and the great company in the laboratory.

Thank you to the people who helped me during the course of my PhD: Mr Olaolu Akinsete for the Cdc22-mEos2 cells preparation, Dr Gokhan Akman for the preparation of the DNA sample used in the combing experiment, Dr Alex Herbert for interesting discussions on cross-correlation for stage drift correction and Dr Julian Thorpe for letting me use the TEM facilities.

I am grateful to all the members of the Osborne Lab that made work become a convivial experience. Thanks to Alastair, Simon, Alex, Asuka, Amal, Zainab, Hope, Asma and JK for making my stay at Sussex enjoyable.

Outside of work, I would like to thank my parents and grandparents for their support over the years; I would not have been able to complete this PhD without you. Thanks also to all my friends from France for being there when I wanted a break from correlation functions.

Finally I would like to say a special thank you to my little friend Jenny for her constant help and support during those past three years.

Table of Contents

List of Figures

List of Tables

List of Abbreviations

ADP	Adenosine Diphosphate
ADU	Analogue-to-Digital Unit
AFM	Atomic Force Microscopy
APD	Avalanche Photon Detector
ATP	Adenosine Triphosphate
BALM	Bleaching/blinking Assisted Localisation Microscopy
bp	Base Pair
BSA	Bovine Serum Albumin
CCD	Charge Coupled Device
CDP	Cytidine Diphosphate
DNA	Deoxyribonucleic Acid
dNDP	Deoxynucleoside Diphosphate
dNTP	Deoxynucleoside Triphosphate
DOPI	Defocused Orientation and Position Imaging
DORIS	Direct Object Resolution by Image Subtraction
ds	Double Stranded
DSB	Double Strand Break
EGFP	Enhanced Green Fluorescent Protein
EM	Electron Microscopy
EMCCD	Electron Multiplying Charge Coupled Device
FCS	Fluorescence Correlation Spectroscopy
FFT	Fast Fourier Transform
FIONA	Fluorescence Imaging with One Nanometer Accuracy
FLIM	Fluorescence Lifetime Imaging Microscopy
FLIP	Fluorescence Loss In Photobleaching
FPALM	Fluorescent Photoactivation Localisation Microscopy
FRAP	Fluorescence Recovery After Photobleaching
FRET	Forster Resonance Energy Transfer
FWHM	Full Width at Half Maximum
GDP	Guanosine Diphosphate
GFP	Green Fluorescent Protein

GSD	Ground State Depletion
ICS	Image Correlation Spectroscopy
I^nM	Image Interference
MDF	Molecule Detection Function
NA	Numerical Aperture
NALMS	Nanometer-Localised Multiple Single-molecule
NDP	Nucleoside Diphosphate
NSOM	Near-field Scanning Optical Microscopy
PAINT	Point Accumulation for Imaging in Nanoscale Topography
PALM	Photoactivation Localisation Microscopy
PBS	Phosphate Buffered Saline
PCH	Photon Counting Histogram
pcSOFI	Photochromic Stochastic Optical Fluctuation Imaging
PFG-NMR	Pulsed Field Gradient-Nuclear Magnetic Resonance
PSF	Point Spread Function
QD	Quantum Dot
RCA	Replication Combing Assay
RESOLFT	Reversible Saturable Optical Fluorescence Transition
RhB	Rhodamine B
RNR	Ribonucleotide Reductase
ROI	Region Of Interest
SBR	Signal to Background Ratio
SDS-PAGE	Sodium Dodecyl Sulfate-Polyacrylamide Gel Electrophoresis
sFCS	Scanning Fluorescence Correlation Spectroscopy
SHREC	Single molecule High Resolution Colocalisation
SHRimP	Single molecule High Resolution Imaging with Photobleaching
SIM	Structured Illumination Microscopy
SNR	Signal to Noise Ratio
SOFI	Super-resolution Optical Fluctuation Imaging
Spd1	S Phase Delay Inhibitor 1
S. pombe	*Schizosaccharomyces pombe*
STED	Stimulated Emission Depletion
STORM	Stochastic Optical Reconstruction Microscopy
TEM	Transmission Electron Microscopy
TIRFM	Total Internal Reflection Fluorescence Microscopy
TMR	Tetramethyl Rhodamine
UDP	Uridine Diphosphate

List of Publications

Rémi L. Boulineau and Mark A. Osborne, *Direct object resolution by image subtraction: a new molecular ruler for nanometric measurements on complexed fluorophores*, Chemical Communications, Royal Society of Chemistry, 2013. 49 (49): p. 5559-5561.

Chapter 1

Introduction

The influence of nanometre scale molecular organisation on the behaviour of macroscopic structures has retained a great deal of attention during the past decades. Whilst this interest in understanding the underlying causes of many fundamental processes might seem relatively recent to a contemporary reader, it is worth noting that nano-sized materials have been used throughout the past millennium of human history. Perhaps the most famous demonstration is the Lycurgus cup, a roman artifact dated from the fourth-century A.D. and made of glass containing gold-silver alloyed nanoparticles. The distribution of these components has an impact on the appearance of the cup depending on the incident light source position: its usual green colour under reflected light becomes a brilliant red when a light source is placed inside the artifact. Other applications have been developed as well in different civilisations, such as the azure pigment introduced by the Mayas around A.D. 800 in which the indigo dyes were stabilised inside clay nanopores. The skilled artisans of those days did not rationalise the cause of modification of the material properties and rather used a trial and error approach to obtain the best results. In 1857, Michael Faraday attempted to attribute the variety of colours of cathedrals' windows by their content in metal particles, an approach which was completed by Gustav Mie in 1908. However, the first visionary contribution triggering the rise in nanotechnology research is often attributed to Richard Feynman, who won the Nobel Prize in 1965 for his work in quantum electrodynamics. He predicted the immense possibilities

offered by the detection of single molecule *in vivo* in a 1959 speech called "There is plenty of room in the bottom" [1]. An abstract of his talk is especially relevant to the context of this thesis:

« It is very easy to answer many of these fundamental biological questions; you just look at the thing! [...] Unfortunately, the present microscope sees at a scale which is just a bit too crude. Make the microscope one hundred times more powerful, and many problems of biology would be made very much easier. »

The importance of single molecule detection has risen since then in multiple and various fields, and research at the nanoscale level continues to expand. Many biological structures can be considered as nanostructures and hence be systems of choice in the nanofield: for instance, proteins have typical sizes ranging from 4 to 50 nm. The main aim of this thesis was to develop techniques to improve the level of information details obtained by detection of signal arising from single fluorescent molecules involved in important biology processes.

1.1 Fluorescence Microscopy

The main motivation for single molecule experiments is to unravel individual properties of the different components of a heterogeneous system. Ensemble averaging of a bulk sample makes it impossible to retrieve structural or kinetic properties of small subpopulations. Sub-ensemble behaviours are of particular importance in biology where single protein molecules perform crucial interactions during the cell cycle [2]. The first demonstration of single molecule detection by Moerner *et al.* [3] was followed by applications in numerous fields, such as deoxyribonucleic acid (DNA) sequencing [4], particles optical trapping [5], protein folding [6], enzyme kinetics [7] or polymer dynamics [8].

The invention of the microscope is usually dated to 1590, when Hans and Zaccharias Hansen used series of lenses to produce magnified images of objects. Galileo Galilei developed a device composed of two lenses in 1610, for which the word "microscope" (from the Greek μικρόν "small" and σκοπεῖν "to look at") was coined in 1625 [9]. Microscopic organisms were first discovered during the period 1665-1683 by Robert Hooke and Antoni van Leeuwenhoek using simple microscopy [10, 11]. The technique was used since then to investigate the cell's structure and organisation [12].

The first fluorescent microscope was introduced by Heimstadt in 1911 and used to image bacteria [13]. Despite the success of this first step, only autofluorescence of the sample could be observed at the time and dark field condensers were needed to separate the fluorescent emission from the excitation source, which consequently hindered the technique development. One of those two obstacles was overcome in 1929 when Philipp Ellinger and August Hirt invented the epifluorescent microscope and managed to limit the amount of incident light detected [14], an approach later completed by the introduction of band-pass filters called dichroic mirrors [15]. In 1941, Max Haitinger demonstrated the possibility of labelling biological samples with fluorescent dyes [16], which allowed the investigation of specific molecules. The requirement to find an excitation source able to provide a power sufficient to excite emitters at a high rate was met in the 1960's thanks to the development of lasers. The coherent, monochromatic and highly energetic beam provided by these devices is indeed ideally suited to perform stable and efficient excitation of fluorescent dyes. Xenon and mercury arc lamps can also be used in combination with a monochromator to obtain a broad and flexible spectral coverage [17].

The extraction of the Green Fluorescent Protein (GFP) from jellyfish *Aequorea victoria* [18] and the development of a highly specific tagging method using antibodies, named immunofluorescence [19], have been followed by tremendous progress in the biological field. Behaviour of various cell's components can be studied, providing detailed information on localisation and kinetics of individual biomolecules, as well as potential interactions between multiple fluorescent-tagged targets. The enhancement of fluorescent proteins photophysical properties, combined with recent advances in super-resolution microscopy, enabled to gain a great insight of live cells organisation [20, 21].

1.1.1 Principles of Fluorescence

Light production is usually obtained by heating a given material to high temperature. However, light can in some cases be emitted by non-incandescent sources, via a phenomenon called "luminescence" which can be triggered by various processes such as a chemical reaction (chemiluminescence) or exposition to incident photons (photoluminescence) [22]. Fluorescence is a particular type of photoluminescence which was observed for the first time by Sir John Hershel in a solution of sulphate of quinine [23, 24]. Georges Gabriel Stokes further described the phenomenon in 1852, when he observed that the fluorite mineral (fluor spar) emitted in the visible part of

the wavelength spectrum when exposed to UV light [25]. The exact process causing this red-shifted phenomenon was later elucidated as the radiative emission of a fluorophore relaxing from an excited electronic state to its ground state, with energy losses due to vibrational and rotational transitions (internal conversion). The different states of a fluorescent molecule can be visualised in a Jablonski diagram (Figure 1.1).

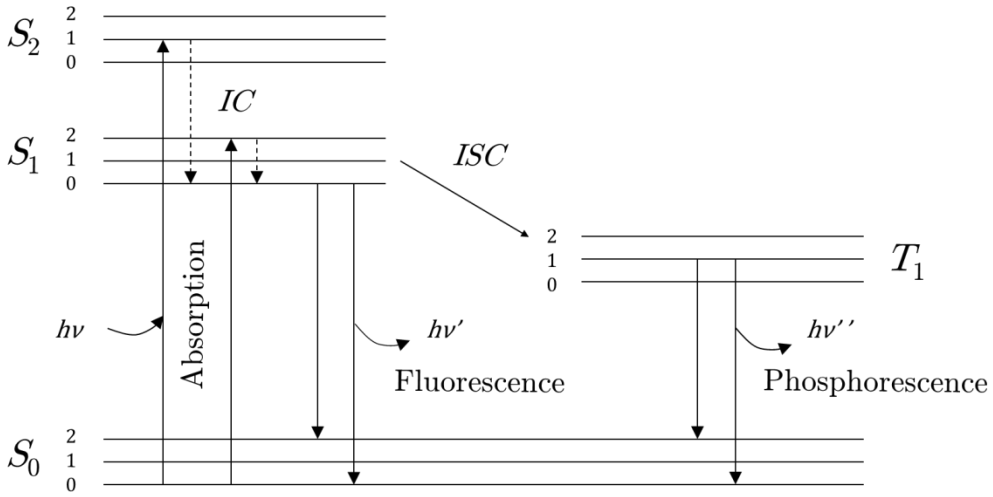

Figure 1.1. Simplified Jablonski diagram. S_0 refers to the electronic ground state, S_1 and S_2 the first and second excited state, T_1 the triplet state. Lines 0, 1, 2 represent the different vibrational levels. Examples of internal conversion (IC) and intersystem crossing (ISC) are also displayed on the diagram (adapted from [26]).

Electrons of the molecule can be excited from ground state level (S_0) to the first excited level (S_1) upon interaction with the light electric field vector. This excitation occurs on a time scale range of the order of a femtosecond, which is very fast compared to the nuclei displacement according to the Born-Oppenheimer approximation. Therefore, the Frank Condon principle states that after excitation to a new vibrational level, the latter must be instantaneously compatible with the nuclear positions and momenta of the molecule vibrational level in the originating electronic state. If the molecule is excited to a higher vibrational level than the vibrational ground state of the excited state, it can relax almost immediately to the lowest vibration level of the excited state. The time period of molecular vibration relaxation is of the order of 10^{-14} seconds. The molecule then stays in the excited state during a time range of the order of a nanosecond, before relaxing back to the ground state. The total time that the molecule spends in the excited state, of the order of 1-10 nanoseconds, is the fluorescence lifetime. Relaxation to the ground state can occur by different competing paths. This process is called fluorescence if it happens

with spontaneous emission of a photon, but non-radiative relaxation by energy dissipation can also occur.

Electrons in the lowest excited state may also cross to the lowest triplet state (T_1) (intersystem crossing, 10^{-7}s) before relaxing to the ground state, either radiatively (phosphorescence) or not. This process requires a spin flip of the electron, an event that is associated with a very low probability. Once in the triplet state, energy might be transferred back to S_1 before relaxing to S_0, which results in delayed fluorescence, with a characteristic time ranging in the milliseconds to seconds time scale.

Quenching is a non-fluorescent mechanism in which the excited molecule is deactivated by interaction with a second molecule, a process that can be used to study kinetics of conformational changes, for example [27].

The interaction with neighbouring molecules more often manifests itself as photobleaching, the main limiting factor in the imaging of any biological system. This process, although not completely elucidated, involves the creation of an irreversible covalent bond with oxygen molecules during relaxation, which leads to the loss of fluorescence emission. Fluorophores in the triplet state spend a long time in the excited state and therefore have a bigger chance to photobleach. This photobleaching process therefore limits the temporal length of fluorescence imaging, but its influence can be decreased by using oxygen scavengers [28] and lowering excitation intensities to reduce excited state populations.

Another limiting factor in the detection of single molecule fluorescence arises from the finite lifetime of the excited state: the number of photons emitted does not increase linearly with excitation intensity but rather displays an asymptotic saturation plateau at high excitation intensities [29]. Those two processes highlight the importance of a careful characterisation of the emitter's properties in order to select appropriate fluorophores depending on the desired application. For instance, tracking of particles over time requires long and stable fluorescence emission [30] whereas some super-resolution imaging techniques take advantage of triplet state transition and photobleaching [31-33].

1.1.2 Properties of Fluorophores

i. Absorption and emission

The spectral regions of absorption and emission of a given fluorophore are described by an excitation spectrum and an emission spectrum (Figure 1.2). The absorption

spectrum represents the relative probability for the molecule to be excited by a source at a given wavelength. The maximum of the curve is associated to the wavelength corresponding to the energy difference between the ground state and the favoured vibrational level of the first excited state. A second peak at shorter wavelength could be present in the spectrum and is associated to a transition to the second excited state. The width of the excitation peaks reflects the fact that the excitation can occur between all vibrational and rotational levels of the ground state to any vibrational and rotational levels of the excited state, albeit with a finite probability. Similarly, the emission spectrum presents a maximum at the wavelength corresponding to the transition between the most favoured vibrational level of the excited state and the base level of the ground state. The displacement of this maximum towards longer wavelength, called Stokes shift, arises from the dissipation of energy through vibrational relaxation before emission. The large range of energies associated with the excitation of a fluorophore is reflected in the broad shape of the absorption and emission spectrum.

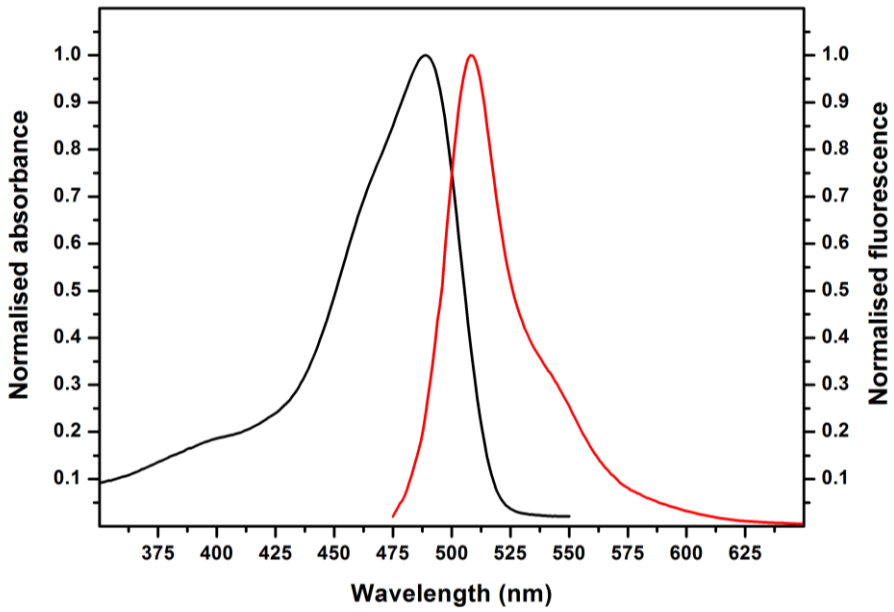

Figure 1.2. Absorption and emission spectra of enhanced GFP at pH 7. The shift in the wavelength between excitation curve (black) and emission curve (red) arises from energy losses due to vibrational relaxation [34].

ii. Fluorescence lifetime

The fluorescence lifetime is defined by the decrease of fluorescence emission over time through radiative or non-radiative decay routes. Multiple fluorophores can be mapped according to their respective fluorescence lifetime in Fluorescence Lifetime Imaging

Microscopy (FLIM) [35]. In this method, the sample is excited by successive laser pulses and the fluorescence emission is monitored at different delay times on the order of the nanosecond. The values acquired are then fitted to a sum of exponential decays to retrieve individual fluorescence lifetimes, characterised as the time necessary for the signal to reach 1/e of its value after the pulse [36] and which may reflect changes in the fluorophore local environment.

The technique has been used in combination with Forster Resonance Energy Transfer (FRET) to obtain acceptor lifetime or investigate donor quenching processes for instance [37, 38]. An accurate value of the spatial distribution of tagged proteins in mouse cell nucleus has been obtained using the FLIM-FRET approach [39].

iii. Brightness

The brightness a fluorophore characterises the number of photons that can be emitted during a given time. It is dependent on the ability of the fluorophore to be driven in the excited state and on the efficiency of conversion into emission radiation. An object must differ in brightness from the background in order to be successfully imaged. This difference in brightness, called contrast, is critical in imaging techniques and needs to be maximised by adjusting experimental parameters.

The extinction coefficient ε quantifies the amount of light that a fluorophore can absorb at a given wavelength and is usually defined as the optical density of a 1 mol/L solution measured with a 1 cm light path.

The parameter that quantifies the emission efficiency compared to the other relaxation pathways is called quantum yield (Φ) and can be described as:

$$\Phi = \frac{k_{\mathrm{f}}}{\sum_{\mathrm{i}} k_{\mathrm{i}}} \tag{1.1}$$

with k_{f} the rate of emission and k_{i} the rate of all other relaxation processes.

The brightness of a fluorophore is proportional to the product of the extinction coefficient and quantum yield. It can vary depending on the environment of the probe, with influential factors such as ionic strength, pH, temperature, covalent and non-covalent interactions. Biomolecules displaying different molecular brightness can be distinguished using a Photon Counting Histogram (PCH) technique [40], in order to investigate concentrations or aggregation states for example.

iv. Saturation

The finite lifetime of the excited state limits the number of photons that can be emitted by a fluorophore at high intensity excitation. The emission signal increases linearly with the excitation intensity until the latter reaches a saturation value, above which the emission signal tends to a horizontal asymptote. The emission profile of Alexa 546 upon increased excitation intensity has been obtained by monitoring the fluorescence emission of a monolayer of the fluorophore, imaged using widefield microscopy with a sequential increase of the sample incident irradiance, following the protocol described in Section 2.3.1 (Figure 1.3).

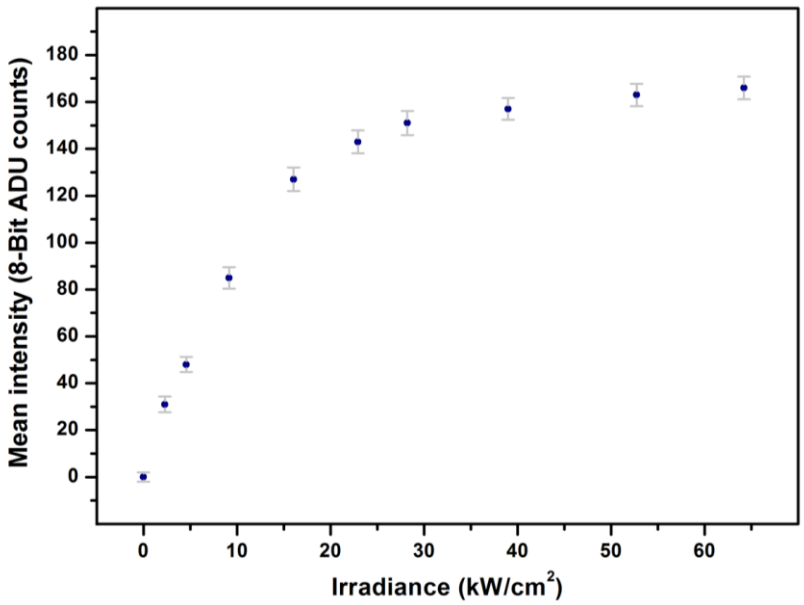

Figure 1.3. Saturation of Alexa 546 dye upon high intensity excitation. Linear increase of signal is limited to the [0-17] kW/cm^2 range of intensity excitation. Emission signal reaches a plateau for incident intensities higher than the irradiance saturation value.

v. Photobleaching

The amount of photons collected from a single fluorophore increases with successive cycles of excitation and relaxation. However, the probability for a fluorophore to undergo photochemical reactions during these repeated passages in the excited state limits the number of cycles that can occur and ultimately the total number of photons collectable per molecule. High resistance to photobleaching is therefore a desirable feature of fluorophores designed for fluorescence microscopy. The average number of cycles that a given fluorophore can undergo before permanently losing the ability to fluoresce depends on its molecular structure and environment.

It is worth noting that the irreversible loss of fluorescence can sometimes be used to gain a valuable insight into biological systems, with techniques such as Fluorescence Recovery After Photobleaching (FRAP). In this approach, a region of the sample is photobleached and the rate of fluorescence recovery caused by diffusion of neighbouring fluorescent proteins into the bleached area is monitored over time. The time necessary for the cell region to regain its original level of emission gives insight on the mobility of components inside the cell [41]. Similarly, Fluorescence Loss In Photobleaching (FLIP) involves multiple photobleaching processes applied to a particular region while the fluorescence in the whole cell is monitored. This technique has been used to investigate exchanges between cell's compartments and provides an assay to measure molecular dynamics and mobility [42].

High intensity laser excitation can induce phototoxicity, whereby light-induced free radical oxygen species interact with organic molecules. This effect is detrimental to *in vivo* imaging and must be limited by using low excitation intensity where possible.

vi. Fluorescence fluctuation and intermittency

The fluorescence signal arising from an emitter can strongly vary over time before undergoing total photobleaching. This phenomenon has very diverse sources and manifestations, but is generally referred to as fluorescence intermittency or "blinking" [43]. Strong variations can be induced by a quenching process caused by interaction with another dye molecule [44], redox reaction [45], intramolecular conformational changes or photoactivated switch [46]. This signal intermittency has been an obstacle for fluorescent particle tracking applications over the years, but has also been exploited for numerous super-resolution applications. In particular, Super-Resolution Optical Imaging (SOFI) performs a correlation analysis on the fluorescence fluctuation of individual blinking emitters to enhance localisation accuracy [47]. Moreover, photophysics of the fluorophores can be tailored experimentally to extend the time spent in the dark state, improving the performance of techniques based on the localisation of individual emitters [48].

1.1.3 Fluorescent Labels

Selection of adequate fluorescent reporters is critical in fluorescence microscopy. The following section details the types of fluorophore that have been used in the experiments carried out in this thesis and their associated photophysical properties.

i. Organic dyes

Organic fluorescent molecules are usually polyaromatic hydrocarbons or heterocyclic molecules. Fluorescence emission arises from the resonance delocalisation of electrons between conjugated bonds, which induces the red shift of the electronic transition. Main requirements for emitters include high brightness, resistance to photobleaching and good chemical compatibility with the target molecule. Typical fluorophores emit around 10^5-10^6 photons before photobleaching. Fluorescence emission can be influenced by various environmental factors such as pH, temperature and ionic strength. For example, fluorescein exhibits a strong quantum yield when in its dianionic form because of its highly resonant structure, but its emission decreases considerably when in its neutral form. Such environment dependency can sometimes bring information on the system [49] but is unwanted in most applications where a maximum fluorescence emission is required for a vast range of conditions. Similarly, most organic emitters can be chemically conjugated to other molecules without significant changes in their photophysical properties. Moreover, their small size ($\sim$ 1 kDa) minimises any potential steric hindrance and conformational stress.

Most of the commonly available fluorescent dyes, such as rhodamine and cyanine derivatives, are commercially available with reactive side groups that enable specific, covalent coupling to biological molecules. For example cysteine reactive groups, like maleimide and iodoacetamide, or amine reactive groups such as succinamide and isothiocyanate are commonly used for site-specific labelling reactions [50].

ii. Fluorescent proteins

Fluorescent proteins are especially relevant in biology since they allow the possibility of tagging target proteins by genetic modification [51]. The resulting protein, or fusion protein, can therefore be used for *in vivo* studies, without compromising the biological environment of the cell. The first development of the GFP protein has been followed by isolation of other natively fluorescent proteins and creation of mutants forms of GFP covering different portions of the visible spectrum, from Blue Fluorescent Protein to red-shifted GFP [52]. Multiple colour tagging allows simultaneous imaging of different proteins, as well as FRET experiments to investigate complex formation between proteins. The relative small size of these tags (238 amino acids and molecular weight of 27 kDa for a monomeric GFP [53]) usually does not cause any stability problems to the expressed fusion protein.

Several studies have demonstrated a significant "flickering" of GFP fluorescence emission over time, behaviour attributed to different isomerisation states and environmental effects [54, 55]. Therefore, new fluorescent proteins such as enhanced GFP (EGFP) and m-Cherry dyes have been introduced to increase brightness and to minimise blinking and photobleaching effects [56].

iii. Quantum dots

Quantum dots (QDs) are semiconductor nanocrystals that exhibit enhanced photophysical properties compared to classical fluorophores. They typically display a brightness value around two to three times higher than organic fluorophores, are more resistant to photobleaching and possess a broader excitation spectrum. These properties arise from the quantum confinement of electrons, holes and excitons (electrons - hole pairs) [57]. When an electron of the valence band is excited to the conduction band, a hole is created in the valence band and the exciton pair is separated by a distance, the exciton Bohr radius. In a semi-conductor bigger than 10 nm, the electron energy is continuous and the bandgap between the covalent and conduction bands is fixed. However, for a QD smaller than the exciton Bohr radius, the associated energy levels become discrete, which is the origin of the enhanced photophysical properties observed. It is possible to tune the emission spectra by changing the bandgap length: the larger the dot the lower the energy it will emit, which makes QDs efficient multicolour fluorescent reporters.

The most widely used QDs are composed of a Cadmium-Selenide (CdSe) core surrounded by a Zinc-Sulphur (ZnS) shell [58, 59]. Several methods have been proposed to circumvent the hydrophobicity of those QDs in order to tag biological systems. Experimental strategies employed to stabilise QDs in aqueous solution include coating with amine-modified polyacrylic acid, derivatisation with dihydroxylipoic acid, embedding on siloxane shells and encapsulation in phospholipids micelles [60]. Inorganic probes can then be conjugated to a linker, either covalently or by electrostatic interactions, in order to ensure specific targeting of biological features and minimum cytotoxicity *in vivo.* However those modifications increase the overall size of the emitter, which can reach 500-750 kDa after conjugation, and could disturb the target mobility and functionality.

QDs are subject to blinking, a photophysical process that has been extensively investigated [61-63] but is not yet completely understood. The generally accepted mechanism for blinking is that photoionisation causes a carrier to be ejected and removed, inducing quenching of the subsequent exciton pairs by the unpaired carrier,

which brings the QD into a non-fluorescent state [64, 65]. The ionisation of the particle leads to a long-lived trapped state of the electron, which is most likely due to a defect site at the QD surface or in the host matrix [65, 66]. New developments suggest the existence of a second blinking mechanism associated with charge fluctuations in the electron accepting surface sites that can intercept electrons before release [67]. Several techniques are available to hinder this blinking effect, such as passivation with thiol moieties [68] or by increasing the inorganic shell size [69].

1.2 Detection of Single Molecule Fluorescence

The detection of single molecules requires enhanced sensitivity of detection because of the intrinsically small signal generated by individual emitters. External sources of detected intensity need to be minimised to avoid swamping the fluorescence signal by background noise. In particular, the contribution of intrinsic noise such as scattering of light from optics, detector electronic noise and fluorescence background must be minimised in order to achieve a sufficient Signal to Noise Ratio (SNR) and Signal to Background Ratio (SBR) for single molecule detection.

1.2.1 Optical Collection Efficiency

The efficiency of fluorescence emission collection needs to be maximised experimentally in order to increase the SNR, which can be achieved with oil immersion objectives possessing a high Numerical Aperture (NA). This parameter represents the ability of the optical component to gather or focus incident light:

$$NA = n \sin(\alpha) \tag{1.2}$$

with n the refractive index of the sample medium and α the half angle of the solid cone representing the collected light, which can be deduced from f and d, respectively the focal length and the diameter of the lens:

$$\alpha = 2\arctan\left(\frac{d}{2f}\right) \tag{1.3}$$

When imaging in aqueous medium, the numerical aperture of the system is limited by the refraction index of water (~ 1.33). This kind of setup typically only collects around 26% of the total isotropic emission [70], which highlights the requirements for sensitive detectors and significant noise reduction.

1.2.2 Spectral Filtering of Fluorescence

Scattering of the excitation wavelength needs to be filtered out before reaching the detection device in order to achieve single molecule sensitivity. In particular, Rayleigh noise due to the elastic scattering of the incident electromagnetic wave by the solvent molecules is an intrinsic factor to be taken into account for biological imaging. Volume reduction techniques can be used in the experimental setup to reduce the contribution of Rayleigh noise relative to the fluorescence signal detected. Moreover, its emission is usually located in a distinct spectral region compared to the fluorescence emission and can be removed efficiently by spectral filtering. Modern dichroic and band-pass filters can achieve 90% transmission efficiency in their spectral region of interest whilst displaying transmission values near 10^{-7} in their blocking region. These two features enable the emission arising from different fluorophores to be isolated, which can be used in applications requiring elaborate sample labelling and quantitative imaging such as FRET [71, 72] or colocalisation studies [73, 74]. A conventional combination of dichroic and band-pass filters used for imaging of EGFP is displayed in Figure 1.4 and detailed in Section 2.1.4.

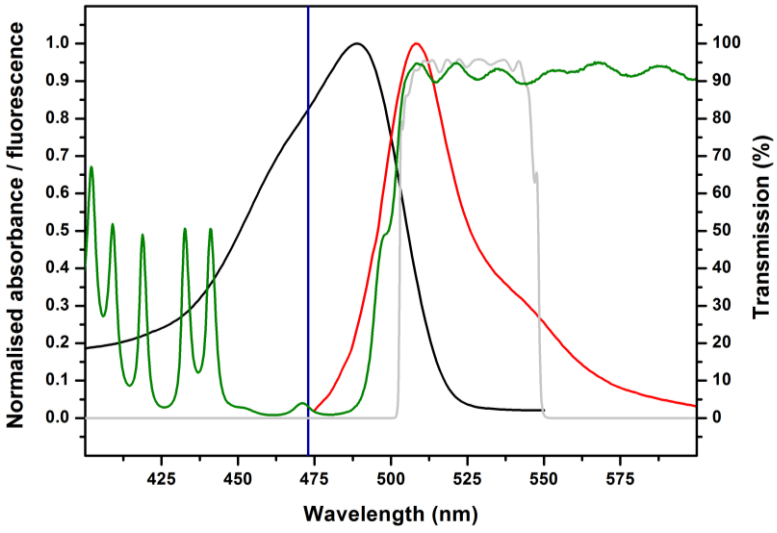

Figure 1.4. Spectral filtering setup used for EGFP imaging. A dichroic mirror (green) is used to reject the 473 nm excitation laser light (blue). A band-pass filter displaying a 45 nm bandwidth centred around 525 nm (grey) allows to collect EGFP fluorescence emission [34].

1.2.3 Detectors and Photon Counting Noise

There are many types of detector that can be used for single molecule experiments, the focus will be made here on the two types that have been used in the scope of this thesis: Avalanche Photon Detectors (APDs) and Electron Multiplying Charge Coupled Devices (EMCCDs).

APDs are single point detectors which convert the energy of photons into free charge carriers and display an internal gain effect under a high voltage via impact ionisation. They typically display a good spectral response over the fluorescent detection range, with quantum efficiency superior to 60% in the 600-800 nm spectral region [70].

EMCCDs are composed of an imaging grid made of multiple charge storage devices (pixels). When photons impact the pixels, electron-hole pairs are generated and the accumulated charge is therefore proportional to the integrated light [75]. The charge is then converted into a voltage and amplified by a "gain" factor (G). The voltage at each pixel location is then digitised to give the final image. EMCCDs are subject to a number of different noise processes, which need to be reduced or at least accounted for. In particular, the quality of a super-resolution process is ultimately limited by the level of noise present in the original dataset.

i. Dark current and readout noise

Dark current arises from a thermal effect which causes stochastic emission of electrons in the detector in the absence of incident light [76]. This source of noise can be reduced to just a few electrons per second if the detector is cooled to -80°C, reducing significantly the associated thermal noise in silicon devices such as EMCCDs.

Readout noise is caused by random fluctuations occurring in the electronics used in Charge Coupled Device (CCD) cameras, depends on camera readout rate [77, 78] but is usually of the order of 10 e^- per pixel in standard CCDs. However, this value becomes equivalent to $(10/G)$ electrons per pixel in EMCCDs, which lowers significantly the influence of this factor on the total noise for high gain values.

ii. Clock induced charge and quantisation noise

Clock induced charge noise is induced by single errors occurring during charge transfer in a process called impact ionisation. It is more pronounced in EMCCD cameras because of the gain register process used to amplify the signal [79].

The quantisation noise is independent of the signal and arises from the digitisation of the detected image into integer values in order to reconstruct the digital image [77]. The main noise source in modern cameras is due to the intrinsic nature of the charge carrier in the device, and all other noise sources are negligible in comparison.

iii. Photon shot noise

Shot noise is caused by the stochastic fluctuation caused by the discrete nature of the electrons that carry the charge. This phenomenon can be described by a Poisson distribution:

$$\mathrm{f}(k,\lambda) = \frac{\lambda^k \exp(-\lambda)}{k!} \tag{1.4}$$

with λ the expected occurrence number value in the interval and k the number of occurrences.

For conventional CCDs, the shot noise scales with the square root of the number of photons detected, whereas for EMCCDs the signal amplification induces an additional shot noise contribution that needs to be taken into account. This excess noise, specific to EMCCD detectors, is introduced by the extra stochastic process taking place during the electron multiplication. It has been demonstrated that for typical EMCCDs, the global shot noise scales with the square root of the number of photons detected multiplied by a factor F that usually tends to the value of $2^{1/2}$ for large gain values [80].

The main noise source in modern detectors comes from the shot noise, because technology progress has made all other noise sources negligible. It is however important to maximise signal strength in order to diminish the noise contribution to the detected signal.

1.2.4 Chemical Background Noise

There are two main sources of potentially strong parasite signal emission in solution. Both of these are caused by probes present in the imaging media alongside the fluorescent emitters of interest.

i. Autofluorescence

Autofluorescence is caused by molecules that are naturally fluorescent in the spectral window of interest and is a significant source of background noise for *in vivo* observations. This source of noise can only be reduced experimentally by following rigorous protocols [81] or imaging in the near-infrared spectral region where the autofluorescence is less pronounced [82]. Post-acquisition mathematical treatment can also correct for its influence on images acquired [83, 84].

ii. Raman scattering

Raman noise is caused by the Raman scattering of solvent molecules upon exposure to the incident light. Unlike the Rayleigh scattering, the wavelength of the associated emission can have either a shorter or longer wavelength. The latter case can be most detrimental, as the Raman scattered light may overlap with the Stokes shifted fluorescence emission, rendering spectral filtering impossible. For example, an aqueous solvent excited at a wavelength of 488 nm would scatter the light at 586 nm [85], which is coincidental with the peak emission of tetramethyl rhodamine (TMR) [70]. The amount of light scattered is proportional to the amount of host scattering probes, which is why an important condition for single molecule experiment is the reduction of both the excitation and detection volume.

1.3 Background Reduction Techniques

It is of critical importance to reduce as much as possible the background noise arising from Raman scattering in single molecule experiments. In addition, if too many molecules are present in the detection volume the signal arising from molecules of interest can be swamped by other fluorescent molecules. This effect is particularly pronounced when dealing with cells because of their often strong autofluorescence.

The main strategy to circumvent this problem is to technically reduce both the excitation and detection volume. This strategy will be introduced in the following section for the two main techniques used in this thesis: confocal microscopy and Total Internal Reflection Fluorescence Microscopy (TIRFM). A characteristic excitation scheme, multiphoton excitation, is introduced as well as a potential complement to confocal microscopy that allows further reduction of the background signal.

1.3.1 Confocal Microscopy

The concept of confocal microscopy relies on the restriction of the detection field in order to remove the background fluorescence arising from out of focus molecules. In this technique, the light collected by the microscope is focused onto a tightly adjusted pinhole, so that only light originating from regions close to the focal plane reaches the detector. This idea has been first introduced in 1955 by Minski [86] and progressively refined [87, 88] but tedious alignment and long exposure time hindered at first its application to biological systems. The introduction of lasers as excitation sources allowed a limitation of chromatic aberrations and a decrease of the excitation volume by focusing the beam to a diffraction-limited volume inside the sample [89], leading to successful application of the technique to cell biology [90, 91]. Thick samples can be investigated by optical sectioning, revealing details that would be lost in a widefield microscopy experiment and enabling 3D imaging applications.

i. Diffraction-limited confocal detection volume

The confocal detection volume is limited by diffraction to a cross-sectional diameter approximated by Abbe's law:

$$d = \frac{\lambda}{2NA} \tag{1.5}$$

The axial resolution of the confocal technique varies from 0.5 to 1.5 μm, depending on the laser wavelength, scattering coefficient of the sample and lens spherical aberration, which makes confocal microscopy a convenient method to apply *in vivo*. Thus, approximating the excitation volume to a cylinder gives detection volumes of the order of a femtolitre. Scanning of the sample is therefore required to investigate samples, which is achieved either by stage movement or incident laser scanning.

ii. Multiphoton confocal excitation scheme

Two-photon excitation is a complementary method to confocal imaging which is used to further decrease the spatial excitation of the sample. The quantum process of multiphoton excitation has been proposed by Maria Göppert-Mayer in 1931 [92] and the first non-linear microscope introduced in 1978 [93].

In a more general concept, multiphoton microscopy exploits a non-linear process to selectively excite a small number of molecules. The idea is that there is a small probability for a molecule to be driven in the excited state by the absorption of multiple photons that have respectively a lower energy than the one required for a single photon excitation. The molecule can be excited if two photons reach a fluorophore within 10^{-18} s. The probability of this event is much smaller than for a one-photon excitation and the fluorescence emission varies with the square of the excitation intensity [94]. It is therefore necessary to use high intensity laser pulses in order to successfully excite a sufficient number of fluorophores, without increasing significantly the photodamage caused to the sample. Unlike classical confocal microscopy, no confocal pinhole is needed, as the only excited area in the sample is the confocal volume. There is therefore a limited photobleaching effect occurring in peripheral regions and samples can be imaged for extended periods of time.

Two-photon excitation improves two to three times the depth penetration into the sample compared to conventional confocal techniques. Recent researches have introduced three and four-photons excitation techniques, which might prove useful in biology for imaging UV emitting probes for example [95].

1.3.2 Total Internal Reflection Fluorescence Microscopy

TIRFM is an elegant way of reducing effectively the excitation field using an evanescent wave [96] and can be used on a wide variety of biological samples [97]. The penetration depth achievable with TIRFM is limited to a scale range of the order of 100 nm [98], which lowers any photophysical damage done to the sample and increases the SBR compared to conventional widefield microscopy technique. The minimum achievable detection volume is of the order of $1/10^{th}$ of the confocal detection volume but is limited to the area of the sample located at the interface with the coverslip. TIRFM is therefore especially suited for single molecule experiments and might be used to investigate cell adhesion and migration [99], or membrane dynamics [100] for instance.

i. Principle of total internal reflection

The refraction of an incident ray of angle θ_i between two media of different refractive index n_1 and n_2 is given by the Snell-Descartes law:

$$n_1 \sin(\theta_i) = n_2 \sin(\theta_t) \tag{1.6}$$

If $(n_1 > n_2)$, the angle of the transmitted beam (θ_t) with respect to the perpendicular of the interface is bigger than the angle of the incident one (Figure 1.5). When θ_i is increased the transmitted ray gets closer to tangency and more and more of the energy of the incident ray is reflected at an angle θ_r.

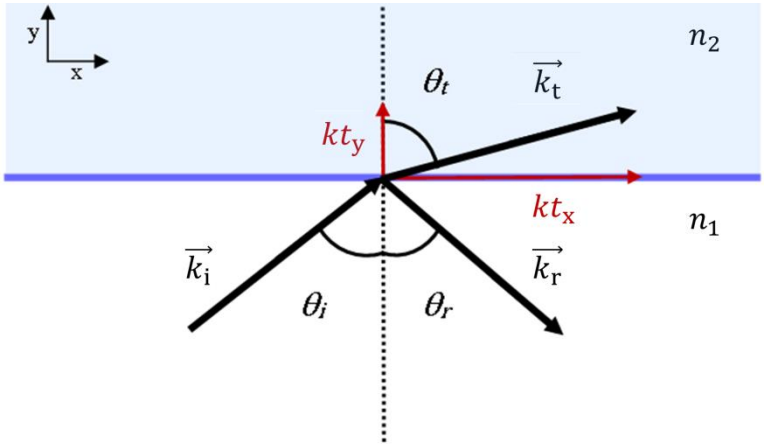

Figure 1.5. Refraction of incident light ray at an interface between two media with different refractive index. Projections of the transmitted ray on the *x* and *y* axis are noted kt_x and kt_y.

The angle θ_t reaches a value of $(\pi/2)$ radian for a value of the incident angle θ_i called critical angle (θ_c), for which there is no propagation into the refracted medium. The value of θ_c can be calculated straightforwardly using Snell-Descartes law:

$$\theta_c = \arcsin\left(\frac{n_2}{n_1}\right) \tag{1.7}$$

In a typical experiment where the interface is the discontinuity between the glass of a coverslip and an aqueous medium the critical angle value is around 61°. For incident angles greater than the critical angle, the light is totally internally reflected, however the incident radiation creates an electromagnetic field called evanescent field next to the interface.

ii. Evanescent field

In order to understand why there is an evanescent wave in the adjacent medium even though the incident light is totally reflected, we need to introduce a more rigorous description of the transmitted electric field wave function in two dimensions [101]:

$$\overrightarrow{E_t} = \overrightarrow{E_{0t}} \exp \mathrm{i}\left(\overrightarrow{k_t}.\vec{l} - \omega t\right) \tag{1.8}$$

with $\overrightarrow{k_t}.\vec{l} = k_t \sin(\theta_t) \times x + k_t \cos(\theta_t) \times y$

$\vec{k}$ being the propagation vector, ω the angular temporal frequency and t the time.

The Snell-Descartes law gives the following relation for the projection on the y axis:

$$k_t \cos(\theta_t) = \pm i k_t \sqrt{\frac{{n_1}^2}{{n_2}^2} \sin^2(\theta_i) - 1} = \pm i\beta \tag{1.9}$$

$k_t \cos(\theta_t)$ is therefore a pure imaginary quantity for $(\theta_i > \theta_c)$, as $\left(\frac{{n_1}^2}{{n_2}^2} \sin^2(\theta_i) > 1\right)$.
Similarly, applying the Snell-Descartes law for the projection on the x axis gives:

$$k_t \sin(\theta_t) = k_t \frac{n_1}{n_2} \sin(\theta_i) \tag{1.10}$$

Therefore we can express Equation (1.8) as a function of the incident angle:

$$\overrightarrow{E_t} = \overrightarrow{E_{0t}} \exp(\pm \mathrm{i}\beta y) \exp\left(\mathrm{i}\left(k_t \times \frac{n_1}{n_2} \sin(\theta_i) - \omega t\right)\right) \tag{1.11}$$

The situation where the exponential function is positive is not physically relevant, and the only expression remaining demonstrates that the amplitude of the wave decays exponentially in the y direction as it penetrates the sample. The disturbance propagates in the x direction as a surface, forming an evanescent wave [102]. The intensity profile decay in the y direction can therefore be described with the equation:

$$I(y) = I(0) \exp\left(-\frac{y}{d}\right) \tag{1.12}$$

with the parameter d easily obtained from Equation (1.11) and the relation between the wavelength λ and the propagation number k, the magnitude of $\vec{k}$ $(k = 2\pi n_2/\lambda)$.

The penetration depth d is often used in the literature and represents the distance from the coverslip at which the intensity has dropped by a factor of 1/e .

$$d = \frac{\lambda}{4\pi\sqrt{{n_1}^2 \sin^2(\theta_i) - {n_2}^2}} \tag{1.13}$$

Equation (1.13) indicates that the parameter d is dependent on the incident angle, it is therefore possible to control to a certain extent the depth of penetration in the sample. The penetration depth d takes a value of 150 nm assuming a laser excitation at 488 nm with an incident angle of 61°, restricting the axial sample illumination to a thin layer. Picolitre detection volume is achieved with a circular excitation beam radius of the order of 50 µm. The molecules located in this highly localised region can be selectively excited without any significant bulk excitation of molecules outside the evanescent field. A schematic representation of the phenomenon is presented in Figure 1.6.

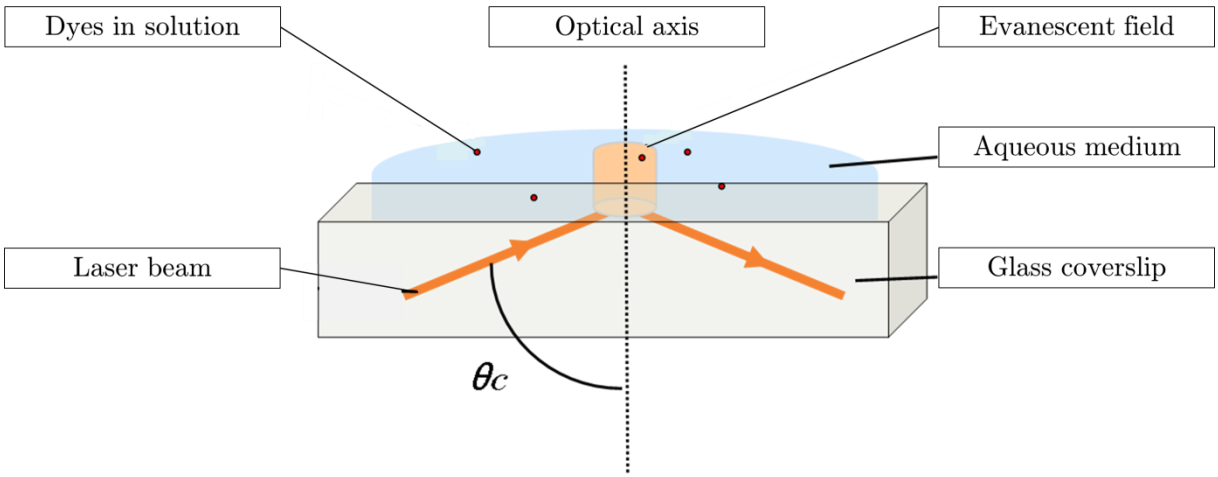

Figure 1.6. Evanescent wave created in TIRFM. The incident angle can be varied to achieve different penetration depths, allowing control of the axial excitation to a certain extent.

The previous section introduced an optimisation of the experimental setup used for single molecule microscopy. Further implementation of super-resolution methods is however required to investigate details of biological processes, such as protein interactions, occurring at a lower length scale. The following section introduces the main techniques that allow the study of single molecule events occurring at distance scales lower than the diffraction limit.

1.4 Super-Resolution Imaging

The diffraction of light limits the minimum feature size that may be resolved by optical microscopy to ~200-300 nm. However many fundamental biological processes occur at a lower distance range and are therefore masked in conventional imaging. Developing techniques aiming to reduce the lower limit of resolution is hence a natural complement to single molecule approaches in biological imaging.

Conventional Electron Microscopy (EM) can achieve near-atomic spatial resolution [103] but requires to cut the sample observed into thin sections (~100 nm of diameter). The sample needs to be chemically fixed and dehydrated before observation under low pressure or in a vacuum. Those requirements limits the applicability of EM to biological systems and makes live cell imaging especially problematic [104]. Many techniques have therefore been developed to improve the resolution of non-destructive optical microscopy techniques. Localisation accuracies up to 1.5 nm can be achieved [105] depending on photons number collected, allowing to study the ultrafine structure of cell's components [106-108].

1.4.1 Point Spread Function

The wave nature of light induces diffraction when transmitted through an aperture. Multiple propagating wavefronts with different amplitudes are created which interfere constructively or destructively, producing a diffraction pattern. In the case of an optical setup, the diffraction pattern associated with a point source is called Point Spread Function (PSF). This finite-sized spot is called Airy disk when projected on a 2D surface and has dimensions of 200-300 nm in the focal plane and 500-700 nm in the axial plane. The PSF is composed of a central region of high amplitude surrounded by rings of progressively decreasing amplitudes, and is described under coherent illumination as [109]:

$$I(r) = 2\,\frac{J_1\left(\pi\left[\frac{r}{r_0}\right]\right)}{\pi\left[\frac{r}{r_0}\right]} \tag{1.14}$$

with J_1 the Bessel function of the first kind, $\left(r = \sqrt{x^2 + y^2}\right)$ the distance from the origin, $(r_0 = \lambda d_i / a)$ a constant dependent on the aperture of the lens a and the distance between the lens and the plane of the image d_i.

The wavefronts arising from a conventional objective lens are not symmetrical, making the PSF an elongated ellipse along the optical axis [110]. Representations of the PSF function in the axial and lateral dimensions can be seen in Figure 1.7.

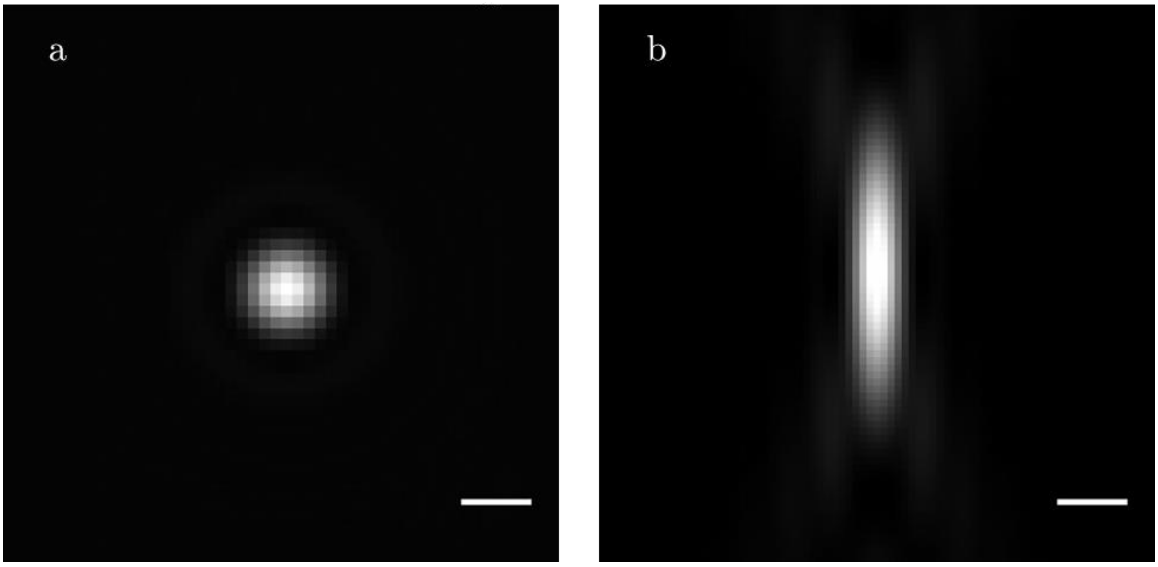

Figure 1.7. Representations of the PSF along the lateral and axial planes. a) The PSF is symmetrical when projected along the lateral plane. b) The PSF has an elongated ellipse shape along the optical axis. Scale bar: 500 nm.

The Fourier transform of the PSF is the optical transfer function and can be used to analyse the spatial frequency range collected by an optical setup [111]. A system is said to be diffraction-limited when the only factor influencing the PSF size is the diffraction of light. In practice, microscopy systems differ from that idealised case because real lenses usually converge peripheral and near-axial rays to a different point of the z axis, leading to spherical aberrations [9].

1.4.2 Spatial Resolution

The formation of an image is an incoherent process in conventional microscopy, which means that the resulting image of two emitters is composed by the sum of the two respective Airy disks. Any multiple features located in a diffraction-limited spot cannot be individually localised, which gave rise to the concept of resolution formulated by Ernst Abbe in 1873 [112] and Lord Rayleigh in 1896 [113]. The Rayleigh criteria defines the limit of resolution between two distinct Airy disks as the distance between the two centres of the PSFs when the maxima of one Airy disk overlaps with the first minima of the second one (Figure 1.8).

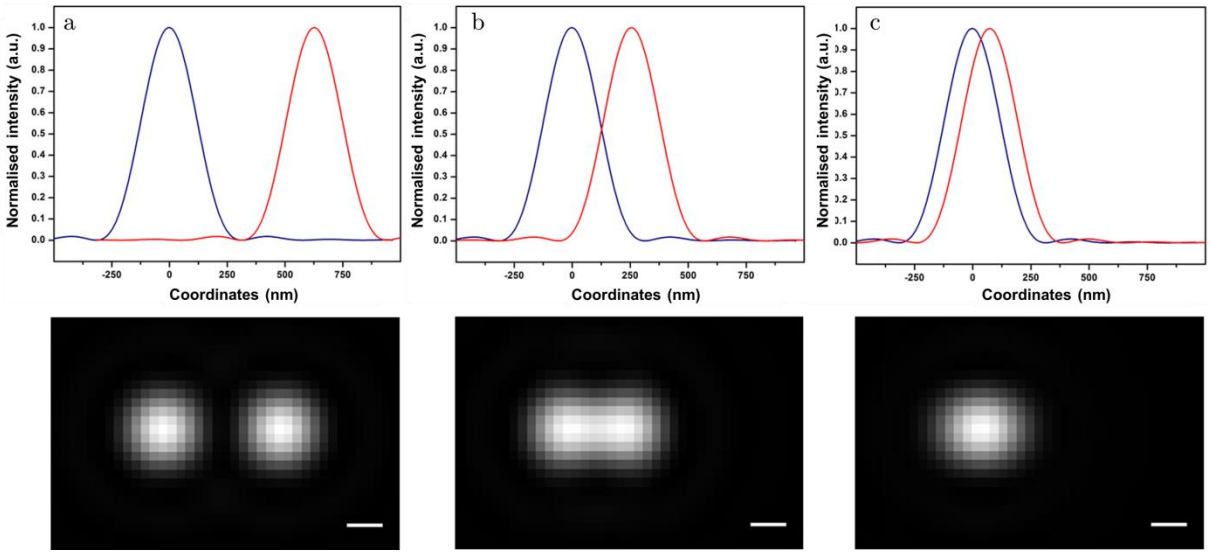

Figure 1.8. Illustration of the resolution limit in one (top pictures) and two (bottom pictures) dimensions. a) PSFs are resolvable. b) Rayleigh criteria limit of resolution between PSFs. c) PSFs are unresolvable. Images obtained from simulations. Scale bar: 200 nm.

The lateral resolution distance can be calculated with the following equation:

$$d_{x,y} = 1.22 r_0 = \frac{0.61\lambda}{NA} \tag{1.15}$$

The resolution in the axial plane is given by:

$$d_z = \frac{2\lambda n}{NA^2} \tag{1.16}$$

with n the refractive index of the sample medium.

The concept of resolution in the axial plane is closely linked with the depth of field of an imaging system. This quantity refers to the size of the portion of the imaged sample that appears in focus when detected: it characterises the fact that different features located at different depths inside the sample will appear equally in focus. It is classically defined as half of the axial size of the PSF. Other criteria can be retained as approximations of the achievable resolution, such as the Full Width at Half Maximum (FWHM) of the PSF or the Sparrow criterion [114], which defines the distance from which the first and second derivatives of the combined PSF disappear. However, the Rayleigh criterion is retained to describe resolution limit in most fluorescent microscopy techniques. It is worth mentioning that these calculations assume no spherical aberration, which is an ideal case non achievable practically.

1.5 Resolution by Deconvolution

Image formation on a detector results from a convolution between the intensity fluctuation function of the emitter and the PSF of the imaging system. The PSF size and shape can be obtained either theoretically or empirically and used in deconvolution algorithms to retrieve fine details of the system [115, 116]. However, this approach is limited to sparsely labelled systems, and noise strongly degrades associated results [117]. Moreover the precision of individual molecules localisation is significantly higher using a fitting model than when performing a deconvolution process [118].

1.6 Near-field Super-Resolution Techniques

There are two different microscopy types that can be used for super-resolution: conventional microscopy techniques such as widefield, confocal, and multiphoton microscopy are far-field, meaning that the distance between the imaged sample and the detector used is bigger than the incident excitation wavelength. The resolution of these methods is therefore limited by the diffraction of light wavefronts through imaging lenses. In near-field microscopy techniques the detector is placed at a distance much smaller than the wavelength of excitation to monitor the evanescent wave generated at the surface. This approach enables one to reach a resolution only limited by the physical length of the nano-sized detector, but is in return only applicable to surface studies of samples. For example, TIRFM is a near-field method because it induces an evanescent field at the interface of two mediums that decays exponentially with the penetration depth, increasing the axial resolution to ~ 100 nm. TIRFM has been used in combination with an interference pattern illumination to study kinesin motion with a spatial resolution of 8 nm and temporal resolution of 100 µs [119]. Several other near-field techniques, such as Surface Plasmon Resonance [120] and Standing Wave Microscopy [121], use standing waves in order to obtain surface details below the conventional diffraction limit.

Near-field Scanning Optical Microscopy (NSOM) technique makes use of a detector placed at the end of a tapered fibre which scans sequentially the sample, in a process analogous to Atomic Force Microscopy (AFM), enabling it to reach 2-15 nm resolution [122]. NSOM has been used to study various biological systems, including membranes of dendritic cells [123] and protein localisation in cells [124].

1.7 Far-field Super-Resolution Techniques

The confocal setup previously described can be used to obtain an enhanced resolution when the pinhole aperture size is reduced to a dimension much smaller than the scanning spot [125]. This improvement is around 1.4-fold in the lateral plane and 2-fold in the axial plane, but significantly decreases the amount of light detected. Several complementary techniques have therefore been developed to increase the resolution achievable while retaining a high SNR.

Image Interference (I^nM) and 4Pi are far-field microscopy methods introducing a second objective lens to collect the fluorescence emission, which increases the *NA* value in either widefield of confocal mode. The periodic interference pattern between the light collected by the two objectives interacts with sample structures that are smaller than the diffraction limit. The acquired signal is then analysed, revealing detailed information about the sample substructure.

The simplest version of I^nM technique (I^2M) recombines the signals arising from the two objectives in the same plane, which creates an interference pattern because of the two identical optical paths. The interference pattern is then analysed to obtain high resolution details. The I^5M techniques combine an illumination pattern in addition to the use of two objectives to improve the resolution to values of the order of 100 nm [126]. However the technique is mainly limited to thin samples, as thick ones disturb the interference pattern.

The exciting light from the two objective lenses is focused at the same focal point in 4Pi microscopy [127] unlike on the entire focal plane in I^nM. Constructive interferences increases the resolution by a factor of 1.5 in the lateral plane and a factor of 7 in the axial plane compared to standard confocal microscopy [128]. A faster acquisition variant of 4Pi, multifocal multiphoton 4Pi-confocal microscopy was used for live cells imaging [129], providing detailed structural information on Golgi apparatus in mammalian cells for instance [130].

1.8 Patterned Excitation Methods

Several techniques based on the modification of the excitation beam shape have been used to obtain images of biological samples with an enhanced resolution. The following section introduces the characteristics of different methods based on this concept.

1.8.1 Structured Illumination Microscopy

Structured Illumination Microscopy (SIM) relies on the modification of the excitation source to extract detailed spatial information. A periodic pattern of known structure is applied to the incident illumination using a transmission grating, creating successive regions of maximal intensities and "zero intensities" (nodes). Characteristic Moiré patterns are then generated when the illumination grid overlays object features of higher spatial frequency. A series of images are collected for different translations and rotations of the incident pattern relative to the specimen and these images are then processed to reconstruct a super-resolution image.

The resolution achievable with SIM is limited by the spatial frequency of the illumination pattern, leading to a maximum increase of 2-fold in lateral resolution [131]. The technique has been applied to the axial plane in a technique called 3D-SIM [132], in which the illumination pattern arises from the interference between three coherent beams moved laterally and axially. This modification leads to an improvement in the spatial resolution, which can reach 100 nm in three dimensions [133].

The SIM techniques called Saturated Structured Illumination Microscopy [134] and Saturated Pattern Excitation Microscopy [135], gave rise to a further improvement of resolution to around 50 nm [104]. The concept is to use a patterned excitation above saturation intensity, which results in a very high probability for molecules located outside the nodes to be in the excited state. As a result, higher harmonics are present in the spatial frequency spectrum of the sample, hence allowing smaller structures to be resolved. This technique is however limited to very photostable emitters because of the strong illumination intensities needed to achieve saturation.

1.8.2 RESOLFT Techniques

Reversible Saturable Optical (Fluorescence) Transition (RESOLFT) microscopy is a group of super-resolution techniques that take advantage of the photophysical properties of fluorophores. The approach is based on the reversible switching between fluorescent and non-fluorescent states and relies on converting the vast majority of the molecules into a dark state upon excitation at intensities higher than the saturation level of the fluorophore. The dark state can be the ground state, the triplet state or the "off" state of a photoswitchable dye, depending on the technique used.

The sample is illuminated by two synchronised collinear sources consisting of an excitation laser pulse immediately followed by a depletion laser pulse. The patterned illumination used is composed of a depletion laser beam that is modified by a phase modulator to feature a node of zero intensity at the focus with intensity increasing exponentially towards the periphery of the beam. The emitters located in the zero intensity node are excited by the incident laser and can fluoresce whereas the fluorophores that are exposed to the depletion beam are sent into a dark state. The gain of resolution of the system can be calculated with the equation [136]:

$$d = \frac{\lambda}{2NA\sqrt{1 + a\left(\frac{I_{\max}}{I_{\text{sat}}}\right)}} \tag{1.17}$$

with $I_{\max}$ the intensity of excitation at the nodes border and a the parameter related to the patterned beam form, which has often a "doughnut" or a line shape.

The factor limiting the achievable resolution of RESOLFT technique is the excitation intensity and therefore the photostability of imaged dyes rather than the conventional diffraction of light. Recent development of RESOLFT technique aimed to reduce the excitation intensity by exploiting dark states that can be saturated upon reduced intensity excitation.

i. Stimulated emission depletion microscopy

Stimulated emission occurs when a fluorophore in an excited state is exposed to a photon whose energy matches the difference between the energies of the excited state and the ground state. The excited molecule returns to the ground state by emitting a photon of similar wavelength as the absorbed one. This process can be used to deplete the population of closely located emitters, sharpening the PSF of individual molecules and therefore increasing the achievable optical resolution.

Stimulated Emission Depletion (STED) method [134] is usually applied on a scanning confocal microscope setup and is achieved using two synchronised, ultrafast, collinear pulsed lasers focused in the sample. The first laser is a conventional imaging excitation source, whereas the second laser emits at a red-shifted wavelength, in order to match the energy difference between the excited state and the ground state. This depletion laser has a doughnut shape and is aligned such that its illumination surrounds the maximum illumination intensity of the first laser. The intensity of the

red-shifted laser is chosen so that it saturates depletion of the fluorophore excited state within the doughnut region, effectively reducing the size of the excitation beam. The two lasers are then scanned across the specimen, providing images with a lateral resolution of around 30 nm [110]. The STED method has been used to complement the 4Pi technique, leading to an axial resolution of 30-40 nm [137]. The main problem of the technique is the large intensity required to reach saturation, using typically picosecond laser pulses of high intensity (~ 1 GW/cm^2) [138].

ii. Ground state depletion microscopy

The fluorophore deexcitation associated with the STED technique must take place at a rate faster than the nanosecond scale fluorescence lifetime in order to ensure efficient depletion. Using a longer lived dark state, such as the triplet state, reduces the rate requirement to a microsecond scale, dividing the intensities required by a factor of around 10^3.

In Ground State Depletion (GSD) microscopy, triplet state saturation can be achieved by repetitively exciting ground state molecules to the first singlet state and increasing the probability of intersystem crossing [139]. The excitation beam is superimposed onto the depletion beam, which has a doughnut shape with a zero intensity node at the centre, and the specimen is raster scanned. Fluorophores trapped in the triplet state need to relax to the ground state, without undergoing photobleaching, before being excited back to a singlet state when imaged. The efficiency of the technique is hence dependent on the fine tuning between intersystem crossing rate, triplet state lifetime, scanning rate and photostability of the fluorophore. Despite these technical challenges, GSD has been successfully applied with several different fluorophores including rhodamine dyes [140].

iii. Fluorophore reversible switching

Another improvement to the RESOLFT technique has been achieved using dyes that can be reversibly driven from a bright state to a dark state upon illumination at a given wavelength. The main underlying principle of this behaviour is a conformational change of the molecule, typically a *cis-trans* isomerisation. Fluorescence of emitters can therefore be inhibited under continuous illumination of the "switch off" laser, at lower intensity than in STED microscopy.

The switch between bright and dark state has to be reversible, as fluorophores have to undergo successive depletion and activation cycles during sample scanning. Multiple reversible photoswitching dyes have been investigated over the years to conduct live cell imaging using super-resolution microscopy. In particular, fluorescent proteins asFP595 from *Anemonia sulcata* have been used to achieve a 50 nm resolution with an 8-fold decrease in incident laser intensity compared to the STED method [138]. A recent study succeeded in imaging dendritic spines in living brain slices at a resolution below 40 nm using photochromic GFP, a fluorescent protein that can be reversibly photoswitched more than a thousand times [141].

1.9 Single Molecule Localisation Techniques

Super-resolution techniques such as STED, GSD or structured illumination microscopies rely on a physical modification of the PSF of the microscope, whereas single molecule localisation techniques are based on a temporal separation of emission from individual emitters. The concept is that a feature position can be determined with a high precision if there are no neighbouring emitters switched on at a distance lower than the Abbe's diffraction limit. Multiple closely spaced photoswitchable molecules can therefore be resolved when they are successively imaged individually. Moreover, microscopy techniques based on this principle do not require extensive modification to the microscope setup and can be applied successfully to multiple *in vivo* experiments using photoswitchable fluorescent proteins.

1.9.1 Gaussian Fitting of the PSF

A fitting model is required to retrieve the centre of emitters located inside a diffraction-limited area. The projection of the PSF onto a surface in the (x, y) plane can be approximated to a Gaussian function (Figure 1.9) centred on (x_0, y_0) of respective width ω_x and ω_y in (x, y):

$$I(x,y) = \mathrm{I}_0 + \mathrm{A}\exp\left(-\frac{1}{2}\left(\frac{(x-x_0)^2}{{\omega_x}^2} + \frac{(y-y_0)^2}{{\omega_y}^2}\right)\right) \tag{1.18}$$

Gaussian fitting is a widely used tool for determining the intensity centre of mass of a single molecule emitter (centroid) and has been proven to be suitable for emitters with no fixed dipole orientation [142]. High image resolution can be achieved by applying a least-squares fit to a Gaussian approximation of the PSF in order to localise each emitter individually, with a precision on the order of tens of nanometres. Although other methods exist to retrieve the positions of individual emitters, Gaussian fitting of fluorescence spots remains the most popular, as it has been demonstrated to give the best results, both in precision and accuracy [143].

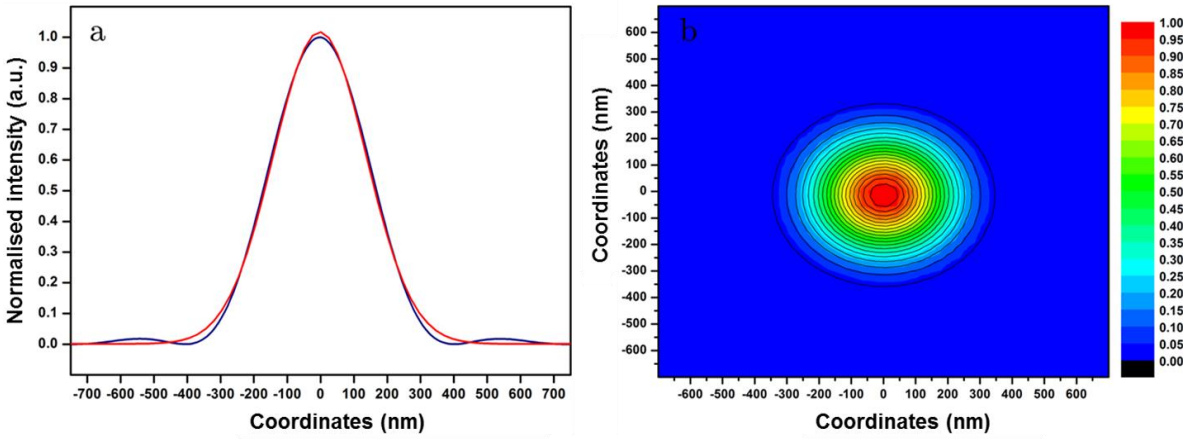

Figure 1.9. Gaussian fitting of the PSF. a) 1D Gaussian fitting. b) Gaussian fitting in 2D. Despite the Gaussian approximation, fitting of the PSF results in accurate results for dipoles displaying no fixed orientation. The determination of an individual emitter position from the PSF intensity distribution is used to surpass the diffraction limit.

1.9.2 Nyquist Criterion and System Magnification

The density of the specimen fluorescent labelling is a critical requirement to achieve super-resolution. The Nyquist-Shannon theorem states that a continuous function can be reconstructed from discrete samples provided it is band limited and at least two sample points can be detected per cycle of the highest frequency component of the function. At least two fluorescent dyes are therefore required per resolution unit in order to ensure the quality of the reconstructed super-resolution image [144, 145]. Moreover the system magnification must be adjusted to control the pixel size (the physical size of one pixel divided by the total magnification) with respect to the PSF width. A pixel size too little increases the uncertainty of the Gaussian fitting process, whereas oversampling results in a decrease of the SNR and therefore degrades the localisation precision. In practice, the best compromise between these two effects is obtained by matching the pixel size to the standard deviation of the PSF width [146].

1.9.3 Localisation Precision: Photons Statistics

The localisation precision is limited by the fundamental characteristics of the imaging system and the number of photons collected. The latter is technically the main limiting factor in conventional single molecule experiments. The uncertainty on the centroid position localisation in the i direction due to photon statistics has been first expressed [147] as:

$$\sigma_{\mathrm{i}} = \sqrt{\frac{{\omega_{\mathrm{i}}}^2}{N} + \frac{a^2/12}{N} + \frac{8\pi{\omega_{\mathrm{i}}}^4 b^2}{a^2 N^2}} \tag{1.19}$$

where parameters ω , a, b and N represent respectively the width of the PSF in the i direction, the pixel size of the image, the standard deviation of the background noise and the number of photons collected.

The first term of the sum is associated to photon noise, while the second and third terms respectively take into account the pixelated effect of the detector and the background noise.

A more rigorous model was later put forward by Mortensen *et al.* [148], which takes into account the excess noise present in EMCCD camera through an excess noise factor F that is equal to 1 for CCD camera and around $2^{1/2}$ for EMCCD detector [80, 149]:

$$\sigma_i = F\sqrt{\left[\frac{16({\omega_{\mathrm{i}}}^2 + a^2/12)}{9N} + \frac{8\pi b^2({\omega_{\mathrm{i}}}^2 + a^2/12)^2}{a^2 N^2}\right]} \tag{1.20}$$

The achievable precision increases with the number of photons collected, it is therefore important to use fluorescent labels displaying high quantum yield and exhibiting a strong resistance to photobleaching.

1.9.4 Probe-based Super-Resolution

Biological samples are usually densely labelled and multiple molecules often share the same diffraction-limited volume, which makes them unresolvable using a simple fitting process. It is thus necessary to separate nearby emitters along another

dimension to resolve them. This experiment was first realised by imaging luminescent centres located in a quantum well and emitting in different wavelength spectra [150]. The success of this method proved that it was possible to individually image the emitters with appropriate discrimination criteria and that centroid positions of individual PSFs could be retrieved with an enhanced precision [151].

The discovery of photoactivatable/photoswitchable fluorescent probes triggered the development of techniques based of that concept. These labels can undergo a chemical modification upon near-UV illumination, which renders them fluorescent (photoactivation) or shifts their emission peak (photoswitch) [152, 153]. Sparse subsets of emitters in densely labelled specimens become fluorescent upon activation and can be imaged before returning to a dark state upon photobleaching. Repeating the cycle of activation/excitation/bleaching allows one to localise the respective centroids of emitters and to recreate a super-resolution image.

The first techniques developed around this concept only differ by the nature of the fluorescent label. Stochastic Optical Reconstruction Microscopy (STORM) is based on the photoswitching behaviour of conventional organic cyanine based dyes Cy3 and Cy5 [154], whereas Photoactivation Localisation Microscopy (PALM) [155] and Fluorescent Photoactivation Localisation Microscopy (FPALM) [156] use photoactivatable or photoconvertible fluorescent proteins. These techniques can achieve a lateral resolution of 25 nm and are used to localise fluorophore, quantify molecule numbers *in vivo* or track individual molecular motions over time [146].

Figure 1.10 displays the result of an FPALM experiment conducted on a *S. pombe* cell containing the protein Cdc22 labelled with mEos2, a monomeric green to red photoswitchable fluorescent protein [157], using QuickPALM plugin for ImageJ [158] and following the protocol described in Section 2.3.2. Multiple cycles of activation of mEos2 with a 405 nm laser line, followed by imaging of the photoswitched subset population with a 561 nm laser, were performed under TIRFM. The centroids of emitters switched on during each cycle were retrieved with a Gaussian fitting process and used to reconstruct the final super-resolution image. Long acquisition and processing times are required to acquire and analyse the large number of data needed for accurate quantification of molecules (~ 10000 frames per experiment in the case of Figure 1.10). The super-resolution image obtained contains information that is otherwise lost using conventional fluorescence imaging. In particular, the precise localisation of molecular centres inside a diffraction-limited spot enables one to perform a quantitative study of proteins involved in important processes occurring during the cell cycle, and may indicate their respective conformations, aggregation states or structural clustering sites for example.

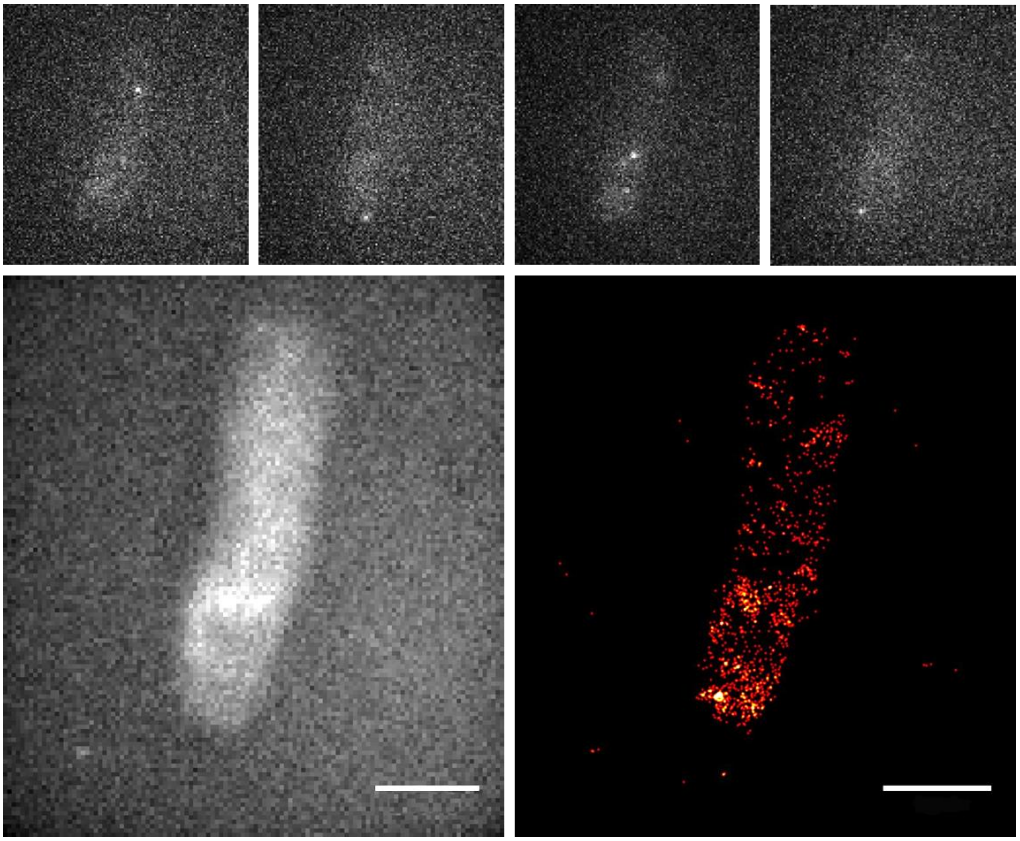

Figure 1.10. Application of FPALM technique on Cdc22-mEos2 in *S. pombe*. Raw data (top four images) leads to an average projection (bottom left) where spatial information details are lost. A super-resolution image was reconstructed from the original dataset using the FPALM approach, which clearly displays areas with a high density of fluorescent molecules, indicating clusters formation in the cell (bottom right). A number of 1715 single molecules were localised in the cell with a mean precision of 19 ± 4 nm. Scale bar: 5 μm.

1.9.5 Individual Emitters Imaging Techniques

Fitting of the PSF can drastically improve the precision of single molecule localisation under the condition that the fluorophore is the only emitter inside the diffraction-limited volume. In particular, the dimeric motor Myosin V motion has been investigated with Fluorescence Imaging with One Nanometre Accuracy (FIONA) technique. Light chain domains of the molecule were labelled and successive Gaussian fits of the moving molecule PSF performed. A step size of 37 nm was determined with a precision better than 1.5 nm, validating the "hand-over-hand" motility model [105]. Further details on the 3D orientation of the structure were obtained by Defocused Orientation and Position Imaging (DOPI) [159]. Single molecule High Resolution Colocalisation (SHREC) is a variant of FIONA applied to multicolour systems, achieving a 10 nm resolution with dynamic systems [160].

Point Accumulation for Imaging in Nanoscale Topography (PAINT) exploits the sequential binding of fluorescent molecules to the surface of target biological systems to accumulate the centroid positions of individual emitters and recreate a high resolution image [161]. Sample labelling with multiple colours has moreover been used to differentiate spectrally the emitters, reaching at best a 10 nm resolution [160].

Photobleaching behaviour of organic dyes can also be used to differentiate between neighbouring molecules, as this stochastic process obeys a Poisson distribution and is not simultaneous for every imaged dye. The intensity fluctuation of multiple fluorophores located inside a diffraction spot therefore displays discrete levels associated with the successive photobleaching events. Single molecule High Resolution Imaging with Photobleaching (SHRImP) has been applied to localise DNA-coupled Cy3 dyes separated by distances ranging from 10 to 50 nm with 1.5 nm precision [33]. The principle is to identify a single emitter PSF after the other closely spaced fluorophore has been switched off by photobleaching. Subtraction of the remaining fluorophore PSF from the image before photobleaching provides the PSF of the photobleached dye molecule. Nanometre-Localised Multiple Single-molecule (NALMS) fluorescence microscopy extends this concepts to the resolution of multiple Alexa 488 dyes bound to a double stranded (ds) DNA [162]. This approach has recently been combined with the PALM method using conventional dye molecules in a technique called Bleaching/blinking Assisted Localisation Microscopy (BALM) [32], which uses a subtraction process on every consecutive frame to identify single emitters in a temporary non-fluorescent state.

Moreover, the blinking behaviour, characterised by periods of emission of fluorescence interspersed with dark state periods, have been exploited in order to achieve super-resolution. For instance, an independent component analysis was applied on temporal fluctuations of a QD pair to identify the position of each emitter [163]. In particular, the distance between two QDs bonded at the ends of a 122 base pairs (bp) ds DNA was determined using the characteristic blinking of respective emitters [164]. In this method, a threshold is applied on intensity profiles in order to map individual QD positions using an extensive fitting process. This method only works under the assumption that the fluorescence intensities of the two QDs vary only slightly during the course of the experiment. The fitting procedure can be time and CPU intensive and the assignment of the PSF may be subject to ambiguity when both QDs are switched on at the same time. To overcome this problem, spectral imaging using a grating pattern has been used on multicolour QD complexes to avoid any bias in the subsequent fitting process [165].

Chapter 2

Instrumentation and Methods

A good knowledge of the capabilities and limitations of the instrumentation used in single molecule spectroscopy is crucial to the quantitative analysis of experimental results. The superior level of sensitivity of single molecule spectroscopy comes indeed at the expense of a number of potential interference factors arising from an excess of other molecules or fluorophore photophysical artifacts. Experimental features of the instrument setup such as illumination profile, excitation source intensity and detection volume must therefore be accurately determined to ensure the correct interpretation of results. Moreover, single molecule experiments require a careful preparation and imaging of the sample. Crucial features of sample preparation include choice of fluorescent label, method of conjugation with the biomolecule of interest, purification process and any surface attachment protocol used. On top of these requirements comes the necessity to limit the autofluorescence arising from sample components such as solvents or imaging buffers. This is a critical step to ensure the conservation of a high SNR and generally requires that multiple control experiments are conducted on isolated sample components.

The following section introduces the experimental setup that has been used for the work performed in this thesis. The custom-built microscopes were calibrated and characterised using reference fluorophores prior to their application in the study of the biological structures of interest. The different sample preparations and imaging protocols are also described, providing the experimental details corresponding to results presented in the following chapters.

2.1 Confocal Microscope Setup

A schematic of a conventional confocal setup used in the work reported in this thesis is displayed in Figure 2.1. The laser beam is reflected by the dichroic mirror and focused inside the sample, exciting the molecules located in the associated detection volume. A pinhole aperture is placed before the detector, such as only fluorescence arising from molecules located in the defined optical section of the sample can reach the detector. Fluorescence arising from molecules excited above or below the focal plane, sometimes referred as "out of focus fluorescence", is rejected by the pinhole. In addition, dichroic mirror and band-pass filter components ensure that a minimal percentage of the excitation beam reaches the detector.

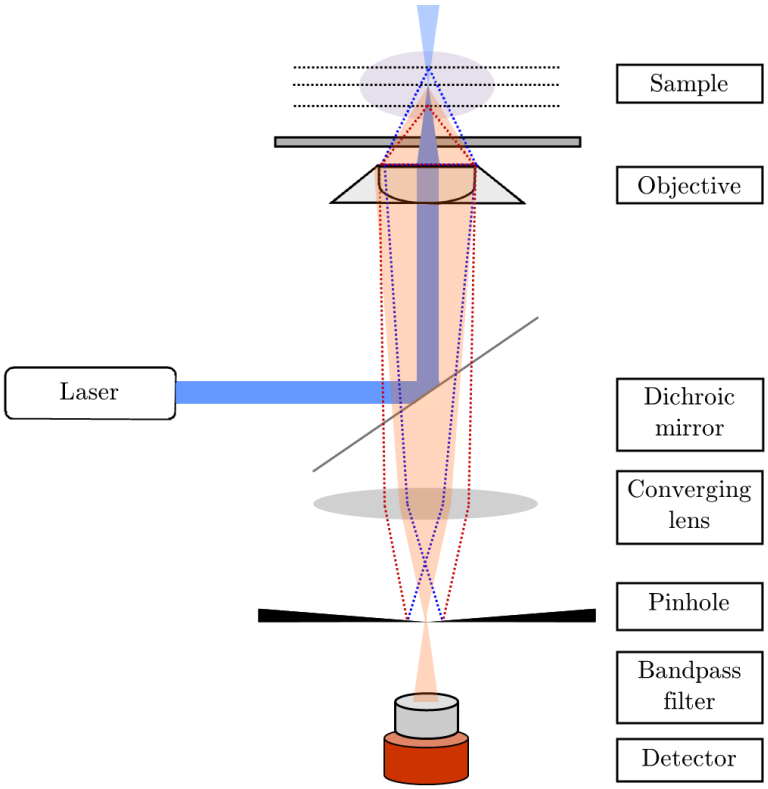

Figure 2.1. Schematic representation of a confocal microscope. Effective reduction of detection volume is achieved by selecting a conjugate plane in the sample with a pinhole.

2.1.1 Experimental Confocal Setup

Fluorescence Correlation Spectroscopy (FCS) was performed on an inverted Nikon TE2000-E microscope. The excitation laser was reflected by a dichroic mirror and directed into a 1.45 *NA*, 100× objective (Plan-APO DICH). The incident excitation

was kept to low powers in order to reduce the photobleaching effect and the pinhole size was adjusted to a width of the order of 40-60 μm. The fluorescence signal arising from the detection volume was collected by the same objective lens, directed to an appropriate band-pass filter and detected by an APD detector (Perkin-Elmer SPCM-AQR-14), working under PMS software (Becker & Hickl, PMS-300 Multiscaler).

Experiments aiming at comparing different species were carried out on the same calibrated setup at close intervals in time, as measurements have been shown to be potentially influenced by experimental factors such as coverslip thickness, astigmatism and laser beam stability [166, 167].

Intensity of the laser beam needs to be carefully adjusted to obtain correct FCS measurements. An excessive excitation leads to saturation of dyes located next to the detection volume centre, increasing the contribution of peripheral molecules [168]. An intensity calibration analogous to Figure 1.3 was therefore performed for each dye used, to ensure that excitation was carried out in the linear absorption regime region.

For all experiments, microscope glass slides were carefully cleaned before use. No. 1 borosilicate coverslips were first flame dried, ozonated for 30 minutes to remove any trace of autofluorescence, incubated in deionised water with 0.05% Tween 20 in order to prevent aggregation or surface adhesion, and rinsed with deionised water.

2.1.2 Autocorrelation Algorithm Test

A concentration of 1 nM of a 45 bp single strand DNA of sequence CCTCCTAAAAAAAAACCTCAAAAAAAAAAAAAAAAAAAAAGGAGG (ATD Bio Ltd) labelled with TMR was used to obtain the data used to test the autocorrelation algorithm. The FCS experiment was conducted at 20.5 ± 0.5°C, using an optical setup similar to the one presented in Figure 2.2.

2.1.3 Detection Volume Calibration: Rhodamine B

A concentration of 1 nM of Rhodamine B (RhB) was obtained by dilution from stock (Eastman Chemical Co., 14352) in purified water solution. The FCS experiment was conducted at 20.5 ± 0.5°C using a solid state 532 nm laser line operating at an excitation power of 300 μW at objective, along with a Semrock FF547/651-Di01-25×36 dichroic beamsplitter and a FF01-593/40-25 single-band bandpass filter. The spectral fitering setup used for RhB imaging is presented in Figure 2.2.

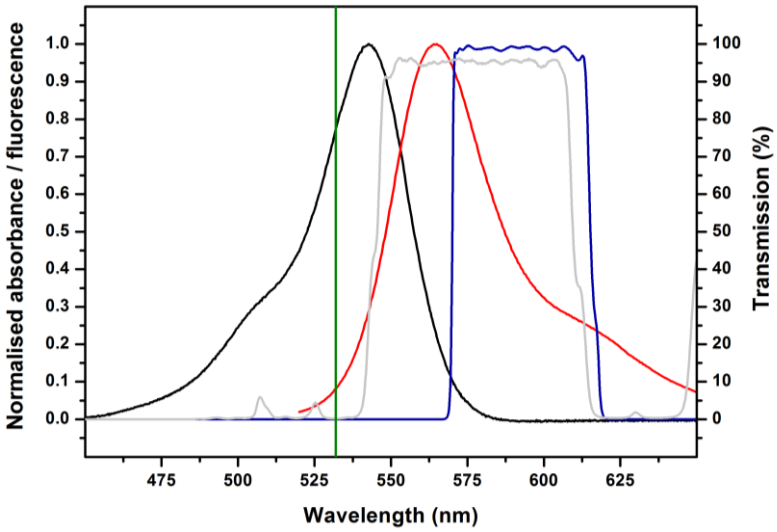

Figure 2.2. Spectral filtering setup used for FCS experiment with RhB. A dichroic mirror (grey) was used to reject the 532 nm excitation laser light (green) and a band-pass filter with a 40 nm bandwidth centred around 593 nm (blue) placed before the detector to collect RhB fluorescence emission [169].

2.1.4 Sensitivity Assay: GFP Experiment

Commercial purified protein GFP (Aviva Systems Biology, OARA01928, 27.5 kDa, 1 mg/mL) was used for the calibration of the detection volume created by focusing the 473 nm laser beam inside the sample. Monoclonal IgG antibody complementary to GFP was purchased from Aviva Biology (OARA01901, 1 mg/mL, 150-160 kDa) and complexed with the purified GFP using the following protocol. 10 µL of GFP stock solution was mixed with 60 µL of GFP antibody in a solution of phosphate-citrate (100 mM) and the mixture incubated for 1 hour at 37°C. The solution was diluted down to 1 nM and the sample was deposited at the surface of a coverslip cleaned following the protocol described in Section 2.1.1.

Further FCS experiments were carried out at 20.5 ± 0.5°C using a 473 nm solid state continuous wave laser operating at a power of 150 µW at objective, a Semrock FF493/574-Di01-25×36 dichroic beamsplitter and FF01-525/45-25 single-band bandpass filter, an optical system similar to the one described in Figure 1.4.

2.1.5 FCS Experiment on Suc22-YFP

The purified recombinant proteins obtained from *Escherichia coli* (provided by Dr A.S. Schreurs, Carr group, GDSC, Sussex University) were thawed on ice, diluted

with filtered Phosphate Buffered Saline (PBS) to obtain a 1 nM concentration. All reagents used were tested for autofluorescence before the experiments were performed. FCS experiments were carried out at 20.5 ± 0.5°C using a 532 nm solid state continuous wave laser operating at 300 µW at objective, a FF547/651-Di01-25×36 dichroic beam splitter and a 550 nm longpass filter (FGL550, Thorlabs). Figure 2.3 displays the spectra associated to the experimental setup.

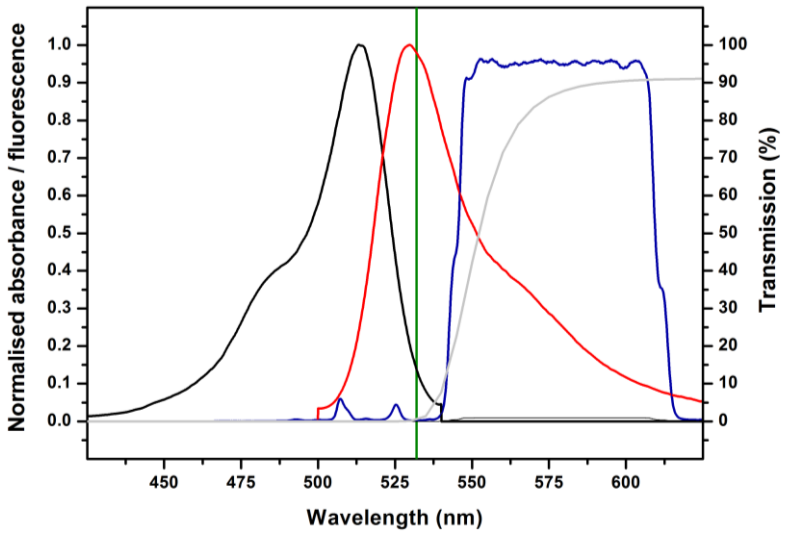

Figure 2.3. Spectral filtering setup used for Suc22-YFP investigation. A dichroic mirror (blue) was used to reject the 532 nm excitation laser light (green) and a longpass filter (grey) to collect fluorescence emission [34].

2.2 TIRFM Setup

The TIRFM setup was built around a Nikon TE2000 inverted microscope with two main excitation sources selected depending on the desired application: a mixed gas ion laser operating at 457, 488, 514 nm (Spectra Physics Beamlock 2060-RM) was used for single channel imaging, and a bank of diode lasers (405, 473, 532 and 561 nm) was chosen for multiple channel imaging. The incoming beam was passed through a monochromator to remove overtones and superluminescence from the argon plasma and a spatial filter which only allowed the central noiseless maximum of the diffraction pattern, giving a closer match to the theoretical Gaussian profile of the laser. This device simply consists in a series of two lenses separated by a pinhole placed in their focal distance: the laser beam is focused down to its diffraction limit, filtered by the pinhole and re-collimated by the second lens. The excitation beam was then circularly polarised by passing through a quarter-wave retarder (Thorlabs UK,

WPMHO5-514) and focused at the back focal plane of a 100× objective lens with a *NA* of 1.458 (PLAN APO Nikon oil immersion CEI). An additional lens, the TIRFM lens, focused the laser light off the optical axis of the objective lens, providing the critical angle needed for the evanescent field creation. Fluorescence emission was collected by the objective and passed through a dichroic beamsplitter. In addition, selective band-pass filters were placed before the EMCCD camera (Evolve 512) to remove any additional scattering from the excitation source. An additional variable zoom component (zoom 1× to 7×, Edmund Optics) was added before the camera in order to increase furthermore the magnification capacity of the system. A schematic representation of the TIRFM setup used in this thesis is described in Figure 2.4.

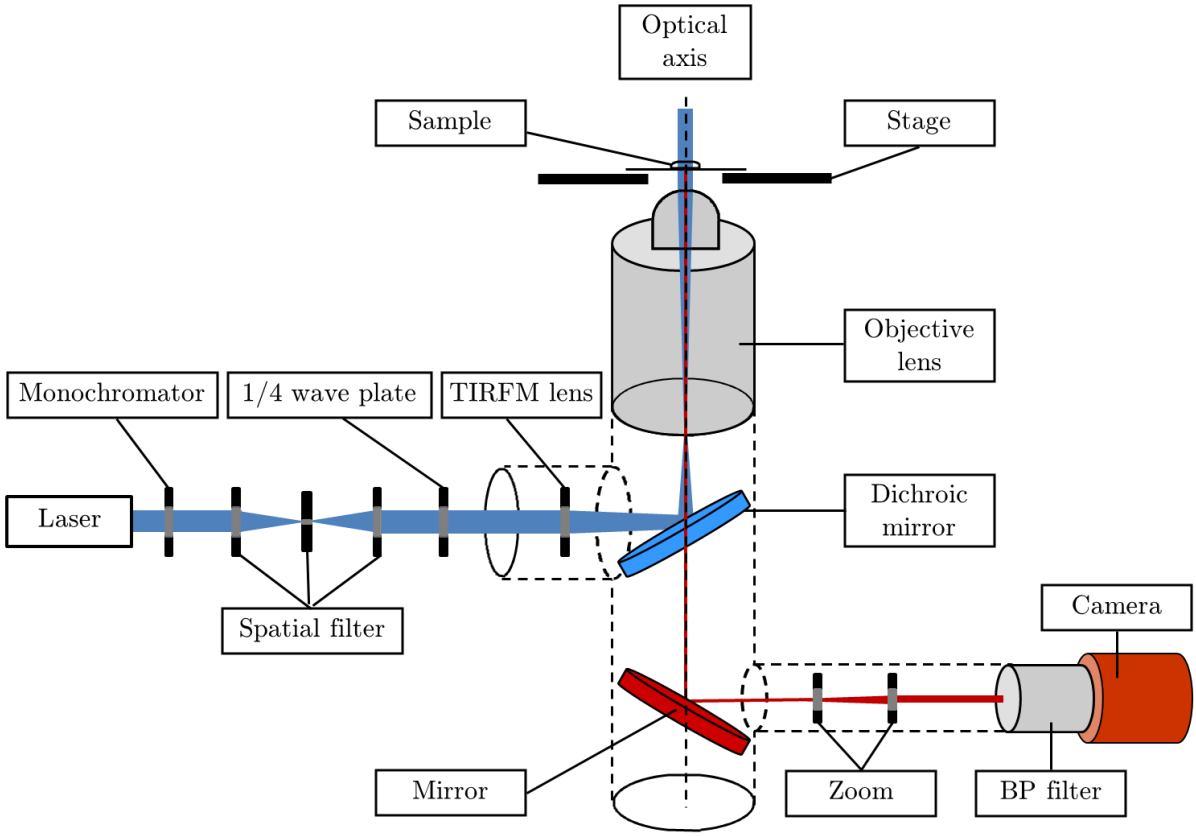

Figure 2.4. Schematic representation of a TIRFM setup. A conventional inverted microscope was transformed into a TIRFM system by adding a lens that can tilt the incident laser beam off the objective optical axis, in order to reach the critical angle.

2.2.1 Laser Power Calibration

Appropriate adjustment of the excitation intensity is needed for the imaging of fluorescent probes, either to limit the influence of photobleaching, determine saturation intensity or simply achieve efficient excitation. The power value reaching

the sample can be determined at the objective, but this method is highly impractical during an experiment. The laser power was therefore measured before entry to the microscope and found to correlate linearly with the measured power at the objective lens (Figure 2.5). The loss of power observed can be explained by some attenuation caused by optical components of the setup.

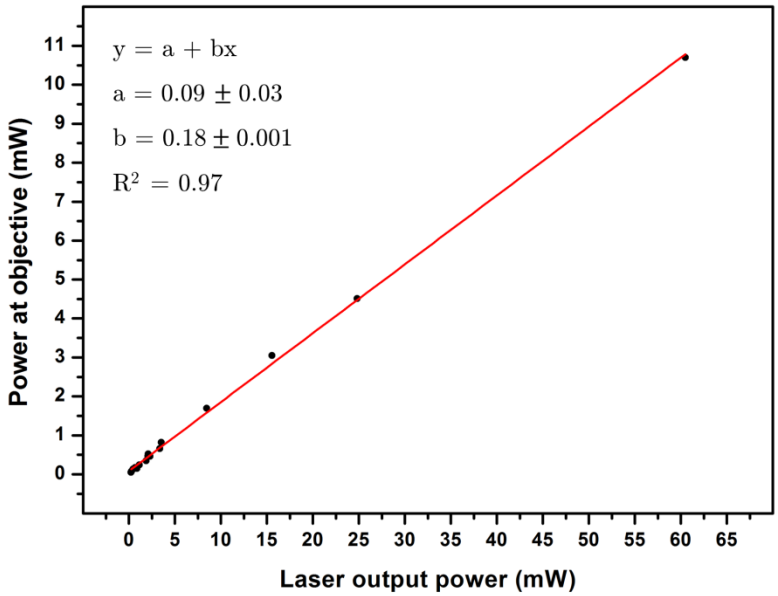

Figure 2.5. Laser power transmission efficiency. The slope of the linear fit performed indicates that 18% of the incident 488 nm laser power reaches the objective. The average error associated to each measurement was 0.03 mW and is not displayed on the figure for clarity purposes.

2.2.2 Polarisation Effects

The polarisation of the incident light represents the orientation of the electric field and influences the polarisation of the evanescent field [102]. This effect can induce a preferential excitation of certain emitters with fixed dipole orientations inside a sample. Typical fluorophores in solution display isotropic emission; this behaviour might however change when the dyes come in contact with an interface, as frequently encountered in TIRFM experiments. Moreover, binding of a fluorophore to a biological structure could drastically affect the orientation of the associated dipole emitter. Fluorescence polarisation has been previously used to study protein domain dynamics [170]. However, it is in general critical to transform the linearly polarised incident light into an unpolarised beam in order to reduce the biasing induced by selective excitation of emitters at the interface [171]. The quarter waveplate placed inside the laser excitation line in the TIRFM setup serves this purpose.

2.2.3 Near-field Enhancement

On approach to total internal reflection, the strength of the evanescent field increases towards the critical angle θ_c, for the dielectric mismatch at the interface. The angular dependence of the irradiance for polarised light has previously been demonstrated [98] and the enhancement predicted to be around 4 for s-polarised light (electric field vector oriented normal to the plane of incidence) and around 3 for p-polarised light (electric field vector in the plane of incidence) [70]. The incident and reflected amplitudes add constructively before reaching the critical value and destructively for a bigger angle, which leads to an important decrease in the irradiance of the sample.

This effect was determined experimentally on the TIRFM setup by imaging a monolayer of Alexa 546 dyes coated on the surface of a coverslip, following the protocol described in Section 2.3.1. The average emission intensity measured under a constant incident illumination was recorded as the incident angle was regularly increased from epifluorescent mode towards the critical angle (Figure 2.6). The incident angle values were retrieved from reference situations: incident beam collinear with optical axis (0°) and maximum detected intensity value (61°). A maximal enhancement factor of 3.2 was observed during the sequential increase of incident angle. The slight difference with theoretical predictions most likely arises from photobleaching effects on the fluorescent monolayer and imperfect optics components.

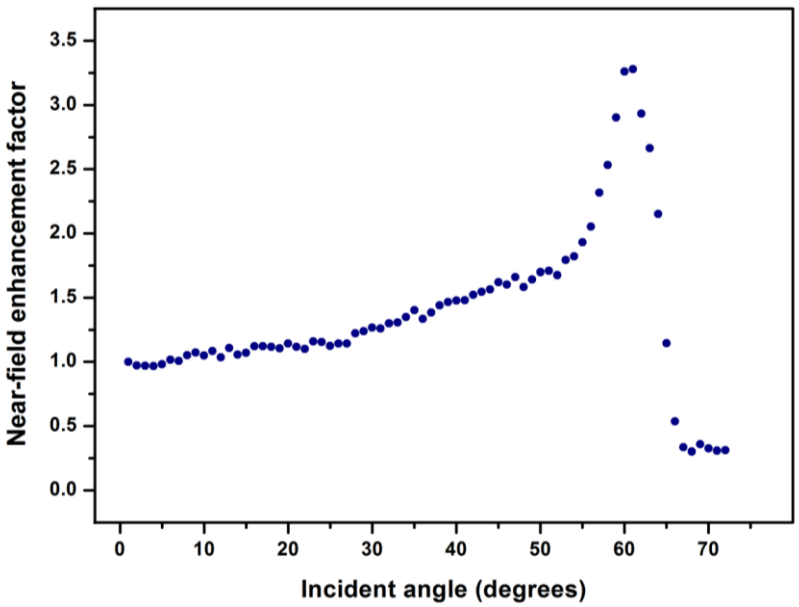

Figure 2.6. Variation of excitation intensity with incident beam angle. A 3.2 enhancement factor is attained in TIRFM at a critical angle of 61 degrees compared to the conventional epifluorescent mode. The incident and reflected amplitudes add destructively for bigger incident angles, leading to a drastic decrease of the emission intensity.

2.2.4 TIRFM Footprint

The variation of the excitation intensity across the field of view is an important parameter to be characterised, as it can lead to biasing in post-acquisition analysis. A rough homogeneous monolayer of Alexa 546 was created by depositing a high concentration (0.1 μM) on a coverslip surface. The resulting sample was imaged under TIRFM to obtain the excitation profile of the sample. The maximum intensity area displays an approximate disk shape, whose cross section is shown in Figure 2.7. The intensity variation inside the plateau of maximum intensity was inferior to 10%. It was therefore possible to limit the excitation bias by retaining signals arising from molecules located in the area of near-uniform excitation ($\sim 60\ \mu m^2$).

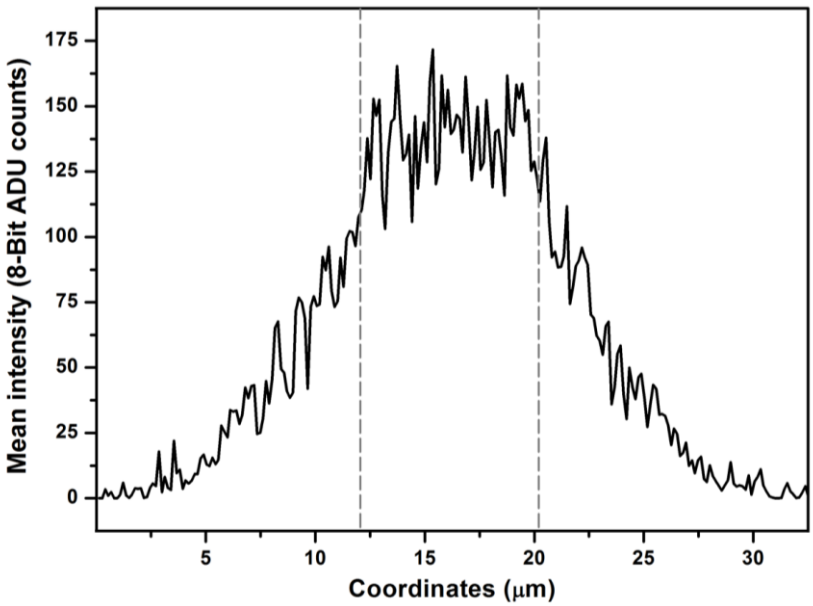

Figure 2.7. Excitation intensity profile under TIRFM. Emission arising from a monolayer of Alexa 546 imaged under TIRFM was detected and excitation area investigated. The central region delimited by the grey lines displayed a mean intensity of 139 ± 15 counts, varying by around 10% on ~ 8 μm.

2.2.5 Image Intensity and Magnification

The pixel size of acquired images must be correlated with real space reference values in order to determine accurately the scale of features of interest. The additional zoom lens installed before the camera displayed seven different magnification configurations, each of which has been associated with its respective pixel size using an optical calibration slide (Edmund Optics 1951 USAF glass slide resolution target).

The minimal pixel size attainable by the system at maximum magnification was found to be 34 nm. However, the additional magnification power afforded by the variable zoom length must be used with caution. The brightness B of a fluorescent image is inversely proportional to the square of the magnification M used [76]:

$$B = \frac{NA^4}{M^2} = NA^4 \times (A \times P)^2 \qquad (2.1)$$

with P the pixel size and A a constant.

A monolayer of Alexa 546 dye was imaged under constant excitation intensity to demonstrate the effect of the magnification on the signal detected. The mean ADU count per pixel inside a 5 μm^2 area was therefore acquired for different pixel sizes. Figure 2.8 displays the variation of intensity detected versus the additional magnification power used and experimental results fitted using a relation of the type of Equation (2.1). The average intensity collected inside the detection area decreases rapidly with zoom level used ($B \propto 1/M^2$), which would ultimately degrade the quality of experimental results and hinder the detection of single molecules. On the other hand, the use of low magnification values can sometimes lead to inaccurate results, especially when a fitting process is necessary (see Section 1.9.2).

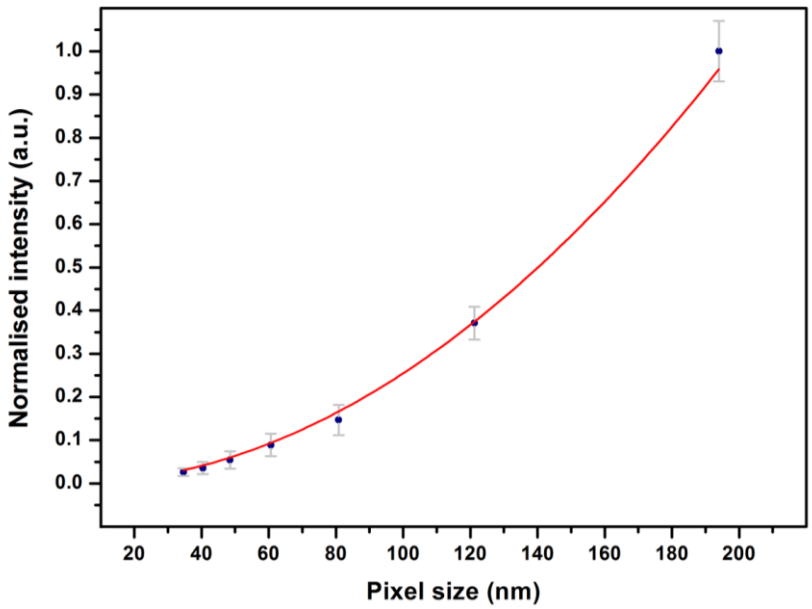

Figure 2.8. Signal intensity dependency to magnification power. The normalised mean intensity per pixel detected inside the detection area (blue points) increases with the pixel size under constant illumination intensity. Data were fitted with an expression similar to Equation (2.1) (red curve).

2.2.6 Photon Counting Camera Calibration

The camera readout is the result of an internal signal amplification process and is generally expressed in Analogue-to-Digital (ADU) units. Applying an accurate conversion of the signal output to retrieve the incident photon counts is especially important for calculating localisation precision. This can be achieved at a given camera multiplication gain G by introducing the conversion factor C, representing the number of photoelectrons per Analogue-to-Digital Unit count (e^-/ADU):

$$N_{\text{photon}} = \frac{(\text{ADU counts} - \text{offset})}{G} \times C \tag{2.2}$$

A calibration of the factor C has been performed for the camera used in the experimental setup. Briefly, a 100×100 pixels region has been imaged under different illumination intensities. The mean intensity value and variance were calculated in each case after appropriate correction of the flat-field effect caused by pixel-to-pixel variations in the camera sensitivity, which creates a noise pattern in the acquired data [172]. The slope of the linear regression of Figure 2.9 was used to determine the sensitivity factor of the camera. A full theoretical explanation of the calibration principle and protocol is given in Appendix I.

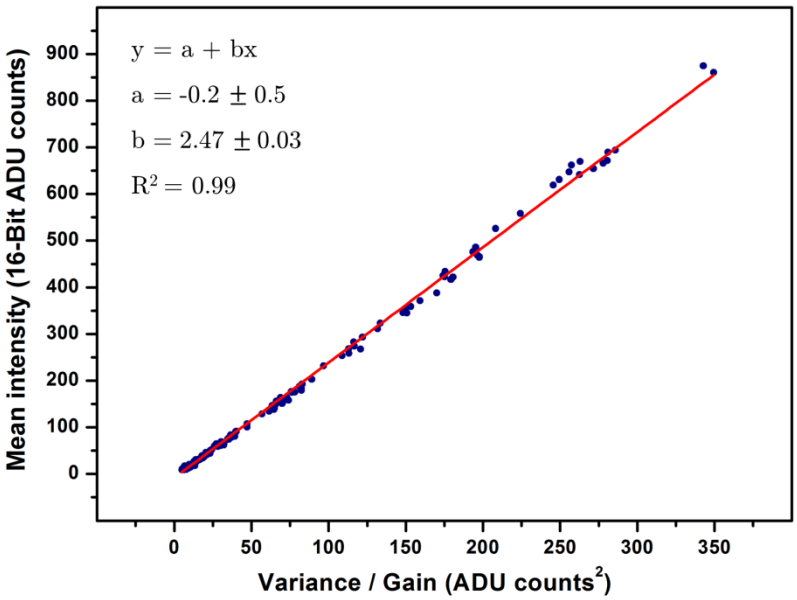

Figure 2.9. Conversion factor calibration. The slope obtained by fitting the average ADU count against the (variance/multiplication gain) value of a 100×100 pixels region for different intensities gives a sensitivity factor of 2.47 ± 0.03 e-/count for a multiplication gain set to 1.

2.2.7 Excess Noise Factor Determination

The excess noise factor associated with the camera used in this thesis has been determined for different gain values by repeating the experiment described in the previous section. The ratios between the linear slopes obtained at different gains and the slope obtained with a unity gain were used to calculate the excess noise factor (Figure 2.10). A more complete theoretical demonstration of this process is given in Appendix I. The factor F^2 associated to the camera used in this thesis was shown to tend to a value of 1.83 ± 0.06 for high multiplication gains.

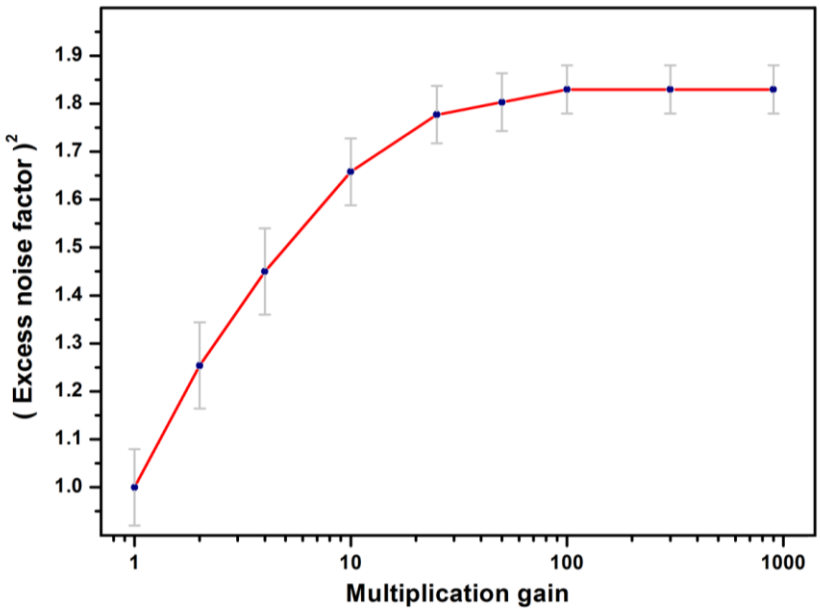

Figure 2.10. Squared excess noise factor dependency to multiplication gain. The factor F^2 reaches a plateau around a value of 1.83 ± 0.06 for high multiplication gains.

2.3 Microscopy Imaging Protocols

The imaging work reported in this thesis was performed using several microscopy methods, which are described below.

2.3.1 Imaging of Alexa 546 with TIRFM

No. 1 borosilicate coverslips were flame dried and ozonated for 30 minutes to remove any autofluorescence before imaging. 100 µL of a solution containing Bovine Serum

Albumin (BSA)-biotin (Sigma, A-8549, 1 mg/ml) in deionised water was incubated for 10 minutes on the coverslip and washed with deionised water. A 100 nM solution of streptavidin conjugated with Alexa 546 (Life technologies, S-11225) was added, allowed to sit for 30 minutes and washed with deionised water. The resulting approximate monolayer was imaged with irradiance values ranging from 0-17 kW/cm^2 and a pixel size of 107 nm. Excitation was performed with a 532 nm solid state continuous wave laser, using Semrock FF547/651-Di01-25×36 dichroic beamsplitter and FF01-593/40-25 single-band bandpass filter. Figure 2.11 displays the setup used during this experiment.

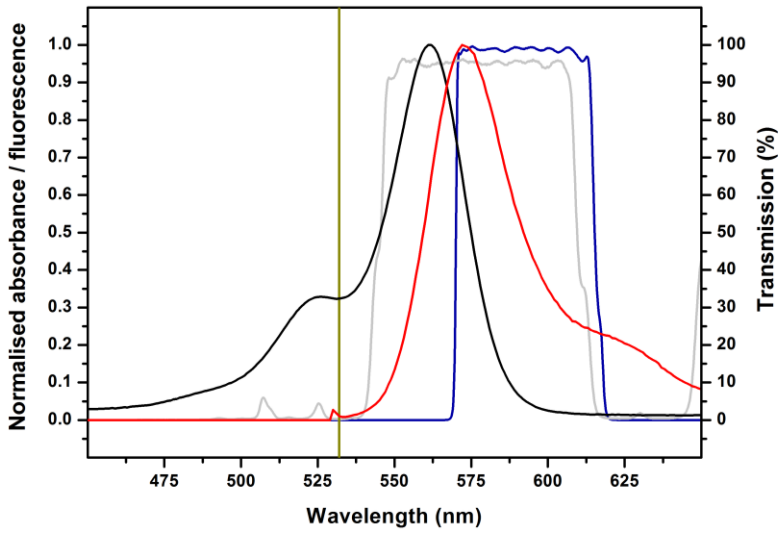

Figure 2.11. Spectral filtering setup used for Alexa 546 imaging. A dichroic mirror (grey) was selected to reject the 532 nm excitation laser light (green) and a band-pass filter with a 40 nm bandwidth centred around 593 nm (blue) used to collect the fluorescence emission [34].

2.3.2 Cdc22-mEos2 Super-Resolution Imaging with PALM

S. pombe cells with Cdc22 labelled with mEos2 were provided by Olaolu Akinsete (GDSC, Sussex University). The cells were grown in nutrient rich yeast medium solution at 30°C for 16 hours and fixed by suspension in methanol.

A variety of lasers was used to activate and excite the mEos2 label with different wavelengths in order to perform activation/excitation/photobleaching cycles. Activation was achieved using a 405 nm solid state continuous wave laser operating at intensity values at the objective varying from 1 to 10 W/cm^2, depending on the number of the converted single molecules. Excitation of photoswitched dyes was performed by a 561 nm laser operating with intensity at objective of the order of 1 kW/cm^2, to obtain the best compromise possible between SNR and acquisition

time. Activation time periods were regularly increased with the cycle number and movies recorded in cycles of 120 seconds with an acquisition time of 60 ms. Cycles of activation/ bleaching were carried out until the number of activated dyes was zero for more than 5 minutes. Room temperature was kept at 16.5 ± 0.5°C in order to prevent thermal relaxation of the microscope components.

Appropriate dichroic and band-pass filters were used for the activation and excitation lasers (respectively Semrock Brightline Di01-R405-25×36 dichroic beamsplitter for the activation and FF570-Di01-25×36 dichroic beamsplitter, FF01-593/40-25 single-band bandpass filter), as displayed in Figure 2.12. Super-resolution images were reconstructed from the original datasets acquired with a spatial resolution of 107 nm/pixel using QuickPALM ImageJ plugin [158].

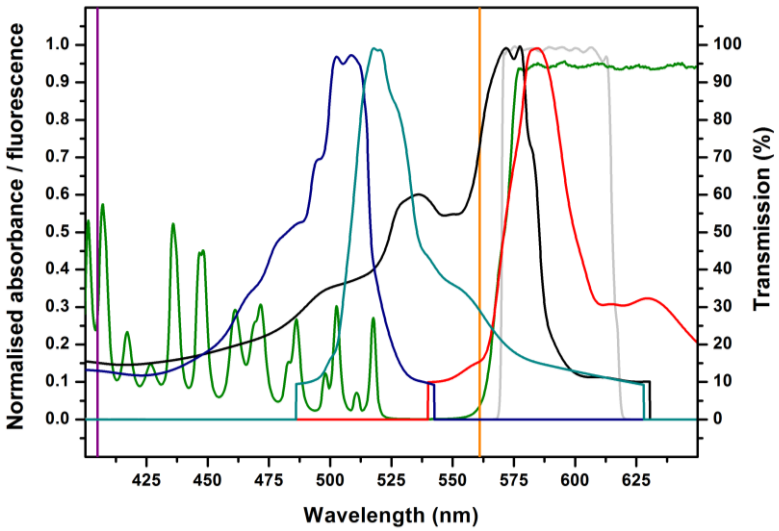

Figure 2.12. Spectral filtering setup used for mEos2 imaging. MEos2 can be converted from its "green" version (absorption and emission spectra respectively in blue and cyan) to its "red" version (black and red curves) upon activation by a 405 nm laser (purple). A dichroic mirror (green) was used to reject the 561 nm excitation light (orange) and a band-pass filter with a 40 nm bandwidth centered around 593 nm (grey) to collect the fluorescence emission [34].

2.3.3 Photobleaching Steps Assay

Slides were incubated with a PBS solution with 5% of BSA. 500 µL of a solution of monoclonal antibody complementary to YFP (0.1 mg/ml, anti-gp16 rabbit IgG, Prot. Group) were incubated at the surface of the coverslip for 15 minutes, and washed twice with PBS/BSA solution with a further 15 minutes of incubation. The coverslip was washed extensively with a filtered solution of PBS, and the purified Suc22-YFP proteins (0.1 nM in PBS solution) left to incubate for 30 minutes before imaging.

The 514 nm wavelength line of a tuneable gas laser (Spectra Physics 164 Argon ion gas laser) was used as the excitation source. A dichroic beamsplitter Semrock FF547/651-Di01-25×36 and a 550 nm longpass filter (FGL550, Thorlabs) were used to separate emission fluorescence from excitation, as displayed in Figure 2.13. Imaging was performed with a lateral resolution of 107 nm/pixel using laser intensity at objective of the order of 1 kW/cm^2.

Several experiments were carried out to control the autofluorescence of materials used: antibodies, BSA and PBS solutions were individually imaged to confirm they did not display significant fluorescence susceptible to degrade experimental results.

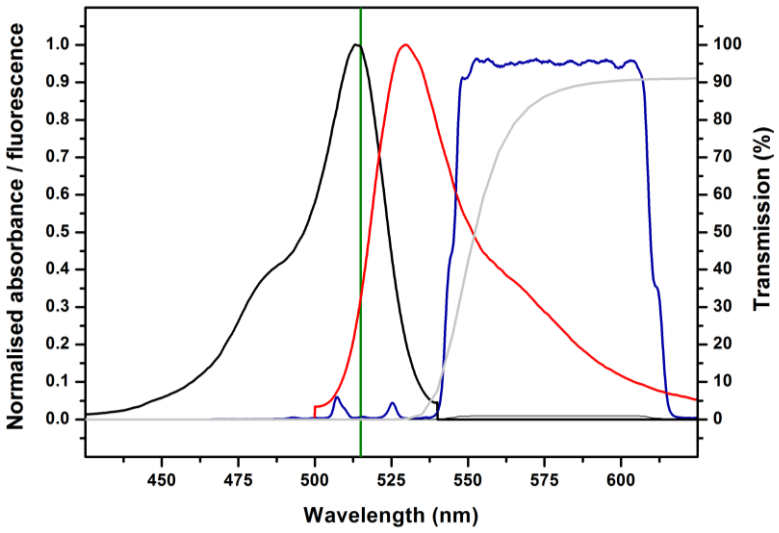

Figure 2.13. Spectral filtering setup used for YFP imaging. A dichroic mirror (blue) was used to reject the 514 nm excitation laser light (green) and a longpass filter (grey) to collect the fluorescence emission [34].

2.3.4 Super-Resolution Optical Fluctuation Imaging

i. QD imaging

QDs (peak emission 585 nm, Life Technologies, Q10111MP) were diluted to 100 pM in a tetraborate solution (50 mM) and incubated at the surface of a coverslip.

The excitation was performed with the 488 nm line of the gas laser, using Semrock FF547/651-Di01-25×36 dichroic beamsplitter and FF01-593/40-25 single-band bandpass filter. Stacks of images were acquired with acquisition times ranging from 30 ms to 100 ms using Micromanager software. Figure 2.14 summarises the spectral profiles of QDs as well as the different components of the imaging setup.

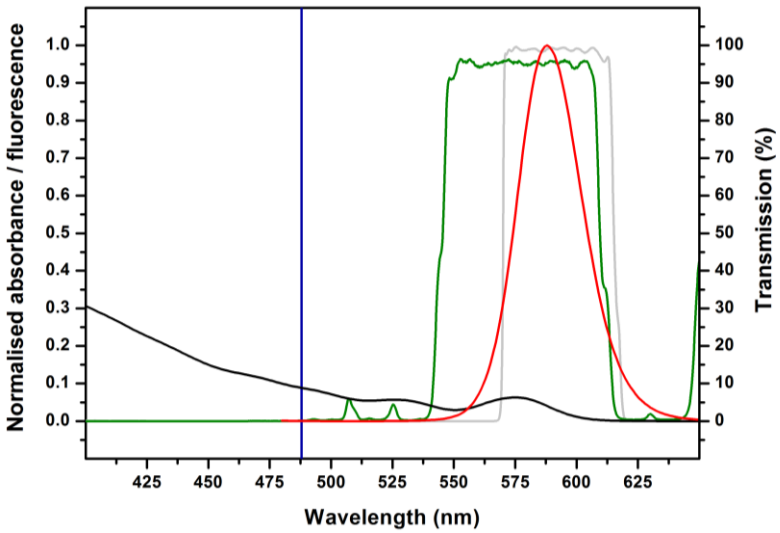

Figure 2.14. Spectral filtering setup used for QD imaging. A dichroic mirror (green) was selected to reject the 488 nm excitation laser light (blue) and a 593 nm band-pass filter with a 40 nm bandwidth (grey) used to collect fluorescence emission [34].

ii. Silanisation of coverslips

Borosilicate coverslips were ozonated for 1 hour, rinsed in acetone, sonicated 20 minutes in 50% methanol (Sigma, 34860)/Milli-Q water and washed thoroughly with Milli-Q water. The slides were then sonicated in chloroform (Sigma, 288306) for 20 minutes, rinsed with Milli-Q water and oven dried at 120°C for 1 hour. The coverslips were sonicated in pure heptane (Sigma, 246654) for 10 minutes and placed in a silanisation-dedicated dish in a mixture of 100 mL of heptane and 100 mL of octenyltrichlorosilane (Sigma, 539279). After gentle swirling, the dish was sealed and stored overnight. The coverslip were then sequentially sonicated in heptane, Milli-Q water, 50% methanol/Milli-Q water, Milli-Q water, chloroform, Milli-Q water, 50% methanol/Milli-Q water, Milli-Q water and sonicated for 2 minutes in chloroform. The coverslips were air-dried, wrapped in aluminium foil and stored at 4°C.

iii. Combed DNA preparation

Schizosaccharomyces pombe (*S. pombe*) genomic DNA extract labelled with iododeoxyuridine (IdU) and chlorodeoxyuridine (CldU) was provided by Dr Gokhan Akman (GDSC, Sussex University).

2 mL of DNA solution were poured into a Teflon reservoir, where a silanised coverslip was incubated for 15 minutes at room temperature. The coverslip was removed from the solution at a constant speed of 300 µm/s using a Molecular

Combing System Station (Genomic Vision). The coverslip was placed on Whatman paper and baked for 2 hours at 60°C to crosslink DNA to the slide.

Immunofluorescence staining was used to attach fluorescent labels to IdU and CldU following sequential incubations: rat anti-CldU (1:50; AbCam, Cambridge, United Kingdom; BU1/75(ICR1)), Alexa Fluor 555 goat anti-rat (Life Technologies, A-21434), mouse anti-IdU (1:20; Becton-Dickinson, Mountain View, CA; B44) and Alexa-488-coupled goat anti-mouse (1:200; Molecular Probes). All solutions were diluted in a mixture of PBS and 0.05% Tween-20 (Sigma, P9416) and all incubations performed at 37°C for 20 minutes.

iv. Combed DNA imaging

Samples were imaged in PBS buffer containing mercaptoethylamine (100 mM, Sigma Aldrich, 641022-5G) mixed with an oxygen scavenger system with 0.8% w/v D-glucose (Sigma Aldrich, G7021-100G), 1 mg/ml glucose oxidase (Sigma Aldrich, 49180-250MG), and 0.04 mg/ml catalase (Sigma Aldrich, C40-100MG).

Alexa 488 imaging setup was performed using the 488 nm line of the tuneable gas laser, Semrock FF493/574-Di01-25×36 nm dichroic mirror and FF01-529/24-25 single-band bandpass filter. Alexa 555 imaging setup consisted of a 561 nm solid state continuous wave laser, Semrock FF570-Di01-25×36 dichroic beamsplitter and FF01-593/40-25 single-band bandpass filter, as summarised in Figure 2.15. Movies were acquired at 33 Hz for 1000 frames with a pixel size of 60 nm and an incident laser intensity at sample of the order of 1 kW/cm^2.

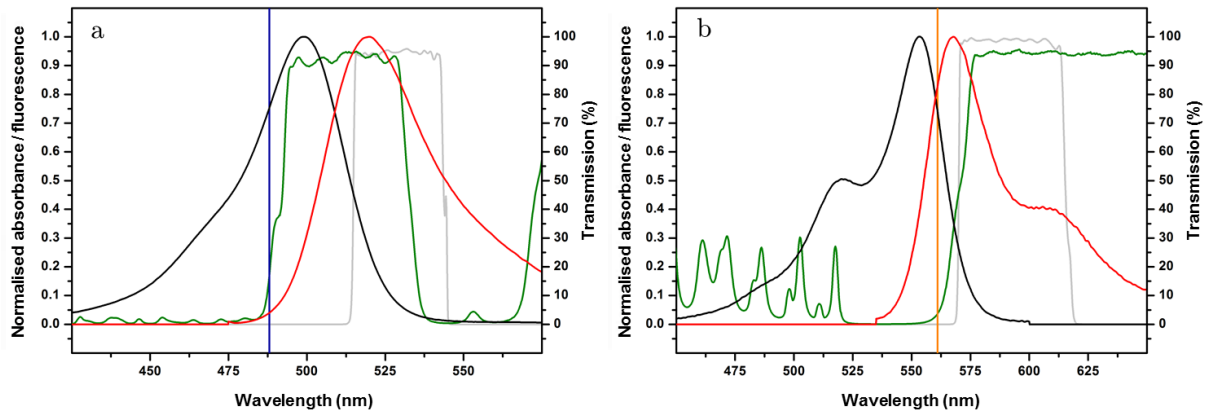

Figure 2.15. Spectral filtering setup used for dual imaging of combed DNA. a) Alexa 488 channel. b) Alexa 555 channel. A dichroic mirror (green) was used to reject the 561 nm incident laser beam (blue or orange) and a further band-pass filter (grey) was selected to collect the fluorescence emission [34].

v. FCS EMCCD viscosity titration

ZnS capped CdSe QDs (8 μM stock, peak emission 585 nm, Life Technologies, Q10111MP) were diluted in various weight percent solutions of glycerol-water mixtures (1 nM in pure water, 5 nM in other mediums). The detection volume was chosen to be a 20×20 pixels region of the EMCCD chip in order to reduce the achievable acquisition time to 10 ms. All experiments were performed at 20.5 ± 0.5°C with a pixel size of 121 nm/pixel. A stack of 20000 frames was acquired for each experiment and images were background corrected by subtracting the minimum value found in a control experiment (glycerol-water mixture under the same illumination intensity). Pixel values inside the detection volume were then summed (ImageJ custom built macro) and the autocorrelation curves obtained using the algorithm presented in Appendix III.

The excitation was performed with the 488 nm line of the Spectra Physics 164 Argon ion gas laser, using Semrock FF547/651-Di01-25×36 dichroic beamsplitter and FF01-593/40-25 single-band bandpass filter, as summarised in Figure 2.14.

vi. Single molecule tracking

QDs (585 nm, Life Technologies, Q10111MP) diffusing in a solution of 80 wt% glycerol-water were recorded for 20000 frames with an acquisition time of 18 ms using the optical system described in the previous section.

2.3.5 Direct Object Resolution by Image Subtraction

i. DNA annealing

Double stranded DNA was obtained by annealing of single stranded DNA of sequence GCA CGA GCG ATA GTC TAT ACG TCT GCG CGT ATG TGA TCC TAG CGC GTA CTG GCG TAT CGA CAT CTG TAC ATG TAG ACA TCT ACT AGA ATT CGA CGA CCG A with complementary strand (ATDBio Ltd). Complementary DNA strands with 5'-biotinylation (50 μM) were mixed in an annealing buffer (10nM tris(hydroxymethyl)aminomethane, Sigma Aldrich 154563-5G), 50 mM NaCl (Sigma Aldrich S7653-250G), 1 mM ehylenediaminetetraacetic acid (EDTA, Sigma Aldrich ED-100G)) and heated 5 minutes at 60°C.

The sample was left to cool down to room temperature, then to 6°C for 20 minutes and subsequently stored at -20°C.

ii. Coupled DNA preparation and imaging

Streptavidin functionalised QDs displaying a peak emission at 585 nm (Life Technologies, Q10111MP) were diluted to 200 pM, mixed accordingly for 15 minutes with the biotinylated 100 bp ds DNA solution in tetraborate solution (50 mM) and imaged after 20 minutes of incubation using a TIRFM setup. The sample was excited by an argon-ion laser (Spectra Physics, 165) operating at 488 nm, using a Semrock FF547/651-Di01-25×36 dichroic beamsplitter and a FF01-593/40-25 bandpass filter (Figure 2.14). This experiment was performed using a pixel size of 97 nm.

iii. TEM imaging

Transmission electron microscopy was performed on a Hitachi-7100, at an accelerating voltage of 75 kV and 10000× magnification, with digital image acquisition on an axially-mounted (2K x 2K pixel) Gatan Ultrascan 1000 CCD camera. A 5 μL aliquot of the diluted streptavidin functionalised 585 nm QDs were spotted on pre-cleaned copper grids and buffer removed by blotting with lens tissue prior to staining with 1% uranyl acetate solution for 1 min and drying under air. QD diameters were measured as the average derived from the pixel area of the dense core-shell centre, segmented from the less opaque protein functionalised surface.

2.3.6 DORIS Applied to Photoswitchable Dyes

i. Sample preparation

Rad22 proteins in *S. pombe* were used to demonstrate the application of DORIS in a cellular environment. This was facilitated by the fact that Rad22 is readily localised at foci upon irradiation [173]. *S. pombe* cells with Rad22 proteins labelled with mEos3 were provided by Tom Etheridge (GDSC, Sussex University). The cells were fixed with formaldehyde, exposed to γ radiation (50 Gy) and immobilised at the surface of the coverslip in a 1.5 w/v% agar (Difco) in PBS.

ii. PALM microscope setup

The PALM system was developed around a commercial inverted fluorescence microscope (Olympus IX71) and an EMCCD camera (Photometrics Evolve 512). The setup was custom-built to implement the selected features required for super-resolution imaging, especially a TIRFM scheme to reduce background fluorescence.

A 405 nm laser (LaserBoxx, Oxxius) was chosen for the activation line in order to reduce the photodamage caused to the sample compared to UV activation. A 488 nm (Toptica, iBeam) and a 561 nm (Cobolt, Jive) laser lines were used to image respectively the non-activated and the converted mEos3 fluorescent proteins. An additional 640 nm laser (Coherent Cube) was implemented for potential applications of PALM with dual colour imaging, or nucleus staining with far-red emitting dyes.

Two sets of absorptive neutral densities filters (Thorlabs NE01B to NE40B) were mounted on a double filter wheel and placed in each laser line to control its output power. A quarter-wave plate (Thorlabs WPQ05M-405 and -488) was implemented to circularly polarise each laser beam and ensure that the sample excitation was not biased by dipoles orientations. A low-pass filter (Semrock FF01-417/60-25, FF02-485/20-25, FF01-561/14-25 and FF01-640/14-25) was introduced in each laser line to remove any unwanted component of the excitation laser. A beam expander constituted from two matching lenses (Thorlabs LA1986 and LA1433 for the 405 nm line, LA1986 and LA1253-A for the three others) was used in combination with an iris (Thorlabs ID25 M) to adjust beam size and power density inside the sample. Automated shutters were introduced to control each laser line individually, enabling one to customise the experimental protocol and automate the data acquisition (fast shutter Thorlab SH05/SC10 for the activation line and Prior Scientific HF202HT for the 488 nm and 561 nm lines). The laser lines were combined with a series of dichroic beamsplitters (Semrock FF458-Di02-25×36, FF552-Di02-25×36, FF605-Di03-25×36) held on kinematic mounts to adjust the beam directions. The resulting beams were focused to the back focal plane of an apochromatic 1.45 NA, 60× TIRF objective (Olympus, UIS2 APON 60×OTIRF) using a 200 mm focal length, 25.4 mm diameter coated plane convex lens (Thorlabs LA1253-A). The four excitation laser beams were separated from the emission light by a multi-band dichroic mirror (Semrock Di01-R405/488/561/635-25×36) displaying tailored transmitting regions, which allowed switching between imaging channels without changing the imaging setup.

The emission beam was further enlarged by a 2.5× beam expander, leading to an optimised pixel size of 107 nm/pixel after projection onto the camera. An additional

motorised filter wheel (Prior HF110A) was mounted between the microscope and the camera and loaded with the imaging band-pass filter (Semrock FF01-580/14-25).

Stability of the system was ensured by building the system on a heavy optical table (Thorlabs PTQ52513) mounted on isolating legs (Thorlabs PTH 603) and replacing the manufacturer stage holder by an accurate motorised stage (ProScan H117E14) using a ProScan III device. The temperature was maintained constant at 16.5 ± 0.5°C to reduce thermal vibration of the microscope system. Stability in the axial direction was furthermore maintained constant with a C-focus device (Mad City Labs).
Shutters, stage, C-focus, emission filter wheel and camera were controlled using Micromanager software and sequential cycles of activation/excitation programmed using the software script panel. A schematic of the experimental setup with the different filter configurations and channels is displayed in Figure 2.16.

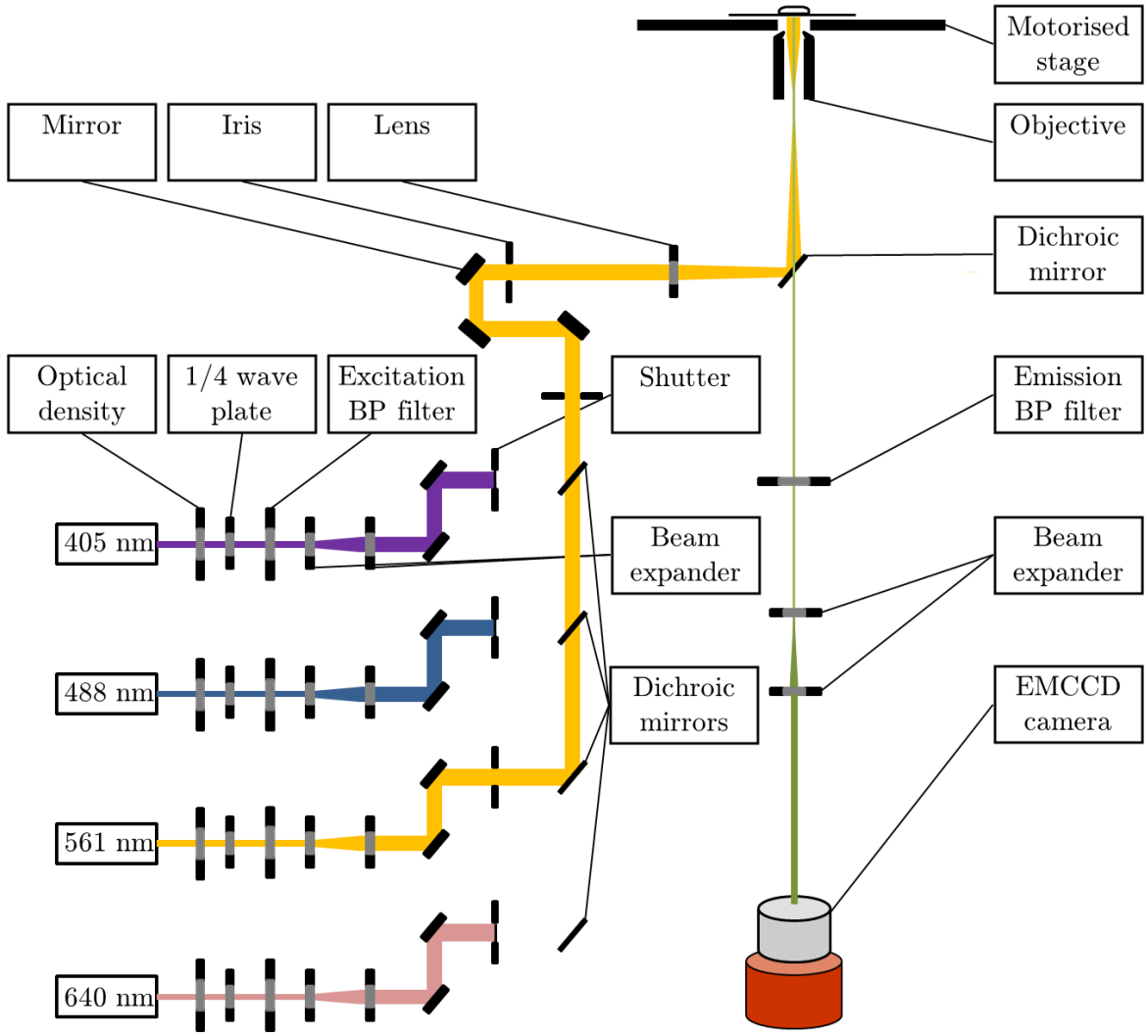

Figure 2.16. Schematic representation of the TIRFM-PALM setup. All shutters are displayed closed, except the one associated with the 561 nm laser line. The control of the state of each shutter allows tailored activation/excitation cycles.

iii. *S. pombe* cell imaging

The spectral setup used for the imaging of mEos3 is displayed in Figure 2.17. Proteins tagged with mEos3 were activated at low power densities (~ 3 W/cm^2) in order to ensure single molecule activation. The opening time of the 405 nm shutter was increased from 100 ms to 1 second throughout the experiment in order to ensure an efficient activation of mEos3 with reasonable experiment duration. Thirty cycles of activation/excitation were performed, each followed by an acquisition of 5 frames with an exposure time of 1 second, using incident intensities of the order of 1 kW/cm^2 for the 561 nm laser. Efficient photobleaching of the fluorescent reporter was verified before the start of a new cycle. Successive frames of each acquisition cycle displaying the PSF of a single emitter were averaged before performing a DORIS analysis. Typically, the long acquisition time was sufficient to have the mEos3 label bleached after the first frame of the acquisition but PSFs associated with the same emitter appeared in more than one frame for nine of the cycles. The sum of frames containing a PSF for each cycle was therefore used to apply the DORIS analysis, in order to increase the number of photons collected.

Background subtraction and smoothing of the stack of frames were performed using the "Rolling Ball Background Subtraction" [174] and the "Smooth" plugins in ImageJ.

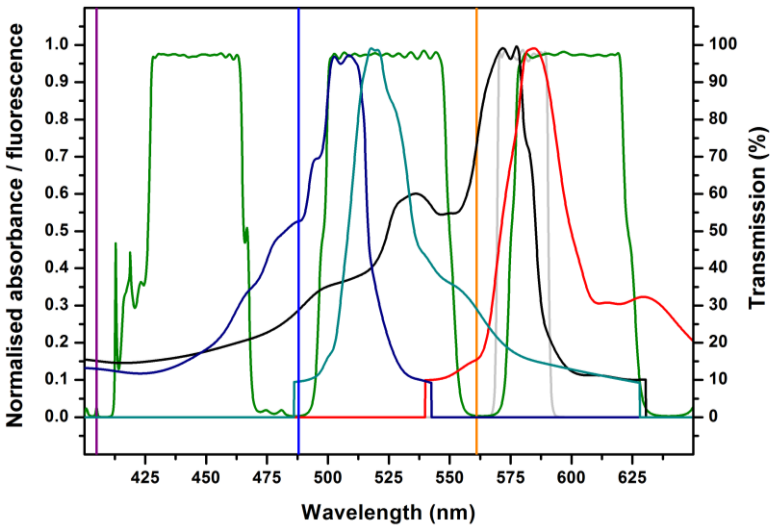

Figure 2.17. Spectral filtering setup used for mEos3 imaging. The "green" version of mEos3 (absorption and emission spectra respectively in blue and cyan) can be imaged with an excitation performed at 488 nm (blue). Photoconversion to its "red" version (black and red curves) was achieved upon activation by a 405 nm laser line (purple). A dichroic mirror (green) displaying multiple transmitting regions is used to reject the 561 nm excitation laser light (orange), as well as the other laser lines used in the optical setup, allowing potential dual-view imaging. A band-pass filter with a 14 nm bandwidth centered around 580 nm (grey) was used to collect mEos3 fluorescence emission [34].

Chapter 3

Fluorescence Correlation Spectroscopy

Fluorescence Correlation Spectroscopy (FCS) is based on the analysis of a signal deviation from its mean value caused by freely diffusing dyes in solution. An autocorrelation function is applied to the temporal fluctuations of the fluorescent signal arising from emitters passing through a detection volume, which enables one to extract various parameters, such as diffusion kinetics, temporal conformational changes or association/dissociation mechanisms.

The concept of analysing signal fluctuations of diffusing molecules was first introduced in 1972 by Magde *et al.* who studied the reversible binding between DNA and ethidium bromide, an inhibitor of nucleic acid synthesis that displays an increase in fluorescence emission upon intercalation with DNA [175]. The development of the technique was however hindered by its poor sensitivity and the requirement for high dye concentrations, until the experiment was implemented with a confocal detection setup [176]. This change turned FCS into an efficient single molecule technique with a temporal resolution ranging from nanoseconds to microseconds. The method has been applied since then to the study of many biological processes, such as the association of DNA strands [177] or dynamics of proteins and peptides [178]. The following chapter focuses on the construction of a FCS system to monitor kinetics and conformational changes of Ribonucleotide Reductase (RNR), a tightly regulated enzyme playing a central role in the cell cycle.

3.1 Ribonucleotide Reductase Form and Function

Self-replication is a fundamental requirement for any sustainable life form. DNA is the genetic material which contains all the necessary information for a cell to replicate, divide and respond to potential damages encountered.

DNA synthesis requires a balanced supply of deoxynucleoside triphosphates (dNTPs), consisting of deoxyadenosine triphosphate (dATP), deoxyguanosine triphosphate (dGTP), deoxycytidine triphosphate (dCTP), deoxythymidine triphosphate (dTTP), and obtained from their corresponding nucleoside diphosphates (NDPs), respectively adenosine diphosphate (ADP), guanosine diphosphate (GDP), cytidine diphosphate (CDP) and uridine diphosphate (UDP) [179]. One of the first catalytic steps of the dNTPs synthesis involves the formation of deoxynucleoside diphosphates (dNDPs) by direct reduction of NDPs (Figure 3.1) in a multicomponent oxidation-reduction cascade [180]. Ribonucleotide reductase (RNR), an allosteric enzyme, provides the cell with appropriate supply of the four dNTPs, which is essential for an accurate DNA synthesis. An unbalanced supply of dNTPs to the cell might lead to misincorporations, inducing genomic instability and mutations [181]. The RNR needs therefore to be tightly regulated to fulfil its key role in the cell cycle.

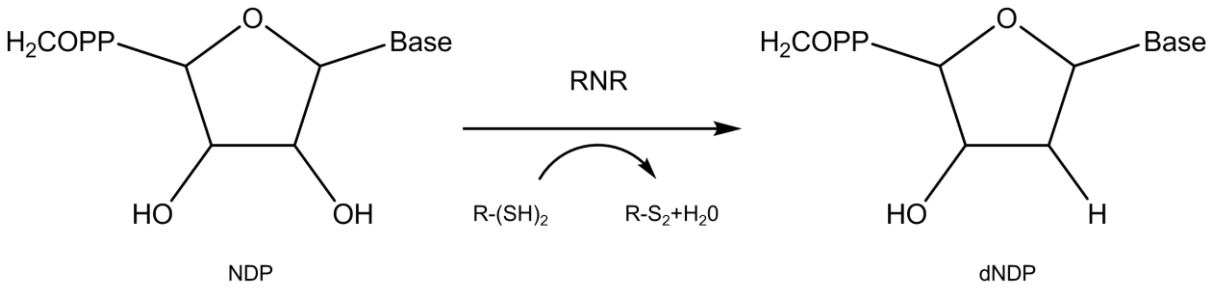

Figure 3.1. Reduction process of nucleotide diphosphate into deoxynucleotide diphosphate catalysed by the ribonucleotide reductase enzyme.

3.1.1 Structure of Ribonucleotide Reductase

In *S. pombe,* RNR displays a tetramer $\alpha_2ß_2$ structure with a large subunit R1 (Cdc22 protein) and a small subunit R2 (Suc22 protein) when active in a complex conformation. The stoichiometry of each group varies depending on the enzyme state and some doubts remain on the quaternary structure *in vivo.* RNR structure presents several active and specificity sites [182] in order to perform allosteric regulation of dNTP levels (Figure 3.2).

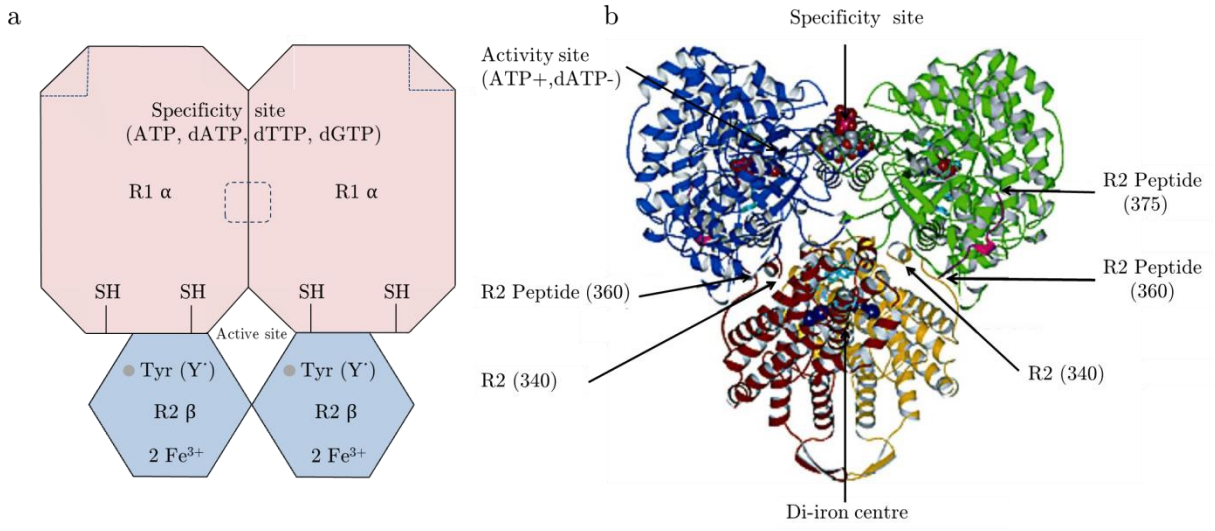

Figure 3.2. Representations of RNR $\alpha_2\beta_2$ structure in *S. pombe.* a) Schematic representation of RNR structure. R_1 displays two allosteric sites: the active site and the specificity site. The interface between R_1 and R_2 constitutes the active site. •Tyr is a tyrosine radical and SH represents the sulfhydryl groups in the active site (adapted from [180]). b) RNR crystal structure in *Escherichia coli* showing the surface complementarity between subunits [183].

R1 is a dimer of molecular weight 90 kDa, whereas R2 is a small RNR subunit of molecular weight 45.5 kDa that is active as a dimer [184]. Each monomer contains a binuclear ferric ion centre and a tyrosil free radical, which are crucial for the enzyme activity [185], as the protein is not functional without these attributes [186].

The redox active sulfhydryls of R1 and the free radical of R2 constitute the active site of the enzyme, which explains the necessity for the two subunits to bind to obtain an active molecule. The overall active site can bind adenosine triphosphate (ATP) or dATP and activates or inhibits its activity depending on the amounts of molecules detected. The specificity site can bind ATP, dATP as well as dTTP and dGTP. A multi-feedback regulation process then controls the amount of dNTPs produced, which ensures that a balanced nucleotide pool is maintained in the cell. In brief, depletion of dATP levels in the cell favours ATP binding at the active site, which initiates NDP reduction. ATP binding at the specificity site will also be favoured in low dNTPs pools and this induces the catalytic site to accommodate the purines CDP and UDP for reduction, ultimately to dCTP and dTTP. As the pool of dTTP increases, ATP is displaced at the specificity site and the redox changes to support GDP reduction. As the dGTP levels increase and compete with dTTP at the specificity site, the catalytic centre is switched again to favour ADP binding and reduction. Finally, RNR activity is shutdown as the dATP pool is replenished and the deoxynucleoside replaces ATP at the active site.

3.1.2 Ribonucleotide Reductase Regulation

Spd1 (S phase delay inhibitor 1) is a small protein (14.2 kDa) with no fixed tertiary structure and able to switch between several conformations [187]. This property enables the protein to easily adopt different structures and bind to other proteins with low affinity but high specificity. Spd1 is only active during certain phases of the cell cycle (Figure 3.3). Its main action is to import Suc22 into the nucleus, which results in its separation from the cytoplasmic Cdc22 and the inhibition of the RNR activity. When the cells are not in S phase, Suc22 is localised in the nucleus and Cdc22 in the cytoplasm. At the entry to the S phase or following DNA damage checkpoint activation, Suc22 is released in the cytoplasm, where it can bind to the Cdc22 to form an active enzyme. Spd1 is then degraded during S phase, or after DNA damage and DNA replication stress. The RNR complex formation and its regulation during the cell cycle are still relatively unknown and continue to be investigated as a potential target in mutation and cancer control.

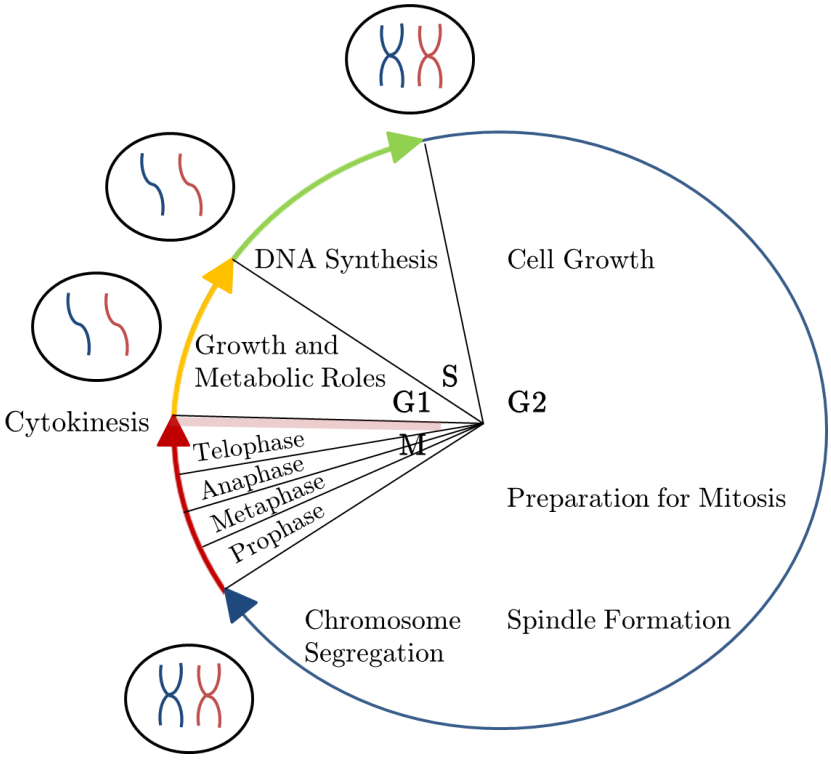

Figure 3.3. Schematic representation of the eukaryotic cell cycle. DNA synthesis (S phase) and mitosis are separated by gap phases G1 and G2, during which the cell grows and prepares for the next phase. The whole cell genome replicates during S phase, a process requiring high protein numbers, large amount of energy and efficient genetic code assembly. G2 phase provides a safety check of DNA replication completion and allows the cell to prepare for mitosis. The M phase includes two processes during which the division of the nucleus (mitosis) is followed by the division of the cytoplasm (cytokinesis). Each resulting cell will then go into G1 phase, during which they will grow and prepare for DNA synthesis.

3.2 Principle of Correlation Spectroscopy

The FCS technique is usually applied with a confocal setup [188], whose detection volume width is defined by the radius of the laser beam in the lateral plane and the pinhole aperture in the axial plane. The fluorescent signal of single molecules going through the detection volume is recorded over time by a high sensitive APD or a photomultiplier tube (Figure 3.4). Those fluorescent "bursts" can be analysed mathematically with an autocorrelation process [189-191] to determine probe local concentrations [192], mobility [193], size [194], binding [195] or conformational changes [196]. The number of molecules located in the detection volume needs to be small enough to significantly contribute to signal fluctuation. The SNR can be enhanced by decreasing the influence of noise sources such as APD detector noise, out of focus fluorescence and laser correlated noise.

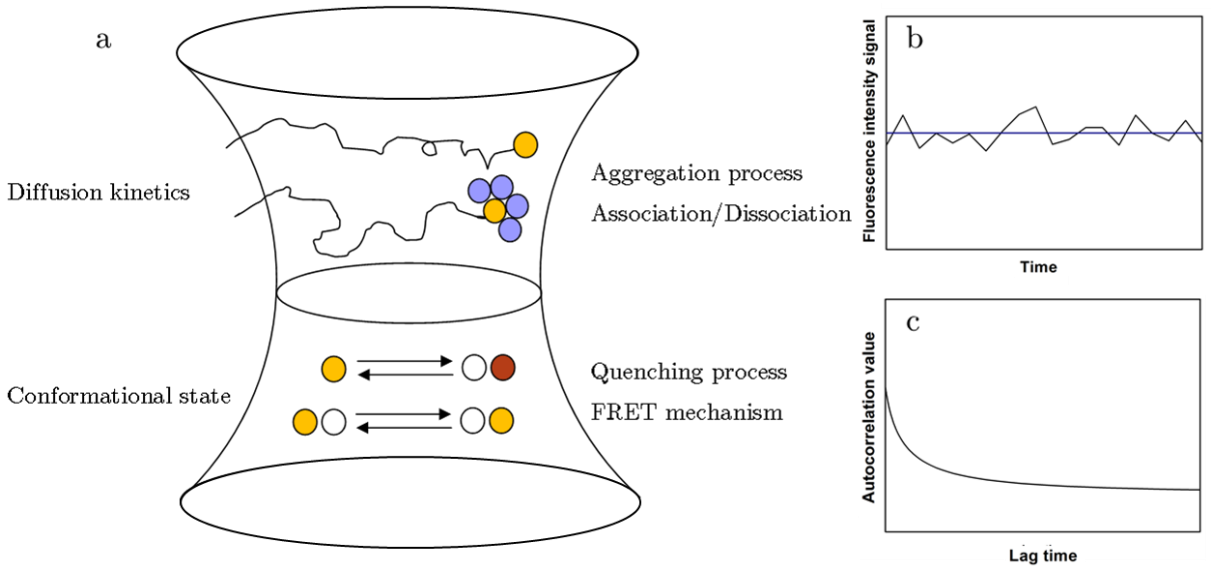

Figure 3.4. Principle of FCS experiments. a) Mechanisms inducing fluorescence fluctuations. b) Signal fluctuating (black) around a mean value (blue). c) The autocorrelation function.

Scanning Fluorescence Correlation Spectroscopy (sFCS) [197] and Image Correlation Spectroscopy (ICS) [198] are extensions of the FCS principle introduced to study systems where diffusion is slow or non-existent. It relies on the accurate scanning of the sample and subsequent correlation analysis across different image pixels. Further implementation includes the two-photon excitation scheme, adapted to FCS to perform live cell investigations that were generally hindered by autofluorescence, scattering and photobleaching effects [199]. Cross-correlation between components labelled with different colours has been used to retrieve information on multiple probe

interactions [200, 201]. The latest development of the technique is the dual-focus FCS, in which the detection region is composed of two identical overlapping detection volumes [202]. This configuration provides an accurate and absolute determination of diffusion coefficients, even when the experimental conditions involve environment crowding or high refractive index mismatch between the sample and the immersion medium [203].

3.2.1 Autocorrelation Function

FCS is a direct method to characterise the underlying dynamics causing fluorescent fluctuations. Autocorrelation measures self-similarity of a time series signal and describes the persistence of information. The normalised correlation curve is obtained from the intensity signal time profile using the following mathematical formalism:

$$G(\tau) = \frac{\langle F(t)F(t+\tau)\rangle}{\langle F(t)\rangle^2} = \frac{\langle \delta F(t)\delta F(t+\tau)\rangle}{\langle F(t)\rangle^2} + 1 \qquad (3.1)$$

with $(\delta F(t) = F(t) - \langle F(t)\rangle)$ and $(\delta F(t+\tau) = F(t+\tau) - \langle F(t)\rangle)$ the amplitudes of fluctuation at times t and $(t+\tau)$ from the mean value $\langle F(t)\rangle$. The lag time τ is the time delay at which a signal is compared with itself. The persistence time of fluctuation can therefore be identified by calculating the value of the autocorrelation function for a large range of time delays τ. The conventional semi-logarithmic plot of the autocorrelation value gives a representation of events occurring on several orders of magnitude of time scales.

3.2.2 Autocorrelation using Fourier Transforms

The correlation function can be calculated efficiently and rapidly using Fourier transforms. The conventional definition of the discrete correlation of two sampled periodic functions $f_{\mathrm{k}}(t)$ and $g_{\mathrm{k}}(t)$ of period N is given by [204]:

$$\mathrm{Corr}(f,g)_{\mathrm{j}} \equiv \sum_{k=0}^{N-1} f_{\mathrm{j}} + {}_{\mathrm{k}} g_{\mathrm{k}} \qquad (3.2)$$

The correlation function is equivalently obtained by multiplying the Fourier transform of the function f by the complex conjugate of function g, as stated by the correlation theorem:

$$\mathrm{Corr}(f,g)_{\mathrm{j}} \Leftrightarrow F_{\mathrm{k}} {G_{\mathrm{k}}}^{*} \tag{3.3}$$

In practice, the autocorrelation function is obtained by applying the Fourier transform process to the times series of interest, multiplying the result by its own complex conjugate and applying an inverse Fourier transform.

3.3 Autocorrelator Development

The development of a custom-built correlator was carried out to complete the experimental setup. This process was motivated by the absence of hardware correlator at the beginning of the research program. The integration of the FCS technique in the universal image processing software ImageJ was selected in order to exploit the powerful representation of Fourier transform tools to one-dimensional datasets. An ImageJ-based algorithm was therefore developed to perform the conversion of signal arising from single photon detectors into a 32-bit image and carry out an autocorrelation process using Fourier transforms.

3.3.1 Types of Autocorrelators

Conventional commercial correlators allow access to the FCS curve directly from the input signal recorded, and are said to be "real-time correlators" when the processing time is shorter than the sampling time. There are several types of processing methods that can be used to obtain accurate FCS results. The most straightforward calculation method is to strictly apply the Equation (3.1) to the signal values recorded for all dividing bins. The method, used in linear-tau correlators, can become time and memory demanding for long correlation times.

The exponential-tau correlator principle reduces the memory requirements by only using the exponentially spaced signal bins that are required for displaying the FCS on a logarithmic scale [205]. Every point on the curve is obtained with the same number of bins, which results in a uniform noise value for each lag time considered.

The last and most common method used is the multiple-tau correlator. The sampling time of each successive signal value retained is increased by a factor of two,

leading to a quasi-exponential separation of lag times covering a large time delay range. The associated bin width is significantly larger for long correlation times, it is therefore important to ensure that the measurement time is at least three orders of magnitude larger than the lower diffusion time of interest in order to obtain comparable results between different types of correlators.

3.3.2 ImageJ Autocorrelation Algorithm

The following section summarises the development strategies used to obtain the autocorrelation function from fluctuation intensity series. The two different algorithms presented in Appendix II and III had their respective performances compared with a commercial correlator to test the consistency of analysis.

i. Linear-tau correlator development with Fourier transforms

The autocorrelation of a time series signal can easily be computed using image processing software. Signal values were converted and stored consecutively as ADU intensity values, with a range of (1-65536) in the case of a 32-bit image (Figure 3.5).

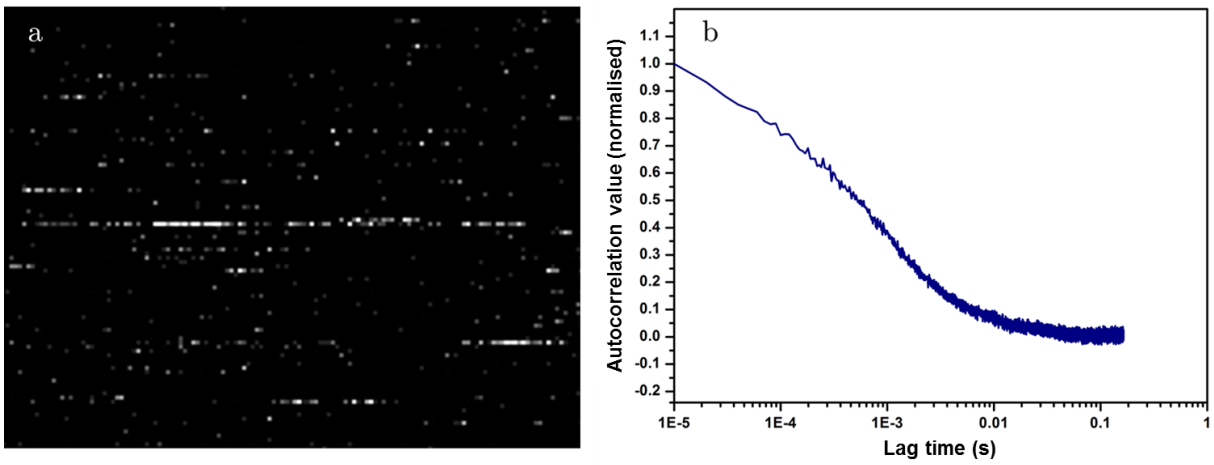

Figure 3.5. FCS autocorrelation process performed in ImageJ. Algorithm is applied to signal arising from a 45 bp single strand DNA labelled with TMR and freely diffusing in solution. a) Conversion of signal into an image. Fluorescent molecules diffusion inside the detection volume can be visualised as lines of increased intensity. b) Associated correlation curve obtained using Fourier transform method. The implementation of Fourier transform processing in ImageJ limits the maximum number of lag times to $\sim 1.64 \times 10^4$.

The conversion of a signal into a 2D "pseudo image" consists of associating the photon count obtained for each original measurement with a 32-bit intensity at a

given spatial position in the image, which was achieved using an approach similar to a raster pattern. Routine Fourier transform operations were performed on time series, using the ImageJ "Convolve 3D" plugin [206] to obtain the appropriate autocorrelation function. This method, however fast and efficient, cannot be applied to images bigger to 32768 pixels because of Convolve 3D plugin limitations. The symmetry of the correlated result obtained further limits the maximum lag time attainable to the acquisition rate multiplied by a factor of 16384 using a linear-tau correlation approach. It has previously been demonstrated that the maximum lag time must be at least 5000 times bigger than the characteristic time in order to achieve an appropriate accuracy [207]. An alternative method of autocorrelation based on the exponential-tau approach was therefore developed in ImageJ.

ii. Exponential-tau correlator development

Let's consider a signal recorded with a fixed sample interval t (which is the typical case in an EMCCD camera) and converted into an image of n pixels with different values $a_1, a_2, \dots, a_n$, acquired at different times $t_1, t_2, \dots, t_n$ (Figure 3.6).

a_1	a_2	.	.	a_n	0	0	0	0	0
0	a_1	a_2	.	.	a_n	0	0	0	0
				.					
				.					
0	0	0	0	0	a_1	a_2	.	.	a_n

Figure 3.6. Schematic representation of the autocorrelation method used in custom-built ImageJ correlator: the signal is sequentially translated and multiplied with the original image. The method of zeros padding at boundaries is displayed here for clarity, whereas in the actual algorithm only a subset of the signal is shifted compared to the whole time series.

Translating the image from a given number of pixel m and multiplying the resulting image with the original image is equivalent to comparing every signal value with the intensity of signal at a time $(t_n + m \times t)$, which is ultimately the principle of autocorrelation with a lag time $(m \times t)$. Sequential translations allow to perform a

single multiplication of images to calculate the autocorrelation value at a given lag time instead of n individual multiplications. The mean value of the pixels in the multiplied image is then easily calculated to return the value of the autocorrelation at a given lag time.

A simple "for" loop therefore enables one to translate sequentially the signal series in order to obtain the autocorrelation value for different lag times. The step size of the shift was set to increase step by step to obtain a pseudo-logarithmic scale and consequently limit the computation time. The number of iterations needed is defined by the logarithmic base and number of bins per group selected. For instance, let us consider an experiment acquisition time Δt analysed with a correlation process using a base 2 with 3 bins per group and a maximum lag time of $(n \times \Delta t)$. The associated lag time values are the following multiple of Δt : 1, 2, 3, 5, 7, 9, 13, 17, 21,…, n, which correspond directly to the lag time shift in pixels.

The efficiency of the technique was tested by comparing the autocorrelation curve obtained with a commercial correlator (Flex2k, Autocorrelator.com) with the result of the custom-built correlator, for a FCS experiment performed on a 45 bp single strand DNA labelled with TMR (Figure 3.7). A 4.7% difference between the half-decay characteristic times of the two curves was calculated with the fitting process described in Section 3.5.2. This validated the method used which enables one to obtain the correlation curve as well as retaining the raw data intensity counts.

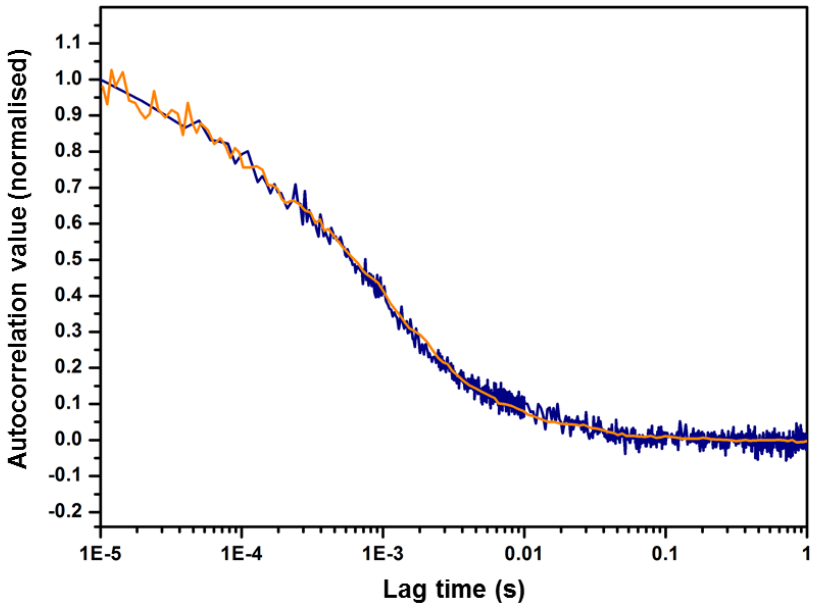

Figure 3.7. Comparison between correlation methods. The autocorrelation curve of the diffusion of a 45 bp single strand DNA-TMR obtained with the custom built exponential-tau correlator (blue) and a commercial multiple-tau correlator (orange) were compared. The half decay characteristic time differed by less than 5% between the two curves.

3.3.3 Removal of Experimental Artifacts

A common problem in FCS experiments is the presence of sample related artifacts, usually caused by photobleaching of the fluorescent background, non-uniform repartition of fluorophores and depletion or aggregation of dyes. This phenomenon results in an additional contribution of parasite fluorescence to the signal fluctuation arising from genuine single molecule dynamics, leading to distorted correlation curves. In order to enhance the accuracy of the FCS curves and the determination of characteristic diffusion times and concentrations, an ImageJ macro program has been built according to the protocol described in reference [208] (Appendix IV).

In this approach, one measurement is split into k short intervals of length Δt on which the autocorrelation curves (referred to as $G_{\mathrm{k}}(\tau)$) are calculated and displayed. The quantity $\mathrm{d}G_{\mathrm{k}}$ is then calculated according to the expression:

$$\mathrm{d}G_{\mathrm{k}} = \langle (G_{\mathrm{k}}(\tau_{\mathrm{i}}) - \langle G_{\mathrm{j}}(\tau_{\mathrm{i}}) \rangle_{\mathrm{j}\neq\mathrm{k}})^2 \rangle_{\mathrm{i}} \qquad (3.4)$$

If $\mathrm{d}G_{\mathrm{k}}$ value is bigger than a threshold value $\mathrm{d}G_{\mathrm{max}}$ the corresponding curve is discarded. After this step, all curves with ($\mathrm{d}G_{\mathrm{k}} < \mathrm{d}G_{\mathrm{max}}$) are averaged, which gives the final, artifact-free autocorrelation curve. The values chosen for Δt and $\mathrm{d}G_{\mathrm{max}}$ are critical for success in the elimination of distorted curves. According to reference [208], Δt value was chosen to obtain a good compromise between removal of random noise and curve fitting accuracy. Similarly, $\mathrm{d}G_{\mathrm{max}}$ was set to a value around one order of magnitude above the minimum $\mathrm{dG_k}$ in order to limit the influence of distortions in the average result while retaining enough curves to keep the noise to a minimum.

3.4 Summary of FCS Implementation

The FCS method was implemented through the application of algorithms to perform a complete autocorrelation analysis of fluorescence time traces. The application sequence is summarised in Figure 3.8, which displays a workflow of the method. The fluorescence signal detected by the APD (Figure 3.8.a) is first converted into a 32-bit image of the type of Figure 3.8.b. The signal autocorrelation of each interval of length Δt is then performed, using the exponential-tau correlator approach previously described in Section 3.3.2, and the resulting correlation functions stored in a pixel array (Figure 3.8.c). The filtering process described in Section 3.3.3 is furthermore

applied to the correlation curves obtained in order to remove experimental artifacts (Figure 3.8.d) and the remaining curves averaged to obtain the final autocorrelation function. Figure 3.8.e displays the autocorrelation curves obtained for two different intervals. The red curve clearly displays a distorted shape and will be removed by applying a filtering process, whereas the blue curve satisfies the filtering criteria set (dG_{max}) because of its similarities with the majority of the other autocorrelation curves, and will be retained for the calculation of the filtered correlation function. The importance of discarding parasite fluorescent signal is highlighted in Figure 3.8.f, where the correlation curve before and after filtering are compared. If the number of intervals associated with an artifact is high, the error on the averaged result curve increases, leading to a distorted autocorrelation curve and erroneous values after fitting. The filtering process measures the difference between curves, removes the potential distortions and improves the accuracy of values obtained by fitting.

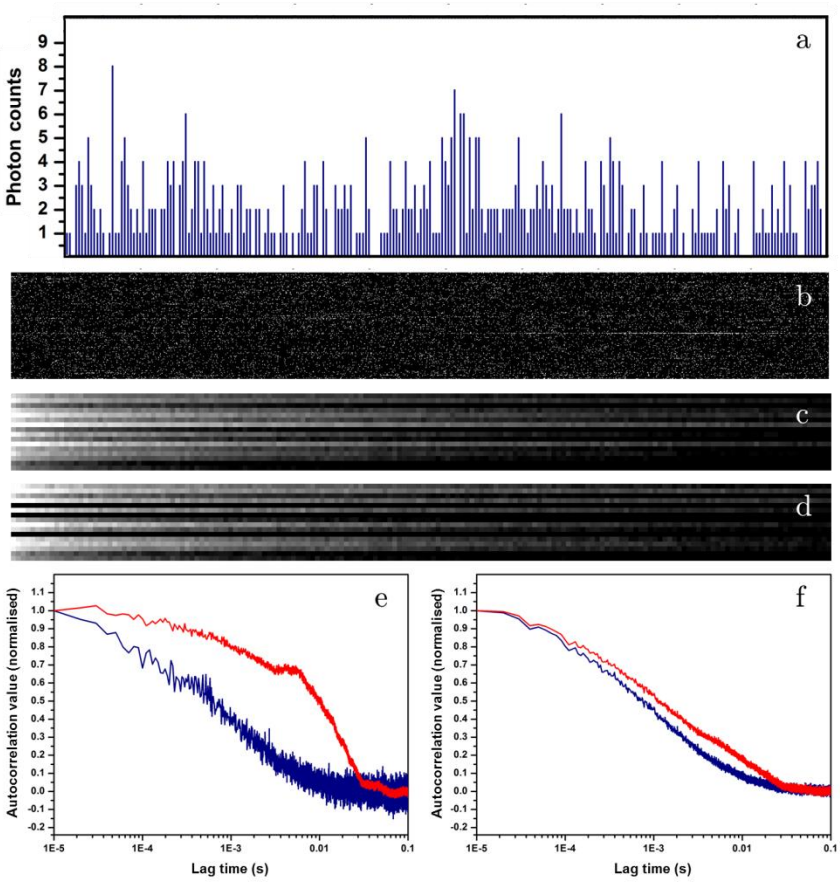

Figure 3.8. Workflow of the FCS analysis performed in ImageJ. a) The fluorescence signal is detected using APDs. b) The signal is converted into a 32-Bit image. c) Autocorrelation curves of each interval selected are calculated and stored into a pixel array. d) The filtering technique is used to discard experimental artifacts. e) The autocorrelation curve that displays a distorted shape is removed by the filtering process (red), whereas the curves that satisfy the filtering criteria (blue) are retained. f) Averaged correlation curve containing the dataset associated with the distortion (red) and artifact-filtered curve (blue).

3.5 Interpretation of FCS Results

Factors that cause a variation in the fluorescence signal on time scale faster than the average time molecules spend in the detection volume will cause a characteristic decay in the associated region of the FCS autocorrelation curve. It is therefore important to identify potential sources of systematic intensity fluctuations in order to successfully interpret experimental results.

3.5.1 Causes of Fluorescence Fluctuation

The most studied factor in FCS experiment is the diffusion of molecules through a detection volume arising from Brownian motion. The translational diffusion coefficient of a particle in a viscous solution is given by the Stokes-Einstein relation [209, 210]:

$$D = \frac{\mathrm{k}T}{6\pi\eta r} \tag{3.5}$$

with k the Boltzmann constant, T the temperature, η the viscosity of the solvent and r the hydrodynamic radius of the particle.

Diffusion, a fast and efficient process at short distances, is the predominating transport mechanism in cellular environment [211], which highlights the importance of studies aiming to determine diffusion coefficient values *in vivo.* Other mechanisms occurring during the diffusion of molecules in the FCS volume, such as triplet crossing, quenching, conformational changes or photobleaching are also displayed on the autocorrelation curve, generally as decays at short lag times.

Decay in the autocorrelation curve can be used to extract valuable information on the process causing the emission fluctuation. The time scale of the event is linked with the decay rate of the curve: the average amount of time spent in the detection volume is related to the half-life of the curve in a purely diffusive study, whereas the crossing rate is linked to the 1/e point in the case of a triplet crossing process. When multiple variation processes occur, the respective amplitudes of decay are related to the contributive strength of each origin of fluctuation, such as the number of molecules undergoing diffusional motion, or the proportion of emitters in the dark state because of triplet state blinking.

A common problem for lag times shorter than 1 μs is the distortion of the correlation curve because of an "afterpulsing" effect, which arises from the probability for a photon to generate two electronic pulses. Cross-correlation between multiple detectors can eliminate this effect [168], but was not used during this work where the scope of interest lays at lag times ranging from 10 μs to 1 ms.

The parameters of the FCS experiments are critical to obtaining accurate results. In all experiments presented, the minimum lag time did not exceed 2/3 of the characteristic decay time τ_d whereas the maximum lag time was at least 5000 times bigger than τ_d. Concentration and averaging time were also varied to check that diffusion constants were consistent between experiments [207].

3.5.2 FCS Curve Fitting

i. Translational diffusion through a Gaussian detection volume

The autocorrelation function for the translational diffusion of a single molecule in a dilute solution in three dimensions is given by [168]:

$$G_{\text{diff}}(\tau) = \frac{1}{N}\left(1 + \frac{\tau}{\tau_d}\right)^{-1}\left(1 + \frac{\tau}{K^2\tau_d}\right)^{-1/2} \tag{3.6}$$

with N the average number of molecules in solution, τ_d the characteristic time of diffusion and K the aspect ratio between the axial and lateral dimensions of the detection volume: $K = \omega_z/\omega_{x,y}$.

It is clear from Equation (3.6) that the amplitude of the correlation function is inversely proportional to the number of molecules in the detection volume. It is possible to integrate triplet kinetics through an additional term in Equation (3.6):

$$G_{\text{global}}(\tau) = G_{\text{diff}}(\tau)\left(1 + \frac{T}{1-T}\exp\left(\frac{-\tau}{\tau_t}\right)\right) \tag{3.7}$$

where T is the fraction of molecules in the triplet state of characteristic lifetime τ_t.

ii. Accuracy of fitting process

The use of an elaborate model to fit experimental datasets requires a careful analysis of the results to confirm trends and validate the outcome of the regression. The coefficient of determination, noted ${R_0}^2$, measures the influence of the variation in the dependent variable described by the regression model and hence the goodness of fit:

$$ {R_0}^2 = 1 - \frac{\sum(y_\mathrm{i} - y_\mathrm{i,model})^2}{\sum(y_\mathrm{i} - \bar{y})^2} \tag{3.8} $$

with y_i the experimental values for the dependent variable, $\bar{y}$ the average of the experimental values and $y_\mathrm{i,model}$ the values predicted by the model for the dependent variable.

It is however preferable to adjust the coefficient of determination for the number of independent variables in the regression model, to prevent artificial increase of this quantity with added variables. The adjusted coefficient of determination R^2 was hence chosen as a measure of the fit accuracy: this quantity may decrease if variables entered in the model do not add significantly to the model fit.

$$ R^2 = 1 - (1 - {R_0}^2)\frac{(n-1)}{(n-k-1)} \tag{3.9} $$

with k the number of independent variables and n the number of sample points.

The coefficient R^2 is displayed in this thesis when a fitting process was performed. Fitting models, or at least parameters derived thereof, were retained when its value was maximal (typically > 0.95).

3.6 Detection Volume Characterisation

The shape of the detection volume is described by the Molecule Detection Function (MDF) that gives the probability of detecting a photon at a given position in space. The MDF is not accessible by direct measurement, therefore the PSF of the confocal volume is instead retained for the description of the detection volume, which is classically described by a three dimensional Gaussian distribution [212-214].

This equivalence holds if the observed dye displays a fast enough rotational diffusion (< 100 ns) leading to a decoupling between excitation and emission [191], a condition that was largely met for the dyes used in the work described in this thesis [215].

The confocal parameters for different laser wavelength detection volumes were determined using several different reference probes. RhB was chosen as the reference fluorophore for the 532 nm laser line. The diffusion coefficient of this dye has previously been determined at 25°C by Plug Broadening/Capillary Flow [216] and Pulsed Field Gradient-Nuclear Magnetic Resonance (PFG-NMR) [217], which provided a reference value for the calibration experiments.

Purified GFP was selected to perform the calibration at the 473 nm laser line. The diffusion coefficient of EGFP, a protein analogous to GFP (mutations of Ser to Thr at amino acid 65 and Phe to Leu at position 64 [218]) has been studied previously using FCS [219] and sFCS [220] at 22.5 ± 0.5°C.

An FCS experiment was performed on each chosen reference dye and the resulting autocorrelation curves fitted with the model described in Equation (3.6). The curve associated to the diffusion of RhB and used to determine the detection volume shape associated to the 532 nm laser is displayed in Figure 3.9.

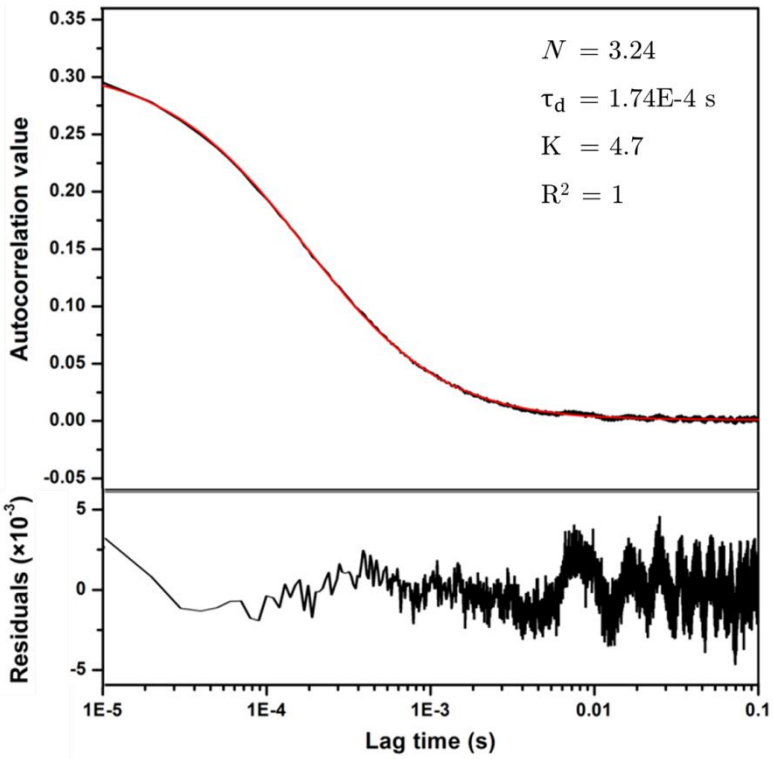

Figure 3.9. FCS detection volume calibration. Autocorrelation curve obtained from the diffusion of the reference dye RhB was fitted to determine the lateral width and the aspect ratio of the detection volume associated with the 532 nm laser line. Associated fits parameter (inset) and residuals components (below) are also displayed.

The lateral dimension of the detection volume $\omega_{x,y}$ was retrieved using the simple relation between the diffusion coefficient D and the average time of occupancy in the detection volume τ_d [190] :

$$\omega_{x,y}{}^2 = 4D\tau_d \tag{3.10}$$

The axial length of the detection volume ω_z has been obtained using results of the fitting process for the parameter K, which caused a high uncertainty in the value obtained as this factor influences only weakly the shape of the autocorrelation function and is strongly correlated with the parameter $\omega_{x,y}$. The confocal volume dimension in the plane was therefore calculated, leading to the determination of an effective volume expressed, under the approximation of a three dimensional Gaussian shape function, as:

$$V_{eff} = \pi^{3/2}\omega_{x,y}{}^2\omega_z = 2^{3/2}V_{conf} \tag{3.11}$$

A summary of reference probe diffusion coefficients and laser detection volume dimensions are displayed in Table 1.

Laser wavelength	*Reference probe* Diffusion Coefficient ($\mu m^2.s^{-1}$)	$\omega_{x,y}$ (μm)	K	V_{eff} (fL)
473 nm	$D_{GFP} = 84 \pm 4$ [219] $D_{GFP} = 91 \pm 2$† [220]	0.35 ± 0.01	3.9 ± 0.9	0.89 ± 0.23
532 nm	$D_{Rhb} = 384 \pm 4$ [216] $D_{Rhb} = 405 \pm 40$† [217]	0.53 ± 0.03	4.7 ± 0.1	3.92 ± 0.90

Table 1. FCS detection volumes determination using reference fluorescent dyes with diffusion coefficients characterised in the literature. Diffusion coefficients were corrected to account for the experiment temperature of 20.5 ± 0.5°C, according to the classical approximation in water: 2% increase for every increase of a degree in the temperature range used, mainly due to decrease of water viscosity with temperature. †Coefficients used for calculation.

Other calibration methods can be used to determine the effective volume, such as performing FCS on a dilution series of a sample with a known concentration or raster scanning a layer of fluorescent beads [221]. However, the technique presented here allows a convenient and repeatable calibration under similar experimental conditions.

3.7 FCS Application to Suc22 Conformation

Recent studies have put forward the hypothesis that Suc22-Cdc22 protein may form an oligomeric complex during inactive states of the cell cycle [187]. With a view to the potential use of FCS to investigate RNR subunit oligomerisation *in vivo*, the technique was first used here to characterise the purified protein Suc22 *in vitro*. The sensitivity of the setup was tested on diffusing probes of different molecular weights and the FCS technique applied to investigate Suc22 protein conformation. An additional photobleaching assay experiment was used in complement in order to determine the stoichiometry of the purified protein.

3.7.1 FCS Molecular Weight Sensitivity: GFP Assay

An experimental assay was carried out on the commercially available purified protein GFP, which displays a molecular weight of 27.5 kDa. The aim of the calibration experiment was to demonstrate that the sensitivity of the FCS setup was high enough to reveal large differences in molecular weight between diffusing species.

The diffusion coefficient is directly related to the hydrodynamic radius of the particle, under the assumption of a spherical shape, by the Stokes-Einstein relation displayed in Equation (3.5). The hydrodynamic radius scales with the third root of the molecular weight, which means that a doubling in the diffusion time requires an 8-fold homogeneous mass increase [190]. This characteristic restricts the application of FCS to systems with large mass differences between components.

The diffusion parameters of the complex formed by GFP and its complementary antibody (150-160 kDa) were compared to the ones obtained from the fit of the autocorrelation curve for the purified protein (Figure 3.10). A theoretical calculation gives a 6.6-fold increase in molecular weight, which would propagate to a 1.9-fold increase in diffusion time under the particle spherical shape approximation. The average diffusion time between the purified GFP and the complex increased by a factor of 2 (Table 2) which is close to the predicted value of 1.9 based on molecular weight differences. The deviation observed might be due to the barrel shape of GFP [222], which differs from the approximation of a spherical structure. Nonetheless, the result obtained confirms the sensitivity of the FCS setup to detect significant variations in molecular weight, a feature expected in the case of an oligomerisation state of RNR.

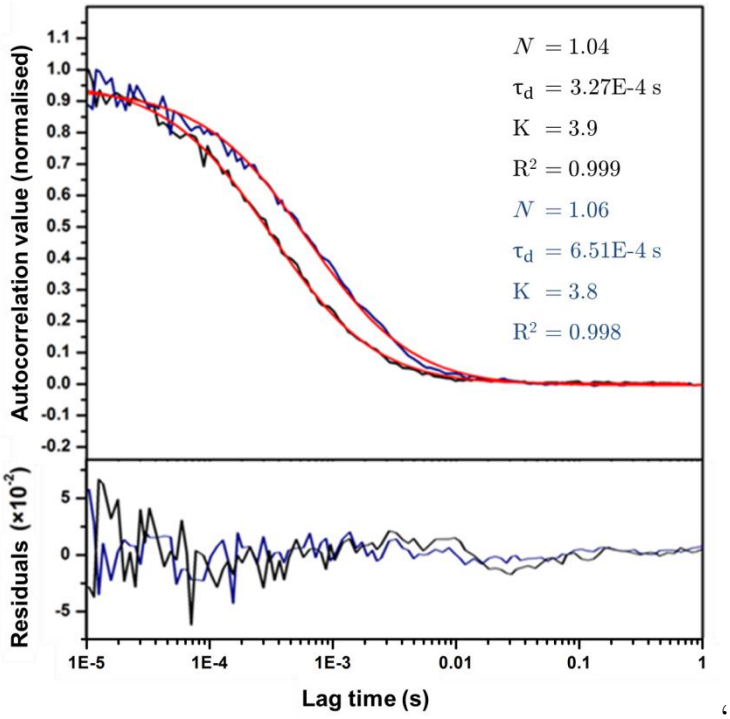

Figure 3.10. FCS sensitivity to molecular weight. Normalised autocorrelation curves corresponding to purified GFP (black) and GFP-antibody complex (blue) are displayed, demonstrating an increase of diffusion time with molecular weight.

	Molecular weight (kDa)	Diffusion time τ_d (ms)
GFP purified protein	27.5 ± 0.5	0.33 ± 0.01
GFP antibody complex	182.5 ± 5.5	0.65 ± 0.13

Table 2. Summary of FCS molecular weight assay. Molecular weights and diffusion times of GFP purified protein and GFP complexed with its complementary antibody are displayed. The diffusion time of the complex increased by a factor 2, which is close to the theoretical value of 1.9 for a 6.6-fold increase in molecular weight.

3.7.2 Suc22 Conformation Investigation

The FCS technique has been used extensively to demonstrate the binding between proteins [223] and molecular aggregation [224-226], which are crucial mechanisms in cellular functions. However this approach is generally limited to tagged probes of small sizes that bind to large complexes, in order to obtain significant differences of

diffusion times. The FCS approach, coupled to a photobleaching assay, has been used below to investigate a potential oligomerisation state of the Suc22 protein.

i. FCS experiment : oligomerisation test

Preliminary experiments using FRET *in vivo* indicated the possible presence of an oligomerised state of proteins forming the RNR complex [187]. A next step in the characterisation of the system was to investigate the purified proteins separately for evidence of multimeric states: it was hoped that recreating the cellular conditions *in vitro* would allow a better understanding of individual proteins behaviour. The aim of the experiment was to use FCS to observe the binding between proteins based on the FRET interaction they display *in vivo*, and study the influence of Spd1 on the RNR complex formation. Unfortunately, difficulties in protein purification did not allow us to achieve this goal, but the stoichiometry of the YFP labelled protein Suc22, purified by Dr A.S. Schreurs (GDSC, Sussex University), was investigated with single molecule techniques. Gel Chromatography confirmed the successive purification of molecules displaying molecular weight of the order of 75 kDa (Figure 3.11), which was consistent with the expected size of monomeric Suc22 (45 kDa) fused to YFP fluorescent protein (27 kDa).

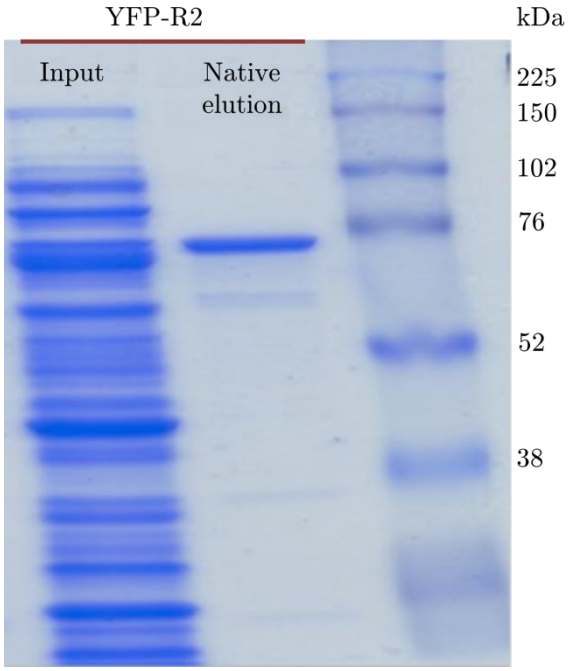

Figure 3.11. SDS-PAGE gel electrophoresis of Suc22-YFP protein before (left band) and after purification (middle band). The control of molecular weight is displayed in the right band. The gel analysis confirms the expected molecular weight around 75 kDa for the tagged purified protein. Work done in collaboration with Dr A.S. Schreurs.

However chromatography is not appropriate in this case to investigate the conformation that the proteins adopt in solution, as the Sodium Dodecyl Sulfate-Polyacrylamide Gel Electrophoresis (SDS-PAGE) denatures the weak binding between subunits during the elution process. A single molecule method was therefore proposed to investigate the system. The average diffusion time of the protein inside the calibrated detection volume was monitored (Figure 3.12) and compared to the reference probe. A significant deviation in the FCS curve from the predicted diffusion time was expected in the case of a high oligomerisation state of the purified proteins.

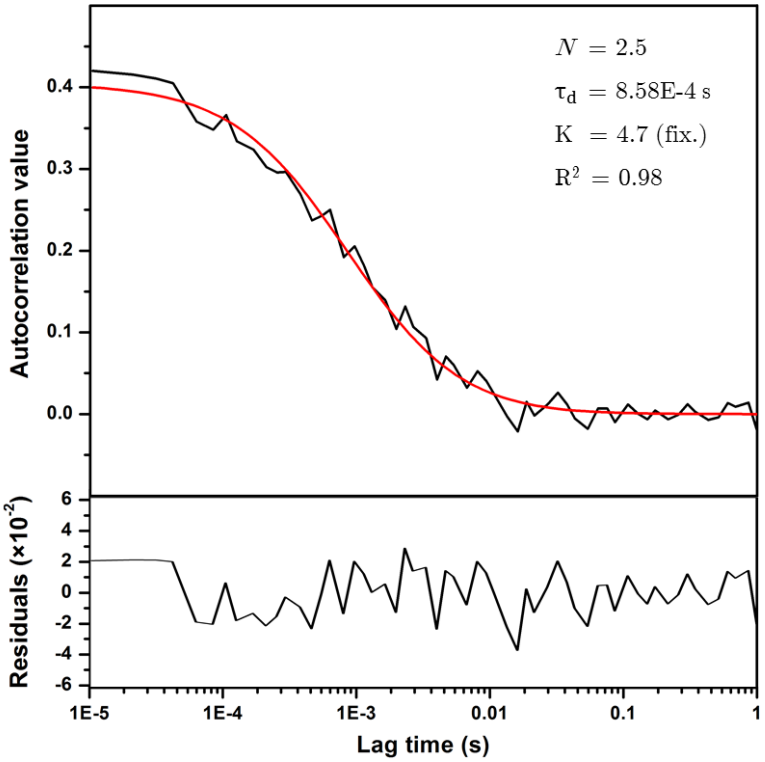

Figure 3.12. Autocorrelation curve of the diffusion of purified proteins Suc22-YFP inside the calibrated FCS detection volume. The parameter K has been fixed to the value determined with the reference dye RhB.

Table 3 displays the experimental values obtained after fitting of the curve that are in good agreement with the monomer conformation hypothesis, which rules out a strong or stable agglomeration of Suc22 proteins in solution. The smaller diffusion time obtained compared to the prediction might be caused by the presence in solution of cleaved YFP proteins that were detected by gel chromatography, and uncertainty in the fitting process. However, the diffusion time is proportional to the molecular weight to a power of three, which leads to a multiplication of the diffusion time by a factor of 1.26 between monomer and dimer conformation. The expected diffusion time for a pure dimer population in solution is 1.13 ms, which does not represent a large

shift for correlation curves. Moreover, a mixture of fluorescent probes with different molecular weights would lead to an averaging of the diffusion time between components, which could hide the presence of dimers in solution. It is therefore difficult to assess the stoichiometry of a sample containing multiple components tagged with fluorescent labels. Suc22 protein stoichiometry was therefore investigated more closely by looking at intensity profiles of immobilised proteins over time.

	Molecular weight (kDa)	Diffusion time τ_d (ms) predicted*	Diffusion time τ_d (ms) experimental
RhB	0.479†	0.17†	0.17 ± 0.01
Suc22-YFP	72 (monomer form)	0.90	0.86 ± 0.03

Table 3. Comparison of FCS results on Suc22-YFP and reference bead RhB. *The predicted diffusion time was obtained using the diffusion time and the molecular weight of RhB. †Reference values obtained from FCS measurements of RhB diffusing in solution.

ii. TIRFM experiment: photobleaching of immobilised proteins

The intensity profiles of individual molecules over time can give useful information on the stoichiometry of tagged molecules in solution, or at least at a surface [227]. The photobleaching effect induces a sudden drop in the fluorescence emission, which happens stochastically at different times for distinct emitters. The characteristic "photobleaching steps" can be quantified, provided the different bleaching steps do not overlap in time, in order to reveal the number of emitters in a diffraction-limited area. The immobilisation of single molecules at a surface is a critical step and has been achieved using the "pull-down" technique [228]: briefly, the coverslip of the microscope was first incubated with a BSA solution and washed, creating a molecular network at its surface. Complementary antibodies were then added at the surface before incubation of Suc22-YFP solution. A small protein concentration (0.1 nM) was used in order to reduce the probability of multiple proteins immobilisation in close proximity. Fifty protein intensity profiles were recorded, which displayed either one or two discrete photobleaching steps (Figure 3.13). Experimental results suggest that a mixture between a majority of monomers (either Suc22-YFP of cleaved YFP protein) and a small population of dimers is present in the purified protein solution.

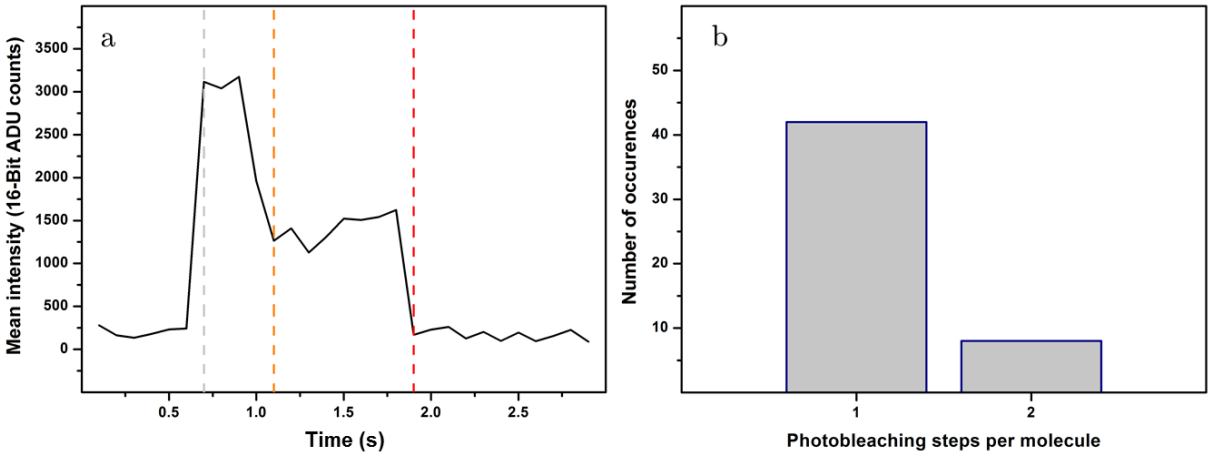

Figure 3.13. Photobleaching steps assay technique. a) Intensity profile of a dimer fluorescent molecule. When the dimer is exposed to an incident excitation (grey line), the emission of fluorescence arises from the two molecules until one photobleaches (first photobleaching step, orange line). The fluorescence emission is lost when the second emitter photobleaches (second photobleaching step, red line). b) Application of photobleaching steps assay to immobilised Suc22-YFP proteins. A minority dimer population was found when the technique was applied to Suc22-YFP (8 dimers against 42 monomers).

3.7.3 Summary of Suc22 Investigation

The purified protein Suc22 investigation using the different single molecule fluorescent techniques described here did not, unfortunately, allow us to conclude successfully on its conformation *in vitro*. Although the FCS experiment appeared to indicate the absence of large oligomer formation and the photobleaching experiment revealed a small population of dimers, the purification of Suc22 proteins was not adequate to distinguish monomeric Suc22-YFP complex from cleaved YFP tag and possibly to retain the integrity of any oligomeric complex. These incomplete results orientated the direction of the work reported in this thesis towards the investigation of proteins in oligomerised states through super-resolution analysis. The idea was to develop techniques applicable to a widefield EMCCD detection scheme that could resolve fluorescent centres corresponding to individual proteins through the analysis of intensity fluctuations, in order to reveal fine structures below the diffraction limit. Suc22 and Cdc22 proteins tagged with photoswitchable fluorescent proteins are currently under investigation using PALM microscopy in collaboration with the GDSC (Sussex University) in order to determine the RNR conformation *in vivo* throughout the cell cycle.

Chapter 4

Super-Resolution Optical Fluctuation Imaging

The need to overcome the diffraction limit has driven numerous studies aimed at exciting selectively a densely labelled sample in order to localise individual emitters. This has been achieved either by replacing the conventional Gaussian laser beam source by a patterned excitation to suppress fluorescence emission around a central imaging beam, or using photoswitchable dyes that can be activated in small numbers and individually imaged. These techniques can provide super-resolution images but are not straightforward to implement. A complex optical setup is required for patterned excitation techniques, whereas elaborate labelling procedures and long acquisition times are needed to reconstruct high quality images.

Here an implementation of the Super-Resolution Optical Fluctuation Imaging technique, created by Enderlein *et al.* [47], is described for use in the ImageJ software package. The method relies on the statistical analysis of temporal fluctuations in signal intensity, which leads to an enhanced resolution and a significant reduction of background noise, using widefield microscope setup and conventional fluorophores. The following section describes an adaptation of the theoretical background to SOFI and details on the technique implementation in ImageJ. Several applications of the technique to the resolution of closely spaced QDs, dual-channel imaging of immunolabelled combed DNA and diffusing systems are also introduced.

4.1 SOFI Theory

The SOFI technique is based on the idea that temporal fluctuations arising from different emitters are independent and stochastic by nature. The statistical analysis of these fluctuation patterns provides a simple way to resolve several closely spaced emitters. The blinking characteristic of fluorophores or QDs, usually considered detrimental in imaging applications, can be taken advantage of to improve spatial localisation, which makes SOFI a powerful tool in fluorescence imaging. It is however important to note that a constant mean value of emission is required, which can be problematic in cases where photobleaching reduces the intensity mean over time.

The concept of SOFI is to apply an autocorrelation analysis to the temporal fluctuations of the signal counts in each pixel of an image. The pixel array is then reconstructed using the autocorrelation amplitude of each pixel, leading to an increase in resolution, as predicted in the mathematical formalism developed below.

The fluorescence distribution $D(t)$ of a single emitter is a time dependent brightness function that can be expressed with a brightness constant ε and a time dependent fluctuation function $d(t)$:

$$D(t) = \varepsilon . d(t) \tag{4.1}$$

Now consider a single emitter fluctuating during a time t. Convolution of the PSF $I(x, y, z)$ of the imaging system and the distribution of the fluorescence source $D(t)$ gives the fluorescence signal $F(x, y, z, t)$:

$$F(x, y, z, t) = I(x, y, z) . \varepsilon . d(t) \tag{4.2}$$

Therefore the fluctuation over the course of an experiment can be retrieved using the time averaged value of $F(x, y, z, t)$, for which will be used the notation $\langle F(x, y, z, t) \rangle_t$.

$$\begin{aligned} \delta F(x, y, z, t) &= F(x, y, z, t) - \langle F(x, y, z, t) \rangle_t \\ &= I(x, y, z) . \varepsilon . (d(t) - \langle d(t) \rangle_t) \\ &= I(x, y, z) . \varepsilon . \delta d(t) \end{aligned} \tag{4.3}$$

Given the expression of the second order autocorrelation function $G_2(x,y,z,\tau)$:

$$G_2(x,y,z,\tau) = \langle \delta F(x,y,z,t).\, \delta F(x,y,z,t+\tau) \rangle_t \tag{4.4}$$

The second order correlation function can be expressed as a function of the source distribution expression and the PSF function:

$$G_2(x,y,z,\tau) = I^2(x,y,z).\, \varepsilon^2.\, \langle (\delta d(t).\, \delta d(t+\tau)) \rangle_t \tag{4.5}$$

This expression is now only dependent on the square of the PSF and on the autocorrelation of the fluctuation function weighted by the square of the brightness of the emitter. Given a three dimensional Gaussian as an approximation of the PSF:

$$I(x,y,z) = \exp\left(-\frac{x^2}{2{\omega_x}^2} - \frac{y^2}{2{\omega_y}^2} - \frac{z^2}{2{\omega_z}^2} \right) \tag{4.6}$$

After a simple multiplication of exponentials, the PSF term for each emitter can be expressed as:

$$I^2(x,y,z) = \exp\left(-\frac{x^2}{2{\widetilde{\omega}_x}^2} - \frac{y^2}{2{\widetilde{\omega}_y}^2} - \frac{z^2}{2{\widetilde{\omega}_z}^2} \right) \tag{4.7}$$

where $\widetilde{\omega}_{x,y,z} = \omega_{x,y,z}/\sqrt{2}$

The equation shows that the width of the PSF is decreased by a factor of $\sqrt{2}$ in each of the three dimensions. The principle of PSF width reduction can be applied with a higher order correlation function:

$$G_n(x,y,z,\tau_1,..,\tau_{n-1}) = \langle \delta F(x,y,z,t).\, \delta F(x,y,z,t+\tau_1) \ldots \delta F(x,y,z,t+\tau_{n-1}) \rangle_t \tag{4.8}$$

Equation (4.7) then becomes:

$$I^n(x,y,z) = \exp\left(-\frac{x^2}{2{\widetilde{\omega}_x}^2} - \frac{y^2}{2{\widetilde{\omega}_y}^2} - \frac{z^2}{2{\widetilde{\omega}_z}^2} \right) \tag{4.9}$$

where it follows that $\widetilde{\omega}_{x,y,z} = \omega_{x,y,z}/\sqrt{n}$

The minimum resolvable separation between two diffraction-limited objects (in the Rayleigh regime, $d_{\mathrm{x,y}} = 0.61\lambda/NA$) is reduced by a factor $1/\sqrt{n}$ with a n^{th} order correlation function, since the standard deviation of the Gaussian representing the PSF is given by $\omega = \lambda/\left(4NA \times \sqrt{2\ln 2}\right)$.

However, a high order correlation function contains, by definition, contributions of lower order correlation functions. Cumulant function $C_{\mathrm{n}}(x, y, z, \tau_1, \ldots, \tau_{\mathrm{n}-1})$ is therefore generally used to eliminate all cross-terms arising from orders inferior to n. Extensive discussion of this mathematical operation can be found in references [47, 229]. The cumulant calculation performed in the ImageJ algorithm used in the work described in this thesis is explained below in Section 4.2.2. In the case of m multiple emitters, Equation (4.5) can be rewritten for the second order correlation as:

$$G_2(x, y, z, \tau) = \langle \sum_{k=1}^{m} I(x, y, z).\varepsilon_{\mathrm{k}}.\delta d_{\mathrm{k}}(t). \sum_{i=1}^{m} I(x, y, z).\varepsilon_{\mathrm{i}}.\delta d_{\mathrm{i}}(t+\tau)\rangle_{\mathrm{t}} \tag{4.10}$$

Because of the stochastic emission of fluorescence of different emitters all terms with $(i \neq k)$ are not correlated and can therefore be discarded, which gives:

$$G_2(x, y, z, \tau) = \sum_{k=0}^{m} I^2(x, y, z).\varepsilon_{\mathrm{k}}^2.\langle(\delta d_{\mathrm{k}}(t).\delta d_{\mathrm{k}}(t+\tau))\rangle_{\mathrm{t}} \tag{4.11}$$

Similarly, the cumulant function to the n^{th} order can be expressed as:

$$C_{\mathrm{n}}(x, y, z, \tau_1, \ldots, \tau_{\mathrm{n}-1}) = \sum_{k=0}^{m} I^{\mathrm{n}}(x, y, z).\varepsilon_{\mathrm{k}}^{\mathrm{n}}.w_{\mathrm{k}}(\tau_1, \ldots, \tau_{\mathrm{n}-1}) \tag{4.12}$$

with $w_{\mathrm{k}}(\tau_1, \ldots, \tau_{\mathrm{n}-1})$ a correlation-based weighting fluctuation function corrected for the contribution of lower order cross-terms.

Equation (4.12) generalises Equation (4.5) to each emitter present in the image. The SOFI method is therefore able to resolve overlapping emitters because of the stochastic nature of their respective intensity fluctuations and induces a reduction in the width of their respective PSFs by the factor $1/\sqrt{n}$ through autocorrelation.

An additional feature of SOFI is the noise reduction in reconstructed images that arises from the autocorrelation of uncorrelated signals. Noise is intrinsically a random

process and therefore the amplitude of the autocorrelation associated with these stochastic events is very low. Applied to noisy images, SOFI provides a simple way to reduce background noise prior to further image processing.

In the following, the development of SOFI algorithm in ImageJ is described and the implementation applied to a number of samples in order to demonstrate the advantages of SOFI in imaging.

4.2 Development of SOFI in ImageJ

The simplicity of SOFI algorithm and its similitudes with the FCS approach enabled its implementation in the image processing open-source software package ImageJ. Different autocorrelation calculation methods were demonstrated and associated performances compared.

4.2.1 Autocorrelation Calculation

A correlation process must be performed on the time series of the signal intensity in each pixel forming the field of view. Following the approach developed in Chapter 3, order n correlation values were obtained by implementing nested loops inside the algorithm displayed in Appendix V. The above method, although efficient, can be demanding in terms of computer time and memory when dealing with large datasets, especially at high orders of correlation. The approximation of setting all lag times to zero, proposed in reference [47], was therefore used to calculate the SOFI images at high orders. This simplification is however not applicable in the case of images with low SNR, for example weakly emitting organic dyes and fluorescent proteins. Setting all autocorrelation lag times to zero is simply equivalent to calculate the variance of the signal at order 2, which evidently does not eliminate the shot noise of the image. On the other hand, computing SOFI images over a range of lag times eliminates this type of noise, since it is uncorrelated in time.

In the case of imaging QDs, where the SNR is high (typically ≥ 500), the approximation with all lag times set to zero has been used to calculate high order cumulants. For experiments involving an organic dye, the order 2 SOFI images have been obtained using the Fourier transform approach described in Chapter 3. The custom-built ImageJ SOFI algorithm is displayed in Appendix V.

4.2.2 Cumulant Calculations and Approximations

The calculation of the cumulants value is crucial at high orders of correlation to achieve super-resolution. The cumulant function contains only the contribution of the higher correlation order, without the effect of lower correlation terms. These cumulant functions can be recursively calculated as [47]:

$$C_2(x,y,z,\tau_1) = G_2(x,y,z,\tau_1) \tag{4.13}$$

$$C_3(x,y,z,\tau_1,\tau_2) = G_3(x,y,z,\tau_1,\tau_2) \tag{4.14}$$

$$\begin{aligned} C_4(x,y,z,\tau_1,\tau_2,\tau_3) = {} & G_4(x,y,z,\tau_1,\tau_2,\tau_3) - G_2(x,y,z,\tau_1).G_2(x,y,z,\tau_3) \\ & - G_2(x,y,z,\tau_1+\tau_2).G_2(x,y,z,\tau_2+\tau_3) \\ & - G_2(x,y,z,\tau_1+\tau_2+\tau_3).G_2(x,y,z,\tau_2) \end{aligned} \tag{4.15}$$

Under the approximation where all lag times to zero to reduce computational demands of the algorithm, Equation (4.12) becomes:

$$C_{\mathrm{n}}(x,y,z,\tau_1=0,\dots,\tau_{\mathrm{n}-1}=0) = \sum_{k=0}^{n} I^{\mathrm{n}}(x,y,z).\varepsilon_k^{\mathrm{n}}.w_{\mathrm{k}}(0,\dots,0) \tag{4.16}$$

This approximation allows the use of the following equation to calculate the cumulant functions recursively using the following equations:

$$C_2(x,y,z,\tau_1) = G_2(x,y,z,\tau_1) \tag{4.17}$$

$$C_3(x,y,z,\tau_1,\tau_2) = G_3(x,y,z,\tau_1,\tau_2) \tag{4.18}$$

$$\begin{aligned} C_{\mathrm{n}}(x,y,z,\tau_1,\dots,\tau_{\mathrm{n}-1}) = {} & G_{\mathrm{n}}(x,y,z,\tau_1,\dots,\tau_{\mathrm{n}}) \\ & - \sum_{i=1}^{n-1} \binom{n-1}{i} C_{\mathrm{n}-\mathrm{i}}(x,y,z,\tau_1,\dots,\tau_{\mathrm{n}-\mathrm{i}-1}).G_{\mathrm{i}}(x,y,z,\tau_1,\dots,\tau_{\mathrm{i}-1}) \end{aligned} \tag{4.19}$$

This recursive expression was implemented in the SOFI algorithm for high correlation orders, with autocorrelation and cumulant functions G_{n} and C_{n} calculated using the approximation of lag times set to zero.

4.2.3 Second Order SOFI Processing in ImageJ

The typical workflow for a second order SOFI analysis of an image stack is schematised in Figure 4.1. Here a 1000 frames movie of a single QD undergoing intensity fluctuation, acquired under TIRFM with an acquisition time of 100 ms, is used to exemplify the SOFI process (Figure 4.1.a). The time trace of each pixel was stored in a single image and associated autocorrelation curves obtained using Fourier transforms. The integral of each curve was calculated from the summation of autocorrelation amplitudes over the range of lag times and this value was used to reconstruct the final order 2 SOFI image. The temporal traces are shown in Figure 4.1.b and the corresponding autocorrelation traces displayed in Figure 4.1.c, where for clarity, only the region of interest (ROI) defined by the blue frame in Figure 4.1.d is displayed. The autocorrelation curves of two different pixels have been plotted in Figure 4.1.e to highlight the background reduction feature of SOFI algorithm.

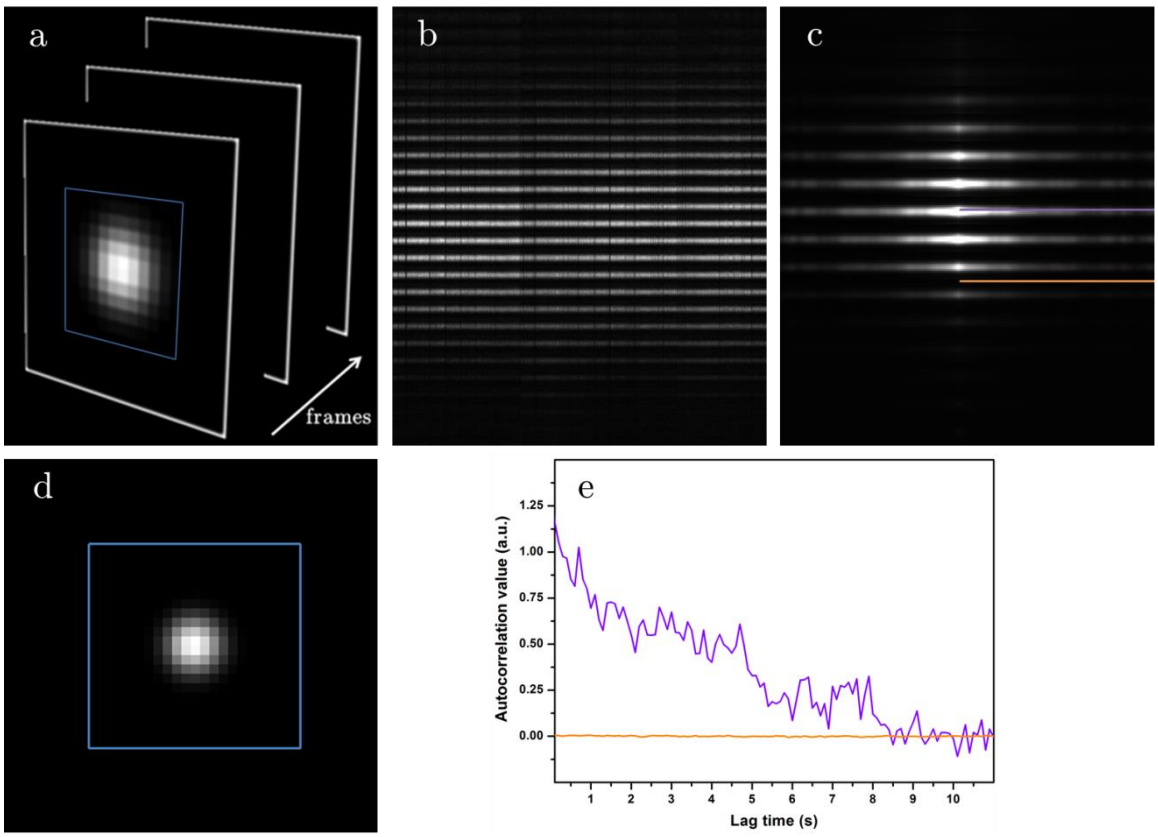

Figure 4.1. Step by step development of SOFI algorithm. a) Emitter intensity fluctuation is recorded as a stack of frames. b) Intensity fluctuation of each pixel is stored in an intermediate image. c) Autocorrelation of each time series is performed. d) Final image is reconstructed using the integral value of the autocorrelation curve. e) Pixel containing only noise has a low integral intensity due to weak amplitude of correlation (yellow curve), while a pixel with genuine emission of fluorescence exhibits strong correlation over 5 seconds and more (purple curve) which results in a high integral intensity.

It is clear that a pixel outside the kernel of the PSF displays a low amplitude correlation curve (yellow in Figure 4.1.c), corresponding to the uncorrelated background noise, whereas a pixel near the PSF peak exhibits a correlation amplitude decay (purple in Figure 4.1.d) that reflects the fluorescent blinking of the QD. Evidently taking the integral under the curves results in a reconstructed image with background pixels significantly suppressed and signal pixels enhanced. Depending on the blinking pattern of the emitter, the values in the pixels forming the PSF in the reconstructed SOFI images can be negative and therefore pixels corresponding to background noise would have a bigger value than the pixel associated with genuine signal. In the following section absolute magnitude value of each pixel is used to obtain the final SOFI images displayed.

4.3 Application of Higher Order SOFI to QDs

The SOFI algorithm was applied to coverslip-immobilised QDs to experimentally test the theoretical dependency of the PSF width with the order of correlation, following the approach described in reference [47]. The impact of experimental parameters such as drift correction and photon statistics on localisation precision was examined to ensure the reliability of results and reduce super-resolution uncertainties.

4.3.1 Sample Drift Correction

Localisation precision in any super-resolution technique is limited, not only by the number of photons detected, but also the stability of the imaging system. Spatial drift of the sample over the time course of an experiment is a factor that must be minimised and corrected for to render localisation uncertainties and, in the case of SOFI, the PSF narrowing meaningful and quantitative.

Sample drift can be caused by vibrations transmission and differential thermal relaxation of microscope components. These problems were addressed by building the microscope on a passive-vibration isolating table and keeping a thermal equilibrium by setting the ambient atmosphere at 20°C. Whatever the mechanism, drift will cause a decrease in the centroid localisation accuracy upon Gaussian fit of the PSF. In particular, where frame averaging over time is used to improve SNR, the PSF will be made artificially wider, affecting both uncertainty in localisation ($\sigma_i = \omega_i/\sqrt{N}$) and the ability to correctly narrow the PSF by $1/\sqrt{n}$ with increasing correlation order.

While temperature control through air-conditioning in the laboratory helped minimised the drift observed to the order of 20-30 nm, correction was nonetheless required to reduce uncertainties in super-resolution images.

Recognising this, a post-acquisition procedure was developed to correct for the mechanical drift of the stage experienced during acquisition of large image stacks. Four single QDs located near to image corners were randomly picked and their positions determined over time using the two-dimensional Gaussian fitting model described by Equation (1.18). Any stage drift was then corrected by taking the averaged mean displacement of those reference QDs in each frame and using this value to correct the entire stack. Frames in which more than two reference QDs were in the "off" state were discarded from the image stack. This method, although reducing the dataset size and requiring more computation time, provided an enhanced accuracy of drift correction.

Figure 4.2 shows the positions of a randomly chosen QD, recorded for 30 seconds with an acquisition time of 100 ms, before and after drift correction. It is clear from these figures that the systematic displacement present in the y direction was reduced after stage drift correction. The uncertainty due to the drift of the system has been calculated from the standard deviation of the centroids distribution in the x and y directions, σ_x and σ_y :

$$\Delta r_{\text{drift}} = \sqrt{{\sigma_x}^2 + {\sigma_y}^2} \tag{4.20}$$

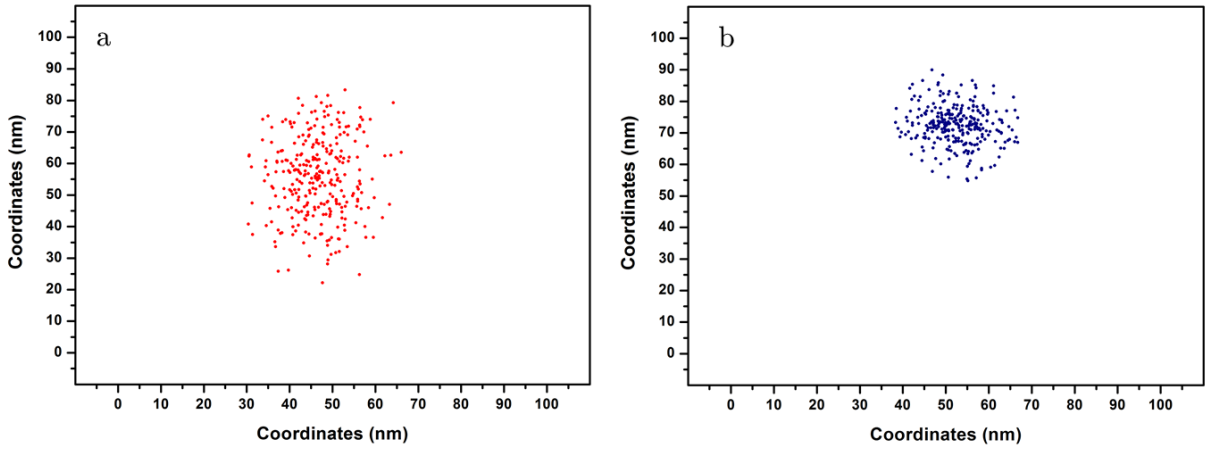

Figure 4.2. Drift correction using a two-dimensional Gaussian fit method. a) Constant drift over time in the vertical direction is clearly displayed in successive positions of a single QD over time. b) Gaussian fitting of reference QDs over time enables to minimise the influence of stage drift. The standard deviation of the emitter positions was reduced from 12.6 nm to 6.8 nm after drift correction.

4.3.2 Precision in Emitter Localisation: Photon Statistics

The total uncertainty in the localisation of a molecule in the imaging system, Δr_{system}, is dependent on both the stage displacement and the inherent photon statistics, which are additive in quadrature:

$$\Delta r_{\text{system}} = \sqrt{\Delta r_{\text{drift}}^2 + \Delta r_{\text{photon}}^2} \tag{4.21}$$

To characterise the overall uncertainty and the stability of the TIRFM system used here in the application of SOFI and subsequent development of super-resolution techniques, image stacks of singular QDs were recorded over time, from which both the uncertainty due to the spatial drift and photon number could be extracted.

The number of photons per PSF was calculated by summing the ADU counts of all the pixels forming the PSF and applying the conversion operation given by Equation (2.2). Different photon numbers were retrieved by varying the frame exposure time. For each exposure time a single QD in the image stack was analysed for drift, as described above, and the standard deviation following correction measured as a function of increasing signal. The localisation uncertainty of the QD in each frame due solely to photon statistics was retrieved by applying Equation (1.20) with the appropriate photon number. The resulting uncertainty due to the correction of the mechanical drift, photon number and the global uncertainty for the single QD of Figure 4.2 are displayed in Figure 4.3. Successive frames of the same stacks were summed to retrieve the photon number emitted and the associated precision.

The uncertainty due to the number of photons collected converges below 1 nm for photon counts around a value of 30000. The photon statistics uncertainty is inferior to sample stage drift for a photon count of around 1000. The large number of photons afforded by QDs drastically reduces the uncertainty due to photon statistics, with the uncertainties in the localisation of the QD dropping to sub-nanometre levels around 0.25 nm after 30 seconds of imaging (300 frames). However, photon statistics become increasingly dominant at typical acquisition time of 100 ms or less, where the photon count is reduced to values inferior to 600. Moreover, the number of photons emitted by an organic fluorophore is typically between two and three times lower than for the QD at the same excitation power [230] and the temporal acquisition is generally limited by photobleaching. These two effects combine to reduce the localisation precision of single organic emitters and fluorescent proteins to around 20 nm.

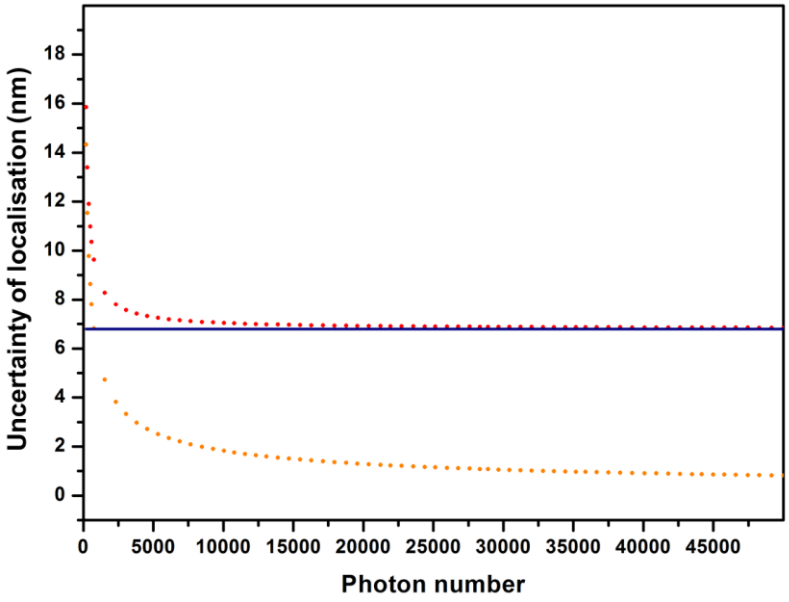

Figure 4.3. Uncertainty in centroid localisation due to photon statistics (orange dots) and stage drift (blue dots). The total uncertainty is plotted in red for a pixel size of 97 nm and a background noise count of 2 photons. The main source of uncertainty for more than 1000 photons collected is the sample drift of the imaging system.

4.3.3 PSF Reduction with SOFI

The SOFI algorithm was tested on a QD image stack of 2000 frames in which the QD displayed significant fluorescence fluctuations at a capture frame rate of 100 ms (Figure 4.4). It is evident from the reconstructed PSF that the width is reduced with increasing the order of correlation applied in SOFI. The reduction of the PSF size by autocorrelation of temporal intensity fluctuation has previously been explained using the Gaussian approximation of the PSF and the mathematical formalism associated to the autocorrelation function in Section 4.1. On a qualitative level, for a single molecule image spot spanning several pixels, the pixels in the wing of the PSF will have a larger noise component than those at the centre and uncorrelated fluctuations in the noise will thus contribute less to the autocorrelation amplitude in these outer pixels.

It is clear from Figure 4.4 that the constant offset present in the average image caused by the background noise is significantly reduced after applying the SOFI algorithm, starting with the order 2 image. This enhancement in the image quality is directly induced by the autocorrelation process performed: the uncorrelated nature of noise results in very low amplitudes of the associated autocorrelation function and emphasises genuine signal in the reconstructed SOFI images.

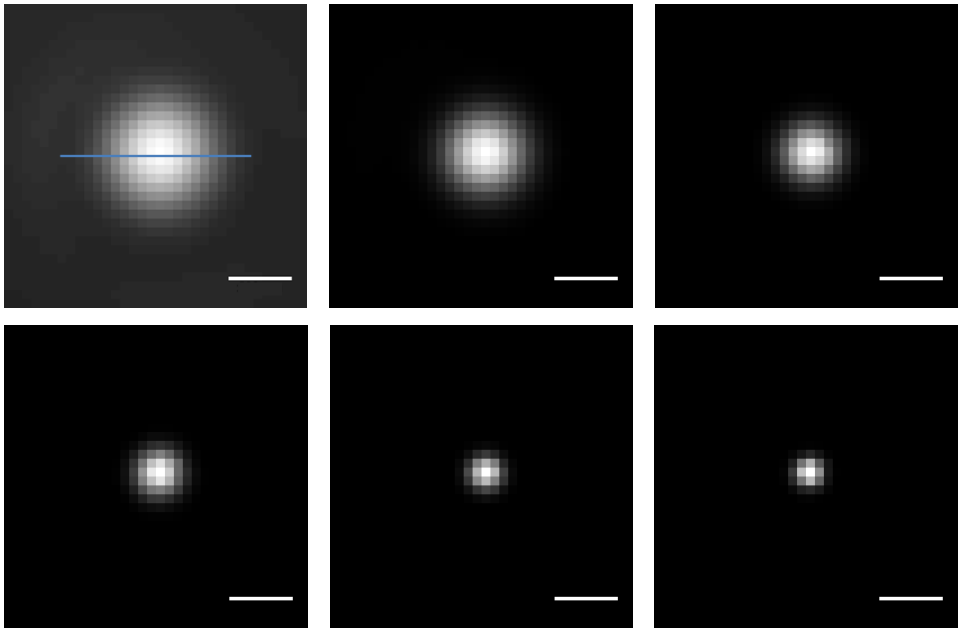

Figure 4.4. Reduction of PSF size induced by SOFI algorithm. Projection of the averaged intensity of the stack frames of a single QD (top left) and associated SOFI images at orders 2, 4, 6, 12 and 16 (bottom right picture) are displayed. Pixel size: 35 nm. Scale bar: 200 nm.

The intensity profiles of the images of Figure 4.4 along the blue line displayed on the average of the original movie have been plotted in Figure 4.5 and fitted with a Gaussian function, using a Levenberg-Marquardt curve fitting in OriginPro 8.0 (OriginLab Corp), to demonstrate the decay of the FWHM with the SOFI order.

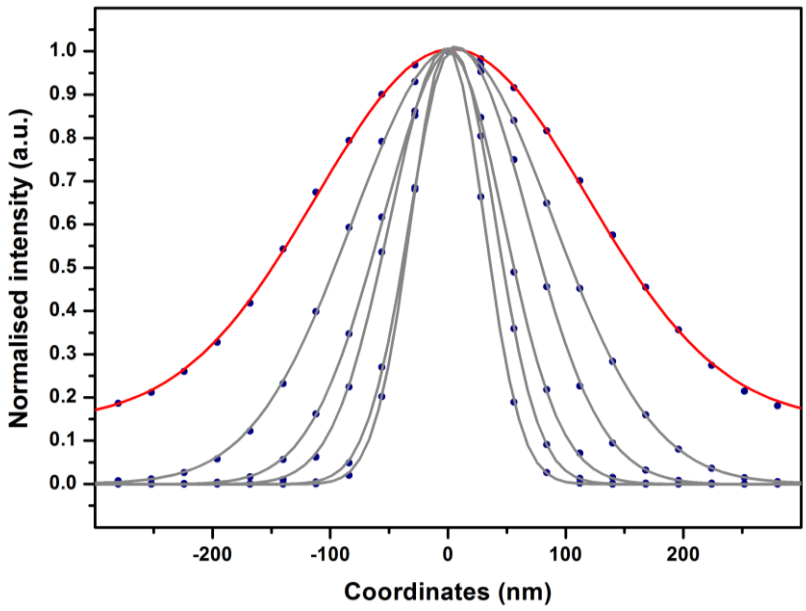

Figure 4.5. PSF profile at different SOFI orders and associated Gaussian fit. The ADU values along the blue line in Figure 4.4 are displayed for the average projection of the stack (red curve) and SOFI orders 2, 4, 6, 12 and 16 (grey curves).

The values of the average FWHM of the PSF in x and y directions have been determined for SOFI orders up to 16 (Figure 4.6) and fitted as a function of correlation orders with the following power law to test the $1/\sqrt{n}$ dependency of the algorithm:

$$A(n) = a \times n^{b} \tag{4.22}$$

where n is the order of the SOFI correlation and $A(n)$ the value of the FWHM obtained from the Gaussian fit.

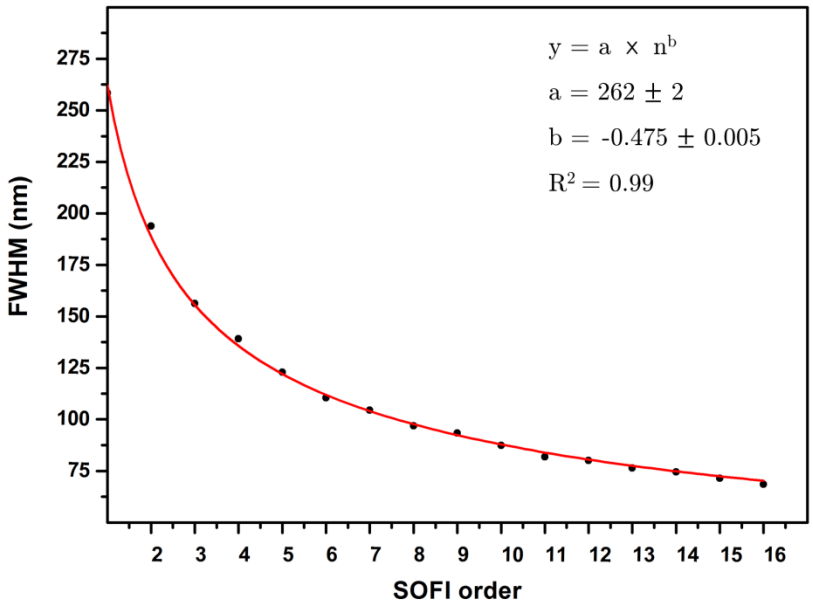

Figure 4.6. Variation of PSF FWHM at different SOFI orders. The red curve was obtained by fitting the result images of SOFI algorithm with Equation (4.22).

A value of $a =$ 262 nm was obtained from fitting the original PSF, which is in accordance with the FWHM of the PSF of the original movie. This is larger than expected for a single QD emitting at 585 nm, where FWHM $\sim \lambda/2NA = 201$ nm. However the high magnification of the system afforded by an additional zoom 7×, giving an image resolution of 35 nm/pixel, is accompanied by slight curvature across the field of view and likely spherical aberration from an imperfectly matched lens system. Here it is only the relative change PSF width that is of interest and the fit of the power law gave a value of -0.48 for the exponent b, which confirms the division of the PSF width by a factor of $\sqrt{n}$ for a n^{th} order SOFI image.

4.3.4 Resolution of Closely Spaced QDs

The ability of SOFI to decrease PSF width given an appropriate blinking characteristic permits the resolution of multiple closely spaced emitters, property which was tested on clustered QDs. The QDs are spaced near the diffraction limit, but are strictly unresolved according to the Rayleigh criteria, which requires the central intensity of combined PSFs to have dropped some 20-30% from the separate maxima.

Figure 4.7 displays the results of SOFI method to the resolution of four closely spaced QDs. The algorithm has been applied on a 1000 frames movie acquired at an acquisition time of 33 ms, in which each of the four QDs displayed significant fluorescence fluctuation. It is apparent that individual PSFs widths are gradually decreasing with the order of SOFI, leading to an improved emitter resolution of the most separated QDs at order 2 and the closest QDs (along the blue line) at SOFI order 5. The SBR is also significantly higher in the SOFI images due to the noise decrease induced by the SOFI algorithm demonstrated in the previous section.

The relative intensities of the QDs in the SOFI images depend on their respective blinking characteristics. It is therefore important to maximise as much as possible the blinking rate of neighbouring emitters in order to enhance the quality of the reconstructed images.

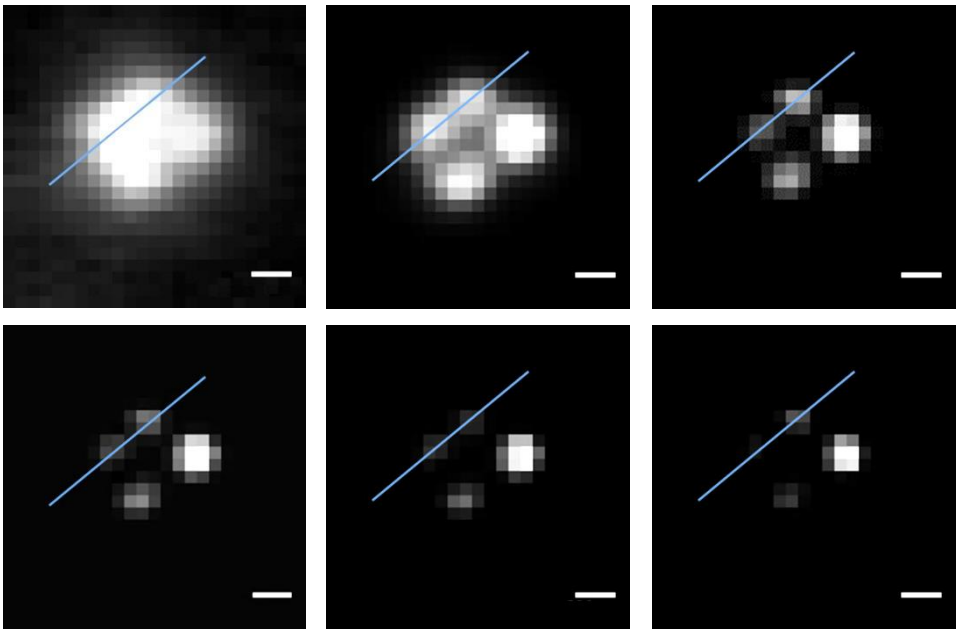

Figure 4.7. SOFI resolution enhancement of four overlapping QDs. The average stack frames projection is displayed on the top left picture, along with results of SOFI at order 2, 5, 7, 9 and 12 (bottom right picture). Pixel size: 60 nm. Scale bar: 200 nm.

The intensity profiles of selected images across the blue line displayed in Figure 4.7 have been plotted in Figure 4.8 in order to highlight the resolution improvement produced by the SOFI technique. The two PSFs centres are clearly not resolved in the average of the original stack of frames, but start to appear in the order 2 SOFI image. At order 9, the two peaks are clearly resolvable and any further Gaussian fitting can be used to reveal with precision the centre of the PSFs.

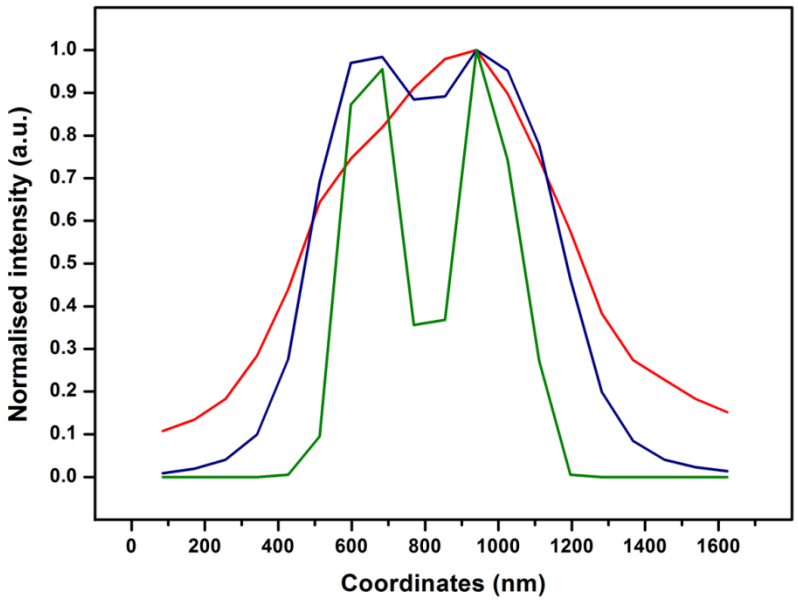

Figure 4.8. Improvement of resolution using SOFI algorithm. ADU profiles along the line displayed in Figure 4.7 are displayed for the average of the original movie (red), SOFI order 2 image (blue) and SOFI order 9 image (green). Note that the background noise present in the original movie is removed in all SOFI images.

In Figure 4.7, some SOFI reconstructed PSFs become difficult to see in high orders SOFI images. This behaviour comes from the expression of Equation (4.12): the intensity value in the reconstructed SOFI image is dependent on the brightness and the blinking pattern of the emitter. If one emitter is particularly bright or displays long fluorescence correlation times due to higher photostability than weaker or faster blinking neighbours, its intensity value in the reconstructed image will be much higher than others, and therefore would appear to dominate in the reconstructed image. This "masking effect" has to be taken into account, especially at high orders of correlation function where it is more pronounced. On the other hand, if one is interested in more than the image representation, the SOFI images contains additional information on the emission process of each fluorophore: this dynamic range of intensities in the reconstructed SOFI image might be put to use to classify dyes in an image according to their degree of fluctuations and/or brightness for example.

4.4 Application of SOFI to Organic Dyes

Although displaying enhanced photophysical properties, QDs are sometimes not suited to the imaging of biological systems because of size, biocompatibility and labelling procedures. It is therefore necessary in certain cases to use organic dyes, which may be conjugated to a biological system of interest via immunostaining, or fluorescent proteins fused at the ends of proteins using genetic modification of the source strains. The experimental and technical adjustments that are required to apply SOFI to organic emitters are detailed in the following section.

4.4.1 Drift Correction by Cross-Correlation

The correction of the stage drift is more complicated to perform using biologically labelled constructs than with QDs: the Gaussian fit requires single fluorophores immobilised and emitting a strong fluorescent signal. It is possible to add references beads to a sample and correct the stage drift by using these reference points, but this solution can risk contaminating samples and was not selected because of technical constraints. Therefore, a plugin that exploits native ImageJ Fourier space routines was used instead of classical Gaussian fits [231]. The alignment is performed using cross-correlation between a reference image (the first image of the stack) and a target image (all successive frames that are aligned with respect to the first one). The plugin computes the correlations for all registration shifts at the same time using Fast Fourier Transforms (FFTs) routines. The shift associated with the maximum correlation value was chosen for the alignment. Cross-correlations in the Fourier domain were calculated using a simple conjugate multiplication, which makes the image correlation very fast to compute once transformed to the Fourier domain. A window function was used to roll-off the image to zero near the borders, which avoids edge artifacts that can deteriorate the alignment accuracy.

4.4.2 Adaptations to SOFI for Organic Probes

The SOFI algorithm requires numerous adaptations in order to be applied to organic emitters [232]. In general these fluorophores exhibit a lower SNR compared to QDs and typically have a characteristic time associated to fluorescence intermittency or blinking in the microsecond range, largely due to triplet state shelving of fast

isomerisation processes. With image acquisition times on the camera limited to the millisecond range, this intermittency manifests more as a flickering than a true blinking process. Moreover, these compounds are prone to relatively rapid photobleaching, which limits the useful number of frames in any acquisition and potentially degrades the performance of the algorithm, since it functions more effectively where the fluorescence signal displays a constant mean value over time.

However, it has been shown that Alexa fluorophores exhibit milliseconds scale blinking behaviour in a PBS buffer containing an oxygen scavenger and mercaptoethylamine, and are therefore suitable for SOFI algorithm [233]. Moreover, it is possible to circumvent the photobleaching effect in SOFI by decomposing a movie stack acquisition into substacks of frames displaying a photobleaching decay over time that does not exceed 5% within each block. The SOFI images obtained from each subset of frames can then be summed to obtain a final super-resolved image. This modified approach to the SOFI algorithm has been successfully applied on a β-tubulin network labelled with Alexa 647 under the strict conditions stated above [232]. This processing method has been applied to DNA labelled with two different labels and immobilised on a coverslip by molecular combing.

4.4.3 Application to DNA Combing

DNA material was labelled with two different organic dyes and immobilised at the surface of a coverslip using a combing process. This immobilisation method consists of removing, at a constant speed, silanised glass slides from a concentrated DNA solution [234]. The binding between DNA and the surface originates either from hydrophobicity and/or an electrostatic interaction between negatively charged DNA and a positively charged coverslip and was first observed on slides coated with a silane possessing a vinyl end group at pH 5.5 [235]. Furthermore, the respective DNA molecule ends are exposed polar groups and therefore have a high binding specificity to the silanised surface [236]. This preferential affinity of the DNA ends with the coverslip surface provides an anchor for the subsequent combing process.

The coverslip is next pulled out of solution with a constant speed (v = 300 μm/s) during which a receding meniscus applies a perpendicular force on the DNA [234], resulting in an homogeneous stretch of the genetic material onto the glass slide (Figure 4.9). The resulting stretching factor is constant (1 μm ~ 2 kb) for all DNA fibers that are aligned in parallel on the coverslip [236].

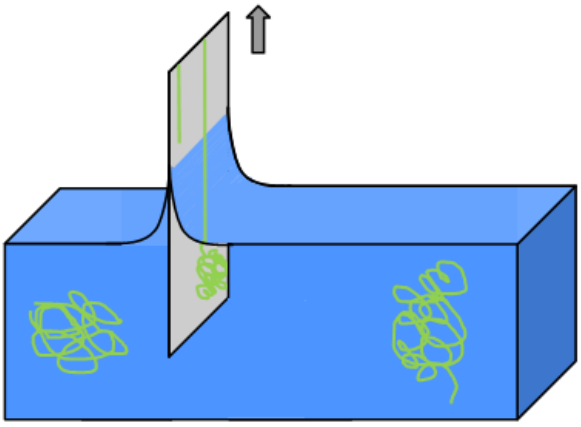

Figure 4.9. DNA combing principle. The chemically modified slide is pulled out of the medium at a regular speed, which results in a linear stretching of DNA linked to its surface.

Molecular Combing enables the spread of around 100 genomes on a single coverslip with a uniform stretching factor, and allows a large statistically significant sample from a single experiment [237]. Replication Combing Assay (RCA) exploits this sampling of large DNA molecule populations to monitor, for example, genome replication processes in normal or cancerous cells.

In a typical experiment, the genomic DNA of cells is successively labelled (pulse-labelling) with different nucleotides derivatives, typically iododeoxyuridine and chlorodeoxyuridine, at different times of the cell cycle. DNA is then extracted and combed on the silanised slide. An immunofluorescence process allows the addition of fluorescent probes bioconjugated to the modified nucleotides previously incorporated in the DNA sample. The analysis of the colour sequences detected, in particular their respective lengths, spacings and repetition patterns, are used to investigate the DNA replication mechanism at a single molecule level [238, 239].

Figure 4.10 shows the averaged dual channel projection of combed DNA labelled with Alexa 488 and Alexa 555 fluorophores. It is clear from the picture that several regions appear to have a yellow colour, as a result of the presence of both fluorophores in the same region of the sample. This behaviour might be explained by a residual amount of fluorophores after the end of a labelling sequence, as well as the imperfect selectivity of the antibody to CldU and IdU. The SOFI technique has been applied on both channels and the final image reconstructed by merging SOFI images of the two imaging channels. The resulting image displayed as expected a major noise reduction, as well as a slight increase of resolution in both channels. The lower reduction of PSF size ($\sim$ 10%) compared to QD experiments might be explained by the photobleaching effect that limits the length of acquisition. The intensity profiles along the blue line of Figure 4.10 in each imaging channel are plotted in Figure 4.11.

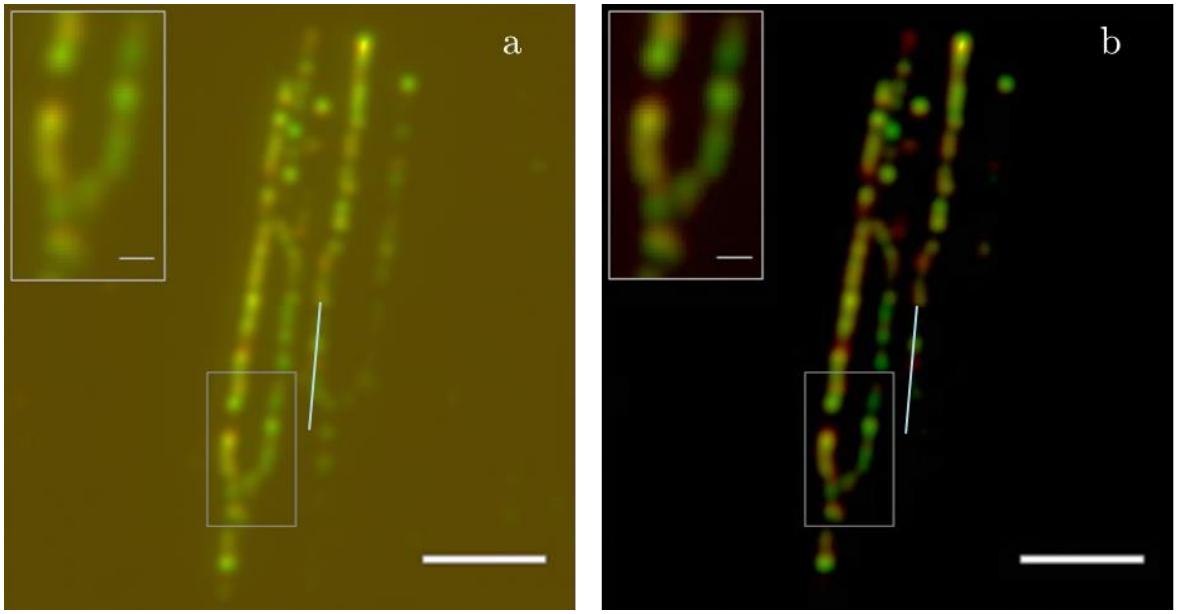

Figure 4.10. Application of SOFI to dual channel imaging of combed DNA labelled with Alexa 488 and Alexa 555 organic fluorophores. a) Average projection of the original movie recorded. b) SOFI order 2 result obtained by summing up SOFI result of substacks of 100 frames. Both images were obtained by merging the two channels into a RGB image, with Alexa 488 channel as "Green" and Alexa 555 channel as "Red". Images are displayed with a similar contrast threshold with respect to image maximum intensity. Scale bar: 3 μm in main images and 500 nm in expansions.

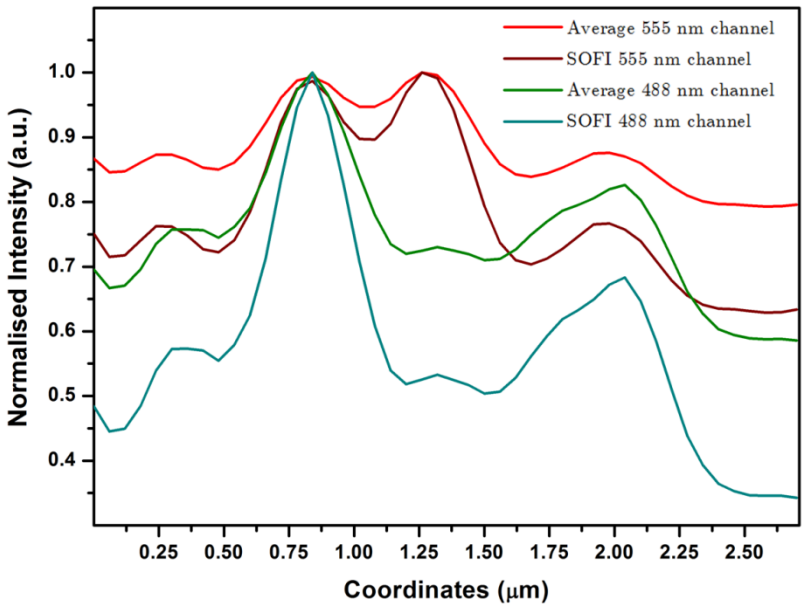

Figure 4.11. SOFI resolution enhancement in dual channel imaging. The normalised intensity profiles along the blue line of Figure 4.10 reveal noise reduction and a moderately improved resolution between peaks, which could lead to enhanced colocalisation accuracy of features appearing in different channels after SOFI analysis.

The resolution of the two successive peaks with centre coordinates located between 0.75 μm and 1.5 μm is slightly emphasised after SOFI analysis in the 555 nm channel,

as well as the colocalisation between the first peak in the 488 nm and 555 nm channels. This could be used in further experiments to determine the respective length of DNA with different labels, allowing one to characterise more precisely the DNA replication process in a RCA-type experiment, or in a colocalisation study.

4.5 Diffusion Processes Analysed with SOFI

The SOFI analysis can be considered as multiple FCS experiments applied to all emitters present in the field of view. Each pixel of the image constitutes a separate detection volume whose intensity fluctuations are recorded and correlated. It should therefore be possible to obtain information about the diffusion rate of the molecules in the sample, providing the emitter concentrations, diffusion constants and camera acquisition rate are adequate for conventional FCS experiments. The aim of the following section is to introduce the SOFI features that allow studying diffusion processes with a microscopy imaging setup. The concept of performing an FCS experiment using an EMCCD camera is first introduced using QDs diffusing freely in solution. The ability of SOFI to map different areas depending on the probe diffusion coefficient is then demonstrated on simulated data and tracking of single QDs performed using pixel-by-pixel temporal correlation analysis.

4.5.1 FCS Coupled with an EMCCD Detection

FCS experiments are usually performed with fast-rate photon counters, which allow sensitive detection of single molecules. An alternative strategy of signal detection consists in taking advantage of the EMCCD used in standard imaging microscopy setup to perform FCS [240]. This approach presents several advantages for multi-spot measurements of different areas of biological samples, which is normally limited by the necessity of using multiple detectors and excitation schemes. The detection of signals arising from multiple detection volumes on the same detector allows flexible parallel measurements albeit at reduced acquisition rates.

i. Detection volume characterisation

The FCS technique has previously been adapted to EMCCD camera detection-type using a TIRFM setup in the study the non-specific binding of immunoglobulin and

insulin to serum albumin-coated fuse silica [241] and the measurement of transport rates through thin sol-gel films [242]. Here, the TIRFM-FCS approach was demonstrated in its simplest form on freely diffusing QDs in solution. The microscope was used in near-TIRFM mode and focused inside the sample next to the coverslip surface to reduce the effective detection volume dimensions, which as a result did not display the conventional Gaussian shape but was rather defined by the depth of field of the microscope in the axial dimension and by the dimensions of the detection area in the EMCCD chip (Figure 4.12). Existing techniques in the literature rely on a conventional microscope in epifluorescent mode and generally use a detection volume of bigger area (typically 256 μm^2) to perform FCS. The detection volume is arbitrarily set by the size of the ROI chosen on the EMCCD chip, which is analogous to varying the pinhole size to change the confocal volume dimensions in standard FCS experiments. The aim of our experiment was to try to directly visualise the PSFs of the fluorescent probes before using a correlation process, which could add further understanding to the interpretation of the FCS data. Moreover, one can imagine that multiple detection volumes could be used in the same excited area, allowing parallel study of close features, inside a cell for instance.

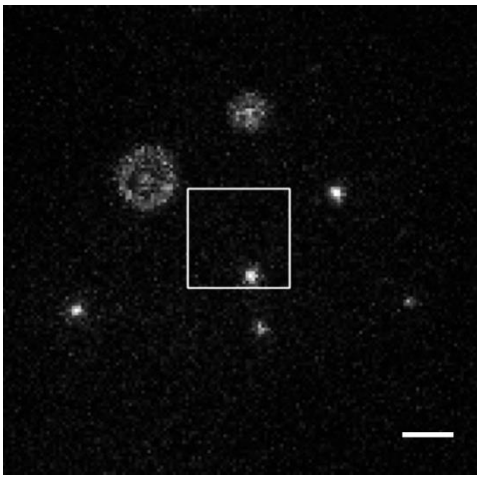

Figure 4.12. EMCCD detection scheme combined with FCS technique. The trajectories of PSFs corresponding to diffusing QDs are recorded when passing through the detection volume (white frame, 16 μm^2). Molecules located off the focal plane display defocused PSF rings. Multiple detection volumes might allow parallel correlation studies. Scale bar: 2 μm.

PSFs associated to single molecules agitated by Brownian motion next to the surface were imaged over time, at a fast acquisition time of the order of 10 ms, which was achieved by reducing the EMCCD array of detection from 512×512 pixels to 33×33 pixels as described in reference [243]. Full details of the experiment are displayed in Section 2.3.4 and in Appendix VI.

ii. Viscosity titration: application to diffusing QDs

An assay of the previous technique was carried out using commercial QDs in different concentrations of glycerol-water mixtures to characterise the influence of viscosity on the autocorrelation curve. The respective samples were imaged for 200 seconds with exposure times of the order of 10 ms per frame. The signal arising from the detection volume was corrected for background intensity and all pixel intensity values summed for each lag time. An autocorrelation process was then performed on the total time varying volume intensity and the resulting curve fitted with a two-dimensional diffusion model. The model is approximate since the detection volume is not strictly described by a Gaussian function in the lateral direction but by the near-TIRFM excitation geometry. However, consistent results were obtained when the detection volume encompasses the centre of the oblique angled laser beam, where the beam approaches a Gaussian profile. Furthermore, in this instance, only the relative differences in transit times through the detection volume were investigated rather than absolute measurements. This principle was used to compare the respective diffusion time of the QDs under different viscosities (Figure 4.13).

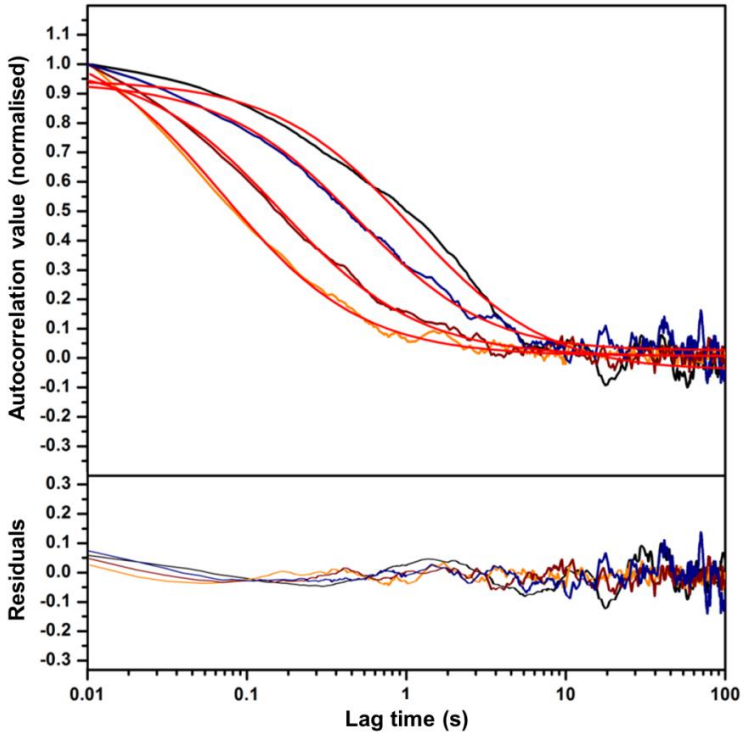

Figure 4.13. Influence of solution viscosity on diffusion time. Autocorrelation curves and fits of diffusing QDs in pure water (orange), 30 wt% (red), 50 wt% (blue) and 67 wt% (black) glycerol-water mixtures are displayed. For clarity purposes, only four of the curves obtained are shown. Remaining curves, along with fitting parameters, are displayed in Appendix VI.

The characteristic diffusion time obtained after fitting was plotted against the viscosity of medium solutions (Figure 4.14), obtained from the weight percent of glycerol diluted in water [244]. The expected result from Equation (3.5) is a linear dependency of the diffusion time, and therefore of the characteristic value obtained from autocorrelation fitting, to the solution viscosity. The values of diffusion times at high viscosity seem to be less accurate, possibly because of index refraction mismatches, small errors in glycerol weight percent or variations in experimental temperature, leading to large error for solutions with high glycerol content. This behaviour might as well reflect the approximation of the 2D fitting model with the experimental detection volume. However the expected dependency of the diffusion time on viscosity is confirmed by the experimental results: the diffusion coefficient increases with viscosity of the solution in a near-linear fashion, in accordance to ($\tau_d \propto 1/D = 6\pi\eta r/kT$). The result highlights the possibility of using an FCS-type approach on an EMCCD with a near-TIRFM excitation scheme. The sensitivity of the system was sufficient to differentiate diffusion times in mediums of different viscosities (η), suggesting also that diffusion coefficients of molecules presenting differences in hydrodynamic radius (r) of the same order of magnitude could be retrieved in a similar manner according to Equation (3.5). Moreover, the widefield excitation scheme allows parallel detection in multiple areas and might enable the comparison of diffusion coefficients in neighbouring regions.

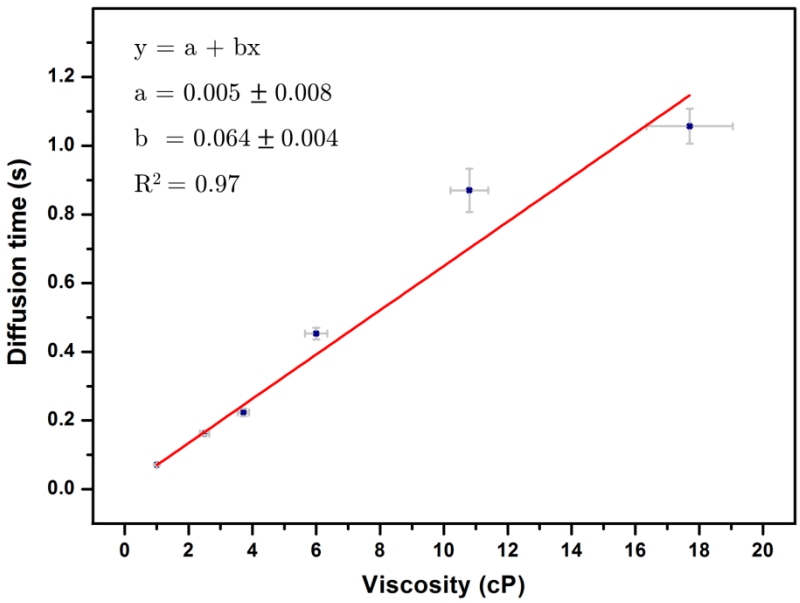

Figure 4.14. Dependency of QD diffusion times on medium solution viscosity. Error values for viscosity are assumed to arise from a 1% error in glycerol concentration (obtained with a linear interpolation of the viscosities from [244]). Full experimental results are displayed in Appendix VI.

4.5.2 Diffusion Dynamics Investigation with SOFI

The size of the detection volume in the FCS-EMCCD scheme can be adjusted arbitrarily, providing the average number of molecules inside is compatible with single molecule sensitivity. SOFI can be considered as multiple simultaneous parallel FCS experiments carried out at the lower limit of detection volume size, where each pixel becomes a single FCS cell. In principle, different characteristic diffusion coefficients present in the field of view may be analysed at single pixel resolution by applying the simple per-pixel correlation method of SOFI. This might be of particular interest for the study of protein diffusion *in vivo*, to measure the heterogeneity of diffusion through cell membranes [245] or obtain information about association dynamics at different protein binding sites [246]. Current methods for determining diffusion coefficients *in vivo* rely mainly on FRAP experiments [247], conventional FCS [248], and single particle tracking [249]. The following section demonstrates the application of SOFI in the study of diffusion processes and molecular tracking.

i. Multi-particle diffusion mapping using SOFI

The ability of SOFI to discriminate between different diffusion domains was tested using simulated data. The Brownian motion of 500 non-blinking emitters was simulated using a bespoke stochastic algorithm programmed in ImageJ. The program generated a two-dimensional random walk over a period of time of 300 seconds using a 100 nm pixel size with an acquisition rate of 10 ms. The algorithm was moreover tested for the correct linear increase in mean square displacement versus time (Appendix VII). The position of each emitter was incremented in a random direction for every time interval τ by a distance randomly sampled from the following probability density [191]

$$P(r,\tau) = \frac{1}{4\pi D_{\mathrm{i}}\tau}\exp\left(-\frac{r^2}{4D_{\mathrm{i}}\tau}\right) \tag{4.23}$$

with D_{i} the diffusion coefficient at the position of the emitter.

The sensitivity of the SOFI algorithm to changes in local diffusion rates was tested by simulating areas where emitters have to adopt different diffusion coefficients. Two regions displaying different diffusion coefficients were placed at different positions

inside the image (D_1 = 0.45 μm^2/s and D_2 = 0.90 μm^2/s) and the resulting stack of frames generated was analysed with the SOFI algorithm.

Figure 4.15 displays the regions with different diffusion coefficients and the image resulting from a second order SOFI analysis. It is clear that the pixels associated with the area of slow diffusion displays bigger intensities than the fast diffusion ones. This result indicates that it is possible to differentiate diffusion dynamics inside a sample using a simple correlation method. It confirms as well that the diffusion of several single diffusing probes during acquisition does not impact greatly the quality of a SOFI super-resolution image [250].

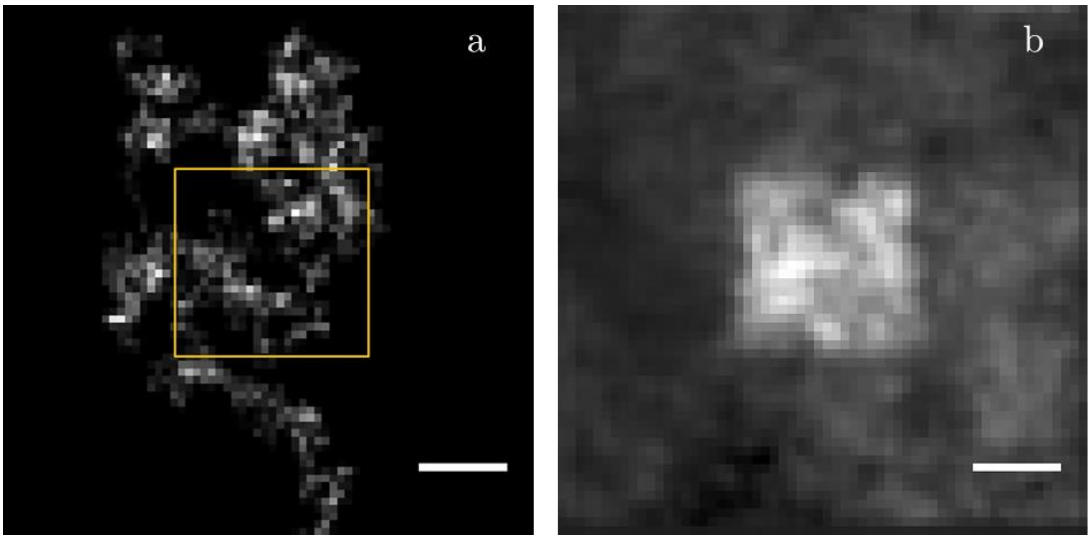

Figure 4.15. Application of SOFI to diffusion-type experiments. a) Projection of the intensity generated by the random walk of a single emitter over time. Pixels inside the yellow frame are associated with a diffusion constant of 0.45 μm^2/s, whereas pixels on the outside represents areas with a diffusion constant of 0.90 μm^2/s. b) SOFI result image of previously described simulation with 500 diffusing emitters. The slow diffusion regions appear brighter than the faster ones in the SOFI image. Scale bar: 1 μm.

ii. Single molecule tracking using SOFI

The SOFI algorithm has been demonstrated to extract trends in diffusion within domains in the field of view, but it is also capable of achieving high level of sensitivity when applied to single particle tracking. Diffusion of three individual QDs in a 80 wt% glycerol-water mixture was recorded for 20000 frames with an acquisition time of 18 ms and the resulting movie analysed using SOFI method. Individual QD trajectories were retrieved using a single particle tracking algorithm (SpotTracker ImageJ plugin [251]) and compared to the average and maximum projections of the original frames stack as well as the order 2 SOFI image (Figure 4.16). It is clear that

details of the different trajectories are lost in the average of the frames, as regions of long residency are the only domains distinguishable above a noisy background. Assigning to each pixel its maximum value in the stack allows one to retrieve more details on each QD's path, despite the noise present in the image. However, this method does not provide information on the average time spent by a molecule in a region associated to a given pixel. Due to the very nature of the maximum projection, a pixel will take the PSF intensity maximum value, whether the molecule stays inside the region represented by the pixel for a period of 1 or n frames. On the contrary, SOFI image displays contributions of individual emitters weighted to their average residency inside a single pixel. The noise reduction induced by the SOFI analysis further provides an additional contrast in the direct display of single molecule trajectories that is not achieved by stack projections. Single pixel temporal correlations can therefore be used to complement existing single molecule tracking algorithms to retrieve trajectories of diffusing probes and identify local diffusion anomalies.

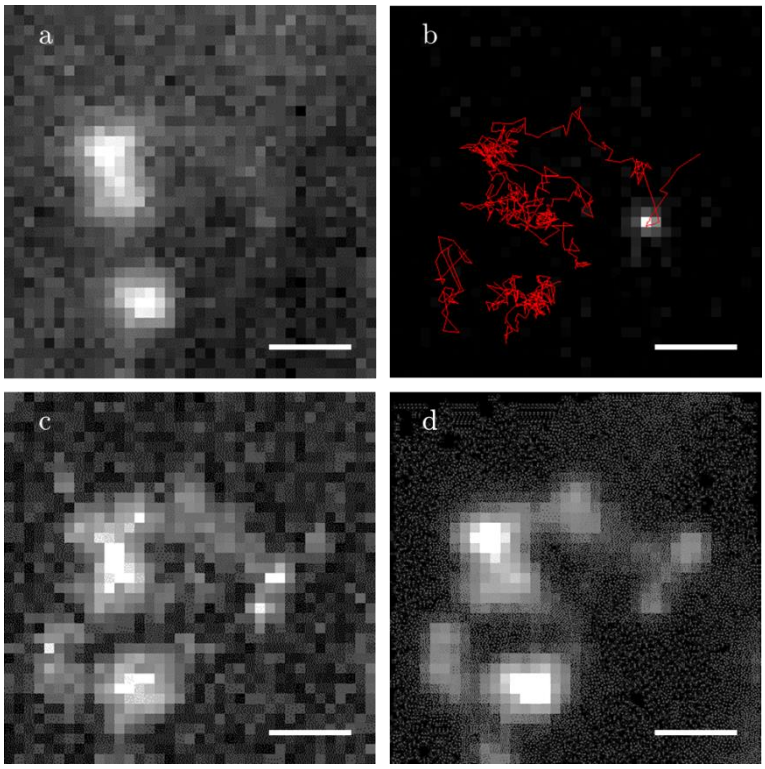

Figure 4.16. Single molecule tracking using SOFI algorithm. a) Average projection of the original dataset. b) Plot of the associated single QD trajectories using a single particle tracking algorithm. c) Maximum projection of the original dataset. d) Order 2 SOFI image. The SOFI image reflects the average time spent by QDs in domains represented by a single pixel. The noise reduction induced by the correlation analysis provides a better visualisation of fast single molecule trajectories compared to stack projections. Scale bar: 5 µm.

4.6 SOFI Refinements and Derivatives

The SOFI method has been improved in numerous adaptations following the first demonstration of the concept. The use of a Fourier reweighting scheme has allowed improved resolution by a narrowing of the PSF that scales with the order of the SOFI correlation instead of its square root [252]. In addition, subpixel information can be obtained by the analysis of cross-correlations between the fluorescence intensities of neighbouring pixels, which has been used in applications with organic dyes [232]. The method has been compared with STORM, showing comparable resolution performances [253]. However, SOFI has been demonstrated to tolerate lower SNRs and does not require any previous characterisation of the photoswitching kinetics and labelling densities. The main drawback for achieving accurate localisation of single emitters in this case is the effect of brightness scaling (with both signal persistence and intensity) as previously described.

A refinement of the SOFI algorithm called balanced-SOFI has been proposed to solve this problem: the cumulant orders are analysed to retrieve several parameters such as concentrations, brightness, molecular-state lifetimes and blinking statistics [254]. Those values are then used to weight the intensities of the different emitters in the final images.

Several investigations have focused on developing emitters with enhanced blinking properties in order to obtain superior results with SOFI. Variance Imaging for Superresolution technique attempts to develop a highly fluctuating CdSe/ZnS core-shell QD nanoprobe by decreasing the thickness of the ZnS shell that normally acts to prevent core-electron loss and interactions between the core and oxygen contained in the aqueous solvent that lead to blinking. This change of QD increases the blinking fluctuation, resulting in a better temporal resolution [255].

The same concept of improving the emission characteristics has been used on organic fluorophores and more precisely on the Dronpa fluorescent protein, a photoswitchable dye usually used in PALM/STORM experiments [250]. This technique called photochromic SOFI (pcSOFI) makes use of an interesting property of the Dronpa dye. In a typical PALM/STORM experiment, a Dronpa labelled sample is cyclically excited at 515 nm until the emission stops and then reactivated using a 405 nm laser. However, the emission of Dronpa does not disappear completely when excited at 488 nm but reaches a low intensity plateau where highly dynamic activation/deactivation processes take place for long temporal periods, typically several minutes [256]. This behaviour has not been fully explained yet but might be

caused by a balancing between the “on” and “off” switching of the dye [257] or a more complex phenomenon involving the protonated and deprotonated forms of the fluorophore [258]. The enhancement of the Dronpa flickering provides a dynamic system of choice for a temporal analysis of fluorescence fluctuation and leads to a better resolution with SOFI analysis. The pcSOFI technique therefore reduces the number of frames required to achieve super-resolution and could be efficiently used for the observation of biological systems where photobleaching is the main factor hindering the conventional SOFI algorithm results.

Chapter 5

Direct Object Resolution by Image Subtraction

The scale range of distances between constituents of biological systems is often below the minimum resolution attainable with SOFI (40-60 nm) or PALM (25-60 nm). Most of the techniques capable of localising such small features exploit a fluorescent probe's photophysical properties to image individual emitters.

A method we named DORIS (Direct Object Resolution by Image Subtraction) is presented in the following chapter as a novel way of identifying diffraction-limited spots corresponding to multiple closely spaced emitters, without the need of complicated optics or potentially time consuming PSF fitting processes [259]. This technique is based on the analysis of small but finite differences between images over time, revealing both the separation and relative orientations of closely spaced individual emitters contributing to an otherwise apparently singular PSF.

A coupled QD system was used as a reference point source and investigated using the DORIS method. Sequential subtractions between QD images proved that monomeric and dimeric states could be readily distinguished, as well as emission states of more highly complexed emitters. A linear relationship between the central gradient in the difference-images and the distance between PSFs centres was also demonstrated and used to directly determinate the QD separation without the need for the individual PSF fitting process associated with conventional localisation microscopies.

5.1 DORIS Principle

The main concept of DORIS relies on the subtraction between temporally separated PSF images. The difference-images can be generated in many ways that are discussed in detail below (Section 5.3.1).

To introduce the technique, let us consider the simplest case of two emitters displaying intermittency in emission and localised at a distance significantly inferior to the Rayleigh limit. Below a certain distance the emitters PSFs overlap significantly and the resulting emission appears to arise from a single point source. However, the subtraction between the two normalised PSFs results in a curve whose maximum and minimum values are not associated with the original coordinates of the Gaussian centres but with coordinates that are more separated and therefore clearly distinguishable (Figure 5.1).

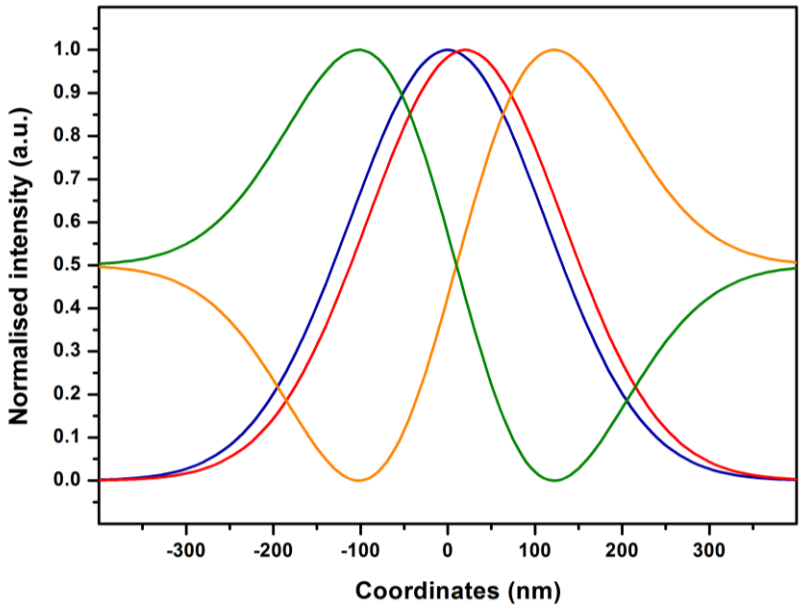

Figure 5.1. Spatial separation highlighted by DORIS technique. Two normalised PSFs separated by 20 nm (blue and red) are subtracted, leading to curves displaying comparatively large differences between minimum and maximum localisation (green and orange).

The amplitude of the curve, representing the difference between its maximum and minimum values, increases with separation, as can be seen in Figure 5.2.a. On the other hand, the positions of the maximum and minimum are not very sensitive to PSF displacement. The 2D images of closely located PSFs are largely indistinguishable from the image of a single PSF, whereas a subtraction process reveals a "dipole pattern" analogous to the 1D cross-section (Figure 5.2.e).

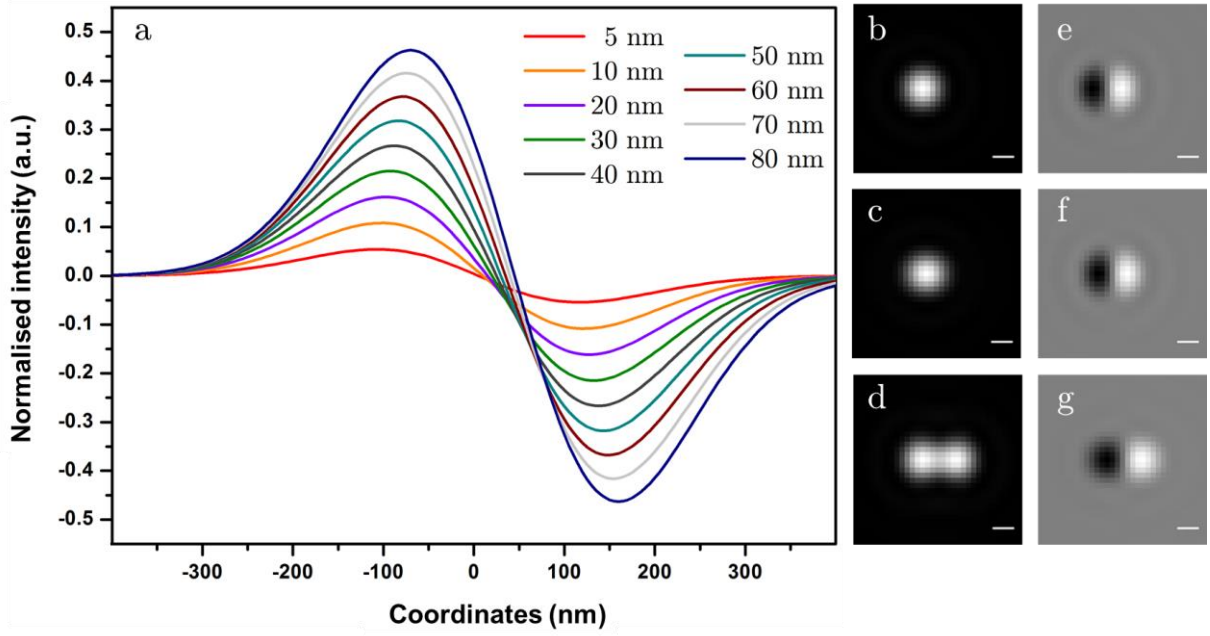

Figure 5.2. Subtracted image amplitude dependency to original PSFs separation. Left-a) 1D evolution of the subtracted curve amplitude with separation distance varied from 5 to 80 nm (red-blue). Right- 2D image simulations of two emitters separated by b) 5 nm, c) 100 nm and d) the Rayleigh diffraction limit. Also shown are the corresponding difference-images between individual PSFs. In 2D, the characteristic lobe structure is due to the localisation of the maximum and minimum intensities on distinct pixels. Scale bar: 200 nm.

The information obtained from the difference-image can be used in a post-acquisition data analysis as a quick and straightforward way to identify diffraction-limited spots arising from two closely spaced emitters during a time-lapse sequence. The subtraction of a frame corresponding to the case where one of the two emitters is switched on from a frame where the other one is emitting leads to the apparition of the dipole pattern, enabling one to determine which emitter is switched on and its relative position compared to the other. An optional fitting process on the resulting frame may be performed to determine more precisely the emitter localisation.

5.2 Difference Amplitude vs Distance Sensitivity

It has been previously seen that the amplitude in the curve resulting from the subtraction of the 1D PSFs increases with the separation (Figure 5.2). Here this dependency has been investigated using 2D simulations of the PSFs, as displayed in Figure 5.3. PSFs were simulated in two dimensions, as described in Appendix VIII, and the DORIS method applied to resulting images. The difference between maximum and minimum intensity pixels was measured for different separation orientations to test for any pixilation effects, particularly with a diagonal

displacement. Amplitudes appear consistent over a large range of distances for all orientations, deviating at most by about 10% at larger displacements toward 100 nm. However, "averaging" of the maximum and minimum values due to pixilation did not introduce a significant difference between amplitude curves at low to moderate displacements, as the pixel size is fixed and the absolute values of the maximum and the minimum values of a given curve are equal.

The near-linear relationship between the amplitude and the PSFs displacement therefore provides a direct and convenient measurement of the separation between emitters, which was tested experimentally in the following section.

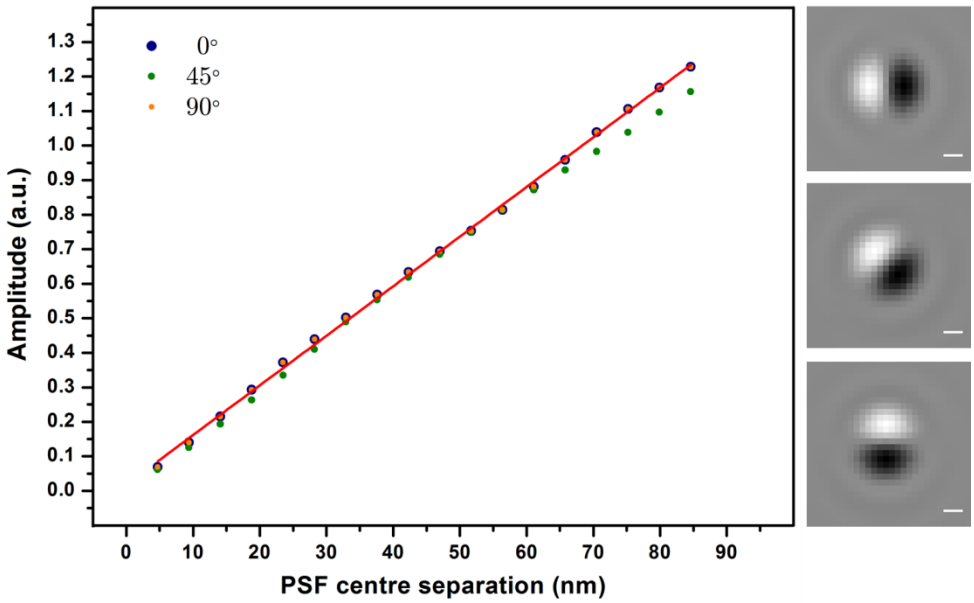

Figure 5.3. Dependency of DORIS amplitude on PSF separation and orientation. DORIS amplitude-to-separation conversion curves for different orientations of emitters are displayed. The amplitude values were obtained by sequential displacements of one simulated PSF relatively to the other along the respective directions considered. The linear fit associated with a 0° lateral displacement is plotted in red. Resulting difference-images for 0°, 45° and 90° displacements are displayed on the right. Small discrepancies between amplitudes arise for a diagonal displacement due to finite image pixilation but are negligible for small separations. Scale bar: 200 nm.

5.3 Length Determination of 100 bp ds DNA

DORIS was realised experimentally by exploiting the linear dependency of the difference-amplitude in order to measure end-to-end distances of a 100 bp ds DNA coupled at both ends with bioconjugated QDs. The aim here was to compare the efficiency of using the DORIS amplitude as a reporter of intermolecular distance with the traditional Gaussian fitting methodology.

5.3.1 DORIS Analysis Method

i. Generation of difference-images datasets

The simplest approach of analysing an image stack of n frames $A = \{1, \dots, n\}$ is to generate the full set of difference-images $B = \{1,2, \dots, n(n-1)/2\}$, given by $(A_i - A_j)$ for all $(i \geq 1)$ and $(j > i)$. In this case, for two coupled QDs independently switching between on and off-states, difference-images of frames with QDs in on/off **[10]** and off/on **[01]**, combinations will give rise to differential structure **[1-1]** and **[-11]** with amplitudes between maxima and minima that are dependent on both QD separation and relative intensities. Here a binary notation has been introduced, representing the state of each QD in an image or frame, symbolised by square brackets [ ], and the result of subtraction.

Normalising QD peaks in each image prior to subtraction removes the intensity dependence. An important consideration is that amplitudes derived from subtracting frames with only one QD on **[01]** from those with both QDs on **[11]** will have a different dependency on PSF separation: that is a different amplitude-to-distance conversion curve. Nonetheless, difference-images displaying dipole-like features directly identify dimeric QD structures that would otherwise appear as singular diffraction-limited spots in the image stack.

This full calculation method might become time and computer consuming for large datasets, but ensure that all information on emitter configuration is retained, especially in the case where emitters do not display clear binary switches between fluorescent states over time. An alternative DORIS calculation based on applying a tailored intensity threshold was retained to investigate discrete fluorescence states of QDs and reduce computing times to isolate coupled QDs candidates.

ii. Application of intensity thresholding

QDs offer superior quantum yields and photostability such that coupled QDs display discrete, quantised levels of fluorescence for one or more emitters, which can be readily observed during an imaging experiment (Figure 5.4.a) and used to correlate the DORIS difference-images with different emission states. Typical coupled QDs intensity profiles show three populations corresponding to the three observable states of the system (0, 1 or 2 QDs in the “on” state).

Fitting of the intensity histogram (Figure 5.4.b) by a sum of two Gaussian functions gives for each peak a mean value of integrated intensity J_i and a standard deviation σ_i. A simple intensity threshold at a value of $(J = J_1 \pm 1.64\,\sigma_1)$, with J_1 being the mean value of intensity of a single QD and σ_1 its distribution width, was applied to retain frames corresponding to **[01]** and **[10]** situations. Similarly frames corresponding to both QDs in the "on" state were retained by applying a threshold at $(J = J_2 \pm 1.64\,\sigma_2)$. The two datasets were normalised and frames **[10]** and **[01]** were subtracted from frames **[11]** to produce the characteristic lobe structure, the orientation and phase of which indicated the QD that was switched on in the original frame from the combined set of single QDs.

Moreover, it is important to note that the resolution of a dipole-like structure in the difference-images allows the unambiguous identification of closely spaced fluorophores that may not be readily assigned through a visual inspection for any frame-to-frame PSF displacement. Indeed PSF localisation by Gaussian fitting may not be sufficient to uniquely identify the individual fluorophores if the separation falls within the localisation uncertainty.

Following individual QD identification, a simple ImageJ macro was used to separate subtracted frames depending on lobe positions and group together frames corresponding to the same QD in the "on" state (**[10]** or **[01]**).

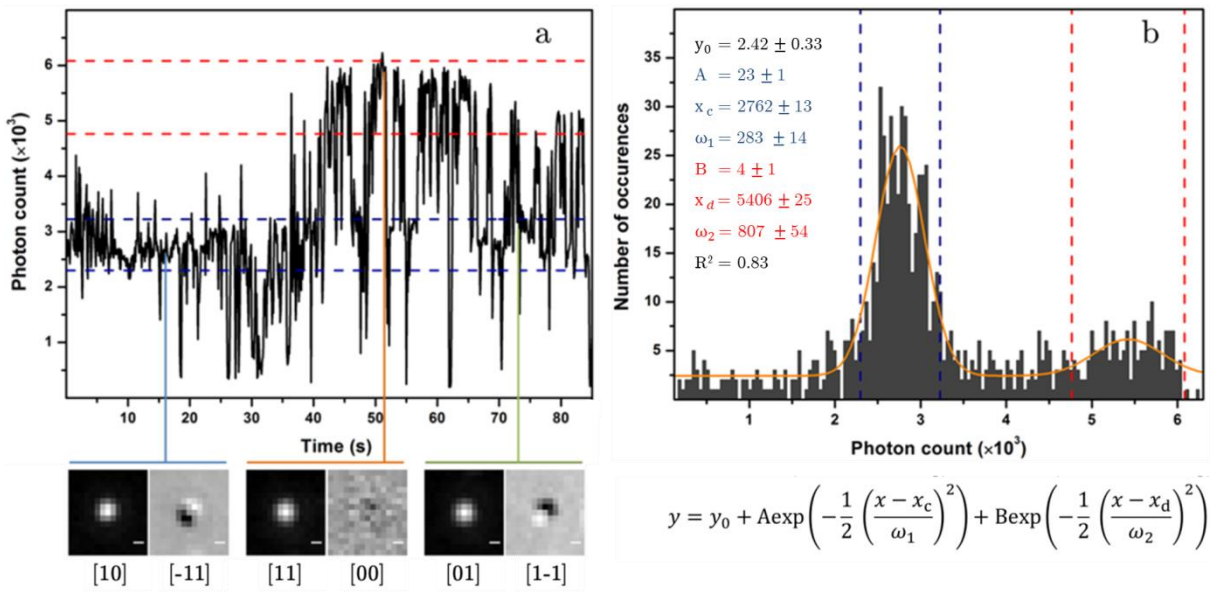

Figure 5.4. Intensity fluctuation of coupled QDs. a) Intensity profile of two coupled QDs and difference-images corresponding to the various configurations possible for a system composed of two emitters. b) Corresponding histogram with double Gaussian fitting parameters and associated thresholds retained, blue for (**[10]** and **[01]**) and red for (**[11]**). Scale bar: 200 nm.

The DORIS method was applied to determine the separation between streptavidin functionalised QDs conjugated at both ends of a 100 bp ds DNA construct by biotinylation. It was used along with intensities in the fluorescence trajectory to identify coupled QDs and to isolate the subset of difference-images that correspond to single emitters in the switched "on" state. A subsequent conventional Gaussian fitting process was used to determine the absolute position of emitters within the normal uncertainty limits associated with noise [148]. The linear dependency of the amplitudes in difference-images to PSFs separation was then exploited in order to determine the inter-QD distances and compare results with those derived from individual QDs localisation.

5.3.2 Localisation of QD Positions with DORIS

The intensity fluctuations of thirty coupled QDs were recorded over time and analysed with the DORIS algorithm. Figure 5.5 displays the resulting difference-images that clearly emphasise the presence of two emitters in close proximity. The images displaying a lobe structure characteristic of coupled QDs were retained and used to retrieve the associated emitter PSF in the original dataset. These frames were further investigated using a Gaussian fitting process in order to find the positions of the respective QDs (Figure 5.5). It is apparent that the relative orientation of closely spaced emitters with respect to each other is displayed in the corresponding difference-images via the lobe orientation in the dipole pattern.

The distance between QDs coupled with a DNA construct was determined to be 50.0 ± 5.8 nm using successive Gaussian fits of the single PSFs (Figure 5.5.a). This separation is close to the theoretical length of an extended 100 bp DNA (~ 34 nm) with an added separation due to the QD diameter, which has previously been determined to be around 20 nm for QDs emitting at 585 nm [260].

An additional population of coupled QDs with a shorter distance of separation than the minimum expected for a 100 bp DNA was found in the dataset (Figure 5.5.b). This is consistent with the work of Thomson *et al.* who reported the presence of a population of coupled QDs in the absence of any DNA linker. The additional distance between coupled QDs was determined to be 19 ± 13 nm, compared to a DNA separated QDs distance of 48 ± 9 nm in their system [164]. This shorter distance between emitters was attributed to an aggregation process, causing a direct and non-specific coupling between QDs which was further investigated in Section 5.3.4.

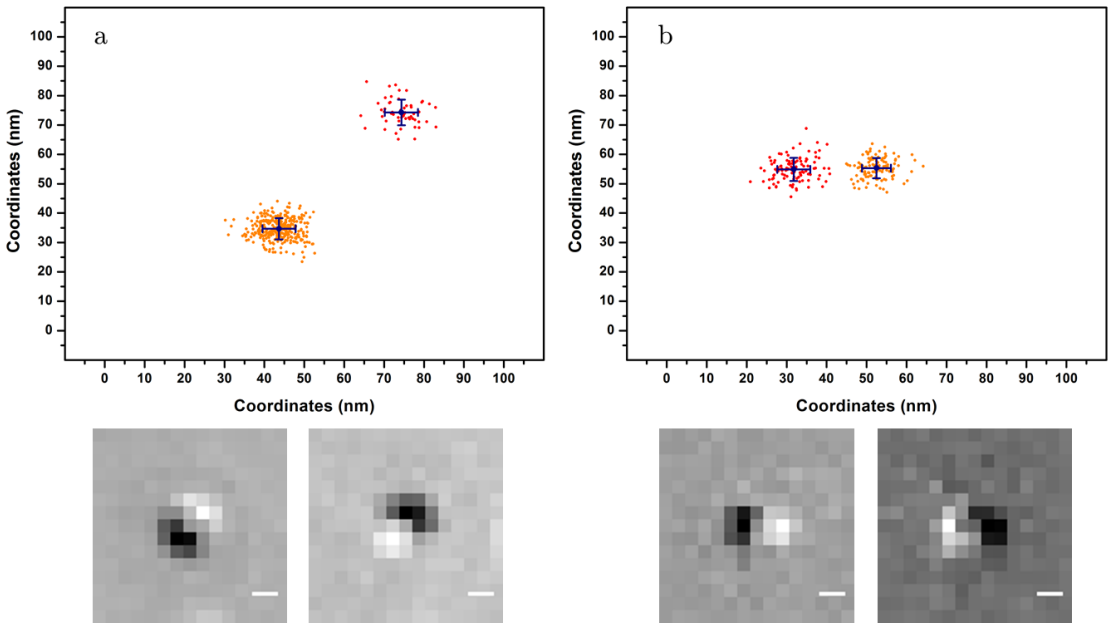

Figure 5.5. Coupled QDs centroid positions and associated difference-images. a) Distance between QDs was found to be 50.0 ± 5.8 nm for DNA-coupled QDs. b) Separation between directly coupled QDs was determined to be 20.7 ± 5.5 nm using a Gaussian fitting process. Corresponding difference-images [1-1] and [-11] are displayed below fitting results and show a lobe orientation in agreement with the Gaussian fitting procedure. Scale bar: 200 nm.

5.3.3 Calibration Curve Method for Distance Measurements

i. Principle

Beyond the identification of multiple close-coupled fluorophores, the DORIS method may be used as a straightforward way to measure QD separation without resorting to fitting procedures. The general concept is to build a calibration curve of the amplitude observed in the difference-images for different emitter separations. To investigate the effectiveness of DORIS in nanometric measurements, an ImageJ-only algorithm that does not require any Gaussian fitting process has been developed and used on the coupled QDs dataset studied in the previous section.

In order to build the calibration curve, the normalised average projection of the **[10]** sub-stack frames (or **[01]** frames) was sequentially translated at different subpixel distances with respect to the original position. A bicubic interpolation was used to ensure that the individual PSF interpolated surface matched at boundaries between pixels with continuous first derivatives [109]. After each displacement, the translated frame was subtracted from the original one, leading to the expected lobe structure. The maxima and minima values of the difference-images were retrieved from the

average intensity of a 2×2 array of pixels placed at the centre of each respective lobe. The maximum amplitude difference between the lobe with positive intensity and the lobe with negative intensity was determined for each displacement and used to build a calibration curve similar to the one displayed in Figure 5.3.

Uncertainty in distance localisation was determined by i) subtracting randomly paired frames from [10] and [01] datasets; ii) taking the difference-amplitude between lobes for each pair of frames; iii) retrieving the associated QD separations using the calibration curve and iv) fitting the histogram of distances with a normal distribution (Figure 5.6).

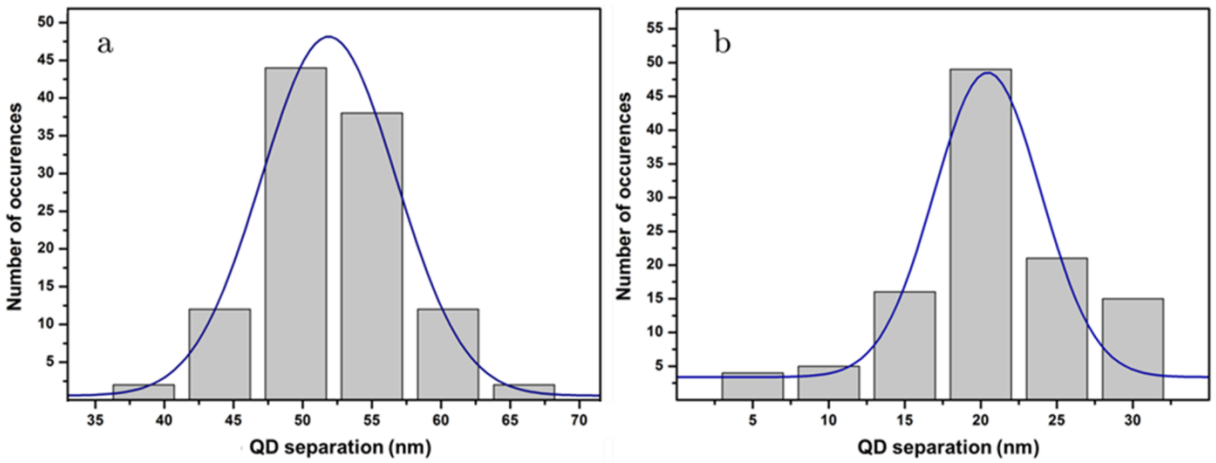

Figure 5.6. Normal distribution fitting of distance histograms for the coupled QDs displayed in Figure 5.5. a) Histogram of DNA-coupled QDs. b) Histogram of directly coupled QDs. The value determined with the calibration curve approach was 52.6 ± 5.9 nm for QDs coupled with the DNA construct and 20.4 ± 6.2 nm for directly coupled QDs, in accordance with values previously determined with the individual emitters localisation approach.

ii. Effect of SNR on technique accuracy

The influence of noise on the DORIS method was investigated by simulating two emitters separated by 5, 20, 50 and 80 nm for different values of SNR. Amplitudes and associated standard deviations from a sample of 100 simulations are plotted as a function of SNR in Figure 5.7. The uncertainty in the amplitude is large for low SNR values, but it is also a function of SNR, scaling as $1/\sqrt{N}$ to the noise-free amplitude with increasing SNR. Convergence to the respective noise-free amplitudes for all distances occurs at SNRs > 100 and for 20 nm or more at SNRs > 30 or about 1000 photons. At signals greater than this, the uncertainty in amplitude is less than 10% at 20 nm separation, corresponding to an error inferior to 5 nm in the DORIS amplitude-to-separation conversion. While photon counts at this level may be

difficult to attain with conventional fluorophores without significant signal integration over long exposures, detection rates in the 10^4 - 10^5 Hz range are readily achieved with QDs due to their large absorption cross sections and high quantum yield.

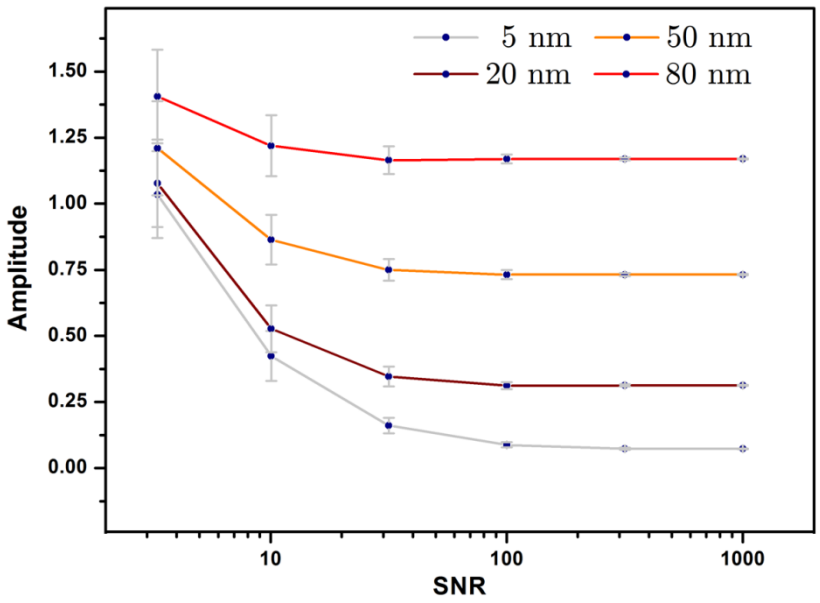

Figure 5.7. Dependence of DORIS amplitudes on SNR in the shot noise limit for different QD separations. The amplitude decreases as the inverse of the shot noise or $1/\sqrt{N}$, where N is the photon count, reaching noise-free limits at signals around 1000 counts for QD separations ≥ 20 nm.

5.3.4 Measurement of Coupled QDs Distances

i. Measurement of the separation between directly coupled QDs

The distance between directly coupled QDs was first determined experimentally on a sample of ten paired QDs in the absence of DNA linker. The normal fit of the resulting distances histogram of paired QDs gives a value of 22.6 ± 6.4 nm, in accordance with the diameter of a single QD determined by Transmission Electron Microscopy (TEM) (Figure 5.8), and previous studies of streptavidin functionalised QDs emitting at 585 nm [260]. The value was used to initialise the parameter corresponding to the distance between directly coupled QDs population for the fitting process described in the following section.

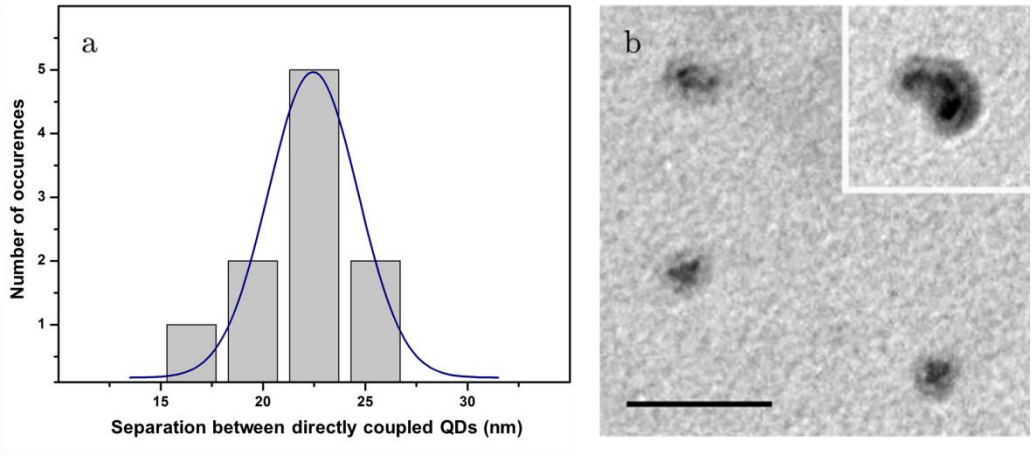

Figure 5.8. Individual QD diameter determination. a) Coupled QDs separation distances in the absence of DNA linker, determined to be 22.6 ± 6.4 nm by fitting process. b) TEM image of individual 585 nm streptavidin functionalised QDs with average core-shell diameter of 23.0 ± 4 nm and (inset) a non-specifically coupled cluster of three QDs showing that distance between centres is not strongly influenced by surface functionality. Scale bar: 100 nm.

ii. Comparison between DORIS and Gaussian fitting method

Thirty coupled QDs intensity traces over time were recorded and used to retrieve individual emitter positions with the conventional Gaussian fitting method. The DORIS calibration curve approach was then used on the same dataset and the respective histograms of distances were compared, with mean QD distances and variances derived from a fit of two normal distributions (Figure 5.9).

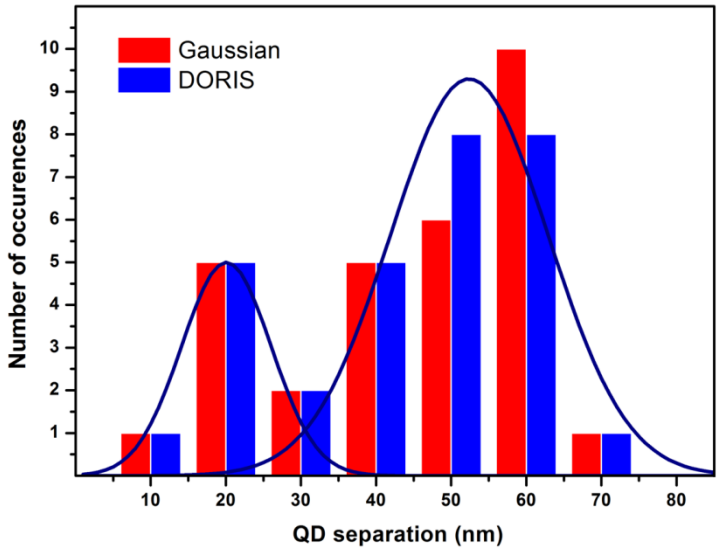

Figure 5.9. Distance histograms obtained with DORIS and Gaussian fits. Histograms (bin size: 10 nm) of calculated distances between coupled QDs were obtained with a conventional Gaussian fitting method and with the DORIS calibration curve approach. Associated normal curve (a two peak fit for DORIS data only is shown for clarity) gives comparable distance values for the different subpopulations using the two different techniques (Table 4).

Comparable results were obtained for both techniques, regardless of the magnitude of the QD separation (Table 4). A near one-to-one correspondence between the independently derived distances supports the quantitative nature of DORIS as an alternative method of determining the separation of emitters in sub-diffraction sized structures (Figure 5.10).

	Gaussian Fitting Method	Calibration Curve Method
DNA Coupled QDs	54.8 ± 11.4 nm	52.4 ± 10.9 nm
Directly Coupled QDs	20.3 ± 7.6 nm	20.1 ± 5.9 nm

Table 4. Results comparison between DORIS and Gaussian fitting method, obtained from the fit of two normal distributions displayed in Figure 5.9.

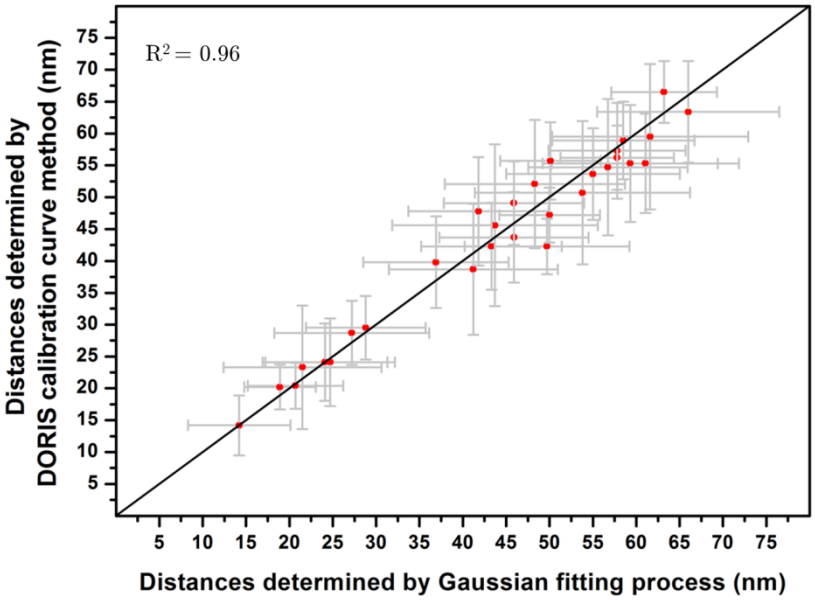

Figure 5.10. Comparison between DORIS method and Gaussian fitting technique. Uncertainties in both measurements were determined from analysis of multiple frames from the image stack of each QDs dimer. A straight line representing the one-to-one correspondence is plotted for guidance.

5.4 Resolution of Multiple Close Emitters

DORIS method was applied to three closely spaced QDs to test its effectiveness in resolving higher order structures and multimeric complexes. Given the tetravalent nature of streptavidin proteins that extends over the entire surface of the QD, multiple DNA binding and formation of complexed QDs is expected. Intensity profiles were analysed and a QD complex displaying four different characteristic intensity levels, indicating the presence of three QDs in close proximity, was retained for analysis (Figure 5.11).

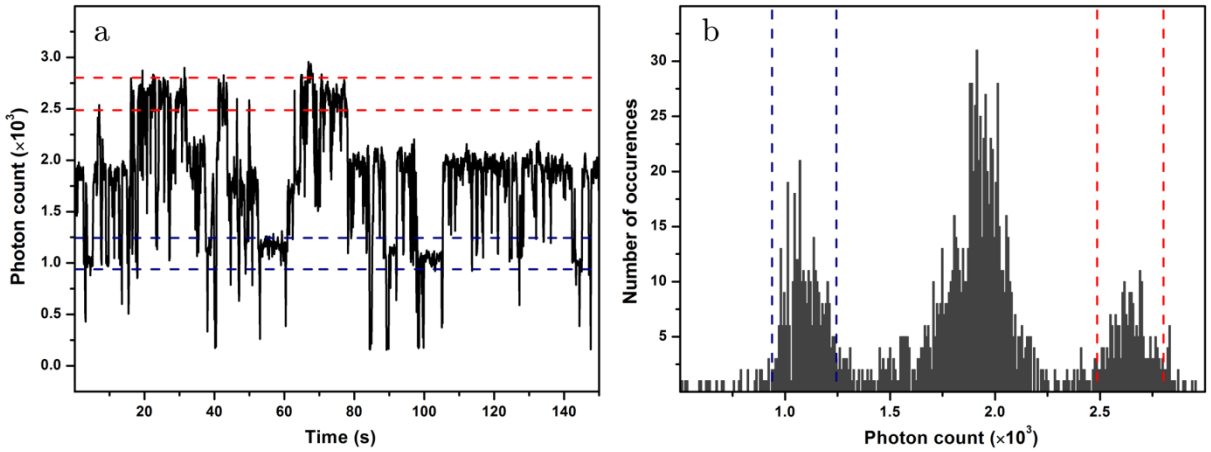

Figure 5.11. Intensity fluctuation of QD complexes. a) Intensity profile of three closely spaced QDs, displaying four levels of emission intensities. b) Histogram of integrated intensities with characteristic thresholds applied (dotted lines).

Figure 5.12 presents a plot of the single molecule localisations arising from an image stack of strongly fluctuating QDs, along with distance measurements derived from a DORIS analysis of the set of difference-images. Figure 5.12 demonstrates the clear resolution of the three emitting centres obtained through application of DORIS to this QDs multimer, with oriented dipole-like structures clearly distinguishable in the difference-images. Respective QD separations determined from amplitudes in the difference-image, 65.4 ± 8.1 nm, 26.5 ± 10.3 nm and 74.6 ± 11.4 nm, are in agreement with the corresponding vectorial distances between centres obtained using an individual localisation approach, 63.0 ± 8.4 nm, 30.6 ± 10.7 nm and 73.2 ± 9.2 nm.

It is interesting to note that one might link these results to the population study carried out in Figure 5.9. It appears that this aggregate of QDs is formed from two DNA-coupled QDs in which one of the QD is part of a directly coupled QDs pair.

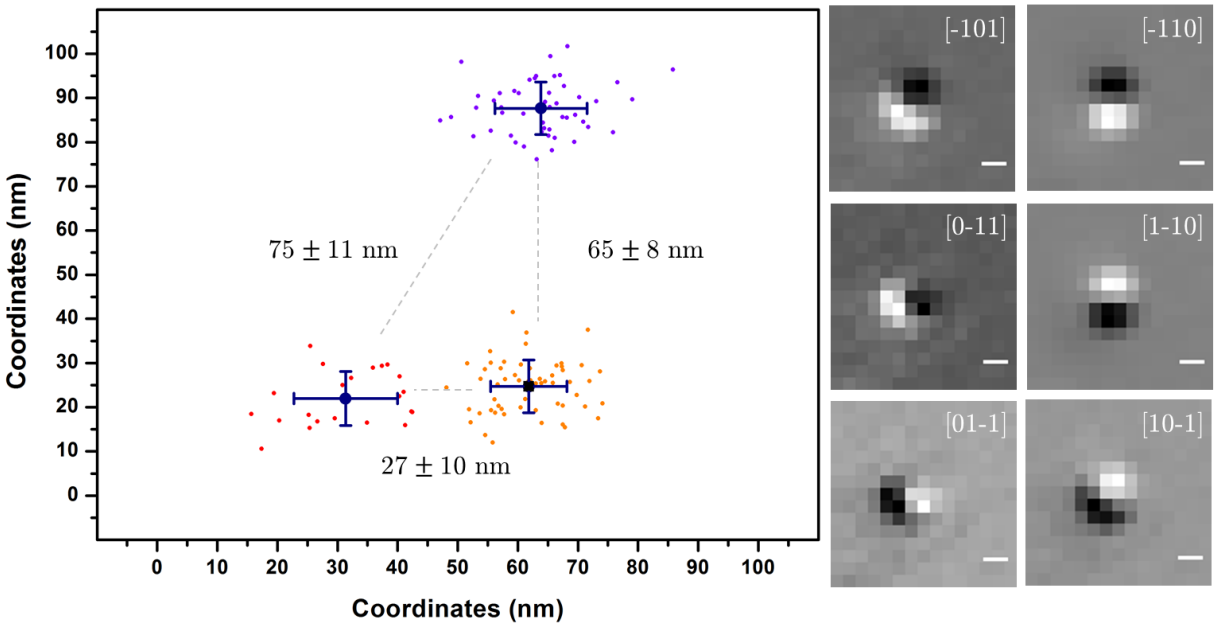

Figure 5.12. Mapping of individual emitters constituting a trimeric complex. Left) Single QDs localisations via Gaussian fitting of individual PSFs with distances determined from a DORIS analysis of amplitudes of the set of difference-images. DORIS derived distances correspond closely to the centre-of-mass separations obtained from the individual QD localisations 65 ± 8 nm (purple-orange), 27 ± 10 nm (orange-red) and 75 ± 11 nm (red-purple). Right) Associated difference-images obtained by respective subtraction between individual emitters. Scale bar: 200 nm.

5.5 Direct Difference-Images Fit in ImageJ

A more direct way of retrieving the separation between emitters is to fit the difference-images with a model including the subtraction between two Gaussian functions. The number of parameters associated might seem too large to obtain accurate results, but the DORIS principle leads to a reduction of variables in the fitting expression: the normalisation process applied to the PSFs inherently removes the dependency on the respective Gaussian amplitudes, which are simply set to unity in the model. The number of independent parameters in the difference-Gaussian fit is therefore reduced to only five parameters, the centroid coordinates $(x,\ y)$ and a single PSF width ω, assuming the emission wavelengths are similar. This fitting process has been implemented in ImageJ, using the built-in "CurveFitting" tool incorporated in bespoke macro (Appendix IX).

It was necessary to transform the three-dimensional dataset of the image, consisting of the coordinates (x,y) and the intensity (z), into a two-dimensional form required to use the ImageJ fitting routine algorithm. This conversion was simply

achieved by transforming the matrix $A_{i,j}$ associated with the difference-image into a line vector $B_{1,j}$ using the transformation shown in Figure 5.13.

$$\begin{pmatrix} a_{1,1} & \cdots & a_{1,j} \\ \vdots & \ddots & \vdots \\ a_{i,1} & \cdots & a_{i,j} \end{pmatrix} \rightarrow \left(a_{1,1}, \ldots, a_{1,j}, a_{2,1}, \ldots, a_{2,j}, \ldots, a_{i,1}, \ldots, a_{i,j}\right)$$

Figure 5.13. Transformation of a difference-image into a one-dimensional array for simple fitting using the ImageJ "Curve Fitting" tool. A representative 1D transformation of the 2D difference-image of two closely spaced emitters (top) and the corresponding geometric transformation (bottom) applied in the macro displayed in Appendix IX.

The intensity values stacked into a linear array can then be fitted by adjusting the mathematical expression for the fitting function to the geometrical modification induced by the matrix conversion. In this case, the expression with three unknowns can be written as a function of the PSF central coordinates $(x_1,\ y_1)$ and $(x_2,\ y_2)$ and the PSF widths ω_1 and ω_2 (considered as equal):

$$z = \exp\left(-\frac{1}{2}\left(\frac{x-x_1}{\omega_1}\right)^2 - \frac{1}{2}\left(\frac{y-y_1}{\omega_2}\right)^2\right) - \exp\left(-\frac{1}{2}\left(\frac{x-x_2}{\omega_1}\right)^2 - \frac{1}{2}\left(\frac{y-y_2}{\omega_2}\right)^2\right) \qquad (5.1)$$

A change of variables enables the adaptation of this expression to accommodate the geometric transformation. The lateral position $u[n]$ in an array of b pixels was linked to the pixel array intensity $v(u[n])$ using the following formula:

$$v = \exp\left(-\frac{1}{2}\left(\frac{u'-x_1}{\omega_1}\right)^2 - \frac{1}{2}\left(\frac{u''-y_1}{\omega_2}\right)^2\right) - \exp\left(-\frac{1}{2}\left(\frac{u'-x_2}{\omega_1}\right)^2 - \frac{1}{2}\left(\frac{u''-y_2}{\omega_2}\right)^2\right) \qquad (5.2)$$

with

$$u' = u - \left(\frac{u}{b} - \frac{1}{2}\right) \times b \qquad u'' = \left(\frac{u}{b} - \frac{1}{2}\right)$$

The routine fitting process that has been implemented in ImageJ has been compared to the conventional 2D fitting process in Origin 8.0 software for a pair of directly coupled QDs (Figure 5.14). Similar separation values were determined with the two methods, which validated the fitting model.

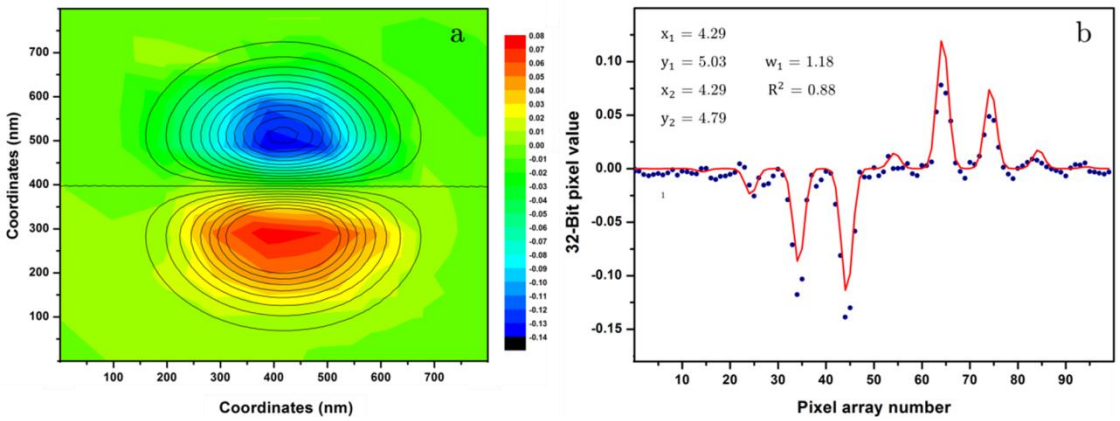

Figure 5.14. Comparison between difference-images fitting processes. a) Multiparameter fitting process in Origin 8.0 software using Equation (5.1). b) Fitting procedure on the linearised image using Equation (5.2) and the "CurveFitting" tool in ImageJ. The fitting parameters are displayed in pixel unit for consistency (pixel size 97 nm). The 23.3 nm separation between PSF centres obtained with a Levenberg-Marquardt algorithm is fully consistent with the result given by the ImageJ algorithm (23.5 nm).

The fitting routine has been applied to the dataset of coupled QDs previously studied in Section 5.3.4. The average of frames displaying QDs in [01] and [10] conformations were subtracted and the resulting difference-image fitted. Results of the fit were compared to single PSF Gaussian fitting and displayed in Figure 5.15. Good correlation is observed between emitter separations determined by both fitting methods, with typically less than 5% difference between values for a SNR > 30. It is noted, however, that convergence of the ImageJ fitting was found to be sensitive to high noise and initialisation of parameters.

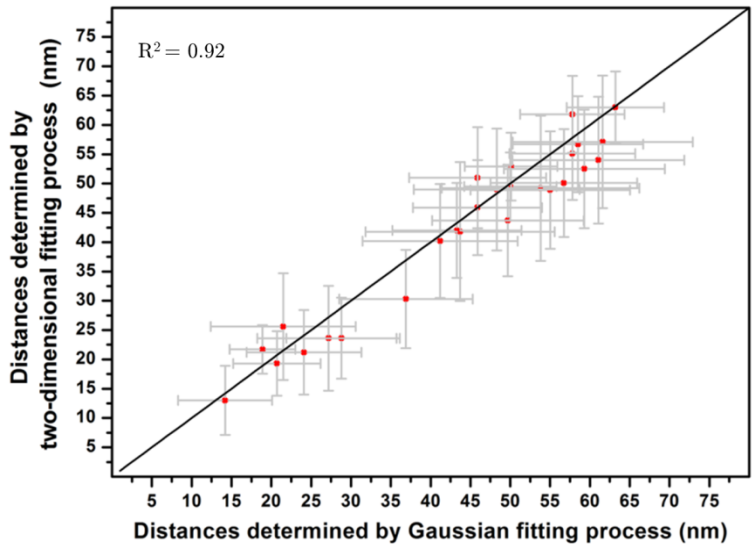

Figure 5.15. Comparison between Gaussian and linearised image fits. A one-to-one correspondence curve (black) is displayed for guidance. The distance separations determined by a 2D Gaussian fitting in Origin and an ImageJ fitting process after matrix conversion are in agreement, validating the fitting method.

5.6 Application of DORIS to Fluctuating Dyes

In principle, the DORIS approach that relies on the subtraction between frames does not require a binary fluorescence emission to reveal information on an emitter location and orientation within a complex. It was speculated that a large variation in the emission intensity between multiple closely spaced emitters would result in the lobe structure previously described in the case of binary switching in QDs, provided the respective contribution of each emitter was highly dynamic and uncorrelated over time.

Simulations of two fluorophores separated by 50 nm undergoing random and independent fluorescence fluctuations were generated to investigate the effect of respective amplitude of fluctuation on objects resolution. The amplitude in the fluorescence fluctuation was controlled by the standard deviation of the normal distribution from which the intensity of each emitter was independently sampled over time. Generated image sets were then summed by randomly pairing independent emitter images to form a dimer set. The stack of frames was analysed by DORIS to obtain mean intensity-amplitudes from the set of difference-images for a large range of modulation-depths in the fluorescence.

The DORIS amplitude obtained for each magnitude of fluctuation is displayed in Figure 5.16. The difference-amplitude is observed to increase with modulation depth and saturates at the limiting value for binary on-off blinking (~ 0.74 for a 50 nm separation distance) as the amplitude of fluctuation approaches several multiples of the mean intensity. At increasing amplitudes, the fraction of fluctuations leading to the complete suppression of fluorescence is consistent with DORIS-amplitudes derived from analogue binary cases. The fluorescence trajectories for two molecules undergoing intensity fluctuations with a standard deviation of 300 ADU counts about a peak mean of 1000 counts is presented in the inset of Figure 5.16, along with the trajectory of the dimer. Also displayed are two difference-images that show resolution of the two fluorophores despite incomplete suppression of fluorescence from either emitter. Importantly, the presence of two fluorophores in the simulation is not evident in the combined fluorescence intensity trajectory of the dimer.

Evidently, direct distance measurement by DORIS may not be permitted at low fluctuation-amplitudes or at best be subject to recalibration of the amplitude-to-separation conversion curve and large uncertainties. Nonetheless the power of DORIS here is to provide an alternative route to the super-resolution of multimeric structures, where flickering in the fluorophore fluorescence prohibits unambiguous

resolution by standard localisation methods or identification of multiple fluorophores by simple analysis of the intensity trajectory. DORIS performance might therefore be increased by tailoring the flickering behaviour of organic dyes and fluorescent proteins [233, 250] which, unlike QDs, do not display discrete fluorescent emission states. Moreover, the recent discovery of bright photoactivatable fluorophores with emission rates of 10^4-10^6 photons per molecule [261] opens the potential for a new range of DORIS applications using organic dyes.

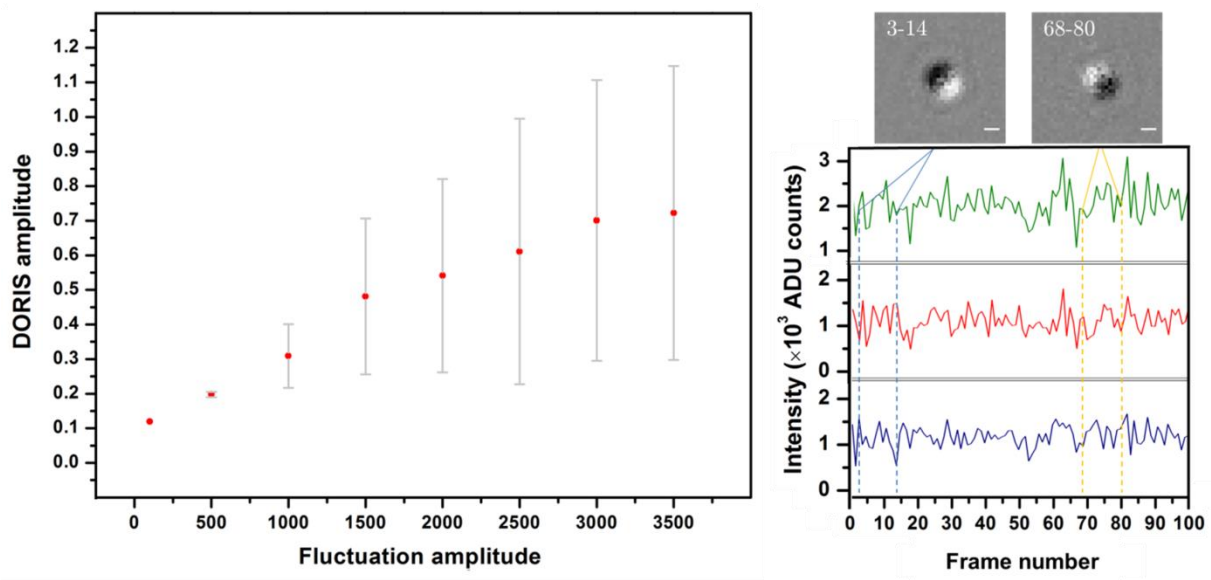

Figure 5.16. Difference-imaging of simulated flickering fluorophores. Left) Mean intensity amplitude in the dataset of difference-images as a function of the amplitude of fluctuation for two closely spaced emitters undergoing various intensity modulations around a mean of 1000 ADU counts per frame. Right) Intensity trajectories for two simulated fluorophores (blue and red) fluctuating with a standard deviation of 300 counts and associated combined trajectory (green) of the dimer. Two difference-images resulting from subtraction between frames in which the contribution of a given emitter is large compared to the other reveal the opposing dipole patterns, despite incomplete switching off of the emitters. Scale bar: 200 nm.

5.7 DORIS with Photoswitchable Dyes

QDs are not always the most suitable fluorescent reporters for biological imaging because their large sizes might disturb the target mobility and functionality. Fluorescent proteins are usually used for *in vivo* imaging, as they can be linked directly to the system of interest by genetic modification. However, the "on-off" characteristic blinking time of such probes is significantly shorter than for QDs, preventing any DORIS analysis under the hypothesis of complete switching off of the dye, as previously performed with QDs in Section 5.3.

However, the DORIS technique can be applied to the subset of fluorescent proteins engineered to photoswitch between a dark or weakly fluorescing state at one wavelength and a bright state at a second wavelength. DORIS was applied to photoswitchable fluorescent proteins in yeast to show: i) difference-imaging can be applied in a "real" biological environment despite the potential of significant background noise to degrade any dipole structure that may exist in the difference-images; ii) high order aggregates or clusters of proteins are readily resolved by image subtraction; iii) DORIS derived distance measurements maintain a strong correlation with emitter separations derived from Gaussian localisation.

A key advantage in the demonstration presented here is that the control of the dark state afforded by the photoconversion of proteins can be exploited to apply image subtraction on a reduced number of frames, instead of relying on a stochastic process such as the blinking of QDs. The temporal segregation given by the random fluorescence intermittency of QDs can be advantageously replaced by successive activation/imaging/photobleaching cycles of emitters, reducing acquisition and computing time.

DORIS was tested *in vivo* on a dedicated *S. pombe* yeast strain. Rad22 proteins were labelled with the fluorescent protein mEos3, which has been previously characterised as a purely monomeric and bright fluorescent reporter allowing to achieve a higher SNR than its ancestor mEos2 [262]. The cells were exposed to ionising radiation, which was demonstrated to induce foci formation in mammalian and budding yeast cells [173]. Ionising radiation has also been shown to induce a wide variety of DNA lesions, most notably DNA double strand breaks (DSBs). If not repaired, DSBs threaten genomic stability and can lead to gross chromosomal rearrangements, one of the hallmarks of cancer [263]. One of the DNA repair mechanisms in eukaryotes is homologous recombination, which involves using the homologous chromosome as a template for repair. When studying DSB repair in fission yeast, one common methodology of detecting the presence of DSBs is by imaging the protein Rad22 (human Rad52) tagged with GFP. Rad22 is involved in the DSB repair pathway and clear Rad22 foci can be seen in the nucleus of the cell upon exposure to damage inducing radiation.

Activation of single emitters was performed with a low 405 nm laser intensity ($\leq$ 3 W/cm^2) in order to decrease the probability of multiple, closely spaced emitters being activated at the same time, and a DORIS analysis carried out on the image stack of single emitters resulting from multiple cycles of activation, imaging and bleaching. Multiple emitters inside the diffraction limit would lead to a distortion of the PSF shape, with asymmetrical elongation of the PSF width, resulting in

inaccurate DORIS results with the calibration approach. On the other hand, if the shape of the average PSF is not strongly affected (i.e. for distances ≤ 20-50 nm), the DORIS results will reflect the distances between the centre of the foci and any measured single emitter. Sequential activation/imaging/photobleaching cycles were performed with an exposure time of one second and DORIS analysis was carried out on a dataset composed of frames corresponding to each imaging cycle.

Further post-acquisition processing was required in order to obtain viable results with DORIS, due primarily to the intrinsically lower quantum yield of the fluorescent proteins compared to QDs. Background subtraction was therefore performed using the "Rolling Ball Background Subtraction" plugin bundled in ImageJ software [174]. A smoothing of the frames in the stack was then carried out using the "Smooth" plugin in ImageJ before the subtraction analysis.

Figure 5.17 displays the average projection of the stack and a difference-image obtained from normalised frames corresponding to two different cycles. The two diffraction-limited foci composed of multiple fluorescent proteins are clearly displayed in the average projection of the imaging cycles, but individual PSFs are indistinguishable in the projected average image. On the other hand, the difference-image reveals the orientations of the fluorescent proteins activated at different aggregation sites. DORIS provides a simple and quick identification method for protein clusters: the characteristic difference-images patterns of closely spaced fluorescent PSFs is revealed by subtraction under the condition that only single emitters are switched on during an individual cycle and all fluorescent proteins are photobleached at the end of each iteration.

The mapping of the fluorescent proteins in multiple foci is efficient because all the mEos3 proteins emit roughly the same number of photons during acquisition. Since the maximum intensity value used for normalisation is retrieved from the intensity of the brightest PSF in each frame, this could compromise the technique if the number of photons emitted was not consistent between emitters. That is, a PSF significantly dimmer in the field of view would not be properly normalised, modifying the lobe shapes and amplitudes compared to the relatively symmetric dipole structures observed in Figure 5.2. Accurate DORIS analyses of individual aggregation sites, such as the one performed in Section 5.3 and the following section, were therefore carried out on a ROI including only the foci of interest in order to perform proper PSF normalisation. The foci highlighted by the ROI (white box) in Figure 5.17 has been further analysed using DORIS. Fourteen frames out the thirty recorded displayed an emitter PSF, resulting in 91 difference-images ($n(n-1)/2$) exhibiting a lobe structure.

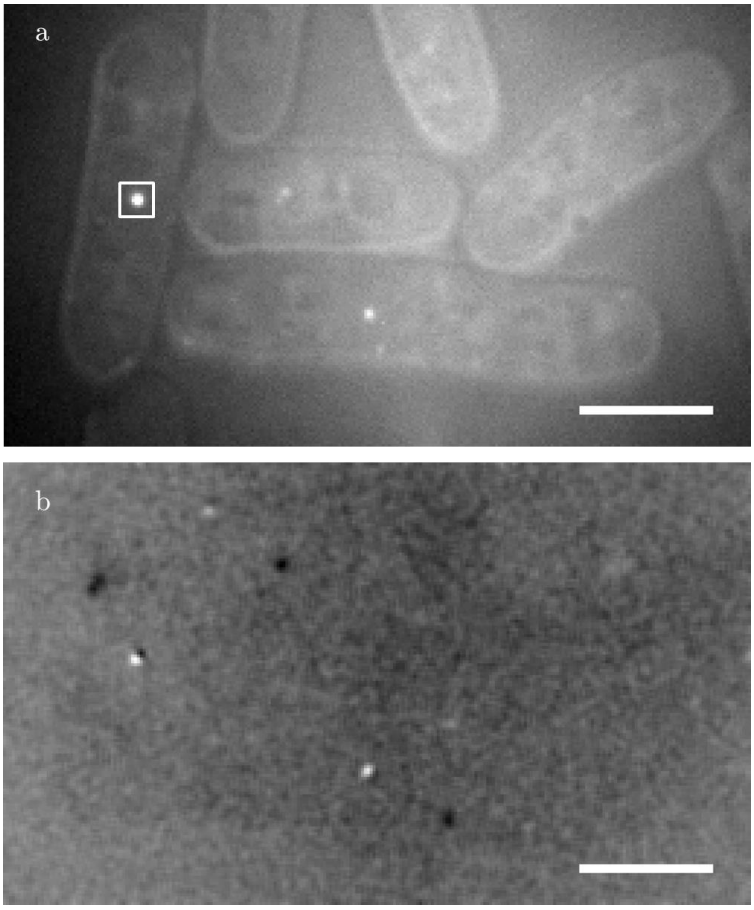

Figure 5.17. DORIS analysis of fluorescent proteins clustering. a) Multiple PSFs are too closely located inside foci to be distinguishable in the projection of all imaging cycles. b) DORIS image subtraction between two normalised images associated with different cycles. The difference-image displays the characteristic lobe structure for the two foci of interest, providing a simple way of mapping protein aggregation sites *in vivo*. Scale bar: 5 μm.

For an image set of n frames $A = \{1, \dots, n\}$, a single set of difference-images $A_{x,j}$ was calculated with x the reference image ($A_{x,j}$ given by $(A_x - A_j)$ for all $(j \neq x)$) and used to investigate the relative positions of all other emitters with respect to the emitter switched on in the reference image x (Figure 5.18). The thirteen resulting difference-images clearly display lobe orientations that locate the relative positions of each emitter with respect to the reference one. The analysis of these orientations appears to rule out any orderly structure inside the foci, with no clear spatial repartition or the partitioning into preferred locations that would appear as a repeated sequence of lobes orientations in the difference-images.

In contrast to previous experiments involving QDs immobilised at the surface of a coverslip, mEos3 emitters are distributed at different axial positions in the foci. Consequently, the distances hereby determined are not absolute measures of the interdistances between emitters but rather between the projections of the PSFs in the focal plane of interest.

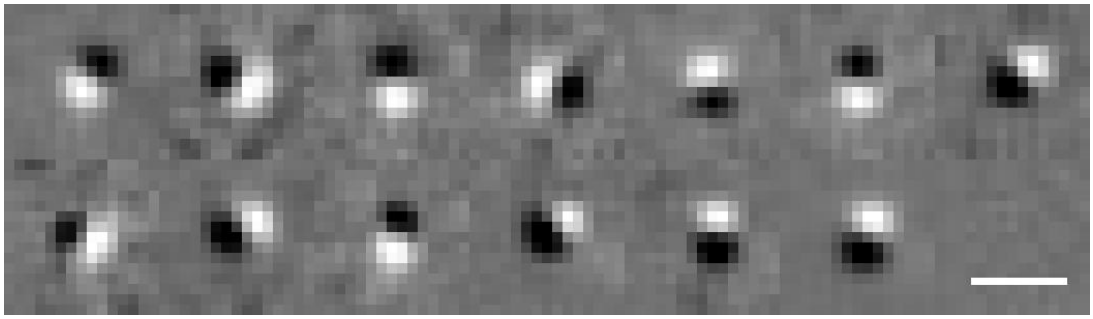

Figure 5.18. Difference-imaging revealing relative protein positions inside foci through lobe orientation. The position of the emitter switched on in the j^{th} frame can be deduced relatively to the reference emitter using the difference amplitude and the orientation of the dipole pattern. Because the intensity of the maximum varies with the original PSF separation, difference-images have been normalised for clarity of display. Scale bar: 1 µm.

Distances between proteins inside the foci have been further studied using a DORIS amplitude-to-separation calibration curve, in order to quantify the disordered partitioning of Rad22 proteins in the foci and test the efficiency of the DORIS technique. The full dataset was analysed following the method previously described in Section 5.3.3, and results compared with the Gaussian fitting method (Figure 5.19).

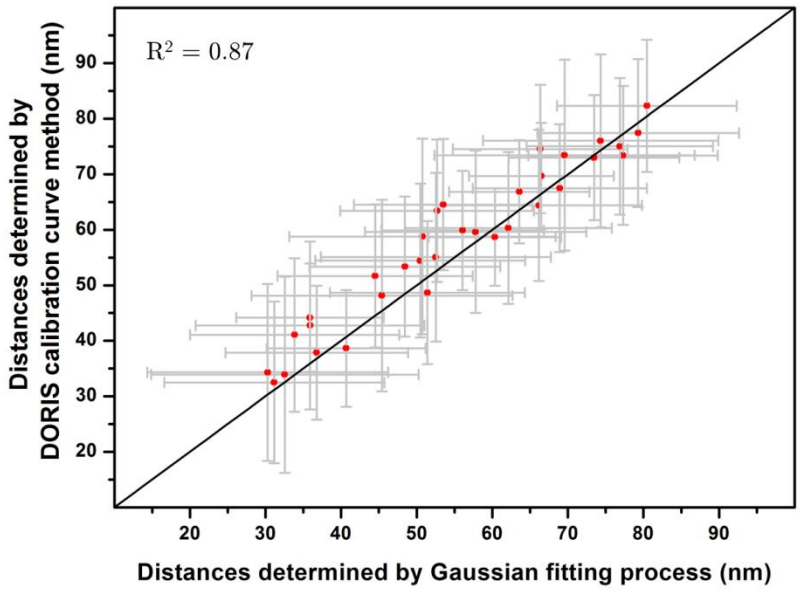

Figure 5.19. Comparison between DORIS and Gaussian fitting, using mEos3 dye. Uncertainties in both measurements were determined from the photon number collected. A straight line representing a one-to-one correspondence is plotted for guidance.

The distances between emitters inside the foci were ranging from 13 to 200 nm, with an average separation value of 97 nm. The uncertainty retrieved from the number of photons collected was typically of the order of 10 nm for a single emitter localisation, which propagated to errors in distances determined of around 15 nm.

The DORIS technique and Gaussian fitting method give comparable results for emitter pairs whose separation correspond to the DORIS efficiency range (30-80 nm), as displayed in Figure 5.19. A strong correlation between the techniques was found for the determination of protein separation, as per the QD analysis performed in Section 5.3, with a near-homogeneous spread of interdistances confirming the hypothesis of a disordered spatial arrangement of the proteins in the foci.

Conclusion and Developments

The potential applications of single molecule spectroscopy techniques in the biological field are so important and diverse that innovations in observation and analysis will open new and exciting fields of investigation. In this thesis, I aimed to develop experimental strategies to unravel structures below the diffraction limit using TIRFM, confocal microscopy and several analyses of fluctuations associated with single molecule fluorescence in a number of forms.

The fluctuation of fluorescence emission caused by the free diffusion of a labelled Suc22 protein, a subunit of RNR, was analysed and used in complement with a photobleaching assay to determine its stoichiometry. Correlation and filtering methods were implemented in the open source, image processing ImageJ software and the performances of the developed algorithms compared with a commercial correlator. The FCS approach will be used in the future to investigate the behaviour and regulation of the RNR enzyme during the cell cycle both *in vitro* and *in vivo*, with a view to understanding more clearly the respective roles and conformations of the protein subunits and their complexation.

The SOFI super-resolution technique was further developed in ImageJ and used to resolve multiple closely spaced QDs, in a distance regime lower than the diffraction limit but ultimately hindered by the order of correlation to around 100 nm. The technique was successfully applied to combed DNA labelled with organic fluorophores to show narrowing of fluorescent features on the DNA backbone, but also the significant suppression of uncorrelated background noise that the correlation technique affords. The SOFI's ability to measure the degree of correlation in an emission signal may be used straightforwardly to realise a dual-channel imaging experiment: one of the main problems inherent to this type of experiment is the ambiguity between labels on different fluorescent channels, although many correction and thresholding procedures have been developed to bring improved accuracy to colocalisation studies [264, 265]. In addition to the inherent noise reduction, the SOFI analysis of emission from a sample labelled with highly dynamic fluctuating probes, such as Dronpa, and a relatively photostable fluorophore would provide information on respective emitter's relative localisation. The combination between the fluorescence

intensities detected in each channel and the degree of correlation of emission could lead to an improved colocalisation accuracy.
In an alternative approach, the SOFI principle was generalised as a multiple, parallel FCS experiments performed at each image pixel and applied in diffusion-type experiments with an EMCCD detection scheme. The expected linear trend of diffusion time with viscosity was retrieved using this setup, and an excellent noise reduction was achieved in tracking trajectories of diffusing QDs, with correlation amplitudes reflecting residence times.

A new super-resolution technique applicable to multiple adjacent fluorescent molecules called Direct Object Resolution by Image Subtraction (DORIS) was developed and tested with QD complexes. The images generated by a DORIS analysis contain information on localisations and orientations of neighbouring emitters. The near-linear relationship between the amplitude, defined by the maximum and minimum intensities in the difference-images of two closely separated single molecules, and the relative displacement of their centres was used to measure distances in QD complexes. Moreover, the concept was applied *in vivo* using photoswitchable fluorescent proteins and proved to be efficient in retrieving intermolecular distances between probes ranging from 30 to 100 nm.
The separation between PSF centres is emphasised in the difference-images, which allows one to readily distinguish multimeric emitters. This approach might be of particular use in FPALM/STORM experimental approaches to further a quantitative analysis of localisations. For example, a single fluorophore can be driven to a dark state after its activation, before returning to a fluorescent state after further activation cycles. A conventional super-resolution algorithm would therefore retain an erroneous value of the number of emitters, or be applied under an inaccurate working hypothesis. An additional DORIS approach can readily identify dimers and single emitters going through the dark state, improving the super-resolution image reconstruction, as well as enabling quantitative experiments. Given the difference amplitude derived from a DORIS analysis of an image stack is directly proportional to the molecular separation (on a 20-100 nm scale) the quantity may also provide additional criteria for distinguishing genuine proteins clustering or aggregation, with small molecular distances within the cluster (of the order of the localisation uncertainties), from repeated blinking of a single fluorescent centre.
Importantly, the DORIS approach only requires high emission fluctuation amplitude and not a complete binary switching on and off of the emitter. This interesting feature implies that the super-resolution approach could be used with organic labels (Cy5, Alexa,…) and fluorescent proteins (Dronpa, rs-TagRFP,…) that can display

highly dynamic emission fluctuation under certain conditions, without the need to use a photobleaching-type or "on-off" blinking approach.

In summary, the investigations described in this thesis have led to the development of various fluorescence analysis methods based on correlations of the fluorescence fluctuations arising from single molecules, whether multiplicative or subtractive. These techniques have been demonstrated to successfully resolve features and provide measurement at the nanometre scale.

Appendix I

EMCCD Camera Calibration

1. Correction for Flat Field Variations

The flat field effect is caused by pixel-to-pixel variations in the sensitivity of the EMCCD. It produces an identical noise pattern in every image exposed to light of similar wavelength and induces a curvature instead of the straight line expected for plots similar to Figure 2.9. It is therefore necessary to correct for this effect in order not to underestimate the conversion factor of the camera. The following introduces the correction protocol used in this thesis that was automated with a custom-built ImageJ macro.

Several pairs of images of the same coverslip region were recorded under different illumination intensities and corrected for offset bias. The variation in the light intensity within each image set was corrected by normalising the images so that they have the same average signal. This was achieved by multiplying one of the images by a constant value, which does not affect the flat field pattern. One image was then subtracted from the other, leading to flat field corrected images. The variance of these images were calculated and divided by a factor of two to account for the doubling of the variance induced by the previous subtraction. The mean values of the corrected regions were then plotted against the associated variances, leading to a linear relationship that was fitted to retrieve the conversion factor.

2. Conversion Factor Calibration

The conversion factor (C) of the camera was determined by measuring the variance and average of the signal arising for various incident illuminations at a given camera multiplication gain (G).

Let's consider the relationship between the signal and noise values recorded in counts units (respectively S_c and N_c) and the signal and noise values recorded in electrons units (respectively S_e and N_e):

$$S_e = \frac{C}{G} \times S_c \qquad\qquad N_e = \frac{C}{G} \times N_c$$

If we consider that the only other noise signal present in the system are the readout noise (R_c in counts units and R_e in electrons units) and the shot noise (σ_c in counts units and σ_e in electrons units), the total noise adds in quadrature, which gives:

$$N_e{}^2 = R_e{}^2 + \sigma_e{}^2 \tag{I.1}$$

The shot noise obeys Poisson statistics and its square value is equal to the signal value, leading to:

$$N_e{}^2 = R_e{}^2 + S_e \quad \Leftrightarrow \left(\frac{C}{G} \times N_c\right)^2 = \left(\frac{C}{G} \times R_c\right)^2 + \frac{C}{G} \times S_c$$

$$\Leftrightarrow \qquad N_c{}^2 = R_c{}^2 + \frac{G}{C} \times S_c \tag{I.2}$$

There is therefore a linear relationship between the variance of the signal and its mean value. A simple rearrangement of the equation shows that the slope associated to the plot of the mean counts value divided by the multiplication gain against the variance gives the conversion factor.

3. Excess Noise Factor Determination

The gain process of EMCCD camera introduces an additional noise factor F^2 that can be defined using previous notations as:

$$N_c{}^2 = \frac{G^2}{C^2} F^2 N_e{}^2 \tag{I.3}$$

The detected photons follow a Poisson distribution, which gives:

$$N_c{}^2 = \frac{G^2}{C^2} F^2 S_e \tag{I.4}$$

Substituting the expression of S_e introduced in the previous section gives:

$$N_c{}^2 = \frac{G}{C} F^2 S_c \tag{I.5}$$

Equation (I.5) induces that the plot of the variance against the mean signal gives the value of the conversion factor with a multiplication gain set to a value of 1 (F=1). Measurement of the conversion factor at a different multiplication gain value was used to characterise the corresponding excess noise factor by simply taking the ratio between the slopes obtained experimentally.

Figure I.1 displays the plot of data obtained for different multiplication gain values. As expected, the slope of the curve increases with the gain applied, highlighting the presence of excess noise. The ratio between the slopes obtained for different multiplication gains and at a multiplication gain set to unity was then calculated in order to quantify the excess noise factor.

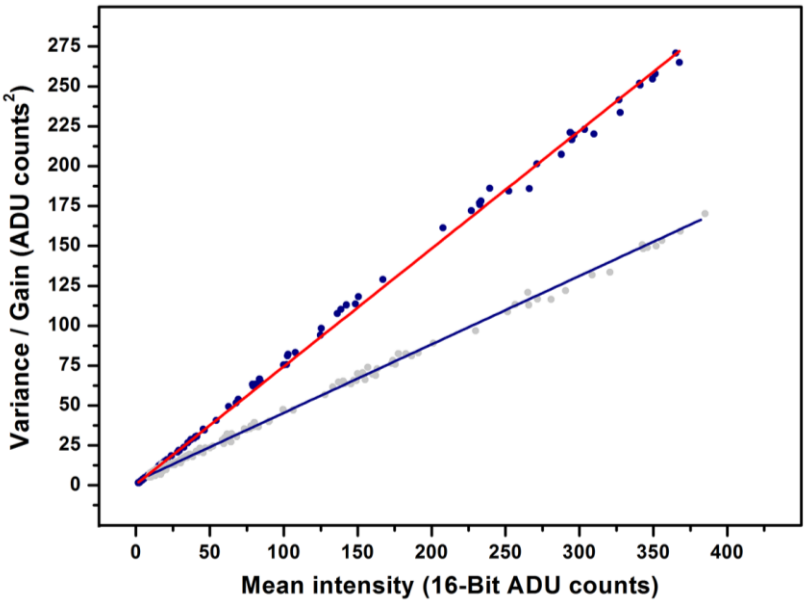

Figure I.1. Excess noise factor calibration. The plot of the variance divided by the multiplication gain against the mean ADU count value is displayed for a multiplication gain of 1 (grey points) and 300 (blue points). Gradients are 0.408 ± 0.005 ($=1/C$) at gain 1 and 0.746 ± 0.026 ($= F^2/C$) at gain 300.

Appendix II

FCS Correlation with Fourier Transforms

```
// To read 32 bit PMS sdt files                                          //
// Returns autocorrelation of two different channels and associated      //
// cross-correlation using Fast Fourier Transforms in ImageJ             //

dir = getDirectory("Choose a Directory ");
setBatchMode(true);
   count = 0;
   countFiles(dir);
      Dialog.create("File count");
      if (count==0) {Dialog.addMessage("No files to process");
Dialog.show();}
      Dialog.addMessage("Processing "+count+" files"); Dialog.show();
      if (count>64 && count<=256) mcsw=2048;
      if (count>16 && count<=64) mcsw=2048;
      if (count>4 && count<=16) mcsw=1024;
      if (count>1 && count<=4) mcsw=512;
      if (count==1) mcsw=256;
      mcsn=65536;
      nrows=mcsn/mcsw; // rows per 65536 channel sdt file for 4096 width //
      mcsh=nrows*count;                    // MCS height for display only //
      fftw=16*mcsw;
      frows=mcsn/fftw; // rows per 65536 channel sdt file for fttw width //
      ffth=frows*count;          // data image height for fft processing //
      newImage("MCS", "32-bit black", fftw, ffth, 2);
n = 0;
```

```
   processFiles(dir);                        // convert files into an image //

   calcProximity(); // calculate proximity ratio (for FRET applications) //
   calcFFT(fftw,ffth);                      // calculate correlation values //
   setBatchMode("exit and display");
   plotCorr(fftw,ffth);                          // plot correlation values //

   saveFiles();                                  // save correlation values //

   function countFiles(dir) {

      list = getFileList(dir);
      for (i=0; i<list.length; i++) {
          if (endsWith(list[i], "/"))
              countFiles(""+dir+list[i]);
          else
              if (endsWith(list[i], ".sdt")) count++;
      }
  }

   function processFiles(dir) {

      list = getFileList(dir); no=0;
      for (i=0; i<list.length; i++) {
          if (endsWith(list[i], "/"))
              processFiles(""+dir+list[i]);
          else { if (endsWith(list[i], ".sdt")){
             showProgress(n++, count);
             path = dir+list[i]; no=no+1;
             processFile(path, no);}
          }
      }
  }

  function processFile(path, no) {
      if (endsWith(path, ".sdt")) {
                  fileid=substring(path, lastIndexOf(path,"_")+1,
indexOf(path, ".sdt"));
            fileno=parseInt(fileid);
```

```
            if (lengthOf(fileid)==2) blockA=2666;
            if (lengthOf(fileid)==3) blockA=2660;
            if (fileno<10) {blockB=64; format="";}
            if (fileno>=10) {blockB=68; format="little-endian";}
            if (fileno>=100) {blockB=68; format="";}

run("Raw...", "open=["+path+"] image=[32-bit Unsigned] width=256 "+
"height=256 offset="+blockA+" number=2 gap="+blockB+" "+format+" use");

file= getTitle();
root = substring(file,0,indexOf(file, ".sdt"));
w=getWidth();
// Read Block A //
selectWindow(file);
setSlice(1);
selectWindow("MCS");
setSlice(1);
xra=0; yra=0;
xwa=0; ywa=(no-1)*frows;
n=0;
while(n<=mcsn-1){
selectWindow(file);
A=getPixel(xra,yra);
if (fileno<100) A=getPixel(xra, yra)/65536;
xra=xra+1;
if (xra>w-1) {xra=0; yra=yra+1;}
selectWindow("MCS");
setPixel(xwa,ywa,A);
xwa=xwa+1;
if (xwa>fftw-1) {xwa=0; ywa=ywa+1;}
n=n+1;
}
// Read Block B //
selectWindow(file);
setSlice(2);
selectWindow("MCS");
setSlice(2);
xrb=0; yrb=0;
xwb=0; ywb=(no-1)*frows;
```

```
n=0;
while(n<=mcsn-1){
selectWindow(file);
B=getPixel(xrb,yrb);
if (fileno>99) B=getPixel(xrb, yrb)/65536;
xrb=xrb+1;
if (xrb>w-1) {xrb=0; yrb=yrb+1;}
selectWindow("MCS");
setPixel(xwb,ywb,B);
xwb=xwb+1;
if (xwb>fftw-1) {xwb=0; ywb=ywb+1;}
n=n+1;
}
selectWindow(file);
close();
}
}

function calcProximity(){

run("Stack to Images");
imageCalculator("Add create 32-bit", "MCS-0001","MCS-0002");
rename("MCS-A+B");
imageCalculator("Divide create 32-bit", "MCS-0001","MCS-A+B");
rename("MCS-P");
run("16-bit");
run("32-bit");
run("Divide...", "value=65536");
selectWindow("MCS-A+B");
close();
run("Images to Stack");
rename("MCS-A-B-P");
}

function calcFFT(fftw, ffth){

run("Set Measurements...", "  mean redirect=None decimal=6");
selectWindow("MCS-A-B-P");
d=nSlices();
```

```
  for (frm=1; frm<=d; frm++){
 selectWindow("MCS-A-B-P");
  setSlice(frm);
 run("Duplicate...", "title=FFT");
  run("Measure");
  Ave=getResult("Mean");
  run("Add...", "value=1");
  run("Convolve 3D", "image=FFT psf=FFT extension=[Zero Pad (usually best)]
correlate create output=Output");
  dc=fftw*ffth*(2*Ave+1);
    run("Subtract...", "value="+dc);
    run("Divide...", "value="+fftw);
    run("Divide...", "value="+ffth);
    run("Divide...", "value="+Ave);
    run("Divide...", "value="+Ave);

  rename("Corr-"+frm);
  selectWindow("FFT");
if (frm==1) {run("Duplicate...", "title=FFT-A"); AveA=Ave;}
if (frm==2) {run("Duplicate...", "title=FFT-B"); AveB=Ave;}
 selectWindow("FFT");
  close();
  }
run("Convolve 3D", "image=FFT-B psf=FFT-A extension=[Zero Pad (usually
best)] correlate create output=Output");
dc=fftw*ffth*(AveA+AveB+1);
run("Subtract...", "value="+dc);
run("Divide...", "value="+AveA*AveB);
run("Divide...", "value="+fftw*ffth);
selectWindow("FFT-A");
close();
selectWindow("FFT-B");
close();
run("Images to Stack");
rename("Corr-AA-BB-PP-AB");
}

function plotCorr(fftw,ffth){
```

```
selectWindow("Corr-AA-BB-PP-AB");
d=nSlices();
  for (frm=1; frm<=d; frm++){
selectWindow("Corr-AA-BB-PP-AB");
setSlice(frm);
  run("Clear Results");
  makeLine(fftw/2+1, ffth/2, fftw-1, ffth/2);
  autoc=getProfile();
  loglag=newArray(autoc.length);
      for (lag=0; lag<autoc.length; lag++) {
      setResult("Value", lag, autoc[lag]);
      loglag[lag]=log(lag+1)/log(10);
      }
      updateResults;
  Plot.create("AutoC-"+frm, "Log(Lag)", "Amplitude", loglag, autoc);
  Plot.show();
  saveAs("Measurements", dir+"AutoC-"+frm+".txt");
  }
}

function saveFiles(){

selectWindow("MCS-A-B-P");
saveAs("Tiff", dir+"MCS-A-B-P.tif");
selectWindow("Corr-AA-BB-PP-AB");
saveAs("Tiff", dir+"Corr-AA-BB-PP-AB.tif");
selectWindow("Results");
run("Close");
}
```

Appendix III

FCS Correlation with Sequential Shifts of Time Series

```
// Macro to extend the maximum lag time reachable with the                //
// autocorrelation process of FCS. This macro is to be applied on the     //
// desired frame of the   "MCS-A-B-P.tif" of Appendix II, renamed         //
// "source". It relies on the sequential shift of the signal compared     //
// to itself and the multiplication of the two images. The image is       //
// fractionated (input "partition") and autocorrelation values for each   //
// part are saved in the selected directory. These values can be          //
// averaged out to decrease the noise present in the final curve.         //
// The associated lag time values are displayed in the "Log" window. The  //
// maximum lag time can be selected, as well as the desired increment     //
// of lag times values, which can be set as pseudo-logarithmic.           //

setBatchMode(true);
dir1 = getDirectory("Choose Source Directory partition ");
i=1;
rf=getNumber("displacement max ", 0);
part=getNumber("partition ", 0);
binnumber=getNumber("bin number ", 4);
basestep=getNumber("base", 2);
selectWindow("source");
aa=getWidth;
ab=getHeight;
ad=nSlices();
uu=ab/part;
      for (i>=1; i<uu; i++) {                          // dataset partition //
      ty=part*i;
      selectWindow("source");
      run("Specify...", "width=aa height=part x=0 y=ty");
```

```
      run("Duplicate...", "title=[original dataset-1.tif]");
      rename("original dataset");
      calculatedataset();
      selectWindow("original dataset");
      close();
      }

function calculatedataset() {        // correlation by sequential shifts //

rename("original dataset");
w=getWidth;
g=getHeight;
d=nSlices();
v=0;
p=1;
a=w*g;
t=a/2;
h=0;
rb=0;
df=0;
newImage("copy_image", "32-bit Black", a,1, 1);
      for (v>=0; v<g; v++) {
      b=v*w;
      selectWindow("original dataset");
      run("Specify...", "width=w height=1 x=0 y=v");
      run("Copy");
      selectWindow("copy_image");
      run("Specify...", "width=w height=1 x=b y=0");
      run("Paste");
      }
run("Set Measurements...", "  mean redirect=None decimal=9");
selectWindow("copy_image");
run("Measure");
Ave=getResult("Mean");
run("Clear Results");
MatriceImage1=newArray(rf);
a=1;
b=0;
ht=1;
```

```
p=1;
y=1;
v=basestep;
      for (p>=1; p<=rf; p++) {
      df=df+1;
      gt=binnumber*a;            // pseudo-logarithmic scale calculation //
      b=b+1;
            if (b>gt) {
                  for (y>=1; y<ht; y++) {
                  v=v*basestep;
                  }
                  ht=ht+1;
                  rb=v-1;
                  a=a+1;
            }
      p=p+rb;
      MatriceImage1[df]=p;
      selectWindow("copy_image");
      run("Duplicate...", "title=[original dataset original-1]");
      rename("1");
      selectWindow("copy_image");
      run("Specify...", "width=t height=1 x=p y=0");
      run("Copy");
      newImage("copy_image_shifted" , "32-bit Black",t ,1, 1);
      run("Specify...", "width=t height=1 x=0 y=0");
      run("Paste");
      imageCalculator("Multiply create 32-bit", "copy_image","1");
      rename("multiplied shift");
      run("Divide...", "value="+Ave);
      run("Divide...", "value="+Ave);
      selectWindow("multiplied shift");
      run("Measure");
      saveAs("Results", dir1+"Results"+i+".txt");
      selectWindow("copy_image_shifted");
      close();
      selectWindow("multiplied shift");
      close();
      selectWindow("1");
      close();
```

```
	}
ILength = MatriceImage1.length;
	for (h=0; h<df; h++) {
	print(MatriceImage1[h]);
	}
}
setBatchMode("exit and display");
```

Appendix IV

Artifact Removal in FCS Curves

```
// Macro to remove artifacts in the FCS curves. This macro is to be      //
// applied on the desired frame of the "MCS-A-B-P.tif" of Appendix II.   //
// The image is fractionated (input "delta t in seconds") with respect   //
// to data acquisition time (input "acquisition time in seconds").       //
// Autocorrelation values for each part are calculated, saved in the     //
// selected directory and compared to the threshold set by the user      //
// (input "dGmax threshold"). The macro displays the autocorrelation     //
// calculated for each part and the average of retained correlation      //
// curves, as well as the minimum and maximum values taken by the        //
// squared difference between the integral of one partition curve        //
// and the average of all others. The dataset parts corresponding to an  //
// artifact event can then be discarded.                                 //


dir = getDirectory("Choose a Directory ");
setBatchMode(true);
A=getNumber("select value of delta t in seconds",0);
B=getNumber("select acquisition time in seconds",0);
C=getNumber("select dGmax threshold",0);
w=getWidth;
g=getHeight;
e=0;
s=0;
p=0;
i=1;
x=0;
y=0;
Avecorr=0;
v=A/B;
t=B*w;
l=A/t;
f=floor((w*g)/v);
```

```
m=floor(l);
kj=2*f+1;
kl=kj-1;
yt=kj-1;
rename("MCS-A.tif");
newImage("Averagecorr" , "32-bit Black", 16384, kj, 1);
selectWindow("MCS-A.tif");

partitiondatas();

averagewithout();

function partitiondatas() {                    // fractionate the datasets //

e=0;
s=0;
p=0;
i=1;
x=0;
y=0;
Avecorr=0;
v=A/B;
t=B*w;
l=A/t;
f=floor((w*g)/v);
m=floor(l);

        while (i<(f+1)) {
        u=m;
        e=v-(w*m);
        n=(w-e);
                if (i==1) {
                selectWindow("MCS-A.tif");
                run("Specify...", "width=w height=m x=0 y=0");
                run("Copy");
                newImage("Correlationsource"+i , "32-bit Black", w, u, 1);
                run("Paste");
                calcFFT();
                plotCorr();
```

```
                selectWindow("MCS-A.tif");
                i=i+1;
                }
                if (i!=1) {
                x=0;
                y=0;
                selectWindow("MCS-A.tif");
                k=(m*(i-1));
                run("Specify...", "width=w height=m x=0 y=k");
                run("Copy");
                newImage("Correlationsource"+i, "32-bit Black", w, m, 1);
                run("Specify...", "width=w height=u x=0 y=0");
                run("Paste");
                calcFFT();
                plotCorr();
                selectWindow("MCS-A.tif");
                i=i+1;
                }
        }
}
function calcFFT(){      // calculate the correlation function using FFT //

dc=0;
Ave=0;
selectWindow("Correlationsource"+i);
run("Set Measurements...", "  mean redirect=None decimal=6");
run("Measure");
Ave=getResult("Mean");
run("Duplicate...", "title=FFT");
run("Add...", "value=1");
run("Convolve 3D", "image=FFT psf=FFT extension=[Zero Pad (usually best)]
correlate create output=Output");
dc=w*m*(2*Ave+1);
run("Subtract...", "value="+dc);
run("Divide...", "value="+w);
run("Divide...", "value="+m);
run("Divide...", "value="+Ave);
run("Divide...", "value="+Ave);
rename("Correlation number"+i);
```

```
selectWindow("FFT");
close();
selectWindow("Correlationsource"+i);
close();
}

function plotCorr(){  // plot the correlation for each partition dataset //

ap=0;
selectWindow("Correlation number"+i);
run("Clear Results");
makeLine(w/2+1, m/2, w-1, m/2);
autoc=getProfile();
loglag=newArray(autoc.length);
        for (lag=0; lag<autoc.length; lag++) {
        setResult("Value", lag, autoc[lag]);
        loglag[lag]=log(lag+1)/log(10);
        ap=ap+autoc[lag];
        selectWindow("Averagecorr");
        jh=i-1;
        setPixel(lag,jh,autoc[lag]);
        }
updateResults;
Plot.create("AutoC-"+i, "Log(Lag)", "Amplitude", loglag, autoc);
Plot.show();
saveAs("Measurements", dir+"AutoCpart"+i+".txt");
selectWindow("Correlation number"+i);
close();
}

function averagewithout() {
                    // average all curves which satisfies input criteria //
run("Set Measurements...", "  mean min redirect=None decimal=9");
x=0;
y=0;
gh=f-1;
run("Clear Results");
selectWindow("Averagecorr");
        for (y>=0; y<=gh; y++) {
```

```
        x=0;
        for (x>=0; x<=16382; x++) {
        po=y+f;
        makeLine(x, 0, x, gh);
        run("Clear Results");
        run("Measure");
        moyenne=getResult("Mean");
        valeurpoint=getPixel(x,y);
        ecartmoyenne=(valeurpoint-((moyenne*f-valeurpoint)/(f-
1)))*(valeurpoint-((moyenne*f-valeurpoint)/(f-1)));
        setPixel(x,po,ecartmoyenne);
        }
        }
        sortaverage();
}

function sortaverage(){                    // store the curves into arrays //

hgp=0;
run("Set Measurements...", "  mean min redirect=None decimal=9");
x=0;
y=0;
run("Clear Results");
selectWindow("Averagecorr");
        for (y>=0; y<=gh; y++) {
        x=0;
        pi=y+f;
        ds=0;
        mn=0;
        makeLine(0,pi, 16382, pi);
        run("Measure");
        max=getResult("Max");
        setPixel(16383,pi,max);

                if (max<C) {
                ds=0;
                ju=0;
                mn=0;
                ok=0;
```

```
                hgp=hgp+1;
                        for (ds>=0; ds<=16382; ds++) {
                        ju=getPixel(ds,y);
                        mn=getPixel(ds,kl);
                        ok=ju+mn;
                        setPixel(ds, kl, ok);
                        }
                }
        selectWindow("Averagecorr");
        }
        getmindifference();
        norm();
}

function getmindifference(){
                        // calculate min and max differences to threshold //
selectWindow("Averagecorr");
makeLine(16383,pi,16383, yt);
run("Set Measurements...", "  min redirect=None decimal=9");
run("Measure");
min=getResult("Min");
print(min);
makeLine(16383,pi,16383, yt);
run("Set Measurements...", "  min redirect=None decimal=9");
run("Measure");
maxi=getResult("Max");
print(maxi);
selectWindow("Averagecorr");
}

function norm(){                                    // normalise correlations //

run("Clear Results");
y=kl;
dg=0;
afg=newArray(16383);
        for (dg>=0; dg<=16382; dg++) {
        jf=getPixel(dg,kl);
        mx=jf/hgp;
```

```
        afg[dg]=log(dg+1)/log(10);
        setPixel(dg, kl, mx);
        }
run("Clear Results");
makeLine(0, kl, 16381,kl);
autoc=getProfile();
loglag=newArray(autoc.length);
        for (lag=0; lag<autoc.length; lag++) {
        setResult("Value", lag, autoc[lag]);
        loglag[lag]=log(lag+1)/log(10);

        }
updateResults;
Plot.create("AutoCoraverage", "Log(Lag)", "Amplitude", loglag, autoc);
Plot.show();
saveAs("Measurements", dir+"AutoCorraverage"+".txt");
}
setBatchMode("exit & display");
```

Appendix V

SOFI Algorithm in ImageJ

```
// SOFI algorithm in ImageJ to use on square stack of frames.            //
// The macro offers the possibility to choose between the correlation at //
// all lag times (performed with Fourier transforms) or with the         //
// approximation   of computed lag times set to zero (performed by       //
// successive multiplications of time series).                           //

setBatchMode(true);
bsx=getNumber("select method of SOFI: 0 for approx lagtime=0;1 for complete
SOFI",0);
mk=getNumber("select order",0);
mj=mk-1;
rename("originalSOFI");
w=getWidth;
g=getHeight;
d=nSlices();
hy=1;
c=0;
rb=2;
f=w*g;

      if (bsx==0) {
      newImage("multiply" , "32-bit Black",d , f, 1);
      newImage("pixeltracesovertime" , "32-bit Black",d , f, 1);
      newImage("imageaftertreatment" , "32-bit Black",w ,g, 1);
      newImage("temp stock of value" , "32-bit Black",d , f, 1);

      collectpoints();         // organise pixels intensities into lines //
```

```
	calccorr();                    // calculate first order correlation //

	getintegralofcorrelation();  // calculate integrals of correlation //

	recreate();            // recreate the image with integrated values //

		for (rb>=2; rb<=mj; rb++) {
		mji=rb+1;
		hy=1;
		correlatedatasandsortinimage();
                                // calculate high order correlation //
		recreatefinal();
                               // recreate the image with integrated values //
		}
		calculofcumulant();              // calculate cumulant values //

		closeundesiredwindows();            // close undesired images //
		}
		if (bsx==1) {
		fp=3*d;
		newImage("correlationsum" , "32-bit Black",fp , f, 1);
		newImage("pixeltracesovertime" , "32-bit Black",d , f, 1);
		newImage("imageaftertreatment" , "32-bit Black",w ,g, 1);
		newImage("temp stock of value" , "32-bit Black",d , f, 1);

		collectpoints1();  // organise pixels intensities into lines //

		calccorr1();             // calculate first order correlation //

		getintegralofcorrelation1();
                              // calculate integrals of correlation //

		recreate1();    // recreate the image with integrated values //
		}
setBatchMode("exit and display");

function collectpoints() {

x=0;
```

```
y=0;
q=0;
j=0;
n=1;
while(n<=d) {
      while(y<g){
            for (x>=0; x<w; x++) {
            selectWindow("originalSOFI");
            setSlice(n);
            a=getPixel(x, y);
            selectWindow("pixeltracesovertime");
            setPixel(c,q,a);
            q=q+1;
            }
      y++;
      x=0;
      }
n=n+1;
c=c+1;
y=0;
x=0;
q=0;
}
}

function calccorr(){

k=0;
dc=0;
Ave=0;
      for (k>=0; k<f; k++) {
      selectWindow("pixeltracesovertime");
      run("Specify...", "width=d height=1 x=0 y=k slice=1");
      run("Copy");
      newImage("corrsource"+k , "32-bit Black",d ,1, 1);
      run("Paste");
      run("Set Measurements...", "  mean redirect=None decimal=9");
      run("Measure");
      Ave=getResult("Mean");
```

```
	run("Subtract...", "value="+Ave);
	run("Duplicate...", "title=FFT");
	imageCalculator("Multiply create", "FFT","FFT");
	rename("Correlation number"+k);
	selectWindow("FFT");
	close();
	ap=0;
	run("Clear Results");
	selectWindow("Correlation number"+k);
	run("Select All");
	run("Copy");
	selectWindow("multiply");
	run("Specify...", "width=d height=1 x=0 y=k slice=1");
	run("Paste");
	selectWindow("Correlation number"+k);
	close();
	selectWindow("corrsource"+k);
	close();
	}
}

function getintegralofcorrelation(){

j=0;
	for (j>=0; j<f; j++) {
	selectWindow("multiply");
	run("Specify...", "width=d height=1 x=0 y=j slice=1");
	run("Measure");
	moyenne=getResult("Mean");
	selectWindow("temp stock of value");
	setPixel(0,j,moyenne);
	}
}

function recreate(){

v=0;
s=0;
u=0;
```

```
	while (u<g) {
	o=u*g;
	t=(u+1)*w;
		for (v>=0; v<t; v++) {
		selectWindow("temp stock of value");
		b=v+o;
		r=getPixel(s,b);
		selectWindow("imageaftertreatment");
		setPixel(v,u,r);
		}
	u=u+1;
	v=0;
	}
selectWindow("imageaftertreatment");
rename("imageaftertreatmentfinale2");
}

function correlatedatasandsortinimage(){

	if (rb>=2) {
	selectWindow("multiply");
	wr=getWidth;
	newImage("correlatedtogether"+rb , "32-bit Black", wr , f, 1);
	kf=1;
	df=0;
	Avf=0;
	mb=rb+1;
	kfa=0;
	kfb=2;
	ucb=0;
	kfc=0;

		for (kfa>=0; kfa<f; kfa++) {
		selectWindow("pixeltracesovertime");
		wn=getWidth;
		gn=getHeight;
		wna=wn/2;
		run("Specify...", "width=wn height=1 x=0 y=kfa slice=1");
		run("Copy");
```

```
newImage("pixeltracesovertimecut"+kfa , "32-bit Black",wn ,1, 1);
  selectWindow("pixeltracesovertimecut"+kfa);
  run("Select All");
  run("Paste");
  run("Set Measurements...", "  mean redirect=None decimal=9");
  run("Measure");
  Ave=getResult("Mean");
  run("Subtract...", "value="+Ave);
  kf=1;

        for (kfb>=2; kfb<=rb; kfb++) {
              if (kfb==2) {
              selectWindow("multiply");
              wn=getWidth;
              gn=getHeight;
              wna=wn/2;
        run("Specify...", "width=wn height=1 x=0 y=kfa slice=1");
              run("Copy");
        newImage("correlatedimage1" , "32-bit Black",wn ,1, 1);
              selectWindow("correlatedimage1");
              run("Select All");
              run("Paste");
              rename("correlatedimageforconvolve1");
              }
        selectWindow("pixeltracesovertimecut"+kfa);
        run("Duplicate...", "title=correlatedimage1");
        selectWindow("correlatedimageforconvolve1");
        rename("correlatedimageforconvolve3");
  imageCalculator("Multiply create 32-bit",
  "correlatedimageforconvolve3","correlatedimage1");
        rename("correlatedimageforconvolve1");
        selectWindow("correlatedimageforconvolve3");
        close();
        selectWindow("correlatedimage1");
        close();
        }
  selectWindow("pixeltracesovertimecut"+kfa);
  close();
  kfb=2;
```

```
            selectWindow("correlatedimageforconvolve1");
            run("Copy");
            wndf=getWidth;
            wvdf=floor(wndf/2);
            wedf=wndf-1;
            newImage("correlatedimageformeasure" , "32-bit Black",d ,2, 1);
            run("Specify...", "width=d height=1 x=0 y=0 slice=1");
            run("Paste");
            run("Specify...", "width=d height=1 x=0 y=0 slice=1");
            run("Measure");
            moyennea=getResult("Mean");
            selectWindow("correlatedtogether"+rb);
            setPixel(0,kfa,moyennea);
            ucb=ucb+1;
            selectWindow("correlatedimageforconvolve1");
            close();
            selectWindow("correlatedimageformeasure");
            close();
            }
      }
}

function recreatefinal(){

      if(rb>1) {
      v=0;
      s=0;
      u=0;
      newImage("imageaftertreatmentfinale"+rb+1 ,"32-bit Black",w, g, 1);
            while (u<g){
            o=u*g;
            t=(u+1)*w;
                  for (v>=0; v<t; v++) {
                  b=v+o;
                  selectWindow("correlatedtogether"+rb);
                  r=getPixel(s,b);
                  selectWindow("imageaftertreatmentfinale"+rb+1);
                  setPixel(v,u,r);
                  }
```

```
            u=u+1;
            v=0;
            }
      }
}

function closeundesiredwindows(){

r=2;
selectWindow("temp stock of value");
close();
selectWindow("pixeltracesovertime");
close();
selectWindow("multiply");
close();
      for (r>=2; r<=mj; r++) {
      selectWindow("correlatedtogether"+r);
      close();
      }
}

function calculofcumulant(){
// approximate expression of cumulants using binomial coefficients.      //
// coefficients are calculated using factorials calculated sequentially  //
ord=1;
facord=0;
facnminus1=0;
facnminus1minusi=0;
fac=0;
ideux=2;
bincoef=0;
ncoef=1;

      for (ord>=2; ord<=mk; ord++) {
            if(ord==2) {
            selectWindow("imageaftertreatmentfinale2");
            run("Duplicate...", "title=cumulantorder2");
            }
            if(ord==3) {
```

```
            selectWindow("imageaftertreatmentfinale3");
            run("Duplicate...", "title=cumulantorder3");
            }
            if(ord==4) {
      imageCalculator("Multiply create",
      "imageaftertreatmentfinale2","imageaftertreatmentfinale2");
            rename("A");
            imageCalculator("Add create", "A","A");
            rename("AA");
            imageCalculator("Add create", "AA","A");
            rename("AAA");
      imageCalculator("Subtract
create","imageaftertreatmentfinale4","AAA");
            rename("cumulantorder4");
            selectWindow("A");
            close();
            selectWindow("AA");
            close();
            selectWindow("AAA");
            close();
            }
            if(ord>4) {
            ordminustwo=ord-2;
            ordminusone=ord-1;
            selectWindow("imageaftertreatmentfinale"+ord);
            run("Duplicate...", "title=cumulantorder"+ord);
                  for (ideux>1; ideux<=ordminustwo; ideux++) {
                  selectWindow("cumulantorder"+ord);
                  rename("H");
                  ordminus1minusi=ordminusone-ideux;
                  fac = ideux;
                  facideux=(factorial(fac));
                  fac = ordminusone;
                  facnminus1=(factorial(fac));
                                                      // calculate factorial //
                  fac = ordminus1minusi;
                  facnminus1minusi=(factorial(fac));
                  bincoef=(facnminus1/(facideux*facnminus1minusi));
                  nminusideux=ord-ideux;
```

```
                  selectWindow("cumulantorder"+nminusideux);
                  run("Duplicate...", "title=cumulorder");
                  selectWindow("imageaftertreatmentfinale"+ideux);
                  run("Duplicate...", "title=G");
                  imageCalculator("Multiply create", "cumulorder","G");
                  rename("product");
                  run("Duplicate...", "title=productoriginal");
                        for (ncoef>=1; ncoef<bincoef; ncoef++) {
                        selectWindow("product");
                        rename("product1");
                  imageCalculator("Add create",
"product1","productoriginal");
                        rename("product");
                        selectWindow("product1");
                        close();
                        }
                  selectWindow("cumulorder");
                  close();
                  selectWindow("G");
                  close();
                  selectWindow("productoriginal");
                  close();
                  imageCalculator("Subtract create", "H","product");
                  rename("cumulantorder"+ord);
                  selectWindow("product");
                  close();
                  print(bincoef);
                  selectWindow("H");
                  close();
                  ncoef=1;
                  }
            ideux=2;
            }
      }
}

function factorial(x) {
      if (x <= 1)
        return 1;
```

```
        else
        return x * factorial(x-1);
      }

function collectpoints1() {

x=0;
y=0;
q=0;
j=0;
n=1;
      while(n<=d) {
            while(y<g) {
                  for (x>=0; x<w; x++) {
                  selectWindow("originalSOFI");
                  setSlice(n);
                  a=getPixel(x, y);
                  selectWindow("pixeltracesovertime");
                  setPixel(c,q,a);
                  q=q+1;
                  }
            y++;
            x=0;
            }
      n=n+1;
      c=c+1;
      y=0;
      x=0;
      q=0;
      }
}

function calccorr1(){

k=0;
dc=0;
Ave=0;
      for (k>=0; k<f; k++) {
      selectWindow("pixeltracesovertime");
```

```
      run("Specify...", "width=d height=1 x=0 y=k slice=1");
      run("Copy");
      newImage("corrsource"+k , "32-bit Black",fp ,1, 1);
      run("Specify...", "width=d height=1 x=d y=0 slice=1");
      run("Paste");
      run("Set Measurements...", "  mean redirect=None decimal=9");
      run("Measure");
      run("Select All");
      Ave=getResult("Mean");
      run("Subtract...", "value="+Ave);
      run("Duplicate...", "title=pixeltracefluctuation");
 run("Convolve 3D", "image=pixeltracefluctuation psf=pixeltracefluctuation
 extension=[Zero Pad (usually best)] correlate create output=Output");
      rename("Trace number"+k);
      selectWindow("pixeltracefluctuation");
      close();
      run("Clear Results");
      selectWindow("Trace number"+k);
      run("Select All");
      run("Copy");
      selectWindow("correlationsum");
      run("Specify...", "width=fp height=1 x=0 y=k slice=1");
      run("Paste");
      selectWindow("Trace number"+k);
      close();
      selectWindow("corrsource"+k);
      close();
      }
}

function getintegralofcorrelation1(){

j=0;
      for (j>=0; j<f; j++) {
      selectWindow("correlationsum");
      wf=fp/2+1;
      wa=fp/2;
      run("Specify...", "width=d height=1 x=wf y=j slice=1");
            // the following calculate mean value before reconstruction //
```

```
	run("Measure");
	moyenne=getResult("Mean");
	selectWindow("temp stock of value");
	setPixel(0,j,moyenne);
	}
}
function recreate1(){

v=0;
s=0;
u=0;
	while (u<g) {
	o=u*g;
	t=(u+1)*w;
		for (v>=0; v<t; v++) {
		selectWindow("temp stock of value");
		b=v+o;
		r=getPixel(s,b);
		selectWindow("imageaftertreatment");
		setPixel(v,u,r);
		}
	u=u+1;
	v=0;
	}
selectWindow("imageaftertreatment");
rename("imageaftertreatmentfinale2");
}
```

Appendix VI

FCS Viscosity Titration Assay

The experiments were conducted at 20.5 ± 0.5°C using the protocol described in Chapter 2. The respective samples were imaged with exposure times ranging from 9.4 to 11.3 ms for 20000 frames. Figure VI.1 displays autocorrelation curves for 40 wt% and 6 wt% glycerol-water mixture that were omitted in Figure 4.13 for clarity purposes. Table 5 displays fitting parameters obtained with Equation (3.6) that confirms a regular increase of diffusion time with the viscosity of the solution.

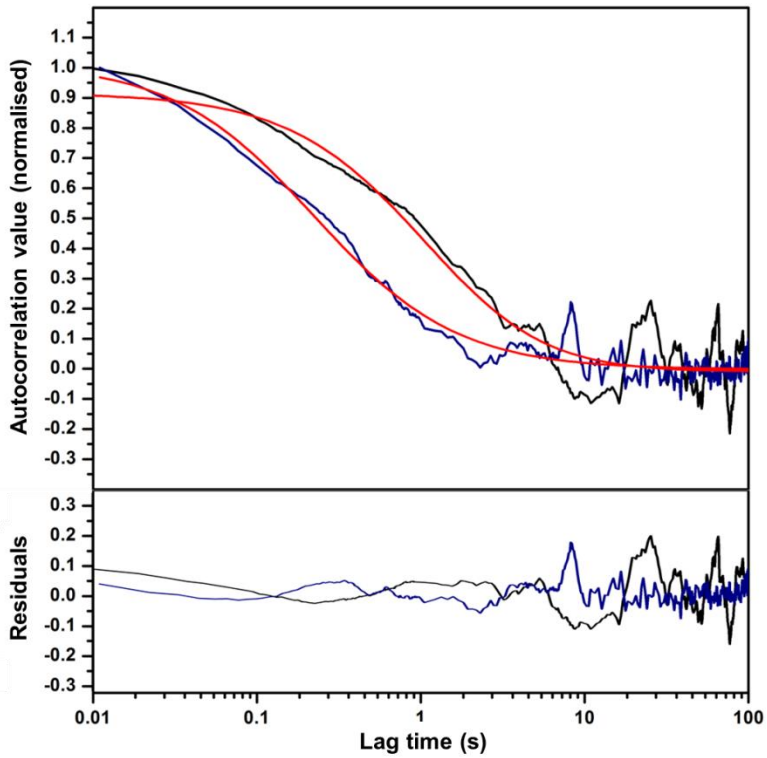

Figure VI.1 Autocorrelation curve, fits and associated residuals of diffusing QDs in 40 wt% (blue) and 60 wt% (black) glycerol-water solutions that were omitted in Figure 4.13 for clarity. The characteristic diffusion time obtained from fits increases with the solution viscosity.

Glycerol (wt%)	0	30	40	50	60	67
Viscosity (cP, 20°C)	1.005	2.50	3.72	6.00	10.8	17.7
τ_d (ms)	71 ± 2	162 ± 4	224 ± 11	453 ± 17	870 ± 63	1057 ± 51
N	4.3	17.5	6.4	10.1	5.8	7.8
R^2	0.98	0.98	0.94	0.97	0.92	0.97

Table 5. Viscosities and fit parameters of the viscosity titration assay for diffusing QDs using a 16 μm^2 detection volume and Equation (3.6).

Appendix VII

Random Walk Simulation

1. Simulation Assessment

The random walk simulation was implemented by creating a stack of frames corresponding to successive images separated by the desired acquisition time. Five hundred molecules were randomly distributed on a 256×256 pixels array. The equiprobability of direction between each molecule step was introduced using the "Random" command in ImageJ. The step length was obtained by sampling randomly a distance from two different distributions, corresponding to Equation (4.23) with $D_1 = 0.45$ μm^2/s and $D_2 = 0.90$ μm^2/s. The process was repeated for every step of each molecule and the stack of frames convolved with a PSF obtained using an ImageJ plugin [266] with the following parameters:

NA= 1.45; refractive index= 1.51; wavelength= 530 nm; lateral resolution= 100 nm;

The simulations were tested for different diffusion coefficients by measuring the average mean squared displacement ($\langle r^2 \rangle$) of the molecules over time, which is simply related to the time by the following relation, for a free diffusion in two dimensions [267]:

$$\langle r^2 \rangle = 4Dt \tag{VII.1}$$

Figure VII.1 displays the mean squared displacement for different values of the diffusion coefficient. The results obtained are consistent with the theoretical value given by Equation (VII.1).

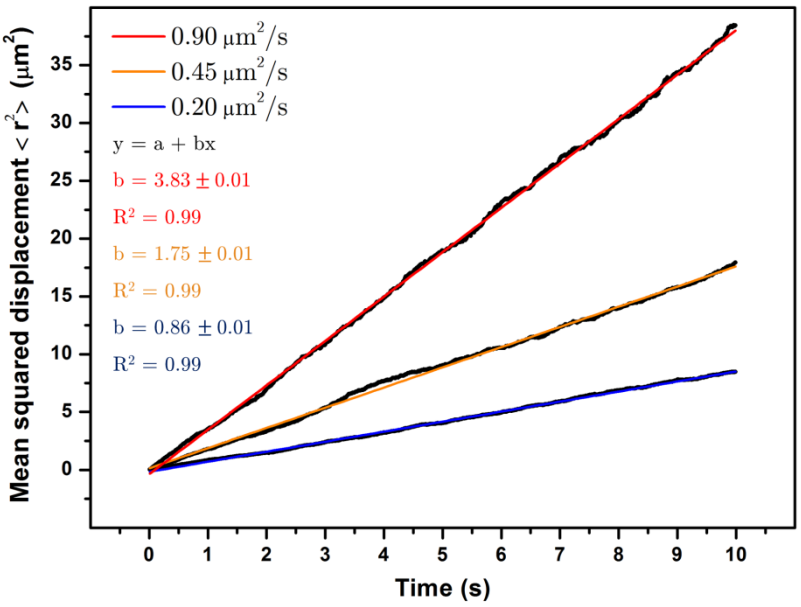

Figure VII.1. Mean squared displacement of 500 simulated emitters with different diffusion coefficients D_i and associated linear fits. The slopes of the linear regressions are in agreement with the expected value of $4D_i$.

2. Random Walk Algorithm

```
// Random walk simulation with areas of different diffusion coefficients //
// Input diffusion coefficients must be converted to match pixel size.   //
// The resulting movie is convolved with a theoretical or experimental   //
// PSF, whose resolution matches the desired pixel size of the movie.    //
// Noise can be added to final movie using RandomJ Poisson ImageJ plugin.//

setBatchMode(true);
x=0;
y=0;
a=getNumber("number of frames ", 0);

aa=getNumber("coordinate zone2 x min ", 0);
ab=getNumber("coordinate zone2 x max ", 0);
ba=getNumber("coordinate zone2 y min ", 0);
bb=getNumber("coordinate zone2 y max ", 0);

d1=getNumber("diffusion coefficient micrometers zone 1", 0.2);
d2=getNumber("diffusion coefficient micrometers zone 2", 0.1);
interval=getNumber("acquisition time seconds", 0.01);
```

```
z=getNumber("number of emitter ", 1);
q=getNumber("image size ", 256);
v=0;
w=0;
newImage("Movie", "32-bit Black",q,q,a);
      for(i=1; i<=z; i++)
      {
      setSlice(1);
      e=round(random*256);
      f=round(random*256);
      setPixel(e, f , 50*random);
            for (h=2; h<=a; h++){
            c=random;
            selectWindow("Movie");
            setSlice(h);
            b=sqrt(-4*d1*interval*log(random));
                  if ((e>=aa) && (e<=ab )) {
                        if ((f>=ba) && (f<=bb )) {
                        b=sqrt(-4*d2*interval*log(random));
                        }
                  }
                  if (c<=0.25)
                  {
                  selectWindow("Movie");
                  e=e+b;
                  setPixel(e, f , 50);
                  }
                  if ((c>0.25) && (c<=0.5 ))
                  {
                  selectWindow("Movie");
                  e=e-b;
                  setPixel(e, f , 50);
                  }
                  if ((c>0.5) && (c<=0.75 ))
                  {
                  selectWindow("Movie");
                  f=f+b;
                  setPixel(e, f , 50);
                  }
```

```
                    if (c>0.75)
                    {
                    selectWindow("Movie");
                    f=f-b;
                    setPixel(e, f , 50);
                    }
               }
          }
setBatchMode("exit and display");
```

Appendix VIII

DORIS Processing

1. Image Acquisition

Movies were recorded as a 512×512 pixel stack of 2500 frames, with an exposure time of 100 ms, using Micromanager Software. All data were then processed using ImageJ custom built macros

2. Image Processing

Images were processed in ImageJ using macro displayed in Section 5 of Appendix VIII. In an initial step all frames within an image stack were realigned to correct of stage drift during acquisition. The set of difference-images was initially produced by subtracting the j^{th} frame, A_{j} from the i^{th} frame, A_{i} for all i and $j >$ i in the raw dataset A. Potential QD dimers were identified as dipole-like objects in the difference-image with discernible intensity gradients across the diffraction-limited profile. Optional additional thresholding was simply added to decrease processing time. Each object was isolated in a ROI (typically 15×15 pixels area, but dependent on magnification). Background subtraction (intensity minimum) and intensity normalisation was performed frame-by-frame prior to repeating the subtraction process to obtain the difference amplitude. In general, intensity maxima and minima in the difference-image were obtained from the intensity mean in a 2×2 area containing the absolute maximum and separately the minimum intensity. In this case, the amplitude-to-separation curve was produced in an equivalent manner.

The set of difference-images, B, was further exploited to identify and hence separate frames in the raw image stack A into subsets in which one **[10]** or other **[01]** QD is switched on. Each QD was then localised in each frame by fitting a 2D Gaussian profile to the PSF using Levenberg-Marquardt, non-linear curve fitting in OriginPro 8.0 (OriginLab Coorp).

To test the effect of shot noise on measured amplitudes, photon statistics were applied to each PSF image, where the mean and variance μ of the Poisson distribution $\mu^{n}\exp^{-\mu}/n!$ is given by the intensity of each pixel. Amplitudes in the difference-image were calculated at increasing peak photon counts of 10^n for $n = 1$ to 6 with the standard deviation in amplitude determined from 100 simulations. Fluorophores undergoing stochastic intensity fluctuations beyond that arising from shot noise were simulated by sampling fluorescence intensities from a standard normal distribution about a mean photon count of 1000 photons. A polar method of sampling was used in which two random numbers u and v , uniform in the square (-1 < u < 1) and (-1 < v < 1) are selected under the condition ($s^2 = u^2 + v^2 < 1$) [268]. The returning value $z = u\sqrt{-\ln(s)/s}$ is then a random number distributed normally around 0 such that photon counts given by ($N = N_0 + \sigma z$) will also be normal about the mean N_0 with standard deviation σ. The single molecule image is generated by scaling the normalised PSF ($NA =$ 1.45, $n =$ 1.52, $\lambda =$ 530 nm and 47 nm/pixel resolution) by the randomly sampled counts. Separate image stacks for two molecules were produced for 100 intensities, one molecule being displaced from the other by translating the PSF source in the manner described above. The image stacks are combined frame by frame in sum, to produce the simulated image stack of a dimer to which shot noise is finally applied.

3. QD Separation Calculation

The distance between two PSFs located respectively at (x_1, y_1) and (x_2, y_2) is given by $r = \sqrt{\Delta x^2 + \Delta y^2}$, where $\Delta x = x_1 - x_2$ and $\Delta y = y_1 - y_2$. The uncertainties $\sigma_{x_1}, \sigma_{y_1}$ and $\sigma_{x_2}, \sigma_{y_2}$ in the coordinates of the two PSF were calculated using the relation [162] :

$$\sigma_d^2 = \frac{(\Delta x)^2}{(\Delta x)^2 + (\Delta y)^2} \times \left(\sigma_{x_1}^2 + \sigma_{x_2}^2\right) + \frac{(\Delta y)^2}{(\Delta x)^2 + (\Delta y)^2} \times \left(\sigma_{y_1}^2 + \sigma_{y_2}^2\right)$$

4. Simulations of Closely Spaced Emitters

PSFs were generated using an ImageJ plugin [266] using a scalar-based diffraction model with parameters defined by the numerical aperture, refractive index of the immersion medium, wavelength light and the system magnification that defines the lateral resolution r (nm/pixel) of the image. To generate amplitude-to-distance conversion curve, two PSFs separated by a distance d nm were simulated by translating one PSF by $(d\sin\theta/r)$ pixels along x and $(d\cos\theta/r)$ along y, where θ is the direction of displacement. The two normalised PSFs were then subtracted to produce a 32-bit image. The amplitude for different displacements of the PSF was calculated as the difference between the maximum intensity and minimum intensity in the difference-image. To test the effect of shot noise on measured amplitudes, photon statistics where applied each PSF image, where the mean and variance of the Poisson distribution is given by the intensity of each pixel.

5. DORIS Algorithm

```
// Full dataset difference algorithm, to be applied on 32-Bit stack      //
// of frames. Simple thresholding processes can be added to reduce       //
// computation time.                                                     //

setBatchMode(true);
rename("LR_Molstack");
Dialog.create("");
Dialog.addCheckbox("Differentiate before Subtration", false);
Dialog.show();
check=Dialog.getCheckbox();
      if (check==true) run("Find Edges", "stack");
      run("Set Measurements...", "  min redirect=None decimal=3");
selectWindow("LR_Molstack");
      for (i=1; i<=nSlices; i++){
      setSlice(i);
      run("Duplicate...", "title=LR_Molstack-1");
      run("Measure");
      max1=getResult("Max");
      run("Multiply...", "value="+1/max1);
```

```
	selectWindow("LR_Molstack");
		for (j=i; j<=nSlices; j++){
		setSlice(j);
		run("Duplicate...", "title=LR_Molstack-2");
		run("Measure");
		max2=getResult("Max");
		run("Multiply...", "value="+1/max2);
		imageCalculator("Subtract create 32-bit", "LR_Molstack-1",
		"LR_Molstack-2");
		run("Measure");
		max=getResult("Max");
		if (max==0) close();
		resetMinAndMax();
		selectWindow("LR_Molstack-2");
		close();
		selectWindow("LR_Molstack");
		}
	selectWindow("LR_Molstack-1");
	close();
	selectWindow("LR_Molstack");
	}
run("Images to Stack", "name=SubN+1 title=[] use");
setBatchMode(false);
resetMinAndMax();
run("Z Project...", "start=1 stop="+nSlices+" projection=[Max Intensity]");
resetMinAndMax();
selectWindow("Results");
run("Close");
```

Appendix IX

Two-dimensional DORIS Fitting Procedure

```
// Direct fitting of difference-images in two dimensions. The (x;y)      //
// array is transformed into a linear vector y=f(x), where (i;j) pixel   //
// intensity is associated to pixel n with y[n] the pixel intensity.     //
// One-dimensional ImageJ built in fitting process "y = f(x)" is         //
// applied according to the previously described mapping:                //
// x=n-round(n/w-0.5)*w                                                  //
// y=round(n/w-0.5)                                                      //
// where w is the width of the image.                                    //

h = getHeight();
w = getWidth();
x=newArray(h*w+1);
y=newArray(h*w+1);
n=0;
print("2D image array to 1D linear array")
print("i       j      x      y");
      for (j=0; j<=h-1; j++){
            for (i=0; i<=w-1; i++){
            x[n] = n;
            y[n] = getPixel(i,j);
            print(i+"     "+j+"     "+x[n]+"     "+y[n]);
            n++;
            }
      }

a = w/2; b= h/2; c = w/2; d = h/2; e=1;
```

```
initialGuesses = newArray(a, b, c, d, e);
GaussHerm =  "y =  (exp(-pow(x-round(x/"+w+"-0.5)*"+w+"-a,2)/(2*e*e))*exp(-
pow(round(x/"+w+"-0.5)-b,2)/(2*e*e))-exp(-pow(x-round(x/"+w+"-0.5)*"+w+"-
c,2)/(2*e*e))*exp(-pow(round(x/"+w+"+-0.5)-d,2)/(2*e*e)))";
Fit.logResults;
Fit.doFit(GaussHerm, x, y, initialGuesses);
Fit.plot;

x1 = Fit.p(0);
y1 = Fit.p(1);
x2 = Fit.p(2);
y2 = Fit.p(3);
s = Fit.p(4);
r = sqrt(pow(x1-x2, 2)+pow(y1-y2, 2))
newImage("Untitled", "32-bit Black", w, h, 1);
      for (y=0; y<=h-1; y++){
            for (x=0; x<=w-1; x++){
            z = (exp(-pow(x-x1,2)/(2*s*s))*exp(-pow(y-y1,2)/(2*s*s))-exp(-
            pow(x-x2,2)/(2*s*s))*exp(-pow(y-y2,2)/(2*s*s)));
            setPixel(x, y, z);
            }
      }
updateDisplay();
run("Enhance Contrast...", "saturated=0.4");
print("");
print("** Fitted parameters **");
print("A: "+a);
print("peak width and position in pixels");
print("sigma: "+s);
print("x1: "+x1+"     y1: "+y1);
print("x2: "+x2+"     y2: "+y2);
print("peak separation in pixels");
print("r : "+r);
```

Bibliography

1. Feynman, R.P., *There's plenty of room at the bottom.* Resonance, 2011. **16**(9): p. 890-905.

2. Weiss, S., *Fluorescence spectroscopy of single biomolecules.* Science, 1999. **283**(5408): p. 1676-1683.

3. Moerner, W.E. and L. Kador, *Optical detection and spectroscopy of single molecules in a solid.* Physical Review Letters, 1989. **62**(21): p. 2535-2538.

4. Eid, J., et al., *Real-time DNA sequencing from single polymerase molecules.* Science, 2009. **323**(5910): p. 133-138.

5. Funatsu, T., et al., *Imaging of single fluorescent molecules and individual ATP turnovers by single myosin molecules in aqueous solution.* Nature, 1995. **374**(6522): p. 555-559.

6. Deniz, A.A., et al., *Single-molecule protein folding: diffusion fluorescence resonance energy transfer studies of the denaturation of chymotrypsin inhibitor 2.* Proceedings of the National Academy of Sciences, 2000. **97**(10): p. 5179-5184.

7. Xie, X.S., *Single-molecule approach to dispersed kinetics and dynamic disorder: probing conformational fluctuation and enzymatic dynamics.* Journal of Chemical Physics, 2002. **117**(24): p. 11024-11032.

8. Bartko, A.P. and R.M. Dickson, *Three-dimensional orientations of polymer-bound single molecules.* The Journal of Physical Chemistry B, 1999. **103**(16): p. 3053-3056.

9. White, G.W., *Introduction to Microscopy*, Butterworths.

10. Hooke, R., *Micrographia: or, some physiological descriptions of minute bodies made by magnifying glasses. With observations and inquiries thereupon*. 1667: printed for James Allestry.

11. van Leeuwenhoek, A. and S. Hoole, *The Select Works of Antony Van Leeuwenhoek, Containing His Microscopical Discoveries in Many of the Works of Nature*. 1800: G. Sidney.

12. Rawlins, D.J., *Light microscopy*. 1992: Bios Scientific Publishers in association with the Biochemical Society.

13. Heimstädt, O., *Das fluoreszenzmikroskop.* Z. Wiss. Mikrosk., 1911. **28**: p. 330-337.

14. Ellinger, P. and A. Hirt, *Mikroskopische beobachtungen an lebenden organen mit demonstrationen (intravitalmikroskopie).* Naunyn-Schmiedebergs Archiv für experimentelle Pathologie und Pharmakologie, 1929. **147**(1-3): p. 63-63.

15. Ploem, J.S.J., *The use of a vertical illuminator with interchangeable dichroic mirrors for fluorescence microscopy with incidental light.* Z Wiss Mikrosk, 1967. **68**(3): p. 129-142.

16. *Nature Milestones: Light Microscopy*. 2009: Nature Publishing Group.

17. Uhl, R., *Arc lamps and monochromators for fluorescence microscopy.* Cold Spring Harbor Protocols, 2012. **2012**(9): p. 931-936.

18. Shimomura, O., F.H. Johnson, and Y. Saiga, *Extraction, purification and properties of Aequorin, a bioluminescent protein from the luminous hydromedusan, Aequorea.* Journal of Cellular and Comparative Physiology, 1962. **59**(3): p. 223-239.

19. Coons, A.H., H.J. Creech, and R.N. Jones, *Immunological properties of an antibody containing a fluorescent group.* Proceedings of the Society for Experimental Biology and Medicine. Society for Experimental Biology and Medicine (New York, N.Y.), 1941. **47**(2): p. 200-202.

20. Gunewardene, Mudalige S., et al., *Superresolution imaging of multiple fluorescent proteins with highly overlapping emission spectra in living cells.* Biophysical journal, 2011. **101**(6): p. 1522-1528.

21. Lippincott-Schwartz, J. and G.H. Patterson, *Photoactivatable fluorescent proteins for diffraction-limited and super-resolution imaging.* Trends in cell biology, 2009. **19**(11): p. 555-565.

22. Rendell, D., et al., *Fluorescence and phosphorescence spectroscopy*. 1987: Published on behalf of ACOL, London by Wiley.

23. Herschel , J., *On a case of superficial colour presented by a homogeneous liquid internally colourless.* Phil Trans Roy Soc London, 1845. **135**: p. 143–145.

24. Herschel , J., *On the epipolic dispersion of light; being a supplement to a paper entitled on a case of superficial colour presented by a homogeneous liquid internally colourless.* Abstracts of the Papers Communicated to the Royal Society of London, 1843. **5**: p. 549.

25. Stokes , G.G., *On the change of refrangibility of light.* Philosophical Transactions of the Royal Society of London 1852. **142**: p. 463-562

26. Lakowicz, J.R., *Principles of Fluorescence Spectroscopy*. 2006: Springer.

27. Bonnet, G., et al., *Thermodynamic basis of the enhanced specificity of structured DNA probes.* Proceedings of the National Academy of Sciences of the United States of America, 1999. **96**(11): p. 6171-6176.

28. Rasnik, I., S.A. McKinney, and T. Ha, *Nonblinking and long-lasting single-molecule fluorescence imaging.* Nat Meth, 2006. **3**(11): p. 891-893.

29. Davies, A.G. and J.M.T. Thompson, *Advances in Nanoengineering: Electronics, Materials, Assembly*. 2007: Imperial College Press.

30. Uphoff, S., et al., *Single-molecule DNA repair in live bacteria.* Proceedings of the National Academy of Sciences, 2013.

31. Dertinger, T., et al., *Superresolution optical fluctuation imaging (SOFI).* 733 ed. Advances in Experimental Medicine and Biology. 2011. 17-21.

32. Burnette, D.T., et al., *Bleaching/blinking assisted localization microscopy for superresolution imaging using standard fluorescent molecules.* Proceedings of the National Academy of Sciences of the United States of America, 2011. **108**(52): p. 21081-21086.

33. Gordon, M.P., T. Ha, and P.R. Selvin, *Single-molecule high-resolution imaging with photobleaching.* Proceedings of the National Academy of Sciences of the United States of America, 2004. **101**(17): p. 6462-6465.

34. Semrock, *SearchLight online database*, 2013.

35. Willem Borst, J. and A.J.W.G. Visser, *Fluorescence lifetime imaging microscopy in life sciences.* Measurement Science and Technology, 2010. **21**(10).

36. Van Munster, E.B. and T.W.J. Gadella, *Fluorescence lifetime imaging microscopy (FLIM)*, 2005. p. 143-175.

37. Chen, Y. and A. Periasamy, *Characterization of two-photon excitation fluorescence lifetime imaging microscopy for protein localization.* Microscopy Research and Technique, 2004. **63**(1): p. 72-80.

38. Wallrabe, H. and A. Periasamy, *Imaging protein molecules using FRET and FLIM microscopy.* Current Opinion in Biotechnology, 2005. **16**(1 SPEC. ISS.): p. 19-27.

39. Chen, Y., J.D. Mills, and A. Periasamy, *Protein localization in living cells and tissues using FRET and FLIM.* Differentiation, 2003. **71**(9-10): p. 528-541.

40. Chen, Y., et al., *The photon counting histogram in fluorescence fluctuation spectroscopy.* Biophysical Journal, 1999. **77**(1): p. 553-567.

41. Lippincott-Schwartz, J., E. Snapp, and A. Kemvorthy, *Studying protein dynamics in living cells.* Nature Reviews Molecular Cell Biology, 2001. **2**(6): p. 444-456.

42. Ward, T.H. and F. Brandizzi, *Dynamics of proteins in Golgi membranes: comparisons between mammalian and plant cells highlighted by photobleaching techniques.* Cellular and Molecular Life Sciences, 2004. **61**(2): p. 172-185.

43. Ha, T. and P. Tinnefeld, *Photophysics of fluorescent probes for single-molecule biophysics and super-resolution imaging*, 2012. p. 595-617.

44. Kawai, K., et al., *Probing the charge-transfer dynamics in DNA at the single-molecule level.* Journal of the American Chemical Society, 2011. **133**(39): p. 15568-15577.

45. Vogelsang, J., et al., *A Reducing and oxidizing system minimizes photobleaching and blinking of fluorescent dyes.* Angewandte Chemie International Edition, 2008. **47**(29): p. 5465-5469.

46. Bates, M., T.R. Blosser, and X. Zhuang, *Short-range spectroscopic ruler based on a single-molecule optical switch.* Physical Review Letters, 2005. **94**(10): p. 108101.

47. Dertinger, T., et al., *Fast, background-free, 3D super-resolution optical fluctuation imaging (SOFI).* Proceedings of the National Academy of Sciences of the United States of America, 2009. **106**(52): p. 22287-22292.

48. Steinhauer, C., et al., *Superresolution microscopy on the basis of engineered dark states.* Journal of the American Chemical Society, 2008. **130**(50): p. 16840-16841.

49. Larsson, A., et al., *Characterization of the binding of the fluorescent dyes YO and YOYO to DNA by polarized light spectroscopy.* Journal of the American Chemical Society, 1994. **116**(19): p. 8459-8465.

50. Sauer, M., J. Hofkens, and J. Enderlein, *Handbook of Fluorescence Spectroscopy and Imaging: From Ensemble to Single Molecules*. 2010: Wiley.

51. Day, R.N. and F. Schaufele, *Fluorescent protein tools for studying protein dynamics in living cells: a review.* Journal of Biomedical Optics, 2008. **13**(3): p. 031202-031202.

52. Shaner, N.C., P.A. Steinbach, and R.Y. Tsien, *A guide to choosing fluorescent proteins.* Nature Methods, 2005. **2**(12): p. 905-909.

53. Cody, C.W., et al., *Chemical structure of the hexapeptide chromophore of the aequorea green-fluorescent protein.* Biochemistryff, 1993. **32**(5): p. 1212-1218.

54. Dickson, R.M., et al., *On/off blinking and switching behaviour of single molecules of green fluorescent protein.* Nature, 1997. **388**(6640): p. 355-358.

55. McAnaney, T.B., et al., *Protonation, photobleaching, and photoactivation of yellow fluorescent protein (YFP 10C): a unifying mechanism.* Biochemistry, 2005. **44**(14): p. 5510-5524.

56. Moerner, W.E., *Single-molecule optical spectroscopy of autofluorescent proteins.* Journal of Chemical Physics, 2002. **117**(24): p. 10925-10937.

57. Reed, M.A., et al., *Spatial quantization in GaAs-AlGaAs multiple quantum dots.* Journal of Vacuum Science and Technology B: Microelectronics and Nanometer Structures, 1986. **4**(1): p. 358-360.

58. Bawendi, M.G., et al., *Luminescence properties of CdSe quantum crystallites: resonance between interior and surface localized states.* The Journal of Chemical Physics, 1992. **96**(2): p. 946-954.

59. Murray, C.B., D.J. Norris, and M.G. Bawendi, *Synthesis and characterization of nearly monodisperse CdE (E = S, Se, Te) semiconductor nanocrystallites.* Journal of the American Chemical Society, 1993. **115**(19): p. 8706-8715.

60. Antao, V.P., S.Y. Lai, and I. Tinoco Jr., *A thermodynamic study of unusually stable RNA and DNA hairpins.* Nucleic Acids Research, 1991. **19**(21): p. 5901-5905.

61. Cook, R.J. and H.J. Kimble, *Possibility of direct observation of quantum jumps.* Physical Review Letters, 1985. **54**(10): p. 1023-1026.

62. Kuno, M., et al., *"On"/"off" fluorescence intermittency of single semiconductor quantum dots.* Journal of Chemical Physics, 2001. **115**(2): p. 1028-1040.

63. Krauss, T.D. and J.J. Peterson, *Quantum dots: a charge for blinking.* Nature Materials, 2012. **11**(1): p. 14-16.

64. Tang, J. and R.A. Marcus, *Single particle versus ensemble average: from power-law intermittency of a single quantum dot to quasistretched exponential fluorescence decay of an ensemble.* Journal of Chemical Physics, 2005. **123**(20): p. 1-6.

65. Kuno, M., et al., *Modeling distributed kinetics in isolated semiconductor quantum dots.* Physical Review B - Condensed Matter and Materials Physics, 2003. **67**(12): p. 1253041-12530415.

66. Nirmal, M., et al., *Fluorescence intermittency in single cadmium selenide nanocrystals.* Nature, 1996. **383**(6603): p. 802-804.

67. Galland, C., et al., *Two types of luminescence blinking revealed by spectroelectrochemistry of single quantum dots.* Nature, 2011. **479**(7372): p. 203-207.

68. Hohng, S. and T. Ha, *Near-complete suppression of quantum dot blinking in ambient conditions.* Journal of the American Chemical Society, 2004. **126**(5): p. 1324-1325.

69. Hollingsworth, J.A., et al. *'Giant' multishell CdSe nanocrystal quantum dots with suppressed blinking: novel fluorescent probes for real-time detection of single-molecule events*. 2009.

70. Gell, C., D. Brockwell, and A. Smith, *Handbook of Single Molecule Fluorescence Spectroscopy*. 2006: Oxford University Press.

71. Gordon, G.W., et al., *Quantitative fluorescence resonance energy transfer measurements using fluorescence microscopy.* Biophysical Journal, 1998. **74**(5): p. 2702-2713.

72. Wallace, M.L., et al., *FRET fluctuation spectroscopy: exploring the conformational dynamics of a DNA hairpin loop.* Journal of Physical Chemistry B, 2000. **104**(48): p. 11551-11555.

73. French, A.P., et al., *Colocalization of fluorescent markers in confocal microscope images of plant cells.* Nat. Protocols, 2008. **3**(4): p. 619-628.

74. Scriven, D.R.L., R.M. Lynch, and E.D.W. Moore, *Image acquisition for colocalization using optical microscopy.* American Journal of Physiology - Cell Physiology, 2008. **294**(5): p. C1119-C1122.

75. Janesick, J.R., *Scientific Charge-Coupled Devices*. 2001: SPIE Press.

76. Petty, H.R., *Fluorescence microscopy: established and emerging methods, experimental strategies, and applications in immunology.* Microscopy Research and Technique, 2007. **70**(8): p. 687-709.

77. Young, I.T., J.J. Gerbrands, and L.J. van Vliet, *Fundamentals of Image Processing*. 1995: TU Delft, Faculty of Applied Physics, Pattern Recognition Group.

78. Young, I.T., *Quantitative microscopy.* Engineering in Medicine and Biology Magazine, IEEE, 1996. **15**(1): p. 59-66.

79. Denvir, D.J. and E. Conroy. *Electron multiplying CCD technology: the new ICCD*. 2002.

80. Robbins, M.S. and B.J. Hadwen, *The noise performance of electron multiplying charge-coupled devices.* IEEE Transactions on Electron Devices, 2003. **50**(5): p. 1227-1232.

81. Neumann, M. and D. Gabel, *Simple method for reduction of autofluorescence in fluorescence microscopy.* J Histochem Cytochem, 2002. **50**(3): p. 437-9.

82. Michalet, X., et al., *Quantum dots for live cells, in vivo imaging, and diagnostics.* Science, 2005. **307**(5709): p. 538-544.

83. Van de Lest, C.H.A., et al., *Elimination of autofluorescence in immunofluorescence microscopy with digital image processing.* Journal of Histochemistry and Cytochemistry, 1995. **43**(7): p. 727-730.

84. Russ, J.C., *The Image Processing Handbook*. 2002: Crc Press.

85. Bartlett, J.S., et al., *Raman scattering by pure water and seawater.* Applied Optics, 1998. **37**(15): p. 3324-3332.

86. Minsky, M., *Memoir on inventing the confocal scanning microscope.* Scanning, 1988. **10**(4): p. 128-138.

87. Petran, M., et al., *Tandem-scanning reflected-light microscope.* J. Opt. Soc. Am., 1968. **58**(5): p. 661-664.

88. Davidovits, P. and M.D. Egger, *Photomicrography of corneal endothelial cells in vivo.* Nature, 1973. **244**(5415): p. 366-367.

89. Draaijer, A. and P.M. Houpt, *A standard video-rate confocal laser-scanning reflection and fluorescence microscope.* Scanning, 1988. **10**(4): p. 139-145.

90. Amos, W.B. and J.G. White, *How the confocal laser scanning microscope entered biological research.* Biology of the Cell, 2003. **95**(6): p. 335-342.

91. Webb, R., *Confocal optical microscopy.* Reports on Progress in Physics, 1996. **59**(3): p. 427.

92. Göppert-Mayer, M., *Über elementarakte mit zwei quantensprüngen.* Annalen der Physik, 1931. **401**(3): p. 273-294.

93. Sheppard, C.J.R. and R. Kompfner, *Resonant scanning optical microscope.* Appl. Opt., 1978. **17**(18): p. 2879-2882.

94. Diaspro, A., G. Chirico, and M. Collini, *Two-photon fluorescence excitation and related techniques in biological microscopy.* Quarterly Reviews of Biophysics, 2005. **38**(02): p. 97-166.

95. Diaspro, A., et al., *Multi-photon excitation microscopy.* BioMedical Engineering Online, 2006. **5**.

96. Axelrod, D., *Cell-substrate contacts illuminated by total internal reflection fluorescence.* The Journal of Cell Biology, 1981. **89**(1): p. 141-145.

97. Mattheyses, A.L., S.M. Simon, and J.Z. Rappoport, *Imaging with total internal reflection fluorescence microscopy for the cell biologist.* Journal of Cell Science, 2010. **123**(21): p. 3621-3628.

98. Axelrod, D., *Total internal reflection fluorescence microscopy in cell biology.* Traffic, 2001. **2**(11): p. 764-774.

99. Fletcher, S.J., et al., *Clathrin-mediated endocytosis regulates occludin, and not focal adhesion, distribution during epithelial wound healing.* Biology of the Cell, 2012. **104**(4): p. 238-256.

100. Groves, J.T., R. Parthasarathy, and M.B. Forstner, *Fluorescence imaging of membrane dynamics*, 2008. p. 311-338.

101. Hecht, E., *Optics*. 2002: Addison-Wesley.

102. Axelrod, D., T.P. Burghardt, and N.L. Thompson, *Total internal reflection fluorescence.* Annual review of biophysics and bioengineering, 1984. **13**: p. 247-268.

103. Cortese, K., A. Diaspro, and C. Tacchetti, *Advanced correlative light/electron microscopy: current methods and new developments using Tokuyasu cryosections.* Journal of Histochemistry & Cytochemistry, 2009. **57**(12): p. 1103-1112.

104. Leung, B.O. and K.C. Chou, *Review of super-resolution fluorescence microscopy for biology.* Applied Spectroscopy, 2011. **65**(9): p. 967-980.

105. Yildiz, A., et al., *Myosin V walks hand-over-hand: single fluorophore imaging with 1.5-nm localization.* Science, 2003. **300**.

106. Schmidt, R., et al., *Mitochondrial cristae revealed with focused light.* Nano Letters, 2009. **9**(6): p. 2508-2510.

107. Biteen, J.S., et al. *Superresolution imaging in live Caulobacter crescentus cells using photoswitchable enhanced yellow fluorescent protein*. 2009.

108. Hess, S.T., et al., *Dynamic clustered distribution of hemagglutinin resolved at 40 nm in living cell membranes discriminates between raft theories.* Proceedings of the National Academy of Sciences of the United States of America, 2007. **104**(44): p. 17370-17375.

109. Wu, Q., F. Merchant, and K.R. Castleman, *Microscope Image Processing*. 2008: Elsevier/Academic Press.

110. Huang, B., M. Bates, and X. Zhuang, *Super-resolution fluorescence microscopy* 2009, Annual Review of Biochemistry. p. 993-1016.

111. Goodman, J.W., *Introduction to Fourier Optics*. 2005: Roberts & Company.

112. Abbe, E., *Archiv für Mikroskopische Anatomie*. 1873: F. Cohen.

113. Rayleigh, L., *On the theory of optical images, with special reference to the microscope.* Philosophical Magazine, 1896. **42**: p. 167-195.

114. Sparrow, C.M., *On Spectroscopic Resolving Power*. Vol. 178. 2004: Society of Photo-Optical Instrumentation Engineers. 6.

115. Cannel, M., A. McMorland, and C. Soeller, *Image Enhancement by Deconvolution*. 2006: Springer.

116. Sarder, P. and A. Nehorai, *Deconvolution methods for 3-D fluorescence microscopy images.* IEEE Signal Processing Magazine, 2006. **23**(3): p. 32-45.

117. Sibarita, J.-B., *Deconvolution microscopy*. 95 ed. Advances in Biochemical Engineering/Biotechnology. 2005. 201-243.

118. Schermelleh, L., R. Heintzmann, and H. Leonhardt, *A guide to super-resolution fluorescence microscopy.* Journal of Cell Biology, 2010. **190**(2): p. 165-175.

119. Cappello, G., et al., *Kinesin motion in the absence of external forces characterized by interference total internal reflection microscopy.* Physical Review E - Statistical, Nonlinear, and Soft Matter Physics, 2003. **68**(2 1): p. 021907/1-021907/7.

120. Notcovich, A.G., V. Zhuk, and S.G. Lipson, *Surface plasmon resonance phase imaging.* Applied Physics Letters, 2000. **76**(13): p. 1665-1667.

121. Bailey, B., et al., *Enhancement of axial resolution in fluorescence microscopy by standing-wave excitation.* Nature, 1993. **366**(6450): p. 44-48.

122. Betzig, E. and J.K. Trautman, *Near-field optics: microscopy, spectroscopy, and surface modification beyond the diffraction limit.* Science (New York, N.Y.), 1992. **257**(5067): p. 189-195.

123. De Lange, F., et al., *Cell biology beyond the diffraction limit: near-field scanning optical microscopy.* Journal of Cell Science, 2001. **114**(23): p. 4153-4160.

124. Enderle, T., et al., *Membrane specific mapping and colocalization of malarial and host skeletal proteins in the Plasmodium falciparum infected erythrocyte by dual-color near-field scanning optical microscopy.* Proceedings of the National Academy of Sciences of the United States of America, 1997. **94**(2): p. 520-525.

125. Heintzmann, R., et al., *Resolution enhancement by subtraction of confocal signals taken at different pinhole sizes.* Micron, 2003. **34**(6–7): p. 293-300.

126. Gustafsson, M.G.L., D.A. Agard, and J.W. Sedat, *I^{5}M: 3D widefield light microscopy with better than 100 nm axial resolution.* Journal of Microscopy, 1999. **195**(1): p. 10-16.

127. Lang, M.C., J. Engelhardt, and S.W. Hell, *4Pi microscopy with linear fluorescence excitation.* Optics Letters, 2007. **32**(3): p. 259-261.

128. Egner, A. and S.W. Hell, *Fluorescence microscopy with super-resolved optical sections.* Trends in Cell Biology, 2005. **15**(4): p. 207-215.

129. Egner, A., S. Jakobs, and S.W. Hell, *Fast 100-nm resolution three-dimensional microscope reveals structural plasticity of mitochondria in live yeast.* Proceedings of the National Academy of Sciences of the United States of America, 2002. **99**(6): p. 3370-3375.

130. Egner, A., et al., *4Pi-microscopy of the Golgi apparatus in live mammalian cells.* Journal of Structural Biology, 2004. **147**(1): p. 70-76.

131. Gustafsson, M.G.L., *Surpassing the lateral resolution limit by a factor of two using structured illumination microscopy.* Journal of Microscopy, 2000. **198**(2): p. 82-87.

132. Gustafsson, M.G.L., et al., *Three-dimensional resolution doubling in wide-field fluorescence microscopy by structured illumination.* Biophysical Journal, 2008. **94**(12): p. 4957-4970.

133. Shao, L., et al., *I^{5}S: Wide-field light microscopy with 100-nm-scale resolution in three dimensions.* Biophysical Journal, 2008. **94**(12): p. 4971-4983.

134. Hell, S.W. and J. Wichmann, *Breaking the diffraction resolution limit by stimulated emission: stimulated-emission-depletion fluorescence microscopy.* Optics Letters, 1994. **19**(11): p. 780-782.

135. Heintzmann, R., *Saturated patterned excitation microscopy with two-dimensional excitation patterns.* Micron, 2003. **34**(6-7): p. 283-291.

136. Hell, S.W., *Far-field optical nanoscopy.* Science, 2007. **316**(5828): p. 1153-1158.

137. Dyba, M. and S.W. Hell, *Focal spots of size $\lambda/23$ open up far-field fluorescence microscopy at 33 nm axial resolution.* Physical Review Letters, 2002. **88**(16): p. 163901.

138. Hofmann, M., et al., *Breaking the diffraction barrier in fluorescence microscopy at low light intensities by using reversibly photoswitchable proteins.* Proceedings of the National Academy of Sciences of the United States of America, 2005. **102**(49): p. 17565-17569.

139. Hell, S.W. and M. Kroug, *Ground-state-depletion fluorescence microscopy: a concept for breaking the diffraction resolution limit.* Applied Physics B Lasers and Optics, 1995. **60**(5): p. 495-497.

140. Kolmakov, K., et al., *Red-emitting rhodamine dyes for fluorescence microscopy and nanoscopy.* Chemistry - A European Journal, 2010. **16**(1): p. 158-166.

141. Grotjohann, T., et al., *Diffraction-unlimited all-optical imaging and writing with a photochromic GFP.* Nature, 2011. **478**(7368): p. 204-208.

142. Stallinga, S. and B. Rieger, *Accuracy of the gaussian point spread function model in 2D localization microscopy.* Optics Express, 2010. **18**(24): p. 24461-24476.

143. Cheezum, M.K., W.F. Walker, and W.H. Guilford, *Quantitative comparison of algorithms for tracking single fluorescent particles.* Biophysical journal, 2001. **81**(4): p. 2378-2388.

144. Shannon, C.E., *A mathematical theory of communication.* Bell System Technical Journal 1948. **27**(3): p. 379-423.

145. Jerri, A.J., *The Shannon sampling theorem; its various extensions and applications: a tutorial review.* Proceedings of the IEEE, 1977. **65**(11): p. 1565-1596.

146. Gould, T.J., V.V. Verkhusha, and S.T. Hess, *Imaging biological structures with fluorescence photoactivation localization microscopy.* Nature Protocols, 2009. **4**(3): p. 291-308.

147. Thompson, R.E., D.R. Larson, and W.W. Webb, *Precise nanometer localization analysis for individual fluorescent probes.* Biophysical Journal, 2002. **82**(5): p. 2775-2783.

148. Mortensen, K.I., et al., *Optimized localization analysis for single-molecule tracking and super-resolution microscopy.* Nature Methods, 2010. **7**(5): p. 377-381.

149. Deschout, H., K. Neyts, and K. Braeckmans, *The influence of movement on the localization precision of sub-resolution particles in fluorescence microscopy.* Journal of Biophotonics, 2012. **5**(1): p. 97-109.

150. Hess, H.F., et al., *Near-field spectroscopy of the quantum constituents of a luminescent system.* Science, 1994. **264**(5166): p. 1740-1745.

151. Betzig, E., *Proposed method for molecular optical imaging.* Optics Letters, 1995. **20**(3): p. 237-239.

152. Heilemann, M., et al., *Photoswitches: key molecules for subdiffraction-resolution fluorescence imaging and molecular quantification.* Laser & Photonics Reviews, 2009. **3**(1-2): p. 180-202.

153. Fernández-Suárez, M. and A.Y. Ting, *Fluorescent probes for super-resolution imaging in living cells.* Nature Reviews Molecular Cell Biology, 2008. **9**(12): p. 929-943.

154. Rust, M.J., M. Bates, and X. Zhuang, *Sub-diffraction-limit imaging by stochastic optical reconstruction microscopy (STORM).* Nature Methods, 2006. **3**(10): p. 793-795.

155. Betzig, E., et al., *Imaging intracellular fluorescent proteins at nanometer resolution.* Science, 2006. **313**(5793): p. 1642-1645.

156. Hess, S.T., T.P.K. Girirajan, and M.D. Mason, *Ultra-high resolution imaging by fluorescence photoactivation localization microscopy.* Biophysical Journal, 2006. **91**(11): p. 4258-4272.

157. McKinney, S.A., et al., *A bright and photostable photoconvertible fluorescent protein.* Nature Methods, 2009. **6**(2): p. 131-133.

158. Henriques, R., et al., *QuickPALM: 3D real-time photoactivation nanoscopy image processing in ImageJ.* Nature Methods, 2010. **7**(5): p. 339-340.

159. Toprak, E., et al., *Defocused orientation and position imaging (DOPI) of myosin V.* Proceedings of the National Academy of Sciences of the United States of America, 2006. **103**(17): p. 6495-6499.

160. Churchman, L.S., et al., *Single molecule high-resolution colocalization of Cy3 and Cy5 attached to macromolecules measures intramolecular distances through time.* Proceedings of the National Academy of Sciences of the United States of America, 2005. **102**(5): p. 1419-1423.

161. Sharonov, A. and R.M. Hochstrasser, *Wide-field subdiffraction imaging by accumulated binding of diffusing probes.* Proceedings of the National Academy of Sciences of the United States of America, 2006. **103**(50): p. 18911-18916.

162. Qu, X., et al., *Nanometer-localized multiple single-molecule fluorescence microscopy.* Proceedings of the National Academy of Sciences of the United States of America, 2004. **101**(31): p. 11298-11303.

163. Lidke, K.A., et al., *Superresolution by localization of quantum dots using blinking statistics.* Optics Express, 2005. **13**(18): p. 7052-7062.

164. Lagerholm, B.C., et al., *Analysis method for measuring submicroscopic distances with blinking quantum dots.* Biophysical Journal, 2006. **91**(8): p. 3050-3060.

165. Shi, X., et al., *Superlocalization spectral imaging microscopy of a multicolor quantum dot complex.* Analytical Chemistry, 2012. **84**(3): p. 1504-1509.

166. Enderlein, J., et al., *Art and artefacts of fluorescence correlation spectroscopy.* Current Pharmaceutical Biotechnology, 2004. **5**(2): p. 155-161.

167. Nagy, A., J. Wu, and K.M. Berland, *Characterizing observation volumes and the role of excitation saturation in one-photon fluorescence fluctuation spectroscopy.* Journal of Biomedical Optics, 2005. **10**(4).

168. Krichevsky, O. and G. Bonnet, *Fluorescence correlation spectroscopy: the technique and its applications.* Rep.Prog.Phys., 2002. **65**: p. 251-297.

169. Du, H., et al., *PhotochemCAD‡: a computer-aided design and research tool in photochemistry.* Photochemistry and Photobiology, 1998. **68**(2): p. 141-142.

170. Forkey, J.N., M.E. Quinlan, and Y.E. Goldman, *Protein structural dynamics by single-molecule fluorescence polarization.* Progress in Biophysics and Molecular Biology, 2000. **74**(1–2): p. 1-35.

171. Wakelin, S. and C.R. Bagshaw, *A prism combination for near isotropic fluorescence excitation by total internal reflection.* Journal of Microscopy, 2003. **209**(2): p. 143-148.

172. Christen, F., et al., *Fast conversion factor (gain) measurement of a CCD using images with vertical gradient*, in *Scientific Detectors for Astronomy 2005*, J. Beletic, J. Beletic, and P. Amico, Editors. 2006, Springer Netherlands. p. 537-542.

173. Meister, P., et al., *Nuclear factories for signalling and repairing DNA double strand breaks in living fission yeast.* Nucleic Acids Research, 2003. **31**(17): p. 5064-5073.

174. Sternberg, S.R., *Biomedical image processing.* Computer, 1983. **16**(1): p. 22-34.

175. Magde, D., E. Elson, and W.W. Webb, *Thermodynamic fluctuations in a reacting system measurement by fluorescence correlation spectroscopy.* Physical Review Letters, 1972. **29**(11): p. 705-708.

176. Rigler, R., et al., *Fluorescence correlation spectroscopy with high count rate and low background: analysis of translational diffusion.* European Biophysics Journal, 1993. **22**(3): p. 169-175.

177. Kinjo, M. and R. Rigler, *Ultrasensitive hybridization analysis using fluorescence correlation spectroscopy.* Nucleic Acids Research, 1995. **23**(10): p. 1795-1799.

178. Nettels, D., A. Hoffmann, and B. Schuler, *Unfolded protein and peptide dynamics investigated with single-molecule FRET and correlation spectroscopy from picoseconds to seconds.* Journal of Physical Chemistry B, 2008. **112**(19): p. 6137-6146.

179. Nordlund, P. and P. Reichard, *Ribonucleotide reductases.* Annual Review of Biochemistry, 2006. **75**(1): p. 681-706.

180. Elledge, S.J., Z. Zhou, and J.B. Allen, *Ribonucleotide reductase: regulation, regulation, regulation.* Trends in Biochemical Sciences, 1992. **17**(3): p. 119-123.

181. Chabes, A. and B. Stillman, *Constitutively high dNTP concentration inhibits cell cycle progression and the DNA damage checkpoint in yeast Saccharomyces cerevisiae.* Proceedings of the National Academy of Sciences of the United States of America, 2007. **104**(4): p. 1183-1188.

182. Cotruvo, J.A. and J. Stubbe, *Class I ribonucleotide reductases: metallocofactor assembly and repair in vitro and in vivo.* Annual Review of Biochemistry, 2011. **80**(1): p. 733-767.

183. Shao, J., et al., *Ribonucleotide reductase inhibitors and future drug design.* Current Cancer Drug Targets, 2006. **6**(5): p. 409-431.

184. Hurd, H.K., C.W. Roberts, and J.W. Roberts, *Identification of the gene for the yeast ribonucleotide reductase small subunit and its inducibility by methyl methanesulfonate.* Molecular and Cellular Biology, 1987. **7**(10): p. 3673-3677.

185. Uhlin, U. and H. Eklund, *Structure of ribonucleotide reductase protein R1.* Nature, 1994. **370**(6490): p. 533-539.

186. Larsson, A., et al., *Radical formation in the dimeric small subunit of ribonucleotide reductase requires only one tyrosine 122.* Journal of Biological Chemistry, 1988. **263**(33): p. 17780-4.

187. Nestoras, K., et al., *Regulation of ribonucleotide reductase by Spd1 involves multiple mechanisms.* Genes and Development, 2010. **24**(11): p. 1145-1159.

188. Schwille, P. and U. Kettling, *Analyzing single protein molecules using optical methods.* Current Opinion in Biotechnology, 2001. **12**(4): p. 382-386.

189. Eggeling, C., et al., *Monitoring conformational dynamics of a single molecule by selective fluorescence spectroscopy.* Proceedings of the National Academy of Sciences of the United States of America, 1998. **95**(4): p. 1556-1561.

190. Haustein, E. and P. Schwille, *Fluorescence correlation spectroscopy: novel variations of an established technique*. 36 ed. Annual Review of Biophysics and Biomolecular Structure. 2007. 151-169.

191. Enderlein, J., et al., *Performance of fluorescence correlation spectroscopy for measuring diffusion and concentration.* ChemPhysChem, 2005. **6**(11): p. 2324-2336.

192. Charier, S., et al., *Reactant concentrations from fluorescence correlation spectroscopy with tailored fluorescent probes. An example of local calibration-free pH measurement.* Journal of the American Chemical Society, 2005. **127**(44): p. 15491-15505.

193. Enderlein, J., et al., *Statistical analysis of diffusion coefficient determination by fluorescence correlation spectroscopy.* Journal of Fluorescence, 2005. **15**(3): p. 415-422.

194. Liedl, T., et al., *Fluorescent nanocrystals as colloidal probes in complex fluids measured by fluorescence correlation spectroscopy.* Small, 2005. **1**(10): p. 997-1003.

195. Rhoades, E., et al., *Quantification of α-synuclein binding to lipid vesicles using fluorescence correlation spectroscopy.* Biophysical Journal, 2006. **90**(12): p. 4692-4700.

196. Sherman, E., et al., *Using fluorescence correlation spectroscopy to study conformational changes in denatured proteins.* Biophysical Journal, 2008. **94**(12): p. 4819-4827.

197. Petersen, N.O., *Scanning fluorescence correlation spectroscopy. Theory and simulation of aggregation measurements.* Biophysical journal, 1986. **49**(4): p. 809-815.

198. Kolin, D. and P. Wiseman, *Advances in image correlation spectroscopy: measuring number densities, aggregation states, and dynamics of fluorescently labeled macromolecules in cells.* Cell Biochemistry and Biophysics, 2007. **49**(3): p. 141-164.

199. Berland, K.M., P.T.C. So, and E. Gratton, *Two-photon fluorescence correlation spectroscopy: method and application to the intracellular environment.* Biophysical Journal, 1995. **68**(2 I): p. 694-701.

200. Schwille, P., F.J. Meyer-Almes, and R. Rigler, *Dual-color fluorescence cross-correlation spectroscopy for multicomponent diffusional analysis in solution.* Biophysical Journal, 1997. **72**(4): p. 1878-1886.

201. Heinze, K.G., et al., *Two-photon fluorescence coincidence analysis: rapid measurements of enzyme kinetics.* Biophysical Journal, 2002. **83**(3): p. 1671-1681.

202. Dertinger, T., et al., *Two-focus fluorescence correlation spectroscopy: a new tool for accurate and absolute diffusion measurements.* ChemPhysChem, 2007. **8**(3): p. 433-443.

203. Müller, C.B., et al., *Dual-focus fluorescence correlation spectroscopy: a robust tool for studying molecular crowding.* Soft Matter, 2009. **5**(7): p. 1358-1366.

204. Seiler, M.C. and F.A. Seiler, *Numerical recipes in C: the art of scientific computing.* Risk Analysis, 1989. **9**(3): p. 415-416.

205. Wohland, T., R. Rigler, and H. Vogel, *The standard deviation in fluorescence correlation spectroscopy.* Biophysical Journal, 2001. **80**(6): p. 2987-2999.

206. Dougherty, B., *Convolve 3D plugin,* http://www.optinav.com, 2005.

207. Tcherniak, A., et al., *Fluorescence correlation spectroscopy: criteria for analysis in complex systems.* Analytical Chemistry, 2009. **81**(2): p. 746-754.

208. Ries, J., et al., *Automated suppression of sample-related artifacts in fluorescence correlation spectroscopy.* Optics Express, 2010. **18**(11): p. 11073-11082.

209. Einstein, A., *Eine neue Bestimmung der Moleküldimensionen: Inaugural-Dissertation*. 1905: Universität Zürich.

210. Einstein, A., *Über die von der Molekularkinetischen Theorie der Wärme Geforderte Bewegung von in Ruhenden Flüssigkeiten Suspendierten Teilchen*. 1905: J. Barth.

211. Purcell, E.M., *Life at low Reynolds number.* American Journal of Physics, 1977. **45**(1): p. 3-11.

212. Kettling, U., et al., *Real-time enzyme kinetics monitored by dual-color fluorescence cross-correlation spectroscopy.* Proceedings of the National Academy of Sciences of the United States of America, 1998. **95**(4): p. 1416-1420.

213. Selvin, P.R. and T. Ha, *Single-molecule Techniques: a Laboratory Manual*. 2008: Cold Spring Harbor Laboratory Press.

214. Rusu, L., et al., *Fluorescence correlation spectroscopy studies of peptide and protein binding phospholipid vesicles.* Biophysical Journal, 2004. **87**(2): p. 1044-1053.

215. Partikian, A., et al., *Rapid diffusion of green fluorescent protein in the mitochondrial matrix.* The Journal of Cell Biology, 1998. **140**(4): p. 821-829.

216. Culbertson, C.T., S.C. Jacobson, and J. Michael Ramsey, *Diffusion coefficient measurements in microfluidic devices.* Talanta, 2002. **56**(2): p. 365-373.

217. Gendron, P.O., F. Avaltroni, and K.J. Wilkinson, *Diffusion coefficients of several rhodamine derivatives as determined by pulsed field gradient-nuclear magnetic resonance and fluorescence correlation spectroscopy.* Journal of Fluorescence, 2008. **18**(6): p. 1093-1101.

218. Li, X., et al., *Deletions of the Aequorea victoria green fluorescent protein define the minimal domain required for fluorescence.* Journal of Biological Chemistry, 1997. **272**(45): p. 28545-28549.

219. Schenk, A., et al., *Photodynamics of red fluorescent proteins studied by fluorescence correlation spectroscopy.* Biophysical journal, 2004. **86**(1): p. 384-394.

220. Petrášek, Z. and P. Schwille, *Precise measurement of diffusion coefficients using scanning fluorescence correlation spectroscopy.* Biophysical Journal, 2008. **94**(4): p. 1437-1448.

221. Rüttinger, S., et al., *Comparison and accuracy of methods to determine the confocal volume for quantitative fluorescence correlation spectroscopy.* Journal of Microscopy, 2008. **232**(2): p. 343-352.

222. Tsien, R.Y., *The green fluorescent protein*, 1998. p. 509-544.

223. Pack, C.G., et al., *Analysis of interaction between chaperonin GroEL and its substrate using fluorescence correlation spectroscopy.* Cytometry, 1999. **36**(3): p. 247-253.

224. Meyer, T. and H. Schindler, *Particle counting by fluorescence correlation spectroscopy. Simultaneous measurement of aggregation and diffusion of molecules in solutions and in membranes.* Biophysical Journal, 1988. **54**(6): p. 983-993.

225. Palmer, A.G. and N.L. Thompson, *Fluorescence correlation spectroscopy for detecting submicroscopic clusters of fluorescent molecules in membranes.* Chemistry and Physics of Lipids, 1989. **50**(3-4): p. 253-270.

226. Sengupta, P., et al., *Measuring size distribution in highly heterogeneous systems with fluorescence correlation spectroscopy.* Biophysical Journal, 2003. **84**(3): p. 1977-1984.

227. Das, S.K., et al., *Membrane protein stoichiometry determined from the step-wise photobleaching of dye-labelled subunits.* ChemBioChem, 2007. **8**(9): p. 994-999.

228. Jain, A., et al., *Probing cellular protein complexes using single-molecule pull-down.* Nature, 2011. **473**(7348): p. 484-488.

229. Mendel, J.M., *Tutorial on higher-order statistics (spectra) in signal processing and system theory: theoretical results and some applications.* Proceedings of the IEEE, 1991. **79**(3): p. 278-305.

230. Chien, F.C., C.W. Kuo, and P. Chen, *Localization imaging using blinking quantum dots.* Analyst, 2011. **136**(8): p. 1608-1613.

231. Herbert, A., *Align FFT plugin, http://www.sussex.ac.uk/gdsc*, 2012.

232. Dertinger, T., et al., *Superresolution optical fluctuation imaging with organic dyes.* Angewandte Chemie - International Edition, 2010. **49**(49): p. 9441-9443.

233. Heilemann, M., et al., *Subdiffraction-resolution fluorescence imaging with conventional fluorescent probes.* Angewandte Chemie - International Edition, 2008. **47**(33): p. 6172-6176.

234. Michalet, X., et al., *Dynamic molecular combing: stretching the whole human genome for high-resolution studies.* Science, 1997. **277**(5331): p. 1518-1523.

235. Bensimon, D., et al., *Stretching DNA with a receding meniscus: experiments and models.* Physical Review Letters, 1995. **74**(23): p. 4754-4757.

236. Bensimon, A., et al., *Alignment and sensitive detection of DNA by a moving interface.* Science, 1994. **265**(5181): p. 2096-2098.

237. Herrick, J. and A. Bensimon, *Single molecule analysis of DNA replication.* Biochimie, 1999. **81**(8-9): p. 859-871.

238. Singhal, G., et al., *Adenovirus E1A oncogene induces rereplication of cellular DNA and alters DNA replication dynamics.* Journal of Virology, 2013. **87**(15): p. 8767-8778.

239. Lebofsky, R., et al., *DNA replication origin interference increases the spacing between initiation events in human cells.* Molecular Biology of the Cell, 2006. **17**(12): p. 5337-5345.

240. Burkhardt, M. and P. Schwille, *Electron multiplying CCD based detection for spatially resolved fluorescence correlation spectroscopy.* Optics Express, 2006. **14**(12): p. 5013-5020.

241. Thompson, N.L. and D. Axelrod, *Immunoglobulin surface-binding kinetics studied by total internal reflection with fluorescence correlation spectroscopy.* Biophysical Journal, 1983. **43**(1): p. 103-114.

242. McCain, K.S. and J.M. Harris, *Total internal reflection fluorescence-correlation spectroscopy study of molecular transport in thin sol-gel films.* Analytical Chemistry, 2003. **75**(14): p. 3616-3624.

243. Kannan, B., et al., *Electron multiplying charge-coupled device camera based fluorescence correlation spectroscopy.* Analytical Chemistry, 2006. **78**(10): p. 3444-3451.

244. *Physical properties of glycerine and its solutions*. 1963: Glycerine Producers' Association.

245. Jacobson, K., A. Ishihara, and R. Inman, *Lateral diffusion of proteins in membranes.* Annual Review of Physiology, 1987. **Vol. 49**: p. 163-175.

246. Saxton, M.J., *Anomalous diffusion due to binding: a Monte Carlo study.* Biophysical Journal, 1996. **70**(3): p. 1250-1262.

247. Miyawaki, A., *Proteins on the move: insights gained from fluorescent protein technologies.* Nat Rev Mol Cell Biol, 2011. **12**(10): p. 656-668.

248. Mütze, J., T. Ohrt, and P. Schwille, *Fluorescence correlation spectroscopy in vivo.* Laser & Photonics Reviews, 2011. **5**(1): p. 52-67.

249. Dahan, M., et al., *Diffusion dynamics of glycine receptors revealed by single-quantum dot tracking.* Science, 2003. **302**(5644): p. 442-445.

250. Dedecker, P., et al., *Widely accessible method for superresolution fluorescence imaging of living systems.* Proceedings of the National Academy of Sciences, 2012.

251. Sage, D., et al., *Automatic tracking of individual fluorescence particles: Application to the study of chromosome dynamics.* IEEE Transactions on Image Processing, 2005. **14**(9): p. 1372-1383.

252. Dertinger, T., et al., *Achieving increased resolution and more pixels with superresolution optical fluctuation imaging (SOFI).* Opt. Express, 2010. **18**(18): p. 18875-18885.

253. Geissbühler, S., C. Dellagiacoma, and T. Lasser, *Comparison between SOFI and STORM.* Biomedical Optics Express, 2011. **2**(3): p. 408-420.

254. Geissbühler, S., et al., *Mapping molecular statistics with balanced super-resolution optical fluctuation imaging (bSOFI).* Optical Nanoscopy, 2012. **1**(1): p. 4.

255. Watanabe, T.M., et al., *Real-time nanoscopy by using blinking enhanced quantum dots.* Biophysical Journal, 2010. **99**(7): p. L50-L52.

256. Habuchi, S., et al., *Reversible single-molecule photoswitching in the GFP-like fluorescent protein Dronpa.* Proceedings of the National Academy of Sciences of the United States of America, 2005. **102**(27): p. 9511-9516.

257. Ando, R., H. Mizuno, and A. Miyawaki, *Regulated fast nucleocytoplasmic shuttling observed by reversible protein highlighting.* Science, 2004. **306**(5700): p. 1370-1373.

258. Habuchi, S., et al., *Photo-induced protonation/deprotonation in the GFP-like fluorescent protein Dronpa: mechanism responsible for the reversible photoswitching.* Photochemical and Photobiological Sciences, 2006. **5**(6): p. 567-576.

259. Boulineau, R.L. and M.A. Osborne, *Direct object resolution by image subtraction: a new molecular ruler for nanometric measurements on complexed fluorophores.* Chemical Communications, 2013. **49**(49): p. 5559-5561.

260. Antelman, J., et al., *Nanometer distance measurements between multicolor quantum dots.* Nano Letters, 2009. **9**(5): p. 2199-2205.

261. Vaughan, J.C., S. Jia, and X. Zhuang, *Ultrabright photoactivatable fluorophores created by reductive caging.* Nat Meth, 2012. **9**(12): p. 1181-1184.

262. Zhang, M., et al., *Rational design of true monomeric and bright photoactivatable fluorescent proteins.* Nat Meth, 2012. **9**(7): p. 727-729.

263. Jackson, S.P. and J. Bartek, *The DNA-damage response in human biology and disease.* Nature, 2009. **461**(7267): p. 1071-1078.

264. Adler, J. and I. Parmryd, *Colocalization analysis in fluorescence microscopy*, in *Cell Imaging Techniques*, D.J. Taatjes and J. Roth, Editors. 2013, Humana Press. p. 97-109.

265. Jovanovic, K., et al., *Anti-LRP/LR specific antibodies and shRNAs impede amyloid beta shedding in Alzheimer's disease.* Sci. Rep., 2013. **3**.

266. Griffa, A., N. Garin, and D. Sage, *Comparison of deconvolution software in 3D microscopy: a user point of view*. Imaging & Microscopy, 2010. **12**(1): p. 43–45.

267. Berg, H.C., *Random Walks in Biology*. 1993: Princeton University Press.

268. Marsaglia, G. and T. Bray, *A convenient method for generating normal variables.* SIAM Review, 1964. **6**(3): p. 260-264.

ChemComm

RSC Publishing

COMMUNICATION

View Article Online
View Journal | View Issue

Cite this: *Chem. Commun.*, 2013, **49**, 5559

Received 21st March 2013,
Accepted 2nd May 2013

DOI: 10.1039/c3cc42072h

www.rsc.org/chemcomm

Direct object resolution by image subtraction: a new molecular ruler for nanometric measurements on complexed fluorophores†

Rémi L. Boulineau and Mark A. Osborne*

A technique for measuring distances between two or more fluorophores spaced in the 10–100 nm range is described. We identify a linear correlation between the intensity–amplitude in the difference-image of single molecules undergoing fluorescence fluctuations and their separation. The transform is used to map distances between coupled fluorophores.

Super-resolution techniques are now providing information on subcellular structures and biological mechanism at spatial scales, previously inaccessible with conventional microscopy.[1–5] While resolutions of 20 nm or less (FIONA)[6] can readily be achieved, experiments can be complex, either in instrumentation or in post-acquisition image analysis and point-spread-function (PSF) fitting. On the other hand, super-resolution optical fluctuation imaging (SOFI)[7] is elegant in its simplicity, based only on the high-order analysis of temporal fluctuations in single molecule fluorescence. However, for emitters only a few tens of nanometers apart, SOFI cannot readily separate the contributions from individual fluorophores. Alternative techniques exploit photobleaching,[8,9] blinking,[10–12] transient adsorption[13] or spectral differences[14] of multiple fluorophores in close proximity to retrieve individual localisations *via* conventional PSF-fitting.

Here we present a novel way to measure the distance between molecular centres directly from information in the difference-image of independently fluctuating single molecules. Specifically, we show a simple linear transform exists between the central intensity gradient in the difference-image of two closely spaced PSFs and their separation. The intrinsic fluorescence intermittency of quantum dots (QDs), coupled to the ends of a 100 bp double-stranded dsDNA (34 nm) in a dimeric complex is used to demonstrate the principle of direct object resolution by image subtraction (DORIS) and application of the technique to a higher order QD multimer highlights the generic nature of the approach. We demonstrate how DORIS can readily distinguish multimeric structures from single QDs and that measurement of the distance between fluorophores separated on the 10–100 nm scale is quantitative.

To illustrate the concept, consider two point emitters separated by a distance much less than the Rayleigh limit, $0.61\lambda/\mathrm{NA}$, for the resolution of their PSFs. Below this limit the PSFs strongly overlap such that emission typically appears to arise from a single source. However, subtraction of the individual PSFs from each other results in a difference-image that contains intensity maxima and minima at locations that are weakly related to, but well separated from, the emitting centres. More significant is the intensity-gradient between the extrema in the difference-image which is strongly correlated with the separation of the PSF centres. The correlation is most clearly highlighted in the difference between the 1D PSF cross-sections of two molecules separated at increasing distances (Fig. 1a). On the other hand, the position of the maxima and minima in the difference curve, appear far less sensitive to PSF displacement. For simulations of closely spaced PSFs in 2D (S1, ESI†), the sum image is

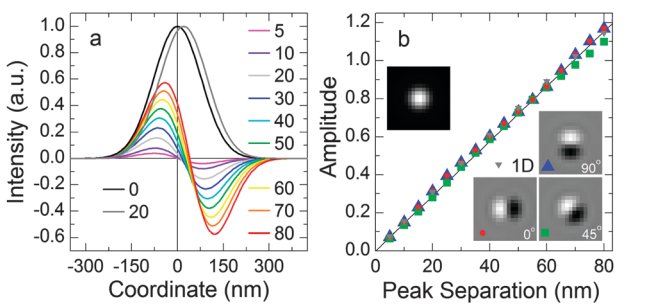

Fig. 1 Direct object resolution by image subtraction. (a) Normalised 1D PSF cross-sections centred at the origin (black) and 20 nm along x (gray). The difference between PSFs (light gray) at 20 nm separation is shown along with difference curves for PSF-separations of 5 to 80 nm showing distance dependent gradients. Here, the Gaussian function $I(x) = \exp(-(x - x_0)^2/2s^2)$ with standard deviation $s = \lambda/4\mathrm{NA}\sqrt{2\ln 2}$, λ = 530 nm and NA = 1.45, is used to represent the PSF cross-section. (b) DORIS amplitude-to-separation conversion curves. Amplitudes are derived from the difference between intensity maxima and minima in the difference-images of two simulated PSFs displaced along a vector at 0°, 45° and 90° to the x-ordinate. Difference-amplitudes from the 1D-Gaussians are also shown along with a linear-fit for guidance.

Department of Chemistry, School of Life Sciences, University of Sussex, Falmer, BN1 9QJ, UK. E-mail: m.osborne@sussex.ac.uk; Fax: +44 (0)1273 78323; Tel: +44 (0)1273 678328

† Electronic supplementary information (ESI) available: Experimental procedure and image analysis, simulation details and analysis of localisation and distance uncertainties. See DOI: 10.1039/c3cc42072h

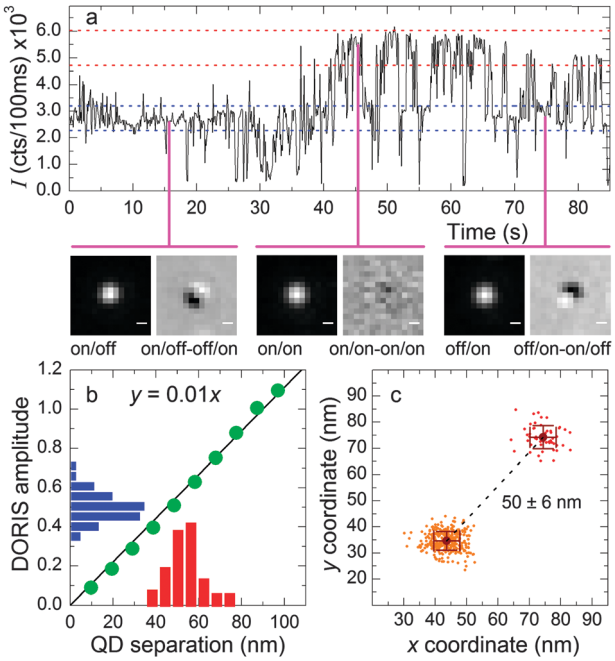

Fig. 2 Direct resolution of a dsDNA-QD dimer by image subtraction. (a) Integrated fluorescence intensity trajectory of a typical diffraction-limited dimer with images of QDs in on/off [10], on/on [11] and off/on [01] states and corresponding difference-images [1−1], [00] and [−11]. Scale bar 200 nm. (b) DORIS amplitude-to-separation conversion curve (green points) for the experimental resolution, 97 nm per pixel at 165× magnification and 2 × 2 pixel averaging of intensity maxima and minima in the difference-image. Also shown are the histograms of difference-amplitudes (blue) centred at 0.51 ± 0.06 and corresponding QD distances (red) centred at 53 ± 6 nm. (c) Localisations of the two QD centres in the dimer from conventional Gaussian fitting showing QD separation is in good agreement with the DORIS derived distance.

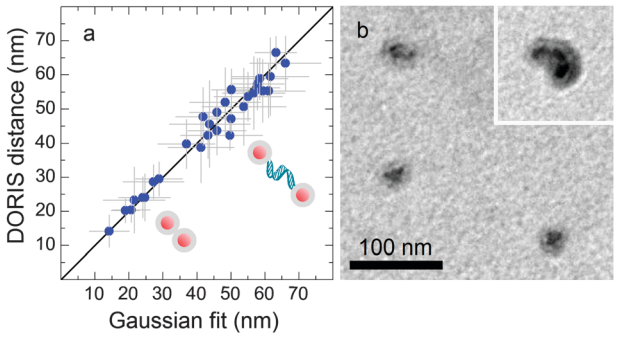

Fig. 3 Correlation plot between couple-QD separations derived from DORIS and distances from single molecule localisations in 30 QD-dimers. Uncertainties in both measurements are determined from the analysis of multiple frames from the image stack of each QD-dimer. A straight line representing the one-to-one correspondence is plotted for guidance. (b) TEM image of individual 585 nm streptavidin functionalised QDs with average core–shell diameter 23 ± 4 nm and (inset) a non-specifically coupled cluster of three QDs showing centre-to-centre distance of approx. 21 nm is not strongly influenced by surface functionality.

largely indistinguishable from the image of a single PSF (Fig. 1b, inset), while image subtraction reveals the same differential structure (in profile) as the 1D cross-section. Intensity variation in the difference-image contains information on the position of each molecule with respect to each other. Here, we exploit the sensitivity of the gradient in the difference-image with respect to PSF separation to generate a linear amplitude-to-distance correlation curve from which distances between molecules can be read directly (Fig. 1b). For simplicity the difference-amplitude rather than gradient is used, since the distance between intensity maxima and minima is insensitive to PSF separation. We find the difference-amplitude for both the 1D PSF cross-sections (Fig. 1a) and 2D PSF simulations show near-identical linear dependences on PSF separation. A small deviation in the correlation curve for 2D PSFs displaced along a vector oriented 45° to the x or y axes, arises from finite pixel size effects, but with an error of less than 10 nm at 80 nm displacement, the amplitude-to-separation conversion curves appear universal and largely independent of the direction of PSF displacement.

In a proof-of-application, we have used DORIS on closely coupled-QDs, where blinking in the fluorescence of at least one QD will result in a shift in centre-of-mass of the PSF and hence well-resolved difference-images. Streptavidin functionalised QDs (M10111P, Life Technologies) were coupled using 100 bp complementary sequences of biotinylated DNA (S2, ESI†) deposited on glass coverslips and imaged using total internal reflection fluorescence (TIRF) microscopy with typical capture rates of 10 fps into stacks of up to 2500 frames. The simplest approach to analyzing the image set of n frames $A = \{1\ldots n\}$, is to generate the set of difference-images, $B = \{1\ldots n(n-1)/2\}$, where each frame $B_{ij} = A_i - A_j$ for all i and $j > i$. In this case, two coupled-QDs independently switching between *on*(1) and *off*(0)-states generate on/off [10] and off/on [01] frame combinations that give rise to difference images [1−1] and [−11] with amplitudes between intensity extrema that are dependent on both QD separation and absolute intensities. Here, we introduced a binary notation to represent the state of each QD in an image frame [ ] and the result of image subtraction for simplicity. Normalizing QD peaks in each image prior to subtraction removes the intensity dependence, allowing QD distances to be read directly using the linear amplitude-to-separation transform.

In general, from the fluorescence trajectory of two QDs in close proximity (Fig. 2a), the [11] state (both QDs on) can be easily identified from the two level intensity trajectory. However, differentiating [10] from [01] states is only made clear through difference-imaging. Difference-images corresponding to [10] − [01] = [1−1], [11] − [11] = [00] and [01] − [10] = [−11] exemplify the DORIS process. Note that image stacks were corrected for stage-drift prior to image subtraction, a process essential to achieving image alignment and reduced uncertainty in localisation and distance measurements (S3, ESI†). Intensity–amplitudes in the difference-images of type [1−1] and [−11], are mapped directly to QD separation using the amplitude-to-separation curve (Fig. 2b green points). The histogram of amplitudes derived from the DORIS analysis across the image stack with mean amplitude 0.51 ± 0.06 (Fig. 2b blue bars) converts to a distribution of distances with mean QD separation of 53 ± 6 nm (Fig. 2b red columns).

We compared QD separations derived from amplitude-to-distance conversion with separations measured between single molecule localisations. DORIS was first used to differentiate [10] frames from [01] frames before locating each QD across all frames in each image set by fitting the 2D Gaussian function $I(x,y) = \exp[-(x - x_{1(2)})^2/2s^2 - (y - y_{1(2)})^2/2s^2] + I_0$ to the PSF of QD 1 and (2) separately (Fig. 2c). QD separations were then determined from the vectorial distance $[(x_1 - x_2)^2 + (y_1 - y_2)^2]^{1/2}$. Uncertainties of $\sigma \pm 7$ nm in the localisation coordinates result

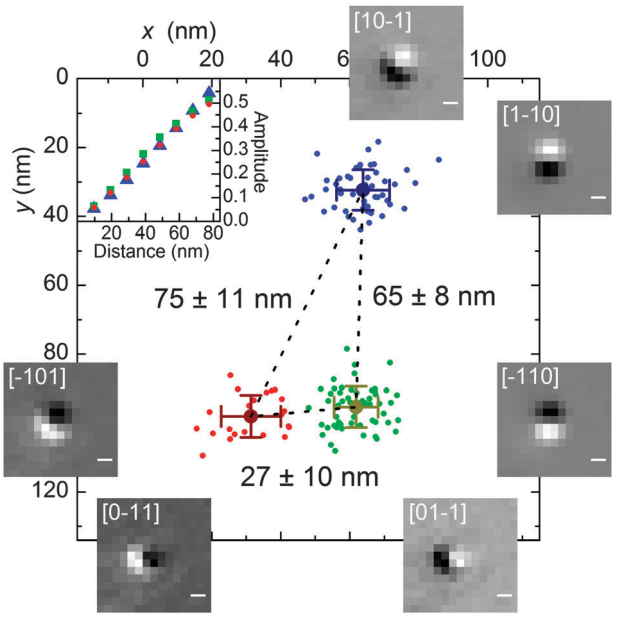

Fig. 4 Resolution of a sub-diffraction limited QD-multimer by DORIS. Single-QD localisations *via* Gaussian-fitting to individual PSFs are shown (red, green, blue) with distances determined from a DORIS analysis of intensity–amplitudes in the set of difference-images (subset shown overlaid). DORIS derived distances in the figure correspond closely to centre-of-mass separations from the individual QD localisations 63.0 ± 8.4 nm (blue-green), 30.6 ± 10.7 (green-red) and 73.2 ± 9.2 (red-blue). Difference-images are shown for the various combinations of pair-wise subtractions of frames in which one QD is on(1) and the others are off(0): blue = [100], green = [010] and red = [001]. Scale bar is 200 nm. (Inset) Amplitude-to-distance conversion curves along the QD displacement vectors (blue triangle = blue-to-green, green square = green-to-red, red circle = red-to-blue).

primarily from stage-drift, but also photon counting (Fig. S4 in ESI†) and ultimately propagate to an error of about ±10 nm in the distance between QDs. We find excellent one-to-one correspondence between DORIS derived distances and those measured by conventional localisation (Fig. 3a) across the population of QD-dimers analyzed. The result supports DORIS as a quantitative method of determining fluorophore separation in sub-diffraction limited nanostructures and complexes. The analysis reveals two populations of dimeric QD structures with different separations. We attribute a population emergent with distances centred at 23 ± 6 nm to directly and non-specifically coupled QDs. The value is consistent with the mean diameter, 23 ± 4 nm for individual streptavidin functionalised 585 nm QDs and centre-to-centre distances in QD clusters measured under TEM (Fig. 3b). A larger population of QDs found at 52 ± 11 nm separation is attributed to dsDNA coupled dimers, a value consistent within error of the QD diameter and an extended 100 bp DNA length of 34 nm.

In a further demonstration of DORIS, we extended difference-imaging to a trimeric-QD complex. Given the functionality of the QD extends over its entire surface and the tetravalent nature of the streptavidin binding protein, multiple DNA binding and formation of multimeric QD structures is expected. A DORIS analysis of the trimeric QD cluster in this case reveals all difference-images derived from combinations of the individual QD *on*-state frames [100], [010], [001] (Fig. 4). Respective QD separations 65.4 ± 8.1 nm, 26.5 ± 10.3 and 74.6 ± 11.4 determined from intensity amplitude-to-distance conversion in the difference-image combinations [1−10], [01−1] and [10−1] again show excellent agreement with the corresponding vectorial distances between Gaussian-localised QDs, 63.0 ± 8.4 nm, 30.6 ± 10.7 nm and 73.2 ± 9.2 nm. In this case, the QD-trimer appears to be constructed of two DNA-coupled QDs (50–60 nm) with a third QD coupled either non-specifically (20–30 nm) or with significantly compressed dsDNA.

We have developed DORIS as a novel method for resolving closely spaced fluorophores, with separations well below the diffraction-limit. Applied to multimeric-QD structures, we have shown that distances derived using DORIS are quantitative (within error) with respect to those calculated by conventional localisation techniques and consistent with TEM measurements. We note that in principle DORIS only requires modulation in the fluorescence with sufficient depth to produce intensity variation in the difference-image (S5, ESI†). For this purpose, fluorescence flickering in organic dyes, switching in fluorescent proteins could be utilized.[15,16] We envisage the method as complimenting established super-resolution techniques of PALM, STORM, SOFI and their derivatives, where high labeling densities or non-specific interactions can prohibit unambiguous resolution of fluorophores by conventional PSF fitting. Alternatively, we expect DORIS will find application in molecular counting in protein–protein(DNA) interactions and higher-order assembly of biological structures and offers the potential to provide structural information from the direct measurement of molecular separations.

We acknowledge the EC (FP7 grant 215148) for supporting R.B. and Prof. A. M. Carr and Dr A.-S. Schruers for their useful comments. We also thank Ms H. Aitchison (Nuffield Foundation undergraduate bursary) for help with aspects of image processing.

Notes and references

1 S. W. Hell and J. Wichmann, *Opt. Lett.*, 1994, **19**, 780–782.
2 M. G. L. Gustafsson, *J. Microsc.*, 2000, **198**, 82–87.
3 E. Betzig, G. H. Patterson, R. Sougrat, O. W. Lindwasser, S. Olenych, J. S. Bonifacino, M. W. Davidson, J. Lippincott-Schwartz and H. F. Hess, *Science*, 2006, **313**, 1642–1645.
4 S. T. Hess, T. P. K. Girirajan and M. D. Mason, *Biophys. J.*, 2006, **91**, 4258–4272.
5 M. J. Rust, M. Bates and X. Zhuang, *Nat. Methods*, 2006, **3**, 793–795.
6 A. Yildiz, J. N. Forkey, S. A. McKinney, T. Ha, Y. E. Goldman and P. R. Selvin, *Science*, 2003, **300**, 2061–2065.
7 T. Dertinger, R. Colyera, G. Iyer, S. Weiss and J. Enderlein, *Proc. Natl. Acad. Sci. U. S. A.*, 2009, **106**, 22287–22292.
8 M. P. Gordon, T. Ha and P. R. Selvin, *Proc. Natl. Acad. Sci. U. S. A.*, 2004, **101**, 6462–6465.
9 X. Qu, D. Wu, L. Mets and N. F. Scherer, *Proc. Natl. Acad. Sci. U. S. A.*, 2004, **101**, 11298–11303.
10 K. A. Lidke, B. Rieger, T. M. Jovin and R. Heintzmann, *Opt. Express*, 2005, **13**, 7052–7062.
11 B. C. Lagerholm, L. Averett, G. E. Weinreb, K. Jacobson and N. L. Thompson, *Biophys. J.*, 2006, **91**, 3050–3060.
12 D. T. Burnette, P. Sengupta, Y. H. Dai, J. Lippincott-Schwartz and B. Kachar, *Proc. Natl. Acad. Sci. U. S. A.*, 2011, **108**, 21081–21086.
13 P. D. Simonson, E. Rothenberg and P. R. Selvin, *Nano Lett.*, 2011, **11**, 5090–5096.
14 X. Shi, Z. Xie, Y. Song, Y. Tan, E. S. Yeung and H. Gai, *Anal. Chem.*, 2012, **84**, 1504–1509.
15 S. Habuchi, R. Ando, P. Dedecker, W. Verheijen, H. Mizuno, A. Miyawaki and J. Hofkens, *Proc. Natl. Acad. Sci. U. S. A.*, 2005, **102**, 9511–9516.
16 M. Heilemann, S. van de Linde, M. Schuttpelz, R. Kasper, B. Seefeldt, A. Mukherjee, P. Tinnefeld and M. Sauer, *Angew. Chem., Int. Ed.*, 2008, **47**, 6172–6176.